Comparative Analysis of Low Temperature Industrial Refrigeration Systems

by

Piyanon Mumanachit

A thesis submitted in partial fulfillment
of the requirements for the degree of

Master of Science
(Mechanical Engineering)

at the

UNIVERSITY OF WISCONSIN-MADISON

2009

Approved by

_____

Professor Gregory F. Nellis

December 19, 2008

Acknowledgements

First and foremost, I would like to express my deepest gratitude to my advisors, Professor Greg Nellis and Professor Doug Reindl, without whom this research project would not have been possible. Thank you, Greg, for your constant guidance, patience and positive encouragement. I have learned so much from you and have understood the responsibilities of a truly selfless giver. You have inspired me to become more than I could have ever imagined. Doug, I am truly grateful for your extraordinary aid and optimism both professionally and personally. You have been nothing but generous and have always provided more knowledge than I could have hoped. It is my great honor to have been one of your students.

Sincere thanks must be extended to many kind people who have provided priceless support for this research project. I would like to thank Bent Wiencke and Bruce Griffith for providing essential technical information support. Special thanks are expressed to Professor Tim Shedd and Dr. Zahid Ayub for their help with heat transfer correlation suggestions.

There are no words to describe my appreciation for the love and support from my family. I would like to thank my parents for their support and faith in their only son, without their support it would have been very difficult for me. I hope that I have fulfilled my responsibilities to the best of my abilities and that I have made you proud. My close friends and my pride and joy, you have made it possible for me to come this far. I cannot thank you enough for your consolation and moral support. I promise to do my best to make a difference as an engineer and as a human being.

Abstract

Nearly all industrial refrigeration systems in the food industry operate using anhydrous ammonia (NH_3) as a working fluid. The refrigerant ammonia has several advantages, including: high efficiency, high heat transfer rate capability, high heat capacity, and low refrigerant cost. Ammonia is also environmentally friendly. However, the toxicity of ammonia is a significant drawback that limits its use in non-industrial applications. Another drawback of ammonia arises at low operating temperatures where the saturation pressure of ammonia decreases and its specific volume increases significantly. The high specific volume of saturated ammonia vapor at low temperature leads to very large compression equipment required for systems that operate at low temperatures (below about -50^{o}F). Alternative refrigeration system designs are being evaluated in the industry in order to address this problem. One of these alternatives is the NH_3/CO_2 cascade refrigeration system configuration which uses CO_2 at low temperature in order to alleviate the undesirable thermodynamic property characteristics of ammonia.

The aforementioned cascade refrigeration system is comprised of two separate refrigeration circuits that are interconnected with an indirect heat exchanger, referred to as a cascade heat exchanger. In this arrangement, carbon dioxide (CO_2) is a refrigerant circulating through a low temperature circuit with ammonia as the refrigerant in a high temperature circuit. A desirable characteristic of CO_2 at low temperatures is its low specific volume (high density), which enables the cascade system to operate with reasonable size and efficient compressors operation and also leads to reduced vessel and pipe sizes. However, one challenge in using CO_2 as a refrigerant is the very large increase in saturation pressure that occurs with increasing saturation temperature (under sub-critical conditions). The use of CO_2 in a cascade arrangement with NH_3 attempts to manage the challenge of high working pressures by limiting its operating envelop to lower operating temperature; thereby, maintaining conditions where both carbon dioxide and ammonia exhibit favorable performance characteristics. The objective of this thesis is the quantitative comparison of the cascade system to a conventional two-stage ammonia system (i.e., a compound system).

This thesis presents a comparison of the performance and economic viability of an ammonia compound system to an NH_3/CO_2 cascade system applied to a low-temperature freezer application with a load of 680 Tons. The comparison is carried out through the development of detailed component models that are integrated in order to obtain a system model that is used to simulate each configuration over a year long operating period. Component-based system-level simulations provide the basis for identifying the relative operating costs of the two systems and therefore the life cycle savings associated with the operating costs. The difference in the capital cost associated with the two configurations is also estimated and used to determine the life cycle savings associated with the hardware costs. The total life cycle savings is the sum of these two components. The results of this analysis allow the selection of the most appropriate system configuration. The simulations indicate that the NH_3/CO_2 cascade system is more attractive than the two-stage NH_3 compound system for evaporating temperatures that are less than approximately -52^{o}F. Further, the cascade heat exchanger that appropriately balances performance with cost should be designed to have a pinch point temperature difference of 10^{o}F at its nominal operating conditions.

Table of contents

List of Figures

List of Tables

Nomenclature list

English Variables

Symbol	Description	SI unit
A	Area	m^2
$\dot{A}$	Availability rate	kW
ACC	Adjusted capital cost	$
ACD	Adjusted capital cost difference	$
AR	Area ratio	-
$\dot{C}$	Capacitance rate	kW/K
CAP	Heat removing capacity	kW
CFM	Volumetric flow rate	m^3/s
COP	Coefficient of performance	-
c_p	Constant pressure specific heat capacity	kJ/kg-K
c_v	Constant volume specific heat capacity	kJ/kg-K
D	Diameter	m
DP	Down payment fraction	%
EF	Enhancement factor	-
f	Flash gas percentage	%
F_h	Heat exchanger height	m
F_{thk}	Fin thickness	m
FC	First cost/capital cost	$
$FFLP$	Fraction of full-load power	%
$frac$	Fraction	%
G	Mass flux	kg/m^2-s
h	Specific enthalpy	kJ/kg
h_{sub}	Enthalpy of sublimation of water	kJ/kmol
hc	Convective heat transfer coefficient	kW/m^2-K
hm	Convective mass transfer coefficient	kg/m^2-K
HP	Fan motor rated power	kW
HPR	High pressure receiver	-
HX	Heat exchanger	-
HX_h	Heat exchanger height	m
HX_L	Heat exchanger length	m
i	General inflation rate	%
i_f	Fuel inflation rate	%
j_a	Colburn factor	-
k	Thermal conductivity	kW/m-K
L	Length	m
Le	Lewis number	-

LCC	Life-cycle cost	$
LCS	Life-cycle cost savings	$
m	Mortgage interest rate	%
MT	Maintenance cost fraction	%
N	Number of (quantity)	-
NTU	Number of transfer units	-
Nus	Nusselt number	-
OC	Operating cost	$
P	Pressure	kPa
P_{fin}	Fin pitch	m
P_L	Tube longitudinal pitch	m
P_t	Tube transverse pitch	m
PDF	Premium difference fraction	%
PLR	Part-load ratio	-
POW	Compressor rated power	kW
PR	Pressure ratio	-
Pr	Prandtl number	-
$\dot{Q}$	Rate of heat transfer	kW
$\dot{q}$"	Heat flux	kW/m^2
$\dot{Q}_C$	Heat rejection at evaporative condensers	kW
$\dot{Q}_L$	Heat load at evaporators	kW
R	Thermal resistance	K/kW
r	Relative humidity	%
$r_{fin,i}$	Equivalent inner fin radius	m
$r_{fin,o}$	Equivalent outer fin radius	m
Re	Reynolds number	-
$\overline{Re}$	Average Reynolds number	-
s	Specific entropy	kJ/kg-K
S	Entropy	kJ/K
SDT	Saturated discharge temperature	K
SST	Saturated suction temperature	K
$STAR$	Shell-to-tube area ratio	-
$STLR$	Shell-to-tube length ratio	-
t	Effective tax rate	%
T	Temperature	K
$\overline{T}$	Average temperature	K
T_{db}	Dry-bulb temperature	K
T_{wb}	Wet-bulb temperature	K
th	Thickness	K
$\overline{u}$	Average flow velocity	m/s
UA	Conductance rate	kW/K
$\dot{W}$	Electrical power input	kW

x	Quality/vapor mass fraction	%
y	Fin parameter	m

Greek symbols

Symbol	Description	SI unit
α	Thermal diffusivity	m^2/s
Δ	Difference	-
ε	Effectiveness	%
η	Thermal efficiency	%
γ	Dimensionless coefficient in pool boiling correlation	-
ω	Humidity ratio	kg_w/kg_a
Σ	Summation	-
ρ	Density	kg/m^3
μ	Dynamic viscosity	Pa-s
ν	Kinematic viscosity	m^2/s

Subscripts

Symbol	Description
0	Ambient condition
a	Air side
act	Actual
avg	Average
B	Booster compressor
b	Bare, without fins
BOOSTER	Booster compressor
C	Expressed in degree Celsius
cas / *cascade*	Cascade heat exchanger/Cascade system
CO_2	Carbon dioxide
comp	Compressor
compound	Compound/Multi-stage system
cond	Condensing
condenser	Condenser
contact	Intersection between fin and tube surfaces
cross	Cross-sectional
des	Destruction
eff	Effective
eq	Equivalent
evap	Evaporating
evaporator	Evaporator
F	Expressed in degree Fahrenheit

face	Face
fan	Fan
fc	Forced-convection
fin	Fin
fin,tube	Fins per tube
FL	Full-load
flow	Flow
gen	Generation
H	High-pressure compressor
h	Height
HPC	High-pressure compressor
HT	Heat transfer
HTC	High-temperature circuit
i	Inlet
II	2nd Law of Thermodynamics
int	Intermediate
L	Length
liq	Saturated liquid phase
LTC	Low-temperature circuit
max	Maximum
min	Minimum
mod	Modified
N	Nominal
nb	Nucleate boiling
NH_3	Ammonia
o	Outlet
PL	Part load
produced	Produced
Q	Associated with heat transfer
r	Refrigerant
res	Resistance
S	Refrigerated space
s	Isentropic
sat	Saturated/condensing section
sh	De-superheating section
shell	Shell/shell side
supplied	Supplied
sur	Surface
TAS	Saturated at air temperature
tip	tip
tot	Total
tp	Two-phase
TRS	Saturated at refrigerant temperature

tube	Tube
v	Vertical direction
vap	Saturated vapor phase
wall	Wall

Chapter 1) Introduction

1.1) Industrial Refrigeration Overview

Industrial refrigeration is descriptive of the technology used to remove heat from controlled temperature spaces and processes in industrial or manufacturing environments. Operating temperatures for these systems can range from -60^{o}C (-76^{o}F) or colder to as high as 15^{o}C (60^{o}F). Typical applications requiring industrial refrigeration includes pharmaceutical productions, chemical processing, food manufacturing, large-scale storage and transportation of perishable products. Providing refrigeration at temperatures much lower than about -70^{o}C (-94^{o}F) is referred to as cryogenics and typically is accomplished using liquefied gas, such as liquid nitrogen or liquid oxygen, instead of conventional volatile refrigerants found in vapor compression systems. Each application or individual processes requiring refrigeration will dictate detailed aspects of refrigeration system design and operation in order to achieve an appropriate range of temperatures for the purpose of removing heat loads. Industrial refrigeration is quite different from industrial air conditioning, which is usually aimed at providing comfortable air conditioning temperatures; air conditioning systems typically operate at higher temperatures and are designed for human comfort only.

1.2) Applications in Food Industry

The idea of preserving food for a long period of time using low temperature storage was discovered by accident in 1880 when meat being shipped from Australia to England froze unintentionally (Lawrence, 2003). The meat was observed to last much longer in its frozen state. This discovery led to the practice of intentionally freezing perishable goods in order to maintain quality. In the early 1900's, Clarence Birdseye experimented with freezing a variety of food products using a plate-type freezer that he had developed. Many years later, the discovery of quick freezing (i.e., freezing products in several hours as opposed to several days) gave rise to the modern day frozen food industry. Today, this industry generates more than $8 billion worth of revenue per year while producing more than 1,500 different items (Stoecker, 1988).

Food processing, beverage processing, refrigerated storage of foodstuffs, and transportation of frozen products are some of the many applications within the food industry that rely on industrial refrigeration. In these end-use applications, even the simplest of operations often require some degree of refrigeration. All types of food plants, from poultry processing to cold storage warehouse to dairy operations, demand a very broad range of controlled temperature environments. For instance, a blast freezing process where products are exposed to cold air at high velocity to lower the product's temperature in a relatively short time period requires a large refrigeration capacity at very low operating temperatures (usually below -40^{o}F). On the other hand, a holding freezer where final products are stored at higher but still sub-zero temperatures (around -20^{o}C (-4^{o}F)) before they are transported to distribution warehouses elsewhere, requires less intensive refrigeration, but warehouse thermal conditions must be well regulated in order to protect product shelf life and quality. In raw product preparation and production areas, circulating air temperature and humidity level must be maintained in narrow bands in order to minimize the growth of bacteria and other pathogens in the space. These facilities often rely on the delivery of temperature-controlled and sanitized supply air.

The need to process, store and transport perishable products at low temperatures, while prolonging product life and sustaining uncompromised quality, is continually increasing. To meet this demand with long-term sustainability, proper system design and appropriate refrigerant choice are crucial.

1.3) Refrigerant Selection

Although many different refrigerants are available, any given refrigerant will have trade-offs that need to be understood for a given application. This section will explore characteristics that are consistent with an appropriate refrigerant as well as discussion of important criteria for refrigerant selection. Basic criteria that should be considered when selecting a refrigerant often includes enthalpy of vaporization, operating pressure range, physical properties, transport properties, toxicity, flammability, cost and extent of environmental impact. It is preferable that a refrigerant possesses reasonably high enthalpy of vaporization because vapor compression refrigeration systems operate based on the heat absorbed by the refrigerant causing it to evaporate. Ammonia (R-717) has a substantially higher heat of vaporization compared to another refrigerant that finds limited use in industrial refrigeration systems, R-22.

Another desirable property of a prospective refrigerant is no or low flammability to avoid danger of fire hazard or explosion by ignition in the case of a leak. Any refrigerant compound containing hydrocarbon, such as methane (CH_4) and propane (C_3H_8), may be flammable depending on the relative amount of the hydrocarbon. If enough of the hydrocarbon is replaced with halogen, then the refrigerant's flammability will become reduced or eliminated. Some of the early refrigerants (e.g., ether, acetone and alcohol) never achieved widespread use due to their high flammability. Another consideration when selecting a refrigerant is toxicity. As noted previously, ammonia's toxicity is a concern and requires careful management since exposure to ammonia at a level of 0.5 (5,000 ppm) to 1% (10,000 ppm) in air for a period on the order of minutes can result in death. Carbon dioxide (CO_2), hydrocarbon compounds and chlorofluorocarbons (CFCs) offer the advantage of lower toxicity. Lower toxicity is one of the reasons that carbon dioxide was used extensively on ships from the late 1800's until 1955 when it was replaced with CFCs. In 1996, CFCs were banned according to Montreal protocol due to their major contribution to ozone depletion (Lawrence, 2003).

Another characteristic of a good refrigerant is a reasonable operating pressure range. Refrigerants that have thermodynamic characteristics that translate into high operating pressures must use special equipment with stronger materials of construction. Typically in an industrial refrigeration system, the highest condensing pressure does not exceed 200 psig (1,480 kPa) with design pressures of equipment on the order of 250 psig or 300 psig. Because carbon dioxide is supercritical with very high corresponding pressures when operating at temperatures corresponding to a traditional heat rejection system. This necessitates refrigeration equipment designs with very high working pressures (Lawrence, 2003). On the other hand, if the refrigerant operating pressure is too low (below atmospheric pressure), in any part of the system, then the system requires vacuum-related equipment and problems associated with outside air and water vapor leaking into the system may occur.

Anhydrous ammonia (R-717) is one of the refrigerants that is most often selected for industrial refrigeration systems because of its high heat transfer coefficient, high heat capacity and low cost. As a natural refrigerant, its impact on the environment is also minimal; its global warming potential (GWP) and ozone depletion potential (ODP) are both zero (Lawrence, 2003). However, ammonia is highly toxic and corrosive to human tissue. Fortunately, ammonia gives off a strong pungent odor which allows easy and early detection in the event of a leak. With hydrochlorofluorocarbons (HCFCs), e.g. R-22, being scheduled for phase-out in the next decade, carbon dioxide is another natural refrigerant that has recently regained interest for industrial refrigeration. It is non-toxic, non-flammable with GWP of 1 and ODP of 0 (Page, 2002). Although carbon dioxide is not as efficient as ammonia at moderate temperatures, it could still be used as an alternative to ammonia at low temperatures where the operating pressure of ammonia and its density are too low. For this research project, ammonia is selected as the primary refrigerant in the multi-stage system and in the high-temperature circuit of the cascade system. Meanwhile, carbon dioxide is selected as the low-temperature circuit refrigerant of the cascade system.

1.4) Baseline Operating Conditions

The baseline operating conditions used for the comparative analysis of the two system configurations presented in this thesis are selected in order to match an existing 680-ton large dry-freezing plant utilizing a cascade system configuration operating with ammonia and carbon dioxide in the high and low temperature circuits, respectively. This particular plant is located in the UK and is operated by Nestle Inc. (Homsy, 2003). The baseline operating conditions, e.g. saturated evaporating and condensing temperatures and the low temperature circuit refrigeration load, for the multi-stage system are assumed to be identical to those of the existing cascade system. The operating parameters for both systems described are summarized as follows.

Table 1-1: Baseline/design operating parameters specified for an initial analysis

Variable	***Parameter***	***Value***
$\dot{Q}_L$	Refrigeration load	680 Tons (2,391 kW)
$T_{evap,sat}$	Evaporating temperature	-40 ^{o}C (-40 ^{o}F)
$T_{cond,sat}$	Saturated condensing temperature	35^{o}C (95^{o}F)
T_0	Dead state temperature	25^{o}C (77^{o}F)
T_S	Refrigerated space temperature	-30^{o}C (-22^{o}F)

These parameters are presented only as a baseline for the system's initial operation, during modeling of the system and economic analyses, some of the parameters will be changed or varied.

1.5) Literature Review

This section is a review of the literature search describing the work that is relevant to the analysis and modeling of ammonia refrigeration and NH_3/CO_2 cascade systems. This survey of literature search extends over the subjects of refrigeration cycle configurations, correlations for heat transfer coefficients for various types of flow, refrigeration system setup consideration, and frost formation mechanisms. A complete list of the literature search that was accomplished during the course of this research project is included in the References section. A description of technical papers and journals that were considered most useful for this thesis follows.

Lee, T.-S., Liu, C.-H., Chen, T.-W., "Thermodynamic analysis of optimal condensing temperature of cascade-condenser in CO_2/NH_3 cascade refrigeration systems", *International Journal of Refrigeration,* Vol. 29, 2006, pp. 1100-1108.

This paper presents a thermodynamic analysis of a cascade vapor compression refrigeration cycle operating with ammonia (R-717) and carbon dioxide (CO_2). The objective of this paper is to determine the optimum cascade condensing temperature and its corresponding maximum COP based on the given saturated condensing temperature, saturated evaporating temperature and cascade condenser pinch-point temperature difference. To make the compressor models more realistic, two correlations for compressor isentropic and volumetric efficiency as a function of pressure ratio, based on experimental data, are utilized in simulation model. This paper also presents exergy analysis to minimize system exergy destruction in each component; the rate of exergy destruction in each system component is shown as a function of the cascade condensing temperature.

Manske, K. A., (1999) *Performance Optimization of Industrial Refrigeration Systems*. M.S. Thesis, Mechanical Engineering, Solar Energy Laboratory, University of Wisconsin-Madison.

This research thesis presents in-depth analyses of performance optimization in every component of an industrial refrigeration system. Performance modeling of the system is created and compared to experimental data taken from a conventional two-stage ammonia refrigeration plant, in Milwaukee, WI, to validate the fidelity of the model. The objective of this project is to utilize the model to create appropriate design and identify the most suitable operating techniques in order to maximize the system performance. All peripheral factors, such as operating condition and different equipment type, attributing to performance efficiency improvement are identified and analyzed for each individual system component. Further, implementation of energy saving tool, such as variable frequency drive (VFD), is analyzed to evaluate its effect on performance efficiency.

Lachner, B. F., (2004) *The Use of Water as a Refrigerant: Impact of Cycle Modifications on Commercial Feasibility.* M.S. Thesis, Mechanical Engineering, Solar Energy Laboratory, University of Wisconsin-Madison.

This research project presents thermodynamic and economic analyses of utilizing water as a refrigerant in a vapor compression refrigeration system. The system operating parameters are given based on a system operating with a 1000-Ton industrial water chiller plant. Several system configurations are proposed and thermodynamic analysis is performed to determine the most efficient setup. This vapor compression cycle operating with water is also compared to similar systems operating with HFC, such as R-134a and R-12. Ultimately, economic analysis of the cycle operating over its life cycle is presented in comparison to an R-134a system. The economic attractiveness is measured by greater life cycle savings (LCS) from lower annual operating cost and initial installation cost.

Stephan, K. and Abdelsalam, M., "Heat Transfer Correlations for Natural Convection Boiling," *Int. J. Heat Mass Transfer*, Vol. 23, 1980, pp. 73-87

This paper discusses an alternative methodology of deriving boiling heat transfer correlations mathematically using existing experimental data. In the literature, there existed no suitable correlations for predicting of boiling heat transfer coefficient. The objective of this paper is to develop suitable correlations in predicting boiling heat transfer coefficient for various kinds of fluids, ranging from water to refrigerants. The general forms of the correlations are presented for each type of fluid and appropriate coefficients and exponents within each correlation are selected based on the experimental data for each specific fluid name and boiling condition.

Zheng, J. X., Jin, G. P., Chyu, M.-C., and Ayub, Z. H., "Flooded Boiling of Ammonia with Miscible Oil Outside a Horizontal Plain Tube", *International Journal of Heating, Ventilating, Air-Conditioning and Refrigerating Research,* Vol. 7, No. 2, 2001, pp. 185-204.

This paper presents experimental results of nucleate boiling heat transfer coefficient of ammonia on a plain steel tube. The tests are conducted with and without miscible lubricant to quantify the effect of oil film residue on shell-side heat transfer coefficient of ammonia. The range of saturation temperatures of ammonia under investigation is from -23.3^{o}C to 7.2^{o}C (-10^{o}F to 45^{o}F) and heat flux up to 60 kW/m^2 (19,000 Btu/hr-ft^2). The results show that the nucleate boiling heat transfer coefficient increases with increasing heat flux as it promotes boiling rate. Since there are not many nucleate boiling heat transfer coefficient data available in the literature, the correlations are developed and presented in this paper based on the experimental results.

Cavallini, A., Censi G., Del Col D., Doretti L., Longo G.A., Rossetto L., "In-tube Condensation of Halogenated Refrigerants," *ASHRAE Transactions*, 2002, paper H-1718.

This paper compares different correlations for predicting the heat transfer coefficient of halogenated refrigerants during condensation inside a smooth surface tube. In the literature, the results do not agree very well and no absolute best correlation could be selected. Even the correlation suggested by ASHRAE in the *2001 ASHRAE Handbook—Fundamentals* is found to be inadequate to predict the heat transfer coefficients, both with old and new generation refrigerants. Thus, this paper presents a generalized heat transfer coefficient and pressure drop prediction model applicable for all halogenated refrigerants under conditions encountered in modern technology refrigeration.

Page, A., "CO_2/NH_3 Refrigeration Replaces R-22 in Large Freeze-Drying Plant", Technical Paper #1, *IIAR Ammonia Refrigeration Conference, Kansas City, Missouri,* 2002, pp. 1-27.

This paper describes the process of replacing an existing 680-Ton freeze-drying plant operating with R-22 with a cascade system using NH_3/CO_2. The technical aspects as well as engineering aspects of this implementation are explored in detail. There are a few attractive system configuration alternatives to the original system with R-22, including conventional two-stage ammonia system, hydrocarbons multi-refrigerant scheme, closed-circuit air cycle refrigeration (CCAR) and CO_2 in cascade with ammonia (NH_3/CO_2). Carbon dioxide proves to cope well with the drawbacks of ammonia when operating at low temperature (below -40^{o}F). In addition, CO_2-related equipments, especially the booster compressors, tend to be smaller than conventional systems due to lower specific volume of CO_2 vapor at low evaporating temperature range. The cascade configuration is favored over the conventional ammonia system also because CO_2 is the refrigerant of choice for it is a natural, odorless, and non-toxic refrigerant with zero GWP and ODP.

Homsy, P., "Ammonia/CO_2 Cascade System in a Large Freeze-Drying Plant: Lessons Learned During Installation and Commissioning", Technical Paper #10, *IIAR Ammonia Refrigeration Conference, Albuquerque, New Mexico,* 2003, pp. 317-355

This technical paper describes essential technical issues and problems encountered during the installation phase of the new cascade system replacing the old system that was operating with R-22. Special consideration and material selection and construction of various system components are listed and described in detail, especially for the two cascade heat exchangers (CHEs). Some of the problems often encountered with the CHEs include oil leakage between oil separation units caused by defective weld on ammonia screw packages unit, which results in a decrease in CHEs performance. This paper also reports energy savings of the new cascade system of more than 20% during the first stage of operation compared to the previous R-22 system.

Aljuwayhel, N. (2006) *Numerical and Experimental Study of the Influence of Frost Formation and Defrosting on the Performance of Industrial Evaporator Coils*. Ph.D. Thesis, Mechanical Engineering, Solar Energy Laboratory, University of Wisconsin-Madison.

This research thesis presents in-depth analysis of frost formation on an ammonia evaporator coil. A computer simulation of the thermal performance of the evaporator under the influence of frost accumulation is described and used to optimization the hot-gas defrost process. The results are validated with experimental data obtained from a 130-kW penthouse evaporator located at Wells' Dairy in Iowa. The frost accumulation model is quasi-steady state with frost density and frost layer thickness predicted given as a function of time based on the integration of the instantaneous rate of frost buildup. The evaporator coil capacity degrades over time when frost accumulates on fin and tube surfaces, primarily because the frost buildup on the evaporator coil physically obstructs the air flow path. As a result, the static pressure across the coil increases causing a reduction in volumetric flow rate of re-circulated air and in evaporator coil cooling capacity.

O'Neal, D.L. and Tree, D.R., "Measurement of Frost Growth and Density in a Parallel Plate Geometry", *ASHRAE Transactions*, 89, 1984, pp. 278-290.

This paper presents an experimental study of frost formation on vertical plates in parallel-plate air-to-air heat exchanger geometry. In previous literature, numerous studies showed diverse experimental results of frost growth and quantified different factors that affect the results. This paper aims to conduct experimental study on frost growth and density in aforementioned geometry over a range of environmental conditions typically encountered by heat pumps. Air temperature, humidity and plate temperature are some of the conditions under investigation to quantify those that do affect frost formation. Further, empirical data of frost growth are created for these given environmental conditions.

O'Neal, D.L. and Tree, D.R., "A Review of Frost Formation in Simple Geometries", *ASHRAE Transactions,* 91, 1985, pp. 267-281.

This paper reviews frost growth studies and correlations taken from various sources in literature within the past 50 years; this paper divides frost growth study into three categories starting with frost properties relevant to frost layer thickness prediction and thermal performance modeling, such as frost density and frost thermal conductivity. The next category presents effect of frost growth on different heat exchanger geometry, including flat plates, parallel plates, cylinder and annuli. The last category involves experimental measurement of heat transfer quantities and implication of empirical correlations in frost growth prediction.

Chapter 2) Cycle Descriptions

The computer model is developed based on a detailed thermodynamic analysis (1st and 2nd Law) of the underlining processes within the multi-stage and cascade vapor compression refrigeration cycles. The following sections describe a step-by-step analysis of the two cycles.

2.1) Multi-Stage Vapor Compression Cycle

The compound cycle is similar to a conventional single-stage vapor compression cycle; however, an additional stage of compression is integrated into the system between the evaporating pressure and condensing pressure. To prevent overheating the high-stage compressor, an intercooler is used to de-superheat the superheated refrigerant leaving the low-stage booster compressors.

2.1.1) Cycle Configuration

A multi-stage, or compound, refrigeration cycle can provide cooling at lower evaporating temperature than a single-stage cycle, which has a shortcoming in high pressure lift across one compression stage. A schematic diagram of an ammonia compound system is illustrated in Figure 2-1.

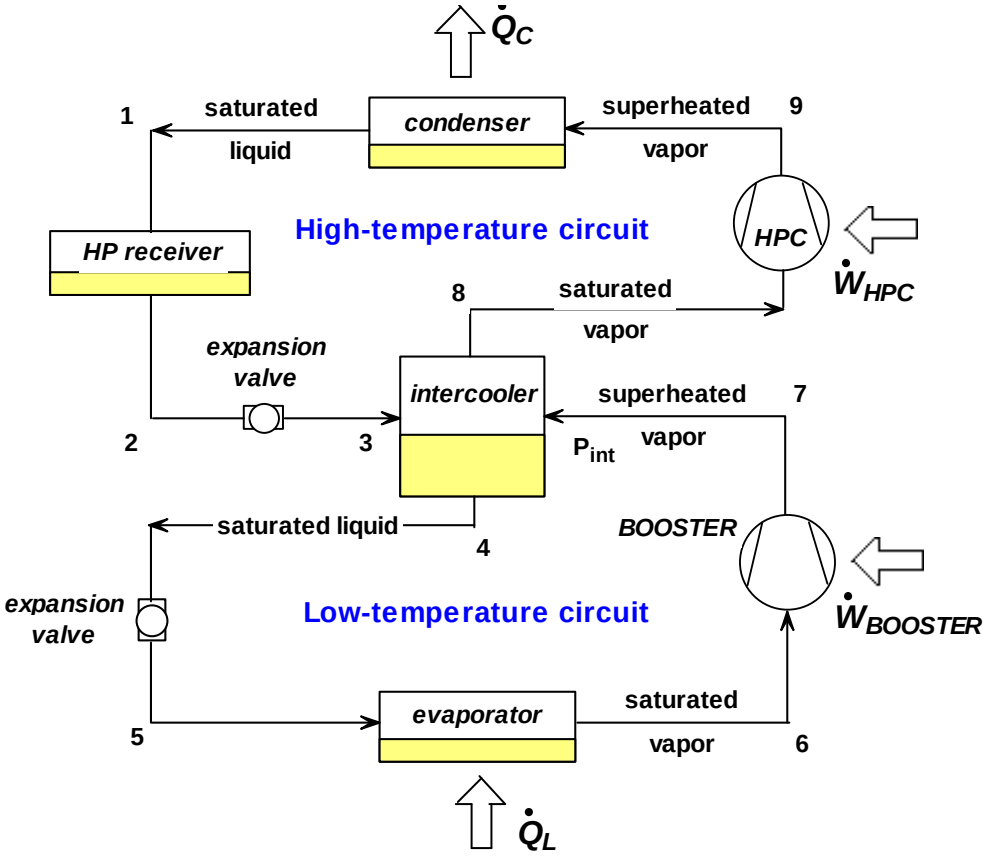

Figure 2-1: Schematic diagram of a multi-stage vapor compression cycle

2.1.2) 1st Law Analysis

In order to run the computer model of a multi-stage compression cycle, it is necessary to input seven parameters, including: refrigerant type (*fluid$*), the saturated temperature of the condensing and evaporating refrigerant ($T_{cond,sat}$ and $T_{evap,sat}$, respectively), the intermediate pressure (P_{int}), the rate of heat transfer to the evaporator ($\dot{Q}_L$), and the isentropic efficiencies for booster and high-pressure compressors ($\eta_{BOOSTER}$ and η_{HPC}, respectively).

It is assumed that the refrigerant leaves the condenser as saturated liquid and pressure loss on the refrigerant side of the condenser is neglected. Therefore, the temperature at state (1) is the user input condensing temperature and this assumption is only true for the design calculation. During actual operation, the saturated condensing pressure corresponding to $T_{cond,sat}$ is determined based on an energy balance of the system that matches the system total heat rejection.

$$T_1 = T_{cond,sat} \tag{2-1}$$

and the quality is equal to zero:

$$x_1 = 0 \tag{2-2}$$

The remaining properties at state (1) include enthalpy (h_1), entropy (s_1), specific volume (v_1), and pressure (P_1); these properties are obtained using EES' built-in property routines evaluated at T_1 and x_1.

The high-pressure receiver (HPR) is a vessel that stores refrigerant flowing out of the condenser. Depending upon operating conditions, (in particular, the mass flow rate in the high-temperature circuit), the amount of refrigerant flow is controlled by valves drawing liquid from the high pressure receiver. In a sense, the receiver provides a degree of freedom for liquid flow since it is capable of increasing, decreasing, or even stopping its outflow of refrigerant to the system while continuing to accumulate condensed liquid from the heat rejection system. However, for steady operation, the refrigerant properties leaving the high-pressure receiver at state (2) are the same as the properties entering the receiver at state (1).

The expansion device in the high temperature portion of the system is assumed to be adiabatic. Therefore, an energy balance on the valve leads to:

$$h_3 = h_2 \tag{2-3}$$

The refrigerant flowing from the high-pressure receiver through the first expansion valve is subjected to the intermediate pressure condition associated with the intercooler. As a result, the throttled refrigerant undergoes phase change. The portion of the refrigerant that is vaporized is called "flash gas." The intermediate pressure is assumed to be spatially uniform and therefore,

all of the refrigerant streams entering or leaving the intercooler, i.e., states (3), (4), (7), and (8), are at the specified intermediate pressure (P_{int}):

$$P_{int} = P_3 = P_4 = P_7 = P_8 \tag{2-4}$$

In this analysis, one approach is to fix the intermediate pressure at the geometric mean between the saturated evaporating pressure ($P_{evap,sat}$) and saturated condensing pressure ($P_{cond,sat}$) of the system. This is to equalize the pressure ratios of the booster and high pressure compressors. For this analysis, P_{int} is defined as,

$$P_{int} = \sqrt{P_{evap,sat}\, P_{cond,sat}} \tag{2-5}$$

where $P_{evap,sat}$ and $P_{cond,sat}$ correspond to absolute values of pressures for P_5 and P_1, respectively.

The remaining properties of the refrigerant leaving the expansion valve are determined by the pressure (P_3) and enthalpy (h_3); these include the temperature (T_3), entropy (s_3), quality (x_3), and specific volume (v_3).

Vapor drawn off of the vapor space in the intercooler enters the high-stage or high-pressure compressor (*HPC*) at state (8). This vapor is assumed to be a saturated vapor; therefore, its quality is equal to one:

$$x_8 = 1 \tag{2-6}$$

The remaining properties at the HPC suction include entropy (s_8), specific volume (v_8), temperature (T_8) and enthalpy (h_8); these properties are obtained using EES' built-in property routines evaluated at P_8 and x_8 .

The ideal compression process is isentropic:

$$s_{9,s} = s_8 \tag{2-7}$$

where $s_{9,s}$ is the entropy leaving a reversible and adiabatic compressor. The pressure drop across between the compressor discharge and the condenser inlet is neglected as is the pressure drop through the condenser and therefore, the HPC discharge pressure is assumed to be equal to the operating pressure of the condenser:

$$P_9 = P_1 \tag{2-8}$$

The enthalpy of the fluid leaving a reversible, adiabatic compressor ($h_{9,s}$) is computed using EES' built-in property routines evaluates at $s_{9,s}$ and P_9. The actual enthalpy at state (9) is computed using the definition of the high-stage compressor isentropic efficiency:

$$\eta_{HPC} = \frac{h_{9,s} - h_8}{h_9 - h_8} \tag{2-9}$$

The remaining properties at state (9) are obtained using EES' built-in property routines evaluated at P_9 and h_9.

The refrigerant exiting the intercooler and entering the low-temperature circuit is assumed to be saturated liquid:

$$x_4 = 0 \tag{2-10}$$

The remaining properties at state (4) include temperature (T_4) entropy (s_4), specific volume (v_4) and enthalpy (h_4); these properties are obtained using EES' built-in property routines evaluated at P_4 and x_4.

The low pressure expansion valve is assumed to be adiabatic; thus, an energy balance leads to:

$$h_5 = h_4 \tag{2-11}$$

The temperature of the fluid leaving the expansion valve is the user input value of the saturated evaporating temperature:

$$T_5 = T_{evap,sat} \tag{2-12}$$

This saturation temperature corresponds to the pressure being maintained in the evaporator by modulating the capacity of the booster compressor(s) based on the prevailing refrigeration load.

The remaining properties at state (5) include quality (x_5), entropy (s_5), specific volume (v_5), and pressure (P_5); these properties are obtained using EES' built-in property routines evaluated at T_5 and h_5.

The rate of heat transfer to the evaporator ($\dot{Q}_L$) coupled with the control of refrigerant supplied to the evaporator causes the refrigerant to exit at state (6) as saturated vapor:

$$x_6 = 1 \tag{2-13}$$

The refrigerant-side pressure drop through the evaporator is neglected and therefore the pressure of the fluid leaving the evaporator is equal to the pressure of the fluid leaving the low temperature expansion valve, state (5):

$$P_5 = P_6 \tag{2-14}$$

The remaining properties at state (6) include temperature (T_6), enthalpy (h_6), entropy (s_6) and specific volume (v_6) and are obtained using EES' built-in property routines evaluated at P_6 and x_6.

The entropy of the refrigerant leaving a reversible and adiabatic booster compressor is:

$$s_{7,s} = s_6 \tag{2-15}$$

The pressure drop across the intercooler is neglected and therefore the exit pressure of the compressor is assumed to be equal to the intermediate pressure. The enthalpy of the fluid leaving a reversible, adiabatic booster compressor ($h_{7,s}$) is computed using EES' built-in property routines evaluates at $s_{7,s}$ and P_7. The actual enthalpy at state (7) is computed using the definition of the booster compressor isentropic efficiency:

$$\eta_{BOOSTER} = \frac{h_{7,s} - h_6}{h_7 - h_6} \tag{2-16}$$

The remaining properties at state (7) including temperature (T_7), entropy (s_7) and specific volume (v_7) are obtained using EES' built-in property routines evaluated at P_7 and h_7.

Both the booster and high-stage compressors isentropic efficiencies ($\eta_{BOOSTER}$ and η_{HPC}) are assumed to be constant at 65% for this analysis. Table 2-1 lists all the refrigerant state point properties for the multi-stage cycle operating at the nominal conditions provided in Table 1-1.

Table 2-1: Cycle state points for a multi-stage system operating with NH_3

State	*T (K)*	*P (kPa)*	*h (kJ/kg)*	*s (kJ/kg-K)*	$\dot{m}$ *(kg/s)*	*x (%)*	*v* (m^3/kg)
1	308.2	1351	346.6	1.279	2.732	0	0.00170
2	308.2	1351	346.6	1.279	2.732	0	0.00170
3	264.8	311.1	346.6	1.342	2.732	15.84	0.0632
4	264.8	311.1	142.2	0.5702	1.919	0	0.00154
5	233.2	71.66	142.2	0.6099	1.919	10.24	0.1603
6	233.2	71.66	1388	5.955	1.919	100	1.553
7	374.5	311.1	1689	6.254	1.919	*superheated*	0.5797
8	264.8	311.1	1433	5.443	2.732	100	0.3909
9	415.3	1351	1759	5.735	2.732	*superheated*	0.1439

Figures 2-2 and 2-3 illustrate the T-s and P-h diagrams associated with the multi-stage system, respectively.

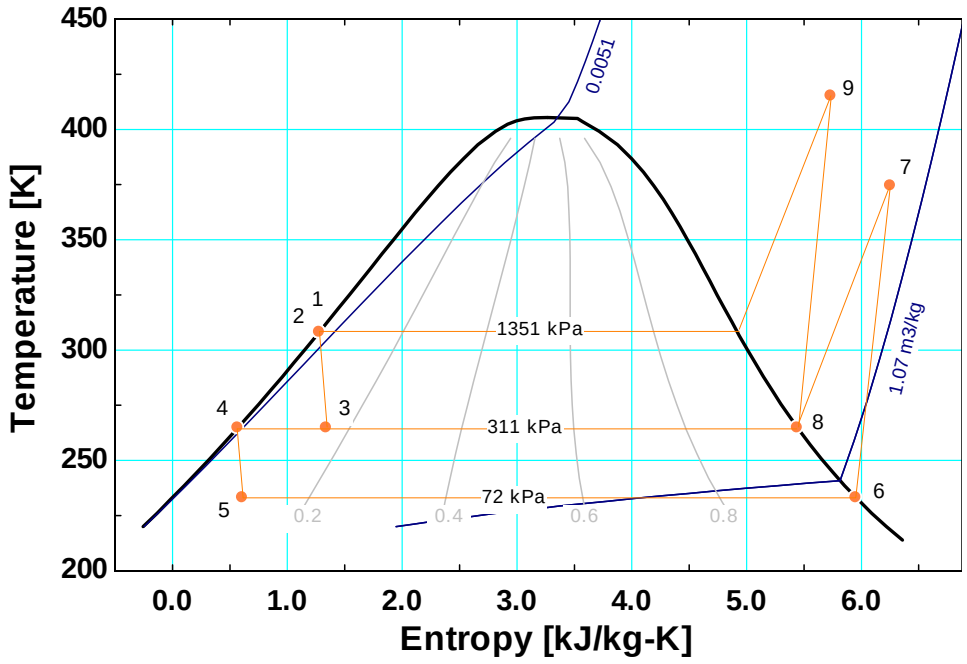

Figure 2-2: T-s diagram of a multi-stage vapor compression cycle

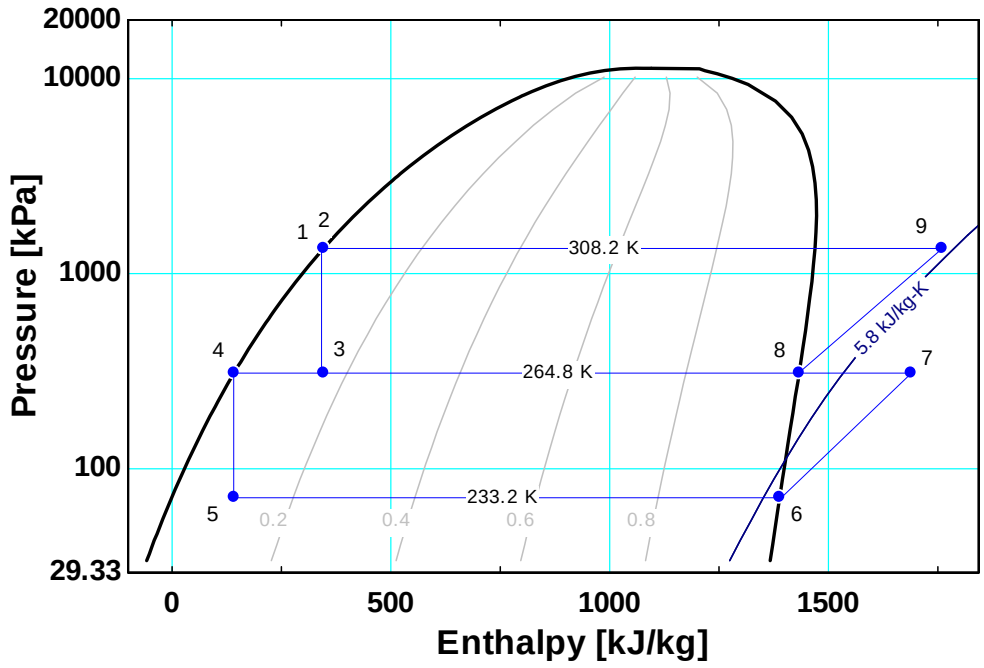

Figure 2-3: P-h diagram of a multi-stage vapor compression cycle

The mass flow rate of refrigerant through the low temperature section of the cycle ($\dot{m}_{LTC}$) can be determined by applying an energy balance at the evaporator:

$$\dot{Q}_L = \dot{m}_{LTC}\,(h_6 - h_5) \tag{2-17}$$

The required electrical power input to the booster compressor is:

$$\dot{W}_{BOOSTER} = \dot{m}_{LTC}\,(h_7 - h_6) \tag{2-18}$$

The mass flow rate through each component on the low temperature side of the system is the same at steady-state:

$$\dot{m}_{LTC} = \dot{m}_4 = \dot{m}_5 = \dot{m}_6 = \dot{m}_7 \tag{2-19}$$

The mass flow rate of refrigerant through the high temperature section of the cycle ($\dot{m}_{HTC}$) can be determined by applying an energy balance at the intercooler:

$$\dot{m}_{LTC}\,h_7 + \dot{m}_{HTC}\,h_3 - \dot{m}_{LTC}\,h_4 - \dot{m}_{HTC}\,h_8 = 0 \tag{2-20}$$

The mass flow rate on the high temperature side of the system is also the same at steady-state:

$$\dot{m}_{HTC} = \dot{m}_1 = \dot{m}_2 = \dot{m}_3 = \dot{m}_8 = \dot{m}_9 \tag{2-21}$$

The required power input to the high-stage compressor is:

$$\dot{W}_{HPC} = \dot{m}_{HTC}\,(h_9 - h_8) \tag{2-22}$$

The rate of required heat rejection to the condenser ($\dot{Q}_C$) is obtained by applying an energy balance on the condenser:

$$\dot{Q}_C = \dot{m}_{HTC}\,(h_9 - h_1) \tag{2-23}$$

The coefficient of performance (COP) of the multi-stage compression cycle is:

$$COP = \left(\frac{\dot{Q}_L}{\dot{W}_{HPC} + \dot{W}_{BOOSTER}} \right) \tag{2-24}$$

The fraction of the liquid that flashes to vapor (flash gas) over the first stage of liquid throttle, in the high-temperature side of the system, is defined as:

$$f = \left(\frac{h_3 - h_4}{h_8 - h_4} \right) \tag{2-25}$$

Figure 2-4 schematically illustrates the definition of flash gas described in Eq. (2-25)

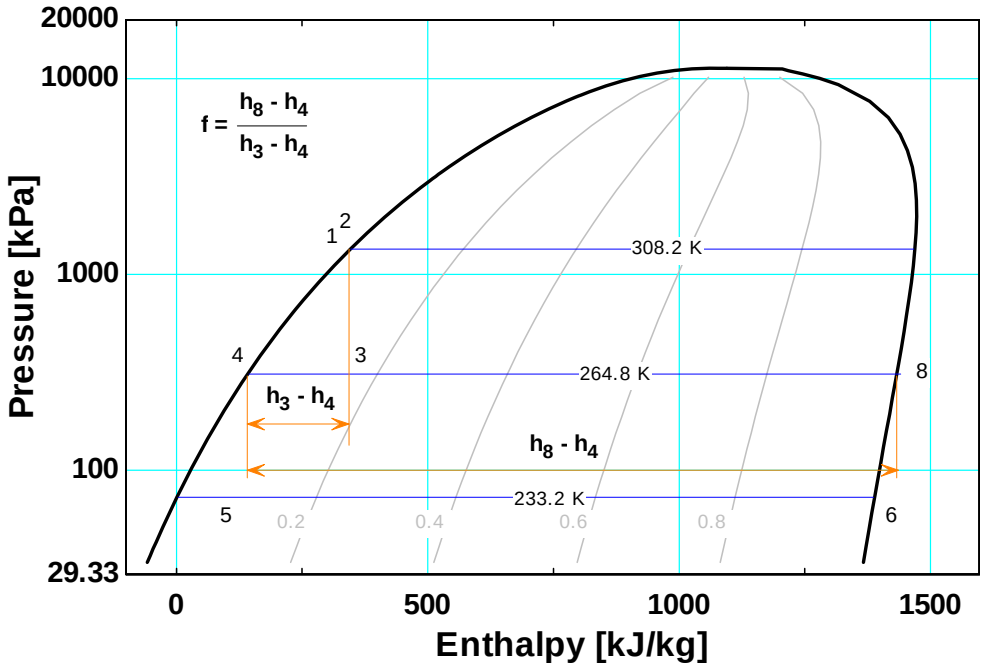

Figure 2-4: Schematic diagram of the refrigerant flashing to vapor from isenthalpic expansion through a throttling device

2.1.3) 2nd Law Analysis

It is useful to compare the availability destruction that characterizes each of the components in the refrigeration system; a second law analysis of this type illustrates characteristics beyond just COP and shows which aspects of the cycles are limiting the overall performance.

The 2nd law analysis is based on an entropy balance. For any component that has the working fluid of the cycle flowing through it, the entropy balance based on the system boundary defined around the component is given as:

$$\sum_{i=1}^{\#inlets} \dot{m}_i s_i - \sum_{o=1}^{\#outlets} \dot{m}_o s_o + \dot{S}_Q + \dot{S}_{gen} = \frac{dS}{dt} \tag{2-26}$$

where $\dot{S}_Q$ is the entropy associated with heat transfer across the boundary, $\dot{S}_{gen}$ is the rate of entropy generation within the control volume, S is the entropy contained in the system, $\dot{m}_i$ and $\dot{m}_o$ are the mass flow rates into and out of the control volume, respectively, and the quantities s_i and s_o are the specific entropies that characterize these flow rates.

This analysis assumes that the system operates at a steady state with only one stream flowing through most system components at constant mass flow rate:

$$\dot{m}\left(s_i - s_o\right) + \dot{S}_Q + \dot{S}_{gen} = 0 \tag{2-27}$$

The entropy associated with heat transfer is:

$$\dot{S}_Q = \int_{area} \frac{\dot{Q}}{T} dA \tag{2-28}$$

where $\dot{Q}$ is the rate of heat transfer across the boundary of the component's control volume and T is the temperature of the control volume boundary. The entropy balance is applied to each component in order to determine the rate of entropy generation ($\dot{S}_{gen}$). The number assigned to the entropy generation for each component corresponds to the state that exists upstream of the component, as illustrated in Figure 2-1 (e.g., the entropy generation associated with state (7) in the multi-stage system corresponds to the booster compressor). For any component that has two fluid streams flowing through, the number assigned corresponds to the upstream state on the high temperature side of the cycle.

Starting at the system condenser state (1), where heat ($\dot{Q}_C$) is rejected to the environment at T_0, the entropy balance is:

$$\dot{S}_{gen,1} = \dot{m}_{HTC}\left(s_1 - s_9\right) + \frac{\dot{Q}_C}{T_0} \tag{2-29}$$

At state (2), the high-pressure receiver is assumed to be adiabatic with controllable refrigerant flow. Therefore, an entropy balance leads to:

$$\dot{S}_{gen,2} = 0 \tag{2-30}$$

At state (3), the high-stage expansion valve is assumed to be adiabatic, thus an entropy balance leads to:

$$\dot{S}_{gen,3} = \dot{m}_{HTC}\left(s_3 - s_2\right) \tag{2-31}$$

The intercooler consists of two refrigerant streams and is externally adiabatic. Therefore, an entropy balance on the intercooler gives:

$$\dot{S}_{gen,4} = \dot{m}_{LTC}\left(s_4 - s_7\right) + \dot{m}_{HTC}\left(s_8 - s_3\right) \tag{2-32}$$

The low-stage expansion valve is also adiabatic, thus the rate of entropy generated in the lower stage expansion valve is:

$$\dot{S}_{gen,5} = \dot{m}_{LTC}\left(s_5 - s_4\right) \tag{2-33}$$

The evaporator is the component that absorbs the heat load ($\dot{Q}_L$) from the refrigerated space at T_S. Therefore, an entropy balance on the evaporator leads to:

$$\dot{S}_{gen,6} = \dot{m}_{LTC}\left(s_6 - s_5\right) - \frac{\dot{Q}_L}{T_S} \tag{2-34}$$

The booster compressor is assumed to be adiabatic but internally irreversible. Thus, an entropy balance on the booster compressor is:

$$\dot{S}_{gen,7} = \dot{m}_{LTC}\left(s_7 - s_6\right) \tag{2-35}$$

The high-stage compressor is also assumed to be adiabatic but irreversible; an entropy balance on the high-stage compressor is:

$$\dot{S}_{gen,9} = \dot{m}_{HTC}\left(s_9 - s_8\right) \tag{2-36}$$

By applying an entropy balance to each system component, the entropy generation ($\dot{S}_{gen}$) associated with that component may be determined. The rate of availability destruction associated with the rate of entropy generation can be obtained using:

$$\dot{A}_{des} = T_0\,\dot{S}_{gen} \tag{2-37}$$

The 2nd law efficiency (η_{II}) of a system is defined as the ratio of availability "produced" to availability "supplied." For a refrigeration system, the availability produced corresponds to the availability associated with the cooling capacity that is provided by the system.

$$A_{produced} = \dot{Q}_L \left(1 - \frac{T_S}{T_0}\right) \tag{2-38}$$

On the other hand, the electrical power input to the compressors to operate the system is the availability "supplied."

$$A_{supplied} = \dot{W}_{BOOSTER} + \dot{W}_{HPC} \tag{2-39}$$

The definition of the 2nd Law efficiency is:

$$\eta_{II} = \frac{A_{produced}}{A_{supplied}} \tag{2-40}$$

Thus,

$$\eta_{II} = \frac{\dot{Q}_L \left(1 - \frac{T_0}{T_S}\right)}{\dot{W}_{BOOSTER} + \dot{W}_{HPC}} \tag{2-41}$$

The rate of entropy generation ($\dot{S}_{gen}$), the rate of availability destruction ($\dot{A}_{des}$) and the fraction of the total availability destruction ($frac_{des}$) within each component of the multi-stage system, operating at the nominal conditions, are summarized in Table 2-2.

Table 2-2: The rate of entropy generation and the rate of availability destruction within each component of a multi-stage system operating with NH_3

State	***Component***	$\dot{S}_{gen}$ ***(kW/K)***	$\dot{A}_{des}$ ***(kW)***	$frac_{des}$ ***%***
1	condenser	0.7723	230.3	24.82
2	high pressure receiver	0	0	0
3	HTC expansion valve	0.1731	51.62	5.563
4	intercooler	0.2977	88.75	9.564
5	LTC expansion valve	0.07633	22.76	2.453
6	evaporator	0.4222	125.9	13.57
7	booster compressors	0.5747	171.4	18.47
9	high-pressure compressors	0.7958	237.3	25.57

2.2) Cascade Vapor Compression Cycle

A cascade refrigeration cycle is a vapor-compression plant consisting of two or more thermally-coupled single-stage circuits with each circuit containing a different refrigerant. The arrangement of the cycle resembles that of the multi-stage or compound system; however, the refrigerants in a cascade system do not physically mix. Rather, the thermal coupling between cycles is accomplished by the use of a cascade heat exchanger.

2.2.1) Cycle Configuration

A cascade refrigeration cycle offers the opportunity to exploit the desirable properties of different refrigerants where each refrigerant is configured to operate over limited temperature ranges to achieve favorable cooling performance and efficiency – particularly at low operating temperatures. As stated in the introduction, ammonia has a significant disadvantage of having an increasingly large specific volume as the suction pressure/temperature decreases. This means that a direct ammonia refrigeration system will require larger and larger compressors at lower evaporator temperatures/pressures. Comparatively, carbon dioxide has a significantly lower suction specific volume at low operating temperatures. Figure 2-5 illustrates a comparison between the specific volume of ammonia and carbon dioxide at low saturation temperature.

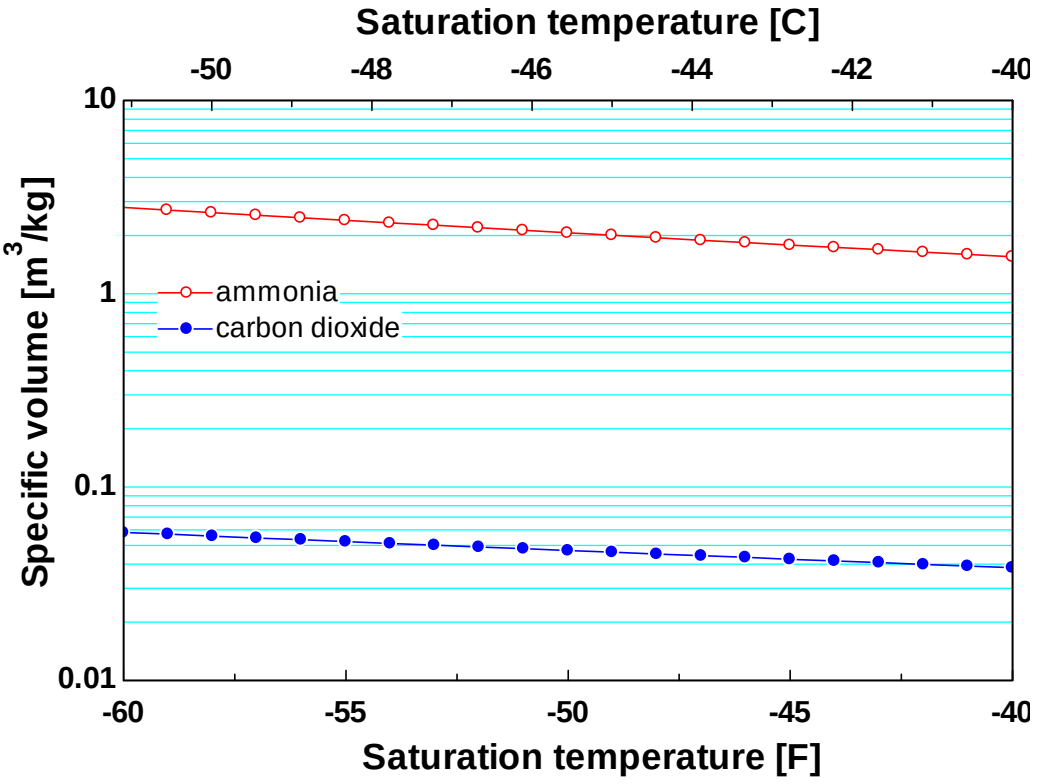

Figure 2-5: Specific volume of ammonia and carbon dioxide at low saturation temperature

Ammonia is both efficient and practical at higher temperatures (warmer than -50°F); therefore, suitable for use in the high-temperature circuit of a cascade system. Carbon dioxide has a much lower specific volume at low saturation temperatures. This combined with its high saturation pressure/temperature relationship tends to suggest it may be a viable option for the low-temperature circuit of a cascade system. Figure 2-6 illustrates a schematic diagram of an ammonia-carbon dioxide cascade refrigeration system.

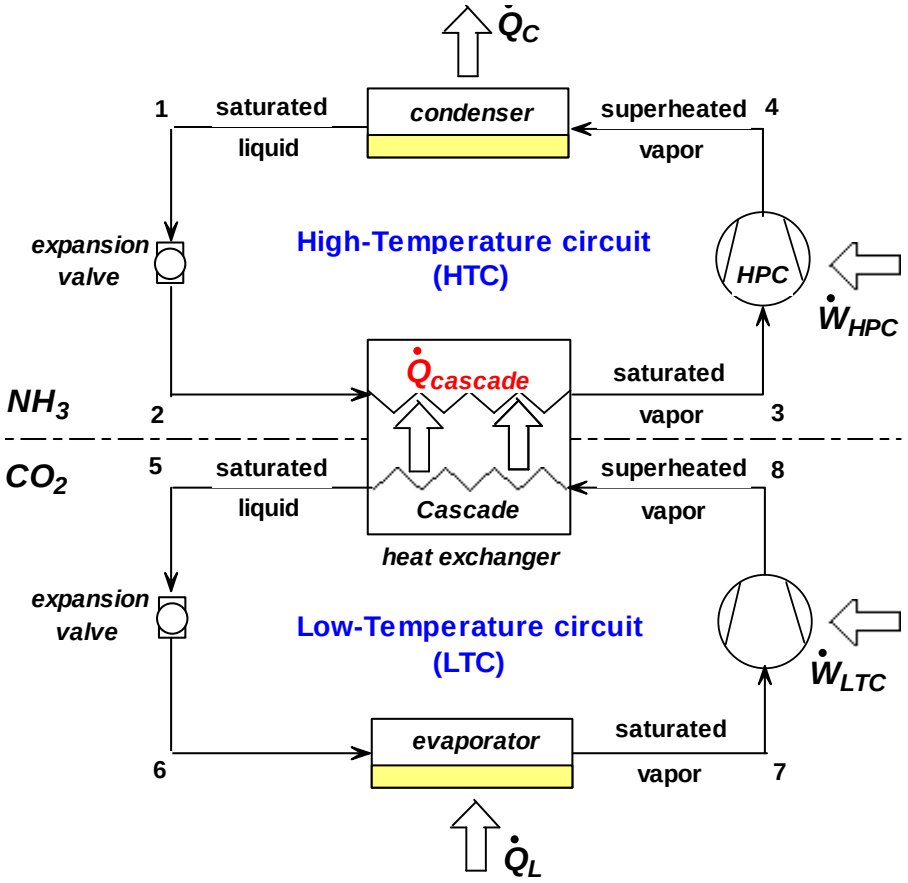

Figure 2-6: Schematic diagram of a cascade vapor compression refrigeration cycle

A computer model is developed based on a detailed thermodynamic analysis (1st and 2nd Law) of the underlining processes within a cascade vapor compression refrigeration cycle shown in Figure 2-6. The model is developed using EES and is flexible with respect to the user input parameters specified. The following sections describe a step-by-step analysis of the cascade system.

2.2.2) 1st Law Analysis

In order to run the computer model of a cascade refrigeration cycle, it is necessary to input seven parameters including: the refrigerant types for both high-temperature and low-temperature circuits ($fluid1\$$ and $fluid2\$$, respectively), the saturation temperatures associated with the condensing, evaporating and cascade heat exchanger ($T_{cond,sat}$, $T_{evap,sat}$ and $T_{cascade}$, respectively), the cascade heat exchanger pinch-point temperature difference ($\Delta T_{cascade}$), and the rate of heat transfer to the evaporator ($\dot{Q}_L$).

The 1st law analysis of a cascade vapor compression system starts at the low temperature side of the cascade heat exchanger where the refrigerant leaving the low temperature circuit of the cascade condenser is assumed to be saturated liquid at the specified cascade temperature.

$$T_5 = T_{cascade} \tag{2-42}$$

$$x_5 = 0 \tag{2-43}$$

The remaining properties at state (5) include enthalpy (h_5), entropy (s_5), specific volume (v_5), and pressure (P_5); these properties are obtained using EES' built-in property routines evaluated at T_5 and x_5.

The low-temperature circuit expansion valve is assumed to be adiabatic. Therefore, an energy balance on the valve leads to:

$$h_6 = h_5 \tag{2-44}$$

The temperature of the refrigerant leaving the valve is equal to the user-specified saturated evaporating temperature:

$$T_6 = T_{evap,sat} \tag{2-45}$$

The remaining properties at state (6) include quality (x_6), entropy (s_6), specific volume (v_6), and pressure (P_6); these properties are obtained using EES' built-in property routines evaluated at T_6 and h_6.

It is assumed that the refrigerant leaves the evaporator as saturated vapor:

$$x_7 = 1 \tag{2-46}$$

The refrigerant-side pressure drop through the evaporator is ignored and therefore, the pressure of the fluid leaving the evaporator is equal to the pressure of the fluid leaving the low-temperature expansion valve:

$$P_7 = P_6 \tag{2-47}$$

The remaining properties at state (7) include temperature (T_7), enthalpy (h_7), entropy (s_7) and specific volume (v_7); these properties are obtained using EES' built-in property routines evaluated at P_7 and x_7.

The entropy state leaving a reversible adiabatic *LTC* compressor is given by:

$$s_{8,s} = s_7 \tag{2-48}$$

The pressure drop across the cascade heat exchanger is neglected and therefore, the exit pressure of the *LTC* compressor is assumed to be equal to the cascade condensing pressure:

$$P_8 = P_5 \tag{2-49}$$

The enthalpy of the fluid leaving a reversible, adiabatic compressor ($h_{8,s}$) is computed using EES' built-in property routines evaluated at $s_{8,s}$ and P_8. The actual enthalpy at state (8) is computed using the definition of the *LTC* compressor isentropic efficiency:

$$\eta_{LTC} = \frac{h_{8,s} - h_7}{h_8 - h_7} \tag{2-50}$$

The remaining properties at state (8) include temperature (T_8), entropy (s_8) and specific volume (v_8) and are obtained using EES' built-in property routines evaluated at P_8 and h_8.

It is assumed that the refrigerant leaves the compressor as saturated liquid:

$$T_1 = T_{cond,sat} \tag{2-51}$$

$$x_1 = 0 \tag{2-52}$$

The remaining properties at state (1) include enthalpy (h_1), entropy (s_1), specific volume (v_1), and pressure (P_1); these properties are obtained using EES' built-in property routines evaluated at T_1 and x_1.

The high-temperature expansion valve is assumed to be adiabatic. Therefore, an energy balance on the valve leads to:

$$h_2 = h_1 \tag{2-53}$$

The refrigerant temperature at state (2) is determined based on the user input cascade temperature and the required cascade heat exchanger pinch point temperature difference (note that a perfect cascade heat exchanger would be consistent with $\Delta T_{cascade}$ = 0°F):

$$T_2 = T_5 - \Delta T_{cascade} \tag{2-54}$$

The remaining properties at state (2) include quality (x_2), entropy (s_2), specific volume (v_2), and pressure (P_2); these properties are obtained using EES' built-in property routines evaluated at T_2 and h_2.

It is assumed that the high temperature refrigerant leaves the high temperature circuit of the cascade heat exchanger as saturated vapor:

$$x_3 = 1 \tag{2-55}$$

It is assumed that the high temperature refrigerant leaves the high temperature circuit of the cascade heat exchanger as saturated vapor:

$$P_3 = P_2 \tag{2-56}$$

The remaining properties at state (3) include enthalpy (h_3), entropy (s_3), specific volume (v_3), and temperature (T_3); these properties are obtained using EES' built-in property routines evaluated at P_3 and x_3.

The entropy of the refrigerant leaving a reversible, adiabatic high temperature circuit compressor is:

$$s_{4,s} = s_3 \tag{2-57}$$

The pressure drop across the condenser is neglected and therefore, the exit pressure of the high-stage compressor is assumed to be equal to the exit pressure of the condenser:

$$P_4 = P_1 \tag{2-58}$$

The enthalpy of the fluid leaving a reversible, adiabatic compressor ($h_{4,s}$) is computed using EES' built-in property routines evaluates at $s_{4,s}$ and P_4. The actual enthalpy at state (4) is computed using the definition of the high-pressure compressor isentropic efficiency:

$$\eta_{HPC} = \frac{h_{4,s} - h_3}{h_4 - h_3} \tag{2-59}$$

The remaining intensive properties at state (4) including temperature (T_4), entropy (s_4) and specific volume (v_4) are obtained using EES' built-in property routines evaluated at P_4 and h_4.

The cascade system operates at the nominal operating conditions listed in Table 1-1. Additional operating conditions necessary for the 1st law analysis are specified in Table 2-3.

Table 2-3: Operating conditions for a cascade system operating with NH_3/CO_2

$T_{cascade}$	$\Delta T_{cascade}$	η_{RECIP}	η_{HPC}
5°F	10°F	65%	65%
258.2 K	5.6 K	65%	65%

Table 2-4 lists all the refrigerant state point properties.

Table 2-4: Cycle state points for a cascade compression system operating with NH_3/CO_2

	State	T (K)	P (kPa)	h (kJ/kg)	s (kJ/kg-K)	$\dot{m}$ (kg/s)	x (%)	v (m^3/kg)
HTC	1	308.2	1351	346.6	1.279	2.677	0	0.001702
	2	252.6	185.4	346.6	1.385	2.677	19.53	0.1255
	3	252.6	185.4	1417	5.623	2.677	100	0.6363
	4	461	1351	1874	5.996	2.677	*SH*	0.162
LTC	5	258.2	2291	52.47	0.2087	8.858	0	0.000992
	6	233.2	1005	52.47	0.225	8.858	16.27	0.006979
	7	233.1	1005	322.4	1.383	8.858	100	0.03828
	8	303.6	2291	376	1.447	8.858	*SH*	0.02213

The properties diagrams illustrating the processes within the cascade vapor compression cycle, operating at the conditions summarized in Tables 1-1 and 2-3, are shown in Figures 2-7 through 2-9.

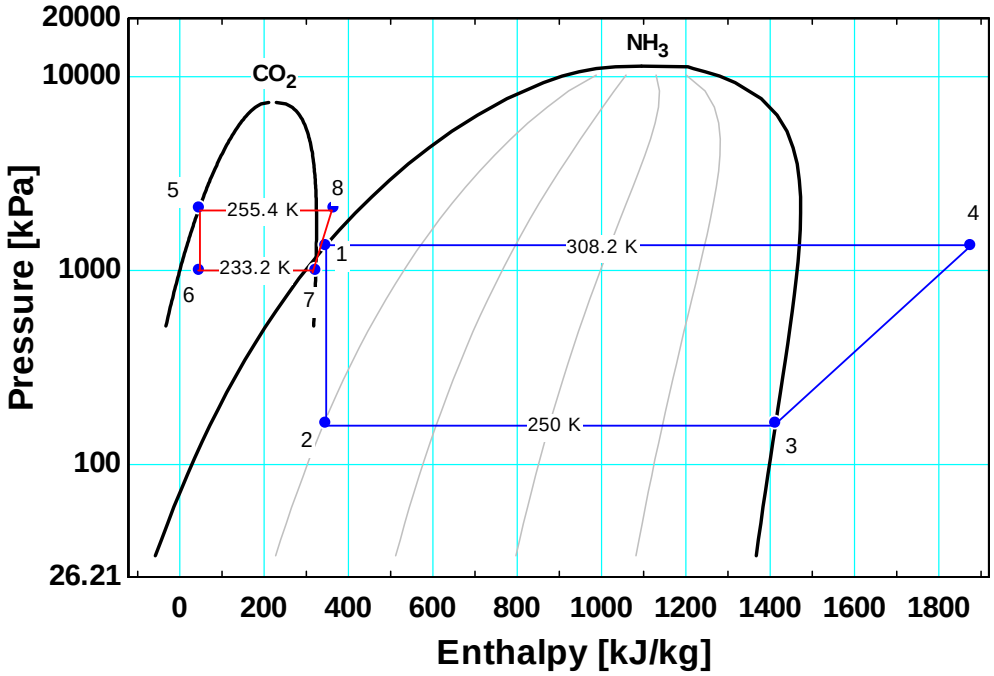

Figure 2-7: P-h diagram of a cascade vapor compression cycle operating with NH_3/CO_2

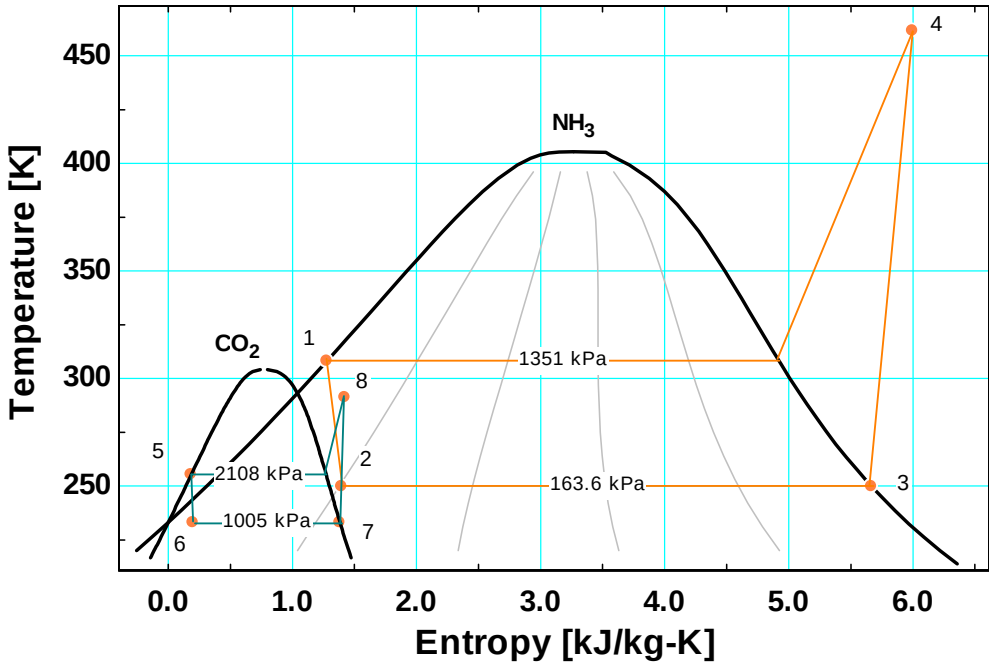

Figure 2-8: T-s diagram of a cascade vapor compression cycle operating with NH_3/CO_2

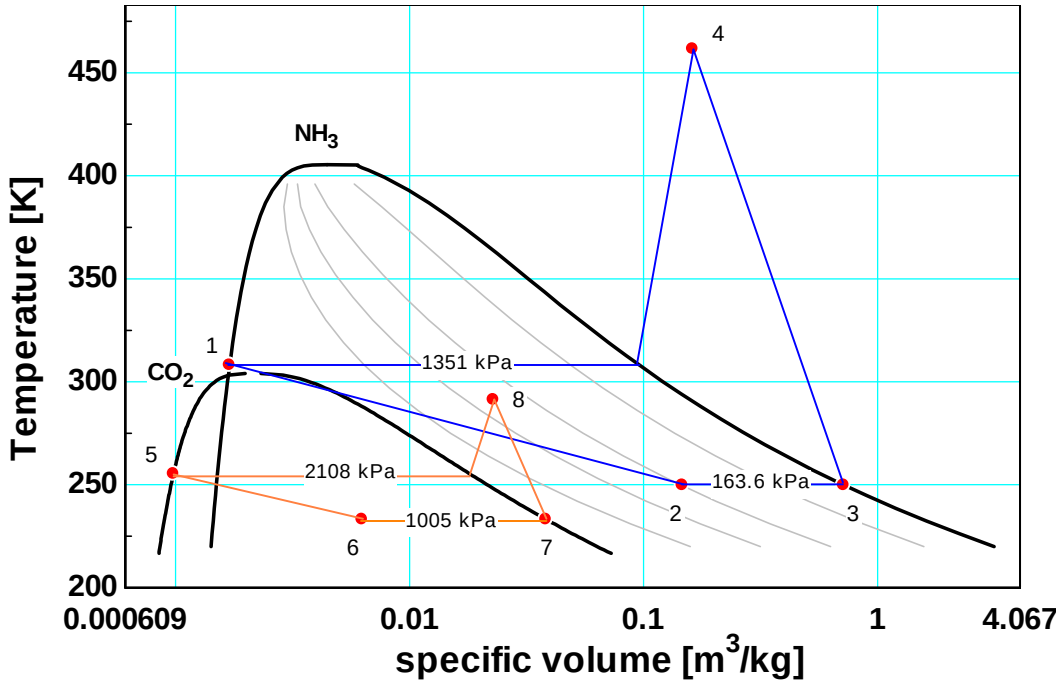

Figure 2-9: T-v diagram of a cascade vapor compression cycle operating with NH_3/CO_2

The operating characteristics of the cycle are obtained using energy balances for each component. The rate of heat absorbed by the evaporator ($\dot{Q}_L$) is used to determine the mass flow rate of the low-temperature circuit ($\dot{m}_{LTC}$) by applying an energy balance on the evaporator:

$$\dot{Q}_L = \dot{m}_{LTC}(h_7 - h_6) \tag{2-60}$$

The mass flow rates at each state point within the low-temperature circuit are the spatially uniform:

$$\dot{m}_{LTC} = \dot{m}_5 = \dot{m}_6 = \dot{m}_7 = \dot{m}_8 \tag{2-61}$$

The actual rate of work input to the *LTC* compressor is:

$$\dot{W}_{LTC} = \dot{m}_{LTC}(h_8 - h_7) \tag{2-62}$$

The rate of heat transfer from the low-temperature circuit to the high-temperature circuit ($\dot{Q}_{Cascade}$) is obtained from applying energy balance at the low-temperature circuit:

$$\dot{Q}_{Cascade} = \dot{Q}_L + \dot{W}_{LTC} \tag{2-63}$$

Mass flow rate of the high-temperature circuit ($\dot{m}_{HTC}$) is obtained by applying energy balance at the cascade heat exchanger:

$$\dot{Q}_{cascade} = \dot{m}_{HTC}\,(h_3 - h_2) \tag{2-64}$$

The high-temperature side mass flow rate is spatially uniform:

$$\dot{m}_{HTC} = \dot{m}_1 = \dot{m}_2 = \dot{m}_3 = \dot{m}_4 \tag{2-65}$$

The power input to high-pressure compressor is:

$$\dot{W}_{HPC} = \dot{m}_{HTC}\,(h_4 - h_3) \tag{2-66}$$

The rate of heat rejected by the condenser $(\dot{Q}_C)$ is obtained by applying an energy balance on the high-temperature circuit:

$$\dot{Q}_C = \dot{m}_{HTC}\left(h_4 - h_1\right) \tag{2-67}$$

One of the most significant performance characteristics of the cascade heat exchanger is its effectiveness ($\varepsilon_{cascade}$), which is defined as the ratio of the actual heat transfer ($\dot{Q}_{cascade}$) to the maximum heat transfer ($\dot{Q}_{cascade,max}$) that could occur given the input conditions. $\dot{Q}_{cascade,max}$ is calculated based on the maximum enthalpy difference that could exist between the hot fluid entering and leaving the heat exchanger [states (8) and (5), respectively]. The minimum enthalpy of the condensing refrigerant leaving the heat exchanger at state (5) ($h_{5,min}$) is defined using EES' properties routine evaluated for the low pressure refrigerant evaluated at P_5 and T_2. Thus, the maximum rate of heat transfer is:

$$\dot{Q}_{cascade,max} = \dot{m}_{LTC}\,(h_8 - h_{5,min}) \tag{2-68}$$

and the cascade heat exchanger effectiveness is:

$$\varepsilon_{cascade} = \frac{\dot{Q}_{cascade}}{\dot{Q}_{cascade,max}} \tag{2-69}$$

The COP of the low-temperature circuit is:

$$COP_{LTC} = \frac{\dot{Q}_L}{\dot{W}_{BOOSTER}} \tag{2-70}$$

The COP of the high-temperature circuit is:

$$COP_{HTC} = \frac{\dot{Q}_{cascade}}{\dot{W}_{HPC}} \tag{2-71}$$

The COP of the cascade refrigeration cycle is defined as:

$$COP = \frac{\dot{Q}_L}{\dot{W}_{HPC} + \dot{W}_{BOOSTER}} \tag{2-72}$$

The overall system COP can be represented in terms of the two temperature circuits COPs alone by manipulating Eq. (2-72):

$$COP = \frac{\dot{Q}_L}{\frac{\dot{W}_{HPC}}{\dot{Q}_{CASCADE}}\left(\dot{Q}_{CASCADE}\right) + \dot{W}_{BOOSTER}} \tag{2-73}$$

substituting for $\dot{Q}_{CASCADE}$ from Eq. (2-63) leads to:

$$COP = \frac{\dot{Q}_L}{\left(\frac{\dot{W}_{HPC}}{\dot{W}_{BOOSTER} + \dot{Q}_L}\right)\left(\dot{W}_{BOOSTER} + \dot{Q}_L\right) + \dot{W}_{BOOSTER}} \tag{2-74}$$

Carrying out the multiplication in the denominator of Eq. (2-74) leads to:

$$COP = \frac{\dot{Q}_L}{\frac{\dot{W}_{HPC}\,\dot{W}_{BOOSTER}}{\dot{W}_{BOOSTER} + \dot{Q}_L} + \frac{\dot{W}_{HPC}\,\dot{Q}_L}{\dot{W}_{BOOSTER} + \dot{Q}_L} + \dot{W}_{BOOSTER}} \tag{2-75}$$

Dividing the denominator of Eq. (2-75) by the numerator leads to:

$$COP = \frac{1}{\left(\frac{\dot{W}_{HPC}}{\dot{W}_{BOOSTER} + \dot{Q}_L}\frac{\dot{W}_{BOOSTER}}{\dot{Q}_L}\right) + \frac{\dot{W}_{HPC}}{\dot{W}_{BOOSTER} + \dot{Q}_L} + \frac{\dot{W}_{BOOSTER}}{\dot{Q}_L}} \tag{2-76}$$

Substituting the definitions of the high temperature and low temperature COPs into Eq. (2-76) leads to:

$$COP = \frac{1}{\left(\frac{1}{COP_{LTC}\,COP_{HTC}} + \frac{1}{COP_{HTC}} + \frac{1}{COP_{LTC}}\right)} \tag{2-77}$$

The overall COP of the cycle expressed in terms of COP_{LTC} and COP_{HTC} is therefore:

$$COP = \frac{COP_{LTC}\, COP_{HTC}}{\left(1 + COP_{LTC} + COP_{HTC}\right)} \tag{2-78}$$

2.2.3) 2nd Law Analysis

The 2nd law analysis of the cascade system is conducted in the same manner as the multi-stage system. The number assigned to the entropy generation in each state corresponds to a state upstream of each system component shown in Figure 2-6, (e.g. state (8) refers to the *LTC* compressor). For any component that has two fluid streams flowing through, the number assigned corresponds to the upstream state on the high temperature side of the cycle.

An entropy balance on the condenser includes the rate of heat rejection to the surrounding at the dead state temperature (T_0):

$$\dot{S}_{gen,1} = \dot{m}_1 \left(s_1 - s_4\right) + \frac{\dot{Q}_C}{T_0} \tag{2-79}$$

The high-stage expansion valve is assumed to be adiabatic, thus an entropy balance leads to:

$$\dot{S}_{gen,2} = \dot{m}_2 \left(s_2 - s_1\right) \tag{2-80}$$

The rate of entropy generation within the cascade heat exchanger occurs due to the transfer of energy between the refrigerant streams through a temperature difference. Thus, an entropy balance leads to:

$$\dot{S}_{gen,3} = \dot{m}_3 \left(s_3 - s_2\right) + \dot{m}_5 \left(s_5 - s_8\right) \tag{2-81}$$

The rate of entropy generated by the high-pressure compressor is:

$$\dot{S}_{gen,4} = \dot{m}_4 \left(s_4 - s_3\right) \tag{2-82}$$

The rate of entropy generation occurring in the low-side expansion valve is:

$$\dot{S}_{gen,6} = \dot{m}_6 \left(s_6 - s_5\right) \tag{2-83}$$

The system evaporator is the component that absorbs heat load ($\dot{Q}_L$) from the refrigerated space (T_S). Therefore, an entropy balance leads to:

$$\dot{S}_{gen,7} = \dot{m}_7 \left(s_7 - s_6 \right) - \frac{\dot{Q}_L}{T_S} \tag{2-84}$$

The *LTC* compressor is assumed to be adiabatic, thus an entropy balance leads to:

$$\dot{S}_{gen,8} = \dot{m}_8 \left(s_8 - s_7 \right) \tag{2-85}$$

By applying an entropy balance at each system component, entropy generation ($\dot{S}_{gen}$) associated with each component can be determined. The rate of availability destruction ($\dot{A}_{des}$) for each component and the 2nd law efficiency (η_{II}) for the cascade system, defined in the same manner as in the compound system, are calculated by using Eq. (2-37) and Eq. (2-41), respectively.

The rate of entropy generated ($\dot{S}_{gen}$), the rate of availability destruction ($\dot{A}_{des}$) and the fraction of the total availability destruction ($frac_{des}$) within each component of the cascade system, operating at the baseline conditions, is summarized in Table 2-5.

Table 2-5: The rate of entropy generation and the rate of availability destruction within each component of a cascade system operating with NH_3/CO_2

State	***Component***	$\dot{S}_{gen}$ ***(kW/K)***	$\dot{A}_{des}$ ***(kW)***	$frac_{des}$ ***%***
1	condenser	1.158	345.3	10.1
2	HTC expansion valve	0.3117	92.92	2.72
3	cascade heat exchanger	7.928	2,364	69.1
4	high-pressure compressor	1.03	307	8.98
6	LTC expansion valve	0.1147	34.21	1.0
7	evaporator	0.4218	125.8	3.68
8	low-pressure compressor	0.5022	149.7	4.38

2.3) 1st Order Comparison

This section features a simple comparison of the performance of the multi-stage and the cascade vapor compression cycles using the simple model based on the 1st and 2nd law analyses presented earlier in Sections 2.1 and 2.2. For the purpose of comparison consistency, both cycles are assumed to operate at the same baseline conditions that are summarized in Table 1-1. However, the performance indicating parameters of each system can vary with many independent factors, especially with the intermediate condition between low and high-temperature circuits. It is helpful to compare system performance when each system is operating at its optimum condition.

2.3.1) Performance Optimization

In a typical refrigeration system, one of the flagship indicators of operating efficiency is it's the *coefficient of performance* (COP). The COP can be expected to vary with evaporating and condensing temperatures, refrigerant type, and compressor efficiency. In some cases, the system performance can be optimized by varying the intermediate condition until an optimal operating condition is established. At this optimal condition, the sum of compressor power between the two stages is minimized. For the cascade system, the COP can be optimized by varying $T_{cascade}$; for the multi-stage system, the performance can be optimized by varying P_{int}. In addition, thermal performance of the cascade system is dependent on pinch-point temperature difference between two fluid streams, thus separate comparison must made for different values of $\Delta T_{cascade}$. The results of the optimization are summarized in Table 2-6.

Table 2-6: Optimized system performance under an ideal comparison between multi-stage and cascade systems at various pinch-point temperature differences

Parameter	***Multi-stage system***	***Cascade system ($\Delta T_{cascade} = 2^oF$)***	***Cascade system ($\Delta T_{cascade} = 5^oF$)***	***Cascade system ($\Delta T_{cascade} = 10^oF$)***
COP	1.63	1.54	1.49	1.41
η_{II}	30.1%	28.3%	27.4%	26.0%
PR_{HPC}	3.79	6.38	6.61	7.01
PR_{LTC}	4.97	2.19	2.24	2.34
$\dot{A}_{des,tot}$	1,032 kW	3,292 kW	3,349 kW	3,446 kW
P_{int}	356 kPa (51.64 psia)	*N/A*	*N/A*	*N/A*
$T_{cascade}$	*N/A*	256.7 K (2.41°F)	257.6 K (3.97°F)	259 K (6.53°F)

The optimization process suggests that the system performance increases when operating at the optimal condition. The results from optimization by varying the intermediate condition for both systems are illustrated in Figure 2-10 and Figure 2-11.

The results from the plots show that, with performance optimization, both systems perform nearly equally; however, this simplistic model comparison is made based only on one particular operating condition and the details of the component performance and size are completely neglected. Thus, this comparison provides only a very first order result and is insufficient to be used to select one system over another. More detailed analysis of component performance and cost must be analyzed and compared. Component modeling is discussed in detail in the following chapter.

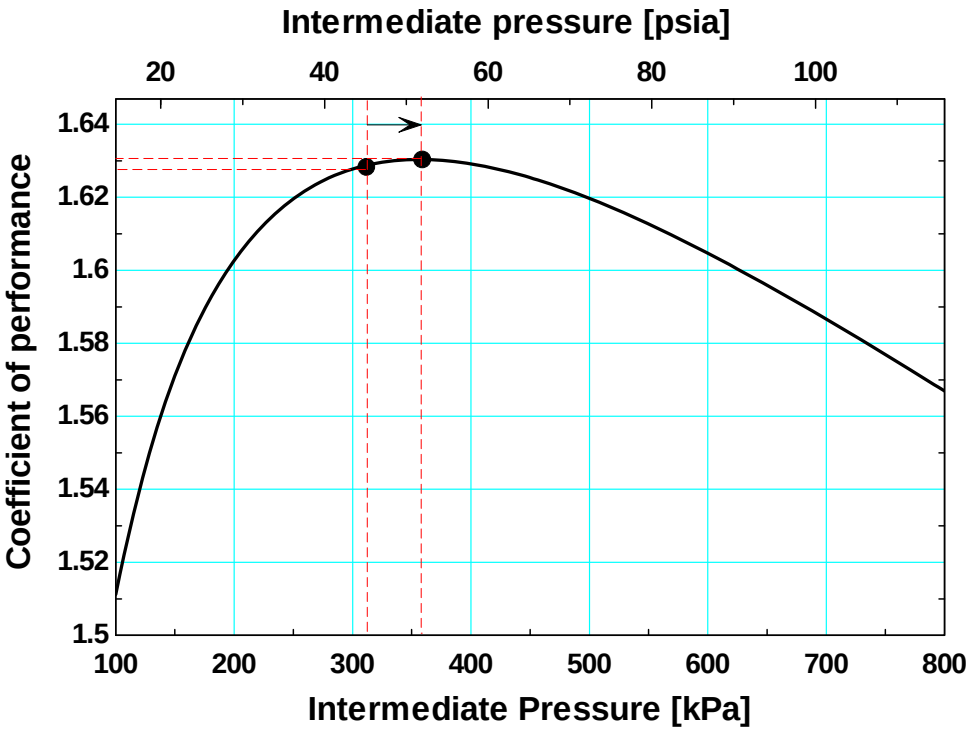

Figure 2-10: Optimal coefficient of performance of the multi-stage system as a function of the intermediate pressure

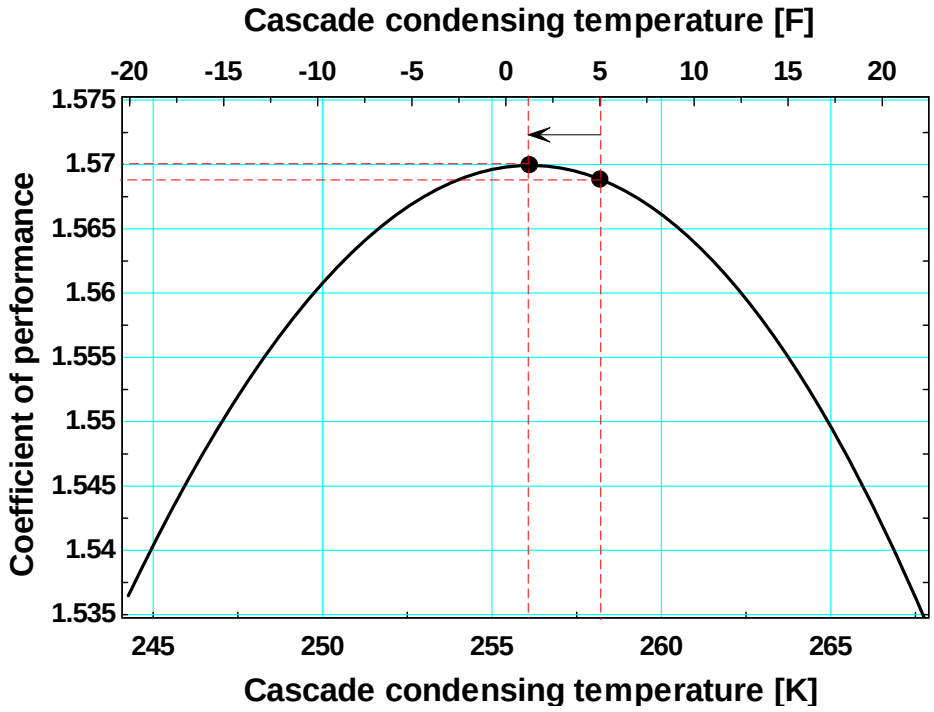

Figure 2-11: Optimal coefficient of performance of the cascade system as a function of the cascade condensing temperature

Chapter 3) System Component Models

Chapter 2 discusses the performance optimization among the two systems; the most efficient system is identified based on a comparison of the COPs using first order, very simple models of each component. However, it is essential to consider more realistic system-level performance based on how components function together in the overall system in order to carry out a more meaningful analysis.

This chapter describes detailed models of each individual system component; this process is accomplished by selecting the appropriate equipment based on the requirements of each system. The system model using these detailed component models is more realistic and allows an economic comparison for each system configuration. Three components are common to both system types: compressors, evaporative condensers and evaporators. Two components are unique to each system: the intercooler (for the multi-stage system) and the cascade heat exchanger (for the cascade system). An intercooler is simply a large storage vessel physically coupling the two temperature circuits of the multi-stage system and acts as a liquid-vapor separator. A cascade heat exchanger is, typically, a shell-and-tube heat exchanger thermally coupling the two temperature circuits of the cascade system. This component is an essential piece of equipment in the cascade system; its thermal performance and size have a significant impact on system efficiency and operating cost.

3.1) Compressors

The process of selecting a compressor for a refrigeration system must consider the maximum expected heat load absorbed by the heat removing components. The aggregate installed compressor capacity at each suction pressure level must equal or exceed the peak load expected for that suction pressure level. For the low-temperature circuit of a cascade system or the low suction pressure level for a two-stage compression system, the aggregate capacity of the installed low-temperature circuit (LTC) compressors must be capable of meeting the full heat load absorbed by the evaporators. Note that only in the multi-stage system the low-temperature circuit compressors are referred to as "booster compressors." In cases where the compressor's capacity exceeds the evaporator load, the compressors will "unload" until the capacity matches the vapor production rate of the evaporators. Compressors installed on a high-temperature circuit of a cascade system must have sufficient capacity to absorb the heat load from the cascade heat exchanger as well as any other evaporators that may be connected to that temperature level. For a two-stage compression system, the high-stage compressors must be capable of absorbing the total heat of rejection for the booster compressor(s) as well as any additional evaporators operating at the intermediate pressure/temperature.

Based on types of refrigerants, compressor technology may also vary. In most industrial refrigeration systems operating with ammonia, screw compressors are used. The compressors installed in a refrigeration system using carbon dioxide or other refrigerants with low vapor specific volume (high vapor density) at low suction pressures are typically reciprocating compressors. The following sections describe models developed for these two types of compressor technologies.

3.1.1) Screw Compressor

Screw-type compressor is one of the fastest growing types of industrial refrigeration compressor. This type of compressor has a wide range of applications in cooling and refrigeration processes. Screw compressors are capable of providing a broad range of cooling capacity and volumetric vapor flow rate, thus making them suitable for many types of refrigerants, especially for ammonia at relatively low temperatures, screw compressors are required to cope with both a low vapor density and high compression ratio requirement.

There are two screw compressor configurations in use for industrial refrigeration systems today: single screw and twin screw. Single-screw compressor consists of the main rotor (screw) with helical grooves and two gate-rotors with engaging teeth. Compression of refrigerant vapor is accomplished by successive reduction of gas volume contained within the helical grooves of the main rotor as it translates down the axis of the screw. The intermeshing gate rotors prevent internal leakage of the gas by forming a seal with the rotor's thread. The compressor is driven by an electric motor which imparts the rotary motion to the main screw, which in turn engages with the two intermeshed gate-rotors. Typically, the cylindrical main screw consists of six helical grooves and gate-rotor each has 11 teeth. The main screw is placed horizontally, in alignment with the driveshaft, and the gate-rotors are parallel to each other and are both perpendicular to the main screw (Vilter VSM bulletin, 2006). Figure 3-1 illustrates a typical single-screw compressor package unit.

(a) (b)

Figure 3-1: (a) VSM single-screw compressor package (courtesy of Vilter Manufacturing LLC), (b) schematic of a single-screw compressor housing (Mitsucom website, 2008)

Twin-screw compressor consists of two main intermeshing rotors. The male rotor lobes are engaged in the female rotor gullies. Typically, compressor driveshaft is connected to the male screw, which drives the female screw. Vapor compression in twin-screw compressors is accomplished by decreasing displacement volume of confined refrigeration vapor through re-meshing of the rotating screws as vapor is helically transported from suction to discharge port. Figures 3-2 illustrates a typical twin-screw compressor configuration.

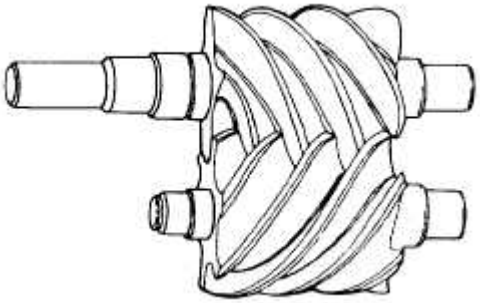

(a)

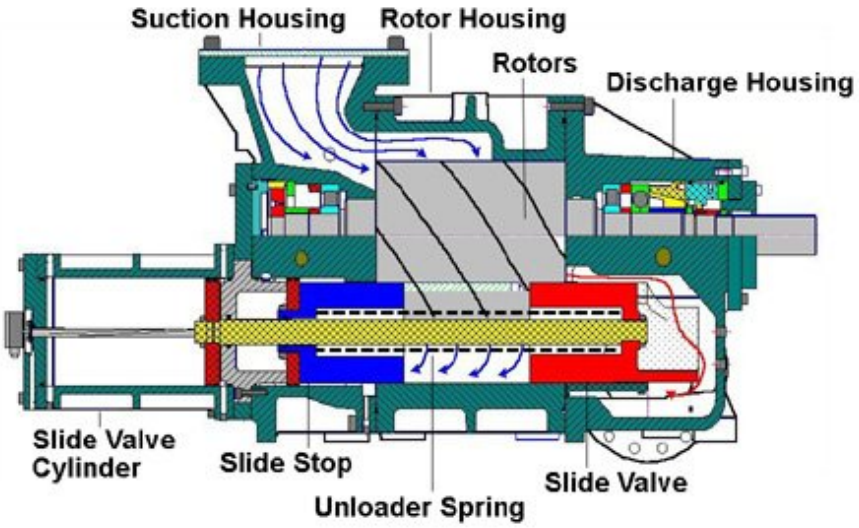

(b)

Figure 3-2: (a) schematic of intermeshing rotors of a twin-screw compressor (tpub website, 2008), (b) cut-away schematic of a twin-screw compressor unit (archrnews website, 2008)

Twin-screw compressor has a larger share of refrigeration industry application compared to single-screw compressor, which is a relatively newer technology (EPD, 2006). This system component model is developed based on this compressor type. There are a variety of performance data for screw compressors readily available from manufacturers. Compressor selection programs are used to guide the process of selecting a suitable twin-screw compressor. In this analysis, Frick's compressor selection software, *Coolware* (Version 7.0.0) was used as the basis for characterizing the operating performance for screw compressors. The software includes

the specifications for a variety of screw compressor models over a large range of capacity. Compressor capacity (CAP_{comp}) and power (POW_{comp}) are usually given as a function of saturated suction and saturated discharge temperatures among other parameters such as oil cooling method, economizing method, side port loads (if applicable), and others. In order to begin the process of selecting a compressor, at least three user-input parameters are required: the saturated suction temperature (SST), the saturated discharge temperature (SDT) and the refrigeration heat load to be met by the compressors ($\dot{Q}_{required}$).

3.1.1.1) Screw Compressor Selection

Based on the low-temperature heat load and the operating conditions summarized in Table 1-1, a few candidate compressors can be selected using *Coolware* (Coolware website, 2008). For the SST range between -60°F to -20°F and SDT range between 0°F to 30°F, the RWF II 676 model is selected for the booster (specified with inter-cooled oil cooling). For the SST range between -5°F to 20°F and SDT range between 75°F to 105°F, the RWF II 177 model is selected for the high-stage. The compressor maps, illustrating full-load capacity and full-load power as a function of SST and SDT, are illustrated in Figures 3-3 through 3-6. Figures 3-3 and 3-4 illustrate full-load capacity and full-load power for an RWF II 676 model, respectively. Figures 3-5 and 3-6 illustrate full-load capacity and full-load power for an RWF II 177 model, respectively.

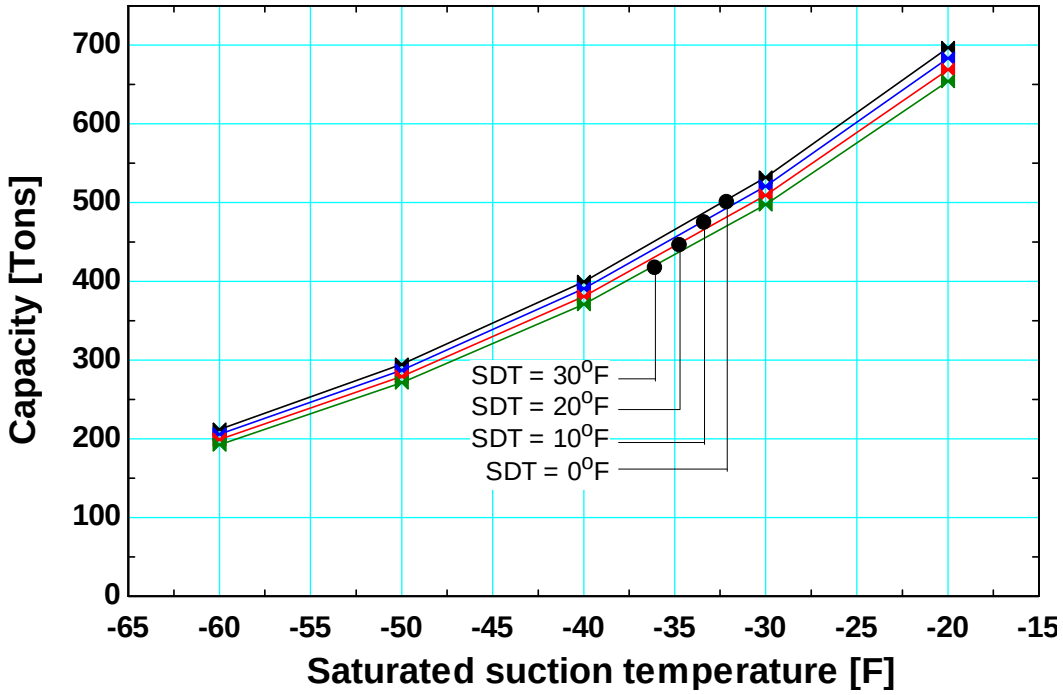

Figure 3-3: Capacity compressor map of RWF II 676 booster compressor operating with NH_3 from "Coolware" compressor selection program

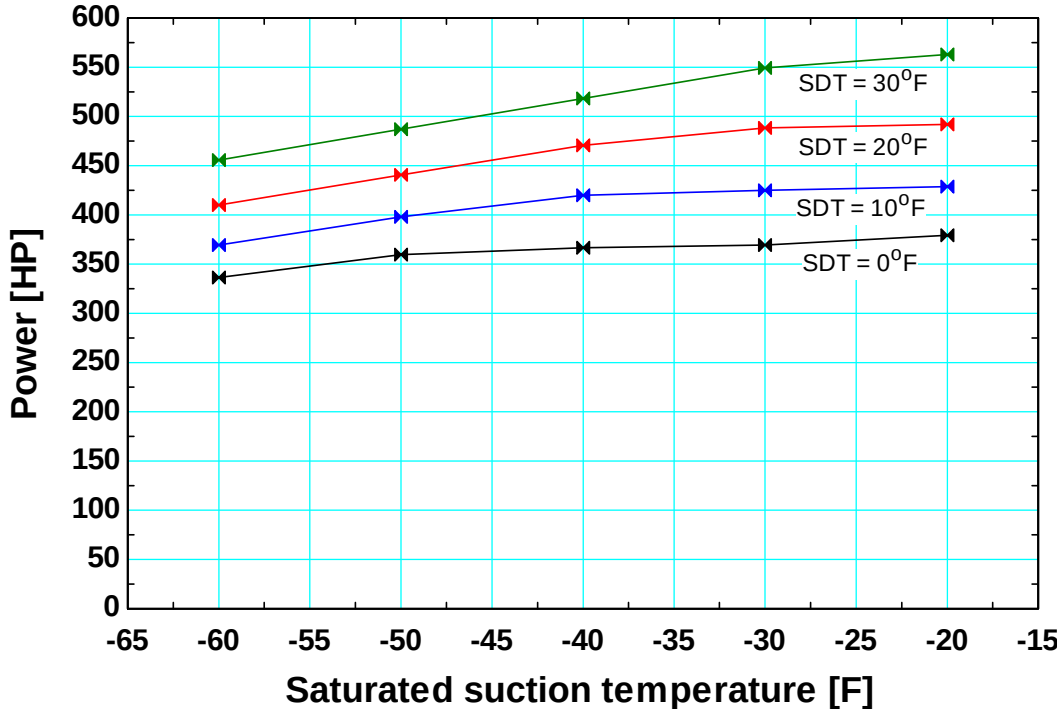

Figure 3-4: Power compressor map of RWF II 676 booster compressor operating with NH_3 from "Coolware" compressor selection program

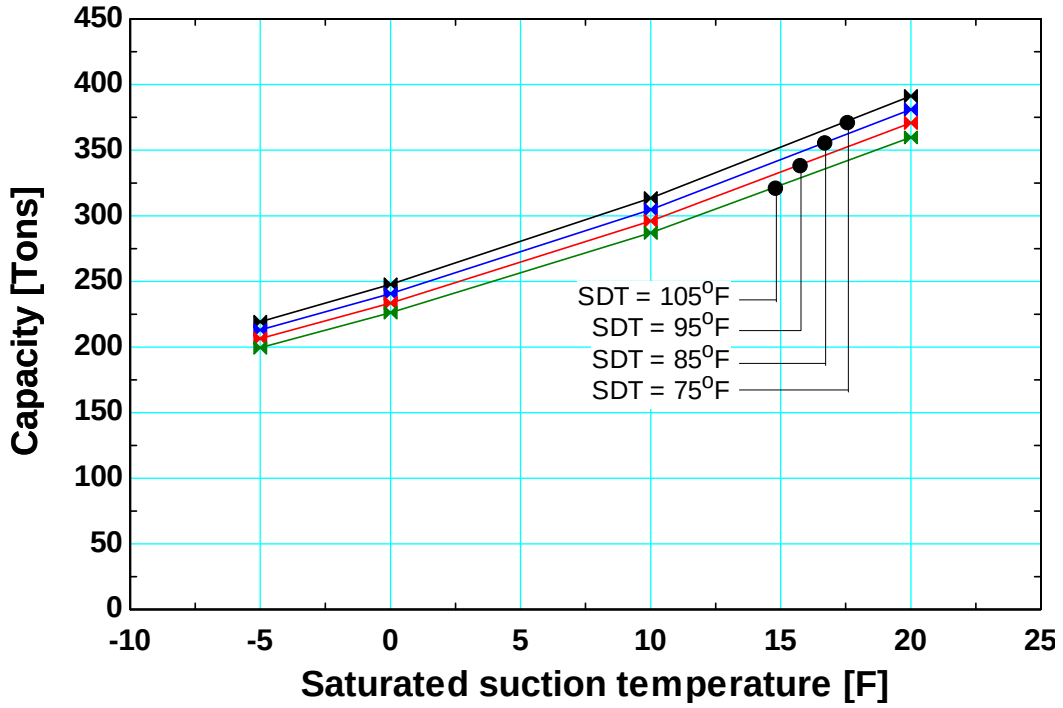

Figure 3-5: Capacity compressor map of RWF II 177 high-stage compressor operating with NH_3 from "Coolware" compressor selection program

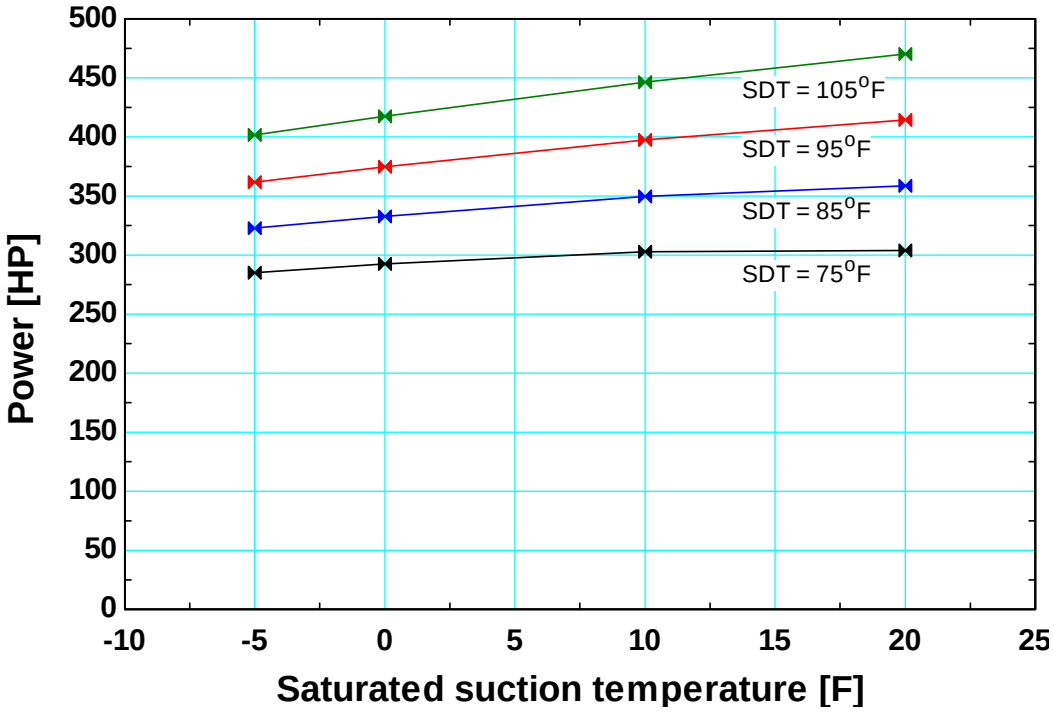

Figure 3-6: Power compressor map of RWF II 177 high-stage compressor operating with NH_3 from "Coolware" compressor selection program

In order to integrate the compressor specifications into the system model, the compressor full-load capacity and full-load power compressor maps of the compressor in each stage are curve-fitted as a bi-quadratic equation as a function of the saturated suction temperature and the saturated discharge temperature. The full-load capacity of the high-pressure compressor (CAP_{HPC}) is defined as,

$$CAP_{HPC} = a + b\,SSTH + c\,SSTH^2 + d\,SDTH + e\,SDTH^2 + f\,SSTH\,SDTH \tag{3-1}$$

where

$$\begin{aligned} a &= 292.89[Tons] \qquad b = 7.177\left[\frac{Tons}{F}\right] \qquad c = 0.0591\left[\frac{Tons}{F^2}\right] \\ d &= -0.513\left[\frac{Tons}{F}\right] \qquad e = -0.0012\left[\frac{Tons}{F^2}\right] \qquad f = -0.0158\left[\frac{Tons}{F^2}\right] \end{aligned} \tag{3-2}$$

The full-load electrical power of the high-pressure compressor (POW_{HPC}) is defined as,

$$POW_{HPC} = a + b\,SSTH + c\,SSTH^2 + d\,SDTH + e\,SDTH^2 + f\,SSTH\,SDTH \tag{3-3}$$

where

$$a = 18.677\left[HP\right] \qquad b = -3.724\left[\frac{HP}{F}\right] \qquad c = -0.0316\left[\frac{HP}{F^2}\right]$$
$$d = 3.265\left[\frac{HP}{F}\right] \qquad e = 0.0051\left[\frac{HP}{F^2}\right] \qquad f = 0.0663\left[\frac{HP}{F^2}\right] \tag{3-4}$$

The full-load capacity and rated power of the booster compressor are defined in a similar manner as in the high-temperature circuit. The full-load capacity of the booster compressor ($CAP_{BOOSTER}$) is defined as,

$$CAP_{BOOSTER} = a + b\,SSTB + c\,SSTB^2 + d\,SDTB + e\,SDTB^2 + f\,SSTB\,SDTB \tag{3-5}$$

where

$$a = 1097\left[Tons\right] \qquad b = 22.76\left[\frac{Tons}{F}\right] \qquad c = 0.1336\left[\frac{Tons}{F^2}\right]$$
$$d = -1.688\left[\frac{Tons}{F}\right] \qquad e = 0.0022\left[\frac{Tons}{F^2}\right] \qquad f = -0.0109\left[\frac{Tons}{F^2}\right] \tag{3-6}$$

The full-load electrical power of the booster compressor ($POW_{BOOSTER}$) is defined as,

$$POW_{BOOSTER} = a + b\,SSTB + c\,SSTB^2 + d\,SDTB + e\,SDTB^2 + f\,SSTB\,SDTB \tag{3-7}$$

where

$$a = 348.34\left[HP\right] \qquad b = -1.948\left[\frac{HP}{F}\right] \qquad c = -0.0357\left[\frac{HP}{F^2}\right]$$
$$d = 6.906\left[\frac{HP}{F}\right] \qquad e = 0.0214\left[\frac{HP}{F^2}\right] \qquad f = 0.0613\left[\frac{HP}{F^2}\right] \tag{3-8}$$

Consequently, the full-load capacity of the selected compressor is used to determine the number of compressors (N_{comp}) that are needed to meet the required refrigeration load ($\dot{Q}_{required}$) in that particular temperature circuit during design conditions. For instance, in the low-temperature circuit of the multi-stage system, the number of booster compressors ($N_{BOOSTER}$) required to meet the load at the evaporators ($\dot{Q}_L$) is determined based on the booster compressor full-load capacity ($CAP_{BOOSTER}$).

$$N_{BOOSTER} = \frac{\dot{Q}_L}{CAP_{BOOSTER}} \tag{3-9}$$

The number of compressors is rounded up to the next highest integer (i.e. if N_{comp} is 3.4, it is rounded to 4); this allows the compressors to meet the maximum cooling capacity required. Operationally, one compressor unit will operate under a part-load condition while the remaining compressors run at full-load. The part-load capacity of the single compressor in this situation will depend on the ratio of the remaining heat load that was not met by compressors operating at full-load relative to the full load capacity of that compressor for the prevailing operating conditions (suction and discharge pressures); this quantity is the part-load ratio (PLR) characterizing the compressor operation and is given by:

$$PLR = \frac{\dot{Q}_{required} - CAP_{comp}\,(N_{comp} - 1)}{CAP_{comp}} \tag{3-10}$$

The Frick twin screw compressors selected are capable of operating at part-load ratios as low as 12%. If the required part-load ratio at any given system operating condition is lower than this value, then the compressor unit is run at the minimum part-load capacity while another compressor starts unloading. When the second compressor stops unloading, the first compressor is shut off. However, in this analysis the compressor part-load operation is assumed to have a capability of reaching no-load condition before the compressor unit is shut off, so that only one compressor is needed for part-load operation. Thus, the unloading performance data are extrapolated beyond 12% part-load ratio down to no-load condition.

The unloading characteristic of screw compressors is non-linear – meaning that the compressor is increasingly less efficient under part-load conditions compared to its full load operation. The power of the compressor while operating at part-load is expressed as a fraction of full-load power of the compressor ($FFLP$) and is some non-linear function of the part-load ratio (PLR). The relationship between these two parameters is illustrated on a part-load curve that is obtained from actual compressor operation and depends on the compressor type, model and operating pressures. Figure 3-7 shows the part-load curve of the RWF II compressors provided by Frick Inc.

A 2rd order polynomial curve fit is used to integrate the unloading characteristics provided by Figure 3-7 into the system model. A relationship between fraction of full-load power ($FFLP_H$) and part-load ratio of the high-stage compressor (PLR_H), both expressed as a percentage, is given as,

$$FFLP_H = a + b\,PLR_H + c\,PLR_H^{\,2} \tag{3-11}$$

where

$$a = 44.06[\%] \quad b = 0.4178[-] \quad c = 0.00148\left[\frac{1}{\%}\right] \tag{3-12}$$

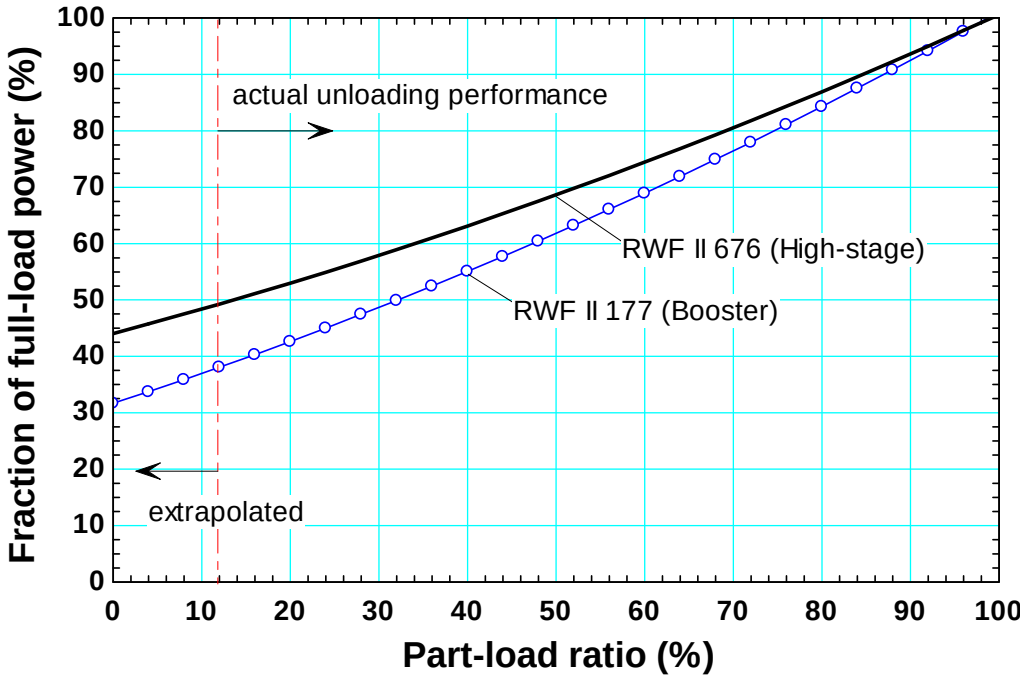

Figure 3-7: Part-load curve of RWF II screw compressors (courtesy of Frick Inc.).

A curve-fit of the booster compressor unloading curve is defined as,

$$FFLP_B = a + b\,PLR_B + c\,PLR_B^{\,2} \tag{3-13}$$

where

$$a = 31.68[\%] \quad b = 0.5120[-] \quad c = 0.00182\left[\frac{1}{\%}\right] \tag{3-14}$$

The part-load power of the high-stage compressor ($\dot{W}_{HPC,PL}$) is given by,

$$\dot{W}_{HPC,PL} = \dot{W}_{HPC,FL}\,FFLP_H \tag{3-15}$$

where $\dot{W}_{HPC,FL}$ is the high-stage compressor full-load power expressed in kW.

The part-load power of the booster compressor ($\dot{W}_{BOOSTER,PL}$) is defined as,

$$\dot{W}_{BOOSTER,PL} = \dot{W}_{BOOSTER,FL}\,FFLP_B \tag{3-16}$$

where $\dot{W}_{BOOSTER,FL}$ is the high-stage compressor full-load power expressed in kW.

The total compressor power ($\dot{W}_{comp}$) for each stage of compression is defined as,

$$\dot{W}_{comp} = \dot{W}_{comp,FL}\left(N_{comp} - 1\right) + \dot{W}_{comp,PL} \tag{3-17}$$

3.1.2) Reciprocating Compressor

Reciprocating compressors, typically, are smaller than screw compressors. They are usually found in systems with low-temperature heat load of less than 1,000 kW (Stoecker, 1988) or in a system where the operating refrigerant vapor density is high enough to exploit smaller compression equipment. The combination of high working pressures associated with carbon dioxide at low saturation pressures and low refrigerant volumetric flow make twin-screw compressors not necessarily the best choice for the low-temperature circuit. Instead, reciprocating compressors are considered for the low-temperature circuit with carbon dioxide in the cascade system configuration. Figure 3-8 illustrates a typical two-cylinder reciprocating compressor.

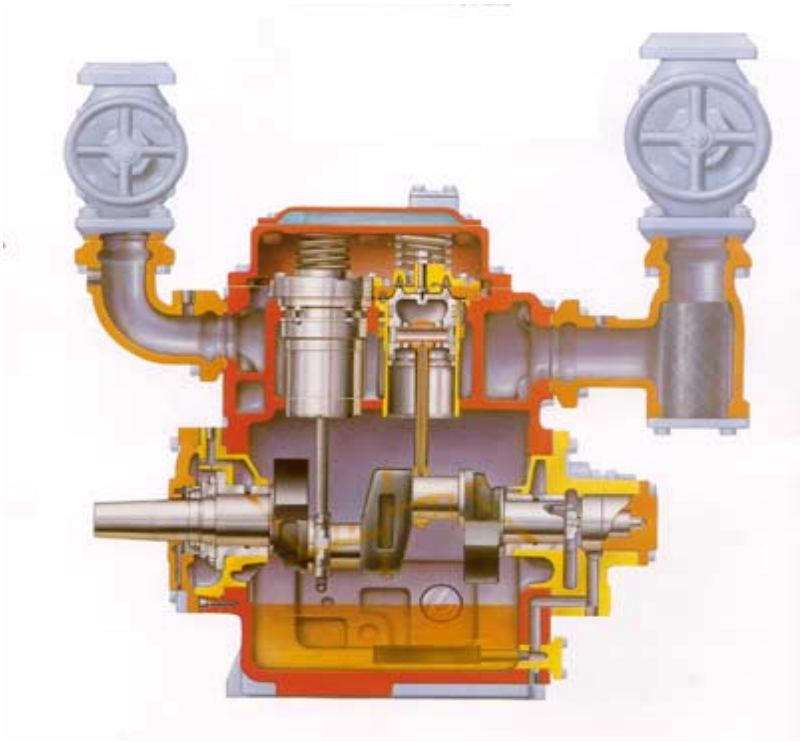

Figure 3-8: Cut-away of a two-cylinder reciprocating compressor (courtesy of Mayegawa Manufacturing Co. Ltd., 2008)

3.1.2.1) Reciprocating Compressor Selection

Similar to screw compressor selection described in the previous section, several reciprocating compressor models are considered. The model that is selected for the low-temperature circuit compressor in the cascade cycle is the 55-HP reciprocating compressor from Grasso Inc. Compressor data based on information provided by Grasso Inc. forms the basis for this selection and performance prediction. Figures 3-9 and 3-10 illustrate, as a function of saturated suction temperature for the 55-HP Grasso reciprocating compressor, full-load capacity and full-load power, respectively.

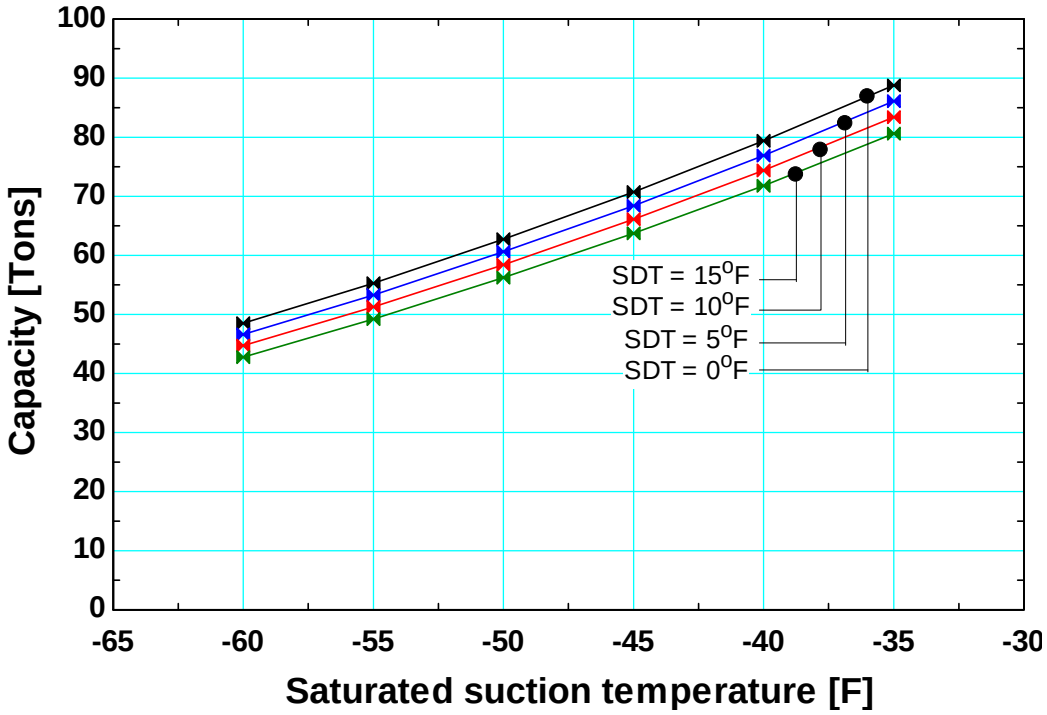

Figure 3-9: Capacity compressor map of 55-HP Grasso reciprocating compressor operating with CO_2 from Grasso Inc.

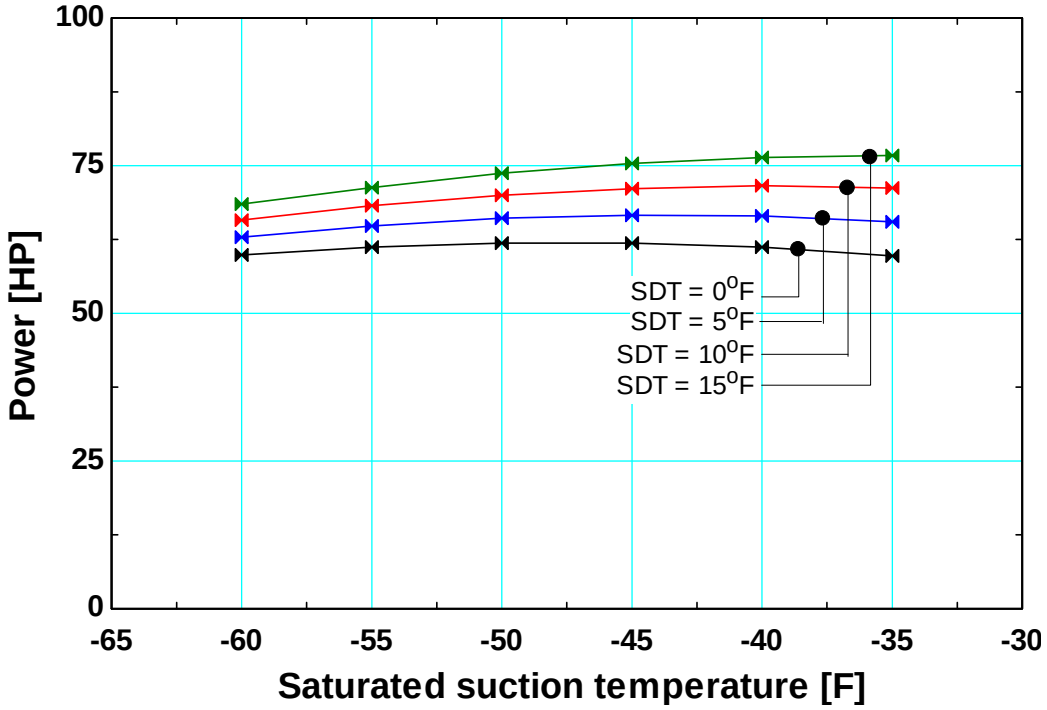

Figure 3-10: Power compressor map of 55-HP Grasso reciprocating compressor operating with CO_2 from Grasso Inc.

Similar to the screw compressors, reciprocating compressor specifications are integrated into the system model by curve-fitting the reciprocating compressor full-load capacity and full-load power, provided in Figures 3-9 and 3-10, as a bi-quadratic equation as a function of the saturated suction temperature and saturated discharge temperature. The full-load capacity of the reciprocating compressor (CAP_{RECIP}) is defined as,

$$CAP_{RECIP} = a + b\,SST + c\,SST^2 + d\,SDT + e\,SDT^2 + f\,SST\,SDT \tag{3-18}$$

where

$$\begin{aligned} a &= 292.89[Tons] \qquad b = 7.177\left[\frac{Tons}{F}\right] \qquad c = 0.0591\left[\frac{Tons}{F^2}\right] \\ d &= -0.513\left[\frac{Tons}{F}\right] \qquad e = -0.0012\left[\frac{Tons}{F^2}\right] \qquad f = -0.0158\left[\frac{Tons}{F^2}\right] \end{aligned} \tag{3-19}$$

The full-load electrical power of the reciprocating compressor (POW_{RECIP}) is defined as,

$$POW_{RECIP} = a + b\,SST + c\,SST^2 + d\,SDT + e\,SDT^2 + f\,SST\,SDT \tag{3-20}$$

where

$$a = 18.677[HP] \qquad b = -3.724\left[\frac{HP}{F}\right] \qquad c = -0.0316\left[\frac{HP}{F^2}\right]$$
$$d = 3.265\left[\frac{HP}{F}\right] \qquad e = 0.0051\left[\frac{HP}{F^2}\right] \qquad f = 0.0663\left[\frac{HP}{F^2}\right] \tag{3-21}$$

The number of reciprocating compressors required (N_{RECIP}) and the part-load ratio (PLR_{RECIP}) in the low-temperature circuit of the cascade system are calculated in a manner that is similar to the multi-stage system,

$$N_{RECIP} = \frac{\dot{Q}_L}{CAP_{RECIP}} \tag{3-22}$$

The part-load ratio is defined as,

$$PLR_{RECIP} = \frac{\dot{Q}_L - CAP_{RECIP}\,(N_{RECIP} - 1)}{CAP_{RECIP}} \tag{3-23}$$

Reciprocating compressors capacity is reduced by unloading vapor compression cylinders. This is achieved by the holding the exhaust valves in each of the cylinders open. Reciprocating compressors capacity is provided by compression of vapor in finite number of compression cylinders, thus the capacity can be reduced in step sizes equal to the rated compressor capacity divided by the total number of cylinders. In order to meet part-load capacity, the reciprocating compressors cycles cylinder exhaust valves on and off. This cycling method produces a linear unloading characteristic and the time-averaged capacity matches the required heat load. Thus, the relationship between $FFLP_{RECIP}$ and PLR_{RECIP} is,

$$FFLP_{RECIP} = PLR_{RECIP} \tag{3-24}$$

The part-load compressor power ($\dot{W}_{RECIP,PL}$) is defined as:

$$\dot{W}_{RECIP,PL} = \dot{W}_{RECIP,FL}\, FFLP_{RECIP} \tag{3-25}$$

Where $\dot{W}_{RECIP,FL}$ is the reciprocating compressor full-load power expressed in kW.

The total compressor power ($\dot{W}_{RECIP}$) for one stage of compression is given by:

$$\dot{W}_{RECIP} = \dot{W}_{RECIP,FL}\left(N_{RECIP} - 1\right) + \dot{W}_{RECIP,PL} \tag{3-26}$$

Since the number of compressors required in each circuit depends on the amount of heat load that the circuit must meet and the full-load capacity of each compressor being deployed, it is desirable to minimize the number of compressors while trying to cope with the load requirement. The advantages of having fewer compressors include capital cost and footprint. In other words, it is impractical to install a group of small compressors in an effort to meet a huge load. The full-load capacity of one compressor is a function of the saturation temperatures at its suction and discharge conditions. Moreover, the intermediate condition between LTC and HTC defines the saturation temperatures at the outlet and the inlet of the booster compressors and high-pressure compressors, respectively. Since the COP of the system varies with the intermediate condition, there is a window of opportunity to maximize the overall COP of the cycle while maintaining the number of compressors in each temperature circuit. Chapter 4 focuses on this performance optimization.

3.2) Cascade Heat Exchanger

In a cascade vapor compression refrigeration system with two refrigerants (Figure 2-6), each flowing in its own circuit, the heat removed from the low-temperature circuit (LTC) is transferred to the high-temperature circuit (HTC) through a heat exchanging device without open mixing of the refrigerants. The cascade heat exchanger needs to be well-designed to minimize the temperature difference between both circuits. Although this heat exchanger can be a plate-and-frame design, more typical in industrial refrigeration applications is the shell-and-tube configuration. The heat exchanging process within the cascade heat exchanger is accomplished by removing heat from the refrigerant (e.g., sub-critical carbon dioxide) compressed in the low-temperature circuit via condensation inside the tube bundle and transferring that heat to the refrigerant evaporating in the shell. Because the LTC refrigerant leaves the booster compressor as a superheated vapor, the first section of the tube-side of the cascade heat exchanger de-superheats the LTC vapor. This section of the cascade heat exchanger responsible for this process is called "de-superheating section". After the LTC refrigerant is de-superheated, it continues flowing through the remainder of the heat exchanger as it condenses before it leaves as a saturated liquid. This portion of the heat exchanger is called "condensing section". The model of the heat exchange process in the cascade heat exchanger separately considers these two distinct sections to model each individual process. A qualitative diagram of the temperature distribution as a function of the position in the heat exchanger is shown in Figure 3-11,

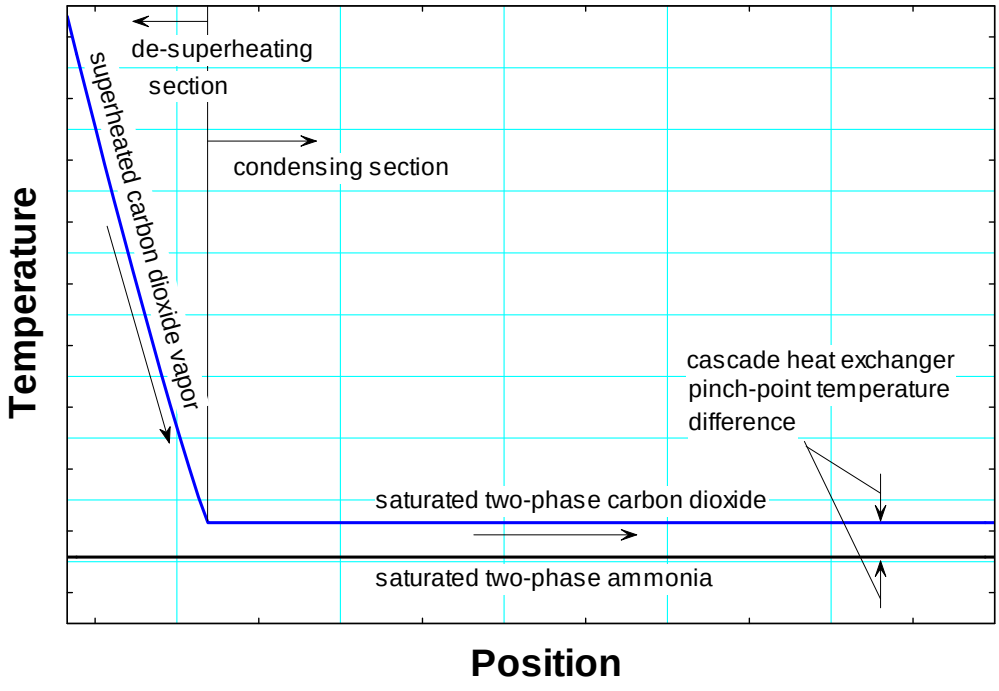

Figure 3-11: Qualitative temperature distribution of carbon dioxide cooling process

3.2.1) Cascade Heat Exchanger Geometry at Design Conditions

The objective of this analysis is to predict the operating characteristics of the cascade heat exchanger based on its configuration, physical size, and geometry as determined to satisfactorily perform at design conditions. The detailed system model will use this physical size and configuration in order to simulate the performance at off-design conditions. Figure 3-12 is a schematic diagram of a cascade heat exchanger using a shell-and-tube configuration.

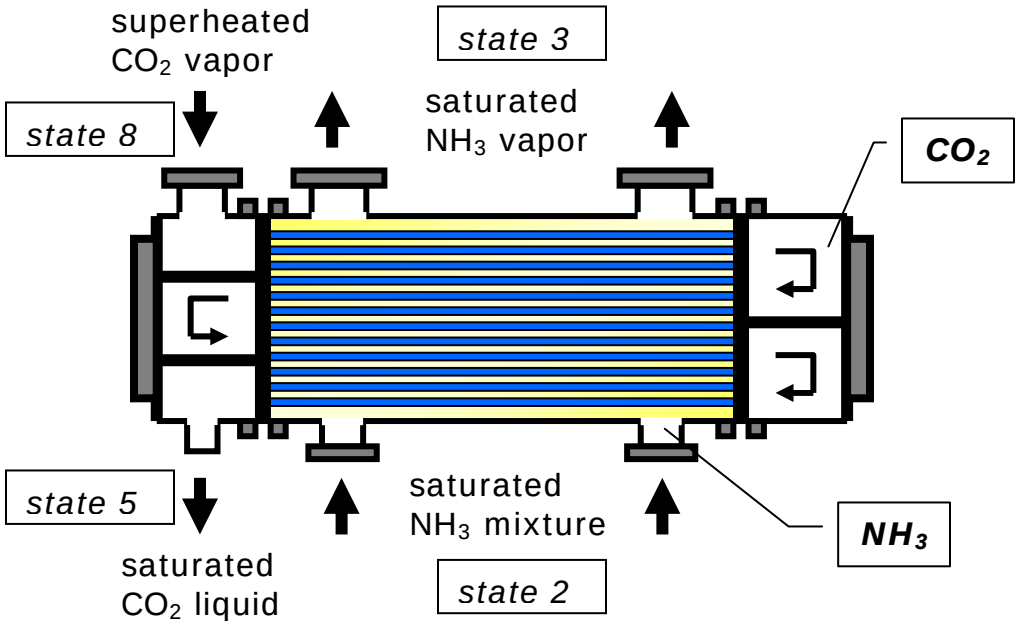

Figure 3-12: Schematic diagram of a 4-pass, shell-and-tube cascade heat exchanger

The design size and operating conditions associated with the cascade system are based on an actual heat exchanger that is installed in an operating cascade refrigeration system at a plant located in Arkansas. The design operating conditions of this particular heat exchanger are listed in Table 3-1 and the design size and geometry are listed in Table 3-2.

Table 3-1: Design operating conditions of an actual cascade heat exchanger operating with NH_3/CO_2

Input	***Description***	***Values***
$T_{cascade}$	saturated condensing temperature of CO_2	258.2 K (5°F)
$\Delta T_{cascade}$	cascade heat exchanger pinch-point temperature difference[1]	2.78 K (5°F)
$\dot{Q}_{cascade}$	total heat load at the cascade heat exchanger	2,835 kW (0.75 x 1,075 Tons)

Table 3-2: Design size and geometry of an actual cascade heat exchanger operating with NH_3/CO_2

Input	***Description***	***Values***
D_o	Outer tube diameter	5/8 in (1.588 cm)
D_i	Inner tube diameter	0.527 in (1.34 cm)
th_{tube}	Tube thickness	0.049 in (1.245 mm)
$L_{tube,\,pass}$	Tube length per pass	380 ¾ in (9.67 m)
L_{shell}	Shell length	445 5/8 in (11.32 m)
D_{shell}	Outer shell diameter	48 in (1.21 m)
AR	Aspect ratio	0.107
STAR	Shell-to-tube area ratio	2.381
STLR	Shell-to-tube length ratio	1.17
pass	Number of tube pass	4
$N_{tube,cas}$	Total number of tubes	2,475

The cascade heat exchanger computer model will include some of the physical parameters listed above as a baseline for this analysis. The model is still part of the same cascade system operating at the baseline operating conditions (Table 1-1 and Table 2-3). All of the design parameters selected in developing a cascade heat exchanger model are summarized in Table 3-3.

[1] The saturated evaporating temperature of the ammonia is equal to the saturated condensing temperature of the carbon dioxide minus the pinch point temperature difference.

Table 3-3: Design operating conditions and geometry of the cascade heat exchanger model operating with NH_3/CO_2

Input	***Description***	***Values***
$T_{cond,sat}$	saturated condensing temperature of NH_3	308 K (95°F)
$T_{cascade}$	saturated condensing temperature of CO_2	258.2 K (5°F)
$T_{evap,sat}$	saturated evaporating temperature of CO_2	233.2 K (-40°F)
$\Delta T_{cascade}$	cascade heat exchanger pinch-point temperature difference	5.56 K (10°F)
$\dot{Q}_{cascade}$	total heat load on the cascade heat exchanger	2,835 kW (0.75 x 1050 Tons)
D_o	Outer tube diameter	5/8" (1.588 cm)
D_i	Inner tube diameter	0.527" (1.34 cm)
th_{tube}	Tube thickness	0.049" (1.245 mm)
AR	Aspect ratio	0.1303
STAR	Shell-to-tube area ratio	2.381
STLR	Shell-to-tube length ratio	1.707
N_{pass}	Number of tube passes	4

With the input parameters provided, a step-by-step 1st law analysis (presented in Section 2.1) is carried out to determine the unknown thermodynamic state parameters necessary for the cascade heat exchanger model. The cascade system encompassing this particular design analysis of the cascade heat exchanger also integrates the compressor models from Section 3.1. The cycle state points are listed in Table 3-4.

Table 3-4: Operating conditions of the design cascade heat exchanger operating with NH_3/CO_2

HTC (NH_3)	***T_2***	***T_3***	***P_2***	$\dot{m}_{HTC}$
English Units	-5°F	-5°F	26.9 psia	350.4 lbm/min
SI Units	252.6 K	252.6 K	185.4 kPa	2.65 kg/s
LTC (CO_2)	***T_8***	***T_5***	***P_5***	$\dot{m}_{LTC}$
English Units	79.79°F	5°F	332.2 psia	1174 lbm/min
SI Units	299.7 K	258.2 K	2291 kPa	8.88 kg/s

The geometry of this cascade heat exchanger model is specified to have four tube passes. From a modeling perspective, these four separate passes are modeled as a tube bundle with a single-pass geometry having four times the length. This is due to the physical operation of the heat exchanger in which refrigerant only flows through a number of tube bundle occupied in one tube pass throughout the heat exchanging process. Computationally, two heat exchanger sections are defined based on this process. Thus, the number of tubes being solved ($N_{tube,pass}$) corresponds to those occupying one tube pass but is four times in length ($L_{tube,cas}$), which is equal to the total tube length. From a heat transfer standpoint, this is equivalent to the total number of tubes in all four passes of the heat exchanger ($N_{tube,cas}$), each with the length of one flow pass ($L_{tube,pass}$). Since the entire tube bundle is submerged under nucleate boiling high-temperature circuit refrigerant, each tube in the bundle is assumed to receive equally distributed heat flux.

In order to determine the required heat exchanger size, the required conductance rate of each section ($UA_{cascade,sat}$ and $UA_{cascade,sh}$) is calculated using the 1st principles of heat transfer. The following sections discuss cascade heat exchanger analysis in details.

3.2.2) Condensing Section

In the heat exchanging process within the condensing section of the cascade heat exchanger, the heat transfer path between carbon dioxide and ammonia streams is defined by three thermal resistances that are in series, as shown in Figure 3-13.

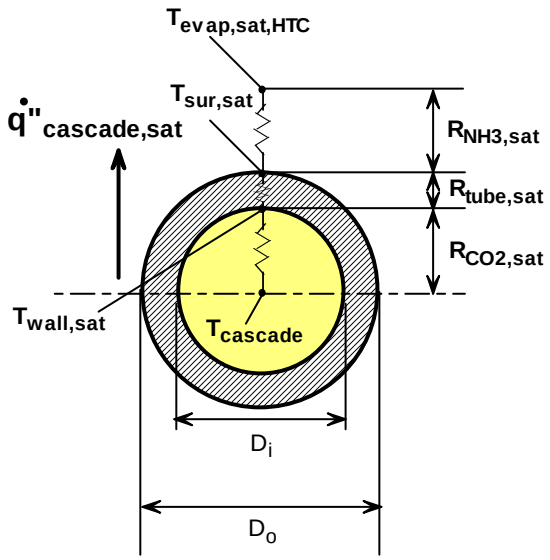

Figure 3-13: Thermal resistance network of the condensing section of a cascade heat exchanger

Because neither the ammonia nor the carbon dioxide temperature varies in the condensing section, the rate of heat transfer inside the condensing section of the cascade heat exchanger is defined as,

$$\dot{Q}_{cascade,sat} = UA_{cascade,sat}\,\Delta T_{cascade} \tag{3-27}$$

To determine the size and geometry of the condensing section of the cascade heat exchanger, the condensing section conductance ($UA_{cascade,sat}$) becomes the constraint for the geometry, where $UA_{cascade,sat}$ is by definition the inverse of the sum of all the thermal resistances between the heat exchanging fluids,

$$UA_{sat,cas} = \frac{1}{R_{CO_2,sat} + R_{Tube,sat} + R_{NH_3,sat}} \tag{3-28}$$

where, $R_{CO_2,sat}$ is the thermal resistance on the condensing refrigerant side, which is the resistance to convection between condensing carbon dioxide and the inside surface of the tube bundles. This resistance is defined by,

$$R_{CO_2,sat} = \frac{1}{hc_{CO_2,sat}\,A_{cond,sat}} \tag{3-29}$$

where $hc_{CO_2,sat}$ is the convective heat transfer coefficient of condensing carbon dioxide and $A_{cond,sat}$ is the internal flow area of the tube in the condensation section,

$$A_{cond,sat} = \pi\, D_i\, L_{tube,sat}\, N_{tube,pass} \tag{3-30}$$

where $L_{tube,sat}$ is the tube length required in the condensing section. The convective heat transfer coefficient of condensing carbon dioxide can be calculated from using a correlation proposed by Cavallini et al. (2002):

$$\overline{Nus}_{CO_2,sat} = 0.05\,\overline{Re}_{CO_2,sat}^{\,0.8}\,Pr_{CO_2,L}^{\,1/3} \tag{3-31}$$

where $\overline{Nus}_{CO_2,sat}$ is the average Nusselt number of condensing carbon dioxide, $Pr_{CO_2,L}$ is the Prandtl number for carbon dioxide in the liquid phase. $\overline{Re}_{CO_2,sat}$ is an average Reynolds number defined by Eq. (3-36), which is related to an equivalent Reynolds number ($Re_{CO_2,eq}$). According to Cavallini et al (2002), the equivalent Reynolds number is:

$$Re_{CO_2,eq} = \frac{G_{cas}\, D_i \left((1-x) + x \left(\frac{\rho_{CO_2,liq}}{\rho_{CO_2,liq}} \right)^{1/2} \right)}{\mu_{CO_2,liq}} \tag{3-32}$$

where $\mu_{CO_2,liq}$ is the dynamic viscosity in the liquid phase of the refrigerant, and $\rho_{CO_2,liq}$ and $\rho_{CO_2,liq}$ are the refrigerant density in the liquid and vapor phase, respectively. G_{cas} is the refrigerant mass flux, which is the rate of carbon dioxide mass flow through tube flow area and is defined as,

$$G_{cas} = \frac{\dot{m}_{LTC}}{A_{flow}} \tag{3-33}$$

where A_{flow} is the total flow area through the tube bundle,

$$A_{flow} = \frac{\pi\, D_i^{\,2}\, N_{tube,pass}}{4} \tag{3-34}$$

The equivalent Reynolds number ($Re_{CO_2,eq}$) in Eq. (3-32) varies with vapor quality of condensing carbon dioxide and in order to simplify the computation of the heat transfer coefficient of carbon dioxide during the condensation process, an average value of the Reynolds number ($\overline{Re}_{CO_2,sat}$) is used,

$$\overline{Re}_{CO_2,sat} = \frac{1}{x}\int_0^1 Re_{CO_2,eq}\, dx \tag{3-35}$$

integrating Eq. (3-35) over the quality region gives,

$$\overline{Re}_{CO_2,sat} = \frac{G_{cas}\, D_i}{2\,\mu_{CO_2,liq}} \left(\left(\frac{\rho_{CO_2,liq}}{\rho_{CO_2,vap}} \right)^{1/2} + 1 \right) \tag{3-36}$$

The Prandtl number ($Pr_{CO_2,liq}$) in Eq. (3-31) is the Prandtl number of carbon dioxide in the liquid phase. The convective heat transfer coefficient of carbon dioxide ($\overline{hc}_{CO_2,sat}$) is determined from the average Nusselt number ($\overline{Nus}_{CO_2,sat}$),

$$\overline{hc}_{CO_2,sat} = \frac{\overline{Nus}_{CO_2,sat}\, k_{CO_2,liq}}{D_i} \tag{3-37}$$

where $k_{CO_2,liq}$ is the thermal conductivity of carbon dioxide in the liquid phase.

The next term in the thermal resistance network in Eq. (3-28) is the conduction resistance through the tube walls ($R_{tube,sat}$). The resistance formula for conduction through cylindrical tubes is provided by Incropera and DeWitt (2002),

$$R_{tube,sat} = \frac{ln\left(\frac{D_o}{D_i}\right)}{2\pi k_{tube,sat} L_{tube,sat} N_{tube,pass}} \tag{3-38}$$

The thermal conductivity of carbon steel at the saturated evaporating temperature of ammonia in the condensing section ($k_{tube,sat}$) is taken from Incropera and DeWitt (2002). The final term of the thermal resistance network in Eq. (3-28) is the resistance due to convection between boiling ammonia outside of the tube bundle (on the shell side), $R_{NH_3,sat}$. This resistance is defined by,

$$R_{NH_3,sat} = \frac{1}{hc_{NH_3,sat} A_{evap,sat}} \tag{3-39}$$

where, $hc_{NH_3,sat}$ is the convective heat transfer coefficient of evaporating ammonia and $A_{evap,sat}$ is the heat transfer area that the ammonia comes into contact with. The heat transfer area for boiling ammonia is:

$$A_{evap,sat} = \pi D_o L_{tube,sat} N_{tube,pass} \tag{3-40}$$

Numerous experiments have been conducted to measure the heat transfer coefficient for boiling ammonia over flooded tube bundles; several empirical correlations have been developed and proposed based on these experiments (for example, Cornwell (1994), Zheng et al (2001) and Ayub (2004)). For this analysis, a correlation proposed by Ayub (2004) has been selected. The correlation predicts the convective heat transfer coefficient of boiling ammonia as a function of the heat flux ($\dot{q}_{cascade,sat}$") in the condensing section:

$$hc_{NH_3,sat} = \gamma \dot{q}_{cascade,sat}{}''^{0.55} \tag{3-41}$$

$hc_{NH_3,sat}$ is expressed in the units of kW/m^2-K and $\dot{q}_{cascade,sat}$" is expressed in the units of kW/m^2. γ is a unit-less constant evaluated as a function of the saturated evaporating temperature of ammonia (T_C, expressed in degree Celcius):

$$\gamma = 0.291 + 0.0039 T_C + 0.000475 T_C{}^2 + 0.0000184 T_C{}^3 + 1.97x10^{-7} T_C{}^4 \tag{3-42}$$

$\dot{q}_{cascade,sat}$"is inversely proportional to the heat transfer area of the condensing section ($A_{evap,sat}$) and is defined by,

$$\dot{q}_{cascade,sat}" = \frac{\dot{Q}_{cascade,sat}}{A_{evap,sat}} \tag{3-43}$$

3.2.3) De-superheating Section

The process of de-superheating carbon dioxide inside the tube bundle involves significant temperature change on the condensing refrigerant side, thus the temperature difference between two refrigerant streams in this section is not constant. An effectiveness-NTU method is an appropriate approach to modeling this section because the specific heat capacity of carbon dioxide vapor is nearly constant. The capacitance rate of the ammonia evaporating on the shell side of the tube bundle has an infinite capacitance rate. The number of transfer units in the de-superheating section ($NTU_{cascade,sh}$) for the case where one fluid stream has an infinitely large capacitance rate is given by Incropera and DeWitt (2002) as,

$$NTU_{cascade,sh} = -ln(1-\varepsilon_{cascade,sh}) \tag{3-44}$$

The effectiveness of the de-superheating section ($\varepsilon_{cascade,sh}$) is defined as,

$$\varepsilon_{cascade,sh} = \frac{T_{CO_2,sh} - T_{cascade}}{T_{CO_2,sh} - T_{evap,sat,HTC}} \tag{3-45}$$

The discharge temperature of superheated LTC refrigerant ($T_{CO_2,sh}$), cascade condensing temperature ($T_{cascade}$) and saturated evaporating temperature of HTC refrigerant ($T_{evap,sat,HTC}$) correspond to T_8, T_5 and T_2 in Figure 2-6, respectively. The minimum capacitance rate in the de-superheating section ($\dot{C}_{min,sh}$) is defined by,

$$\dot{C}_{min,sh} = \dot{m}_{LTC}\, c_{p,CO_2,sh} \tag{3-46}$$

where $\dot{m}_{LTC}$ is the mass flow rate of the de-superheating refrigerant and $c_{p,CO_2,sh}$ is the specific heat capacity of carbon dioxide evaluated at a mean temperature of the de-superheating refrigerant ($\overline{T}_{CO_2,sh}$),

$$\overline{T}_{CO_2,sh} = \frac{T_{CO_2,sh} + T_{cascade}}{2} \tag{3-47}$$

The required conductance rate of the de-superheating section ($UA_{cascade,sh}$) can be expressed based on the number of transfer units ($NTU_{cascade,sh}$) and the minimum refrigerant capacitance rate ($\dot{C}_{min,sh}$) as,

$$UA_{cascade,sh} = NTU_{cascade,sh}\,\dot{C}_{min,sh} \tag{3-48}$$

The heat transfer path in the de-superheating section is defined similarly to that of the condensing section. A schematic diagram of the thermal resistance network of the de-superheating section is shown in Figure 3-14.

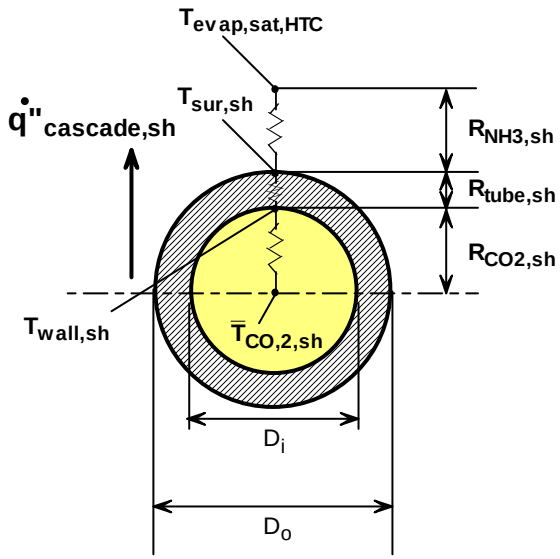

Figure 3-14: Thermal resistance network of the de-superheating section of a cascade heat exchanger

The conductance rate of the de-superheating section is defined as the inverse of the sum of all the resistances across the thermal resistance network separating the two refrigerant streams,

$$UA_{cascade,sh} = \frac{1}{R_{CO_2,sh} + R_{tube,sh} + R_{NH_3,sh}} \tag{3-49}$$

where $R_{CO_2,sh}$ is the thermal resistance to convection between de-superheating carbon dioxide and the inside surface of the tube bundle. This resistance is defined by,

$$R_{CO_2,sh} = \frac{1}{hc_{CO_2,sh}\,A_{cond,sh}} \tag{3-50}$$

where $hc_{CO_2,sh}$ is the convective heat transfer coefficient of de-superheating carbon dioxide and $A_{cond,sh}$ is the internal flow area of the tubes,

$$A_{cond,sh} = \pi D_i L_{tube,sh} N_{tube,pass} \tag{3-51}$$

where $L_{tube,sh}$ is the length of tubing required in the de-superheating section. The length of tubing in each section of the tube bundle is still unknown. The overall tube length is the sum of the tube length required in the superheated and condensing regions:

$$L_{tube,sh} = L_{tube,cas} - L_{tube,sat} \tag{3-52}$$

The convective heat transfer coefficient of de-superheating carbon dioxide ($hc_{CO_2,sh}$) in Eq. (3-50) can be calculated from its Nusselt number ($Nus_{CO_2,sh}$) using the Dittus-Boelter equation (cooling process) described by Winterton (1998) and presented by Incropera and DeWitt (2002),

$$Nus_{CO_2,sh} = 0.023\, Re_{CO_2,sh}^{4/5}\, Pr_{CO_2,sh}^{0.3} \tag{3-53}$$

where $Pr_{CO_2,sh}$ and $Re_{CO_2,sh}$ are the Prandtl number and the Reynolds number of de-superheating carbon dioxide. The Prandtl number is defined as,

$$Pr_{CO_2,sh} = \frac{\nu_{CO_2,sh}}{\alpha_{CO_2,sh}} \tag{3-54}$$

where $\nu_{CO_2,sh}$ and $\alpha_{CO_2,sh}$ are the kinematic viscosity and thermal diffusivity of de-superheating carbon dioxide, respectively; both quantities are evaluated at $\overline{T}_{CO_2,sh}$ and P_8. The Reynolds number of the de-superheating carbon dioxide is defined as,

$$Re_{CO_2,sh} = \frac{\rho_{CO_2,sh}\, \overline{u}_{CO_2,sh}\, D_i}{\mu_{CO_2,sh}} \tag{3-55}$$

where $\rho_{CO_2,sh}$, $\mu_{CO_2,sh}$ and $\overline{u}_{CO_2,sh}$ are the density, dynamic viscosity and average flow velocity of the de-superheating carbon dioxide, respectively. The average flow velocity inside the tube bundle of the de-superheating section ($\overline{u}_{CO_2,sh}$) is determined from the mass flow rate of the refrigerant and the number of tubes in the bundle based on flow continuity,

$$\overline{u}_{CO_2,sh} = \frac{\dot{m}_{LTC}}{\rho_{CO_2,sh}\, A_{flow}} \tag{3-56}$$

The convective heat transfer coefficient of de-superheating carbon dioxide ($hc_{CO_2,sh}$) is,

$$hc_{CO_2,sh} = \frac{Nus_{CO_2,sh}\, k_{CO_2,sh}}{D_i} \tag{3-57}$$

where $k_{CO_2,sh}$ is the thermal conductivity of carbon dioxide evaluated at the its average temperature in the de-superheating section ($\overline{T}_{CO_2,sh}$) and its saturation pressure (P_8).

The next term in the thermal resistance network in Eq. (3-49) is the resistance to conduction through the tube walls ($R_{tube,sh}$) is provided by Incropera and DeWitt (2002),

$$R_{tube,sh} = \frac{ln\left(\frac{D_o}{D_i}\right)}{2\pi\, k_{tube,sh}\, L_{tube,sh}\, N_{tube,pass}} \tag{3-58}$$

The thermal conductivity of carbon steel at the average temperature of the de-superheating section ($k_{tube,sh}$) is taken from Incropera and DeWitt (2002).

The final term of the de-superheating section thermal resistance network in Eq. (3-49) is the resistance to convection between boiling ammonia on the shell side and the outer surface of the tube bundle ($R_{NH_3,sh}$). This resistance is defined as,

$$R_{NH_3,sh} = \frac{1}{hc_{NH_3,sh}\, A_{evap,sh}} \tag{3-59}$$

where, $hc_{NH_3,sh}$ is the convective heat transfer coefficient of evaporating ammonia and $A_{evap,sh}$ is the evaporating surface area or heat transfer area which ammonia comes in contact with. The heat transfer area for boiling ammonia is:

$$A_{evap,sh} = \pi\, D_o\, L_{tube,sh}\, N_{tube,pass} \tag{3-60}$$

$h_{NH_3,sh,cas}$ can be determined similarly to that of the condensing section using Eq. (3-41), where the constant α is evaluated from Eq. (3-42). Despite the uniform evaporation of ammonia in the shell side over the entire tube bundle, the heat flux over the de-superheating section ($\dot{q}_{cascade,sh}$ ") is different from that of the condensing section because of a different outside surface area of the tube bundle in the de-superheating section. The heat flux in this section is defined as,

$$\dot{q}_{cascade,sh}" = \frac{\dot{Q}_{cascade,sh}}{A_{evap,sh}} \tag{3-61}$$

In addition to the 1st principles heat transfer equations for both sections of the cascade heat exchanger presented, geometric parameters given as design baseline must also be integrated into the model.

The aspect ratio of the cascade heat exchanger (AR) is the ratio of the outer shell diameter (D_{shell}) to the shell length (L_{shell}). This parameter is defined as,

$$AR = \frac{D_{shell}}{L_{shell}} \tag{3-62}$$

The shell-to-tube area ratio ($STAR$) is another parameter that is specified for the cascade heat exchanger model and it will remain unchanged for all heat exchanger sizes. This parameter is the ratio of the total cross-sectional area of the outer shell to that of the tube bundle. $STAR$ is defined as,

$$STAR = \frac{A_{shell}}{A_{tube}} \tag{3-63}$$

Where, A_{shell} and A_{tube} are the cross-sectional areas of the outer shell and of the tube bundle, respectively. A_{shell} is given by,

$$A_{shell} = \frac{\pi D_{shell}^{\ 2}}{4} \tag{3-64}$$

A_{tube} is given by,

$$A_{tube} = \frac{\pi D_o^{\ 2}}{4} N_{tube,cas} \tag{3-65}$$

The shell-to-tube length ratio ($STLR$) is the ratio of the shell length to the length of a tube section (one pass). This quantity remains constant for all heat exchanger sizes, when predicted at other design conditions, in order to maintain proper geometry and is defined as,

$$STLR = \frac{L_{shell}}{L_{tube,pass}} \tag{3-66}$$

With the operating parameters of the cascade heat exchanger and required conductance in both condensing and de-superheating sections provided, the number of tubes required for this particular heat exchanger model ($N_{tube,cas}$) is determined, along with other unknown parameters. The predicted size and operating characteristics based on the design conditions provided in Table 3-3 are summarized in Table 3-5.

Table 3-5: Predicted size and operating characteristics of the NH_3/CO_2 cascade heat exchanger at design condition (10^oF pinch-point temperature)

Output	***Description***	***Values***
$N_{tube,cas}$	Total number of tubes	2,973
$L_{tube,pass}$	Tube bundle length (one pass)	35.01 ft (10.67 m)
L_{shell}	Total shell length	40.96 ft (12.48 m)
D_{shell}	Shell diameter	4.38 ft (1.34 m)
A_{shell}	Cross-sectional area of outer shell	15.1 ft^2 (1.40 m^2)
A_{tube}	Cross-sectional area of tube bundle	6.34 ft^2 (0.589 m^2)
$f_{sat,cas}$	fraction of condensing section in tube bundle	89.33%
$f_{sh,cas}$	fraction of de-superheating section in tube bundle	10.67%
$hc_{NH_3,sat}$	convective heat transfer coefficient of ammonia in the condensing section	0.3843 kW/m^2-K
$hc_{NH_3,sh}$	convective heat transfer coefficient of ammonia in the de-superheating section	0.3843 kW/m^2-K
$\overline{hc}_{CO_2,sat}$	average convective heat transfer coefficient of carbon dioxide in the condensing section	1.85 kW/m^2-K
$hc_{CO_2,sh}$	convective heat transfer coefficient of carbon dioxide in the de-superheating section	0.2297 kW/m^2-K
$UA_{cascade,sat}$	conductance rate of the condensing section	432.9 kW/K (820.6 MBtu/hr-F)
$UA_{cascade,sh}$	conductance rate of the de-superheating section	21.68 kW/K (41.1 MBtu/hr-F)

3.2.4) Model Comparison

In order to evaluate the accuracy of the cascade heat exchanger model prediction, the model is used to calculate size and geometry at the same baseline operating conditions, but with a pinch-point temperature of 5^oF instead and results are compared with the design parameters listed for the actual heat exchanger (Table 3-2). These results are summarized in Table 3-6.

Table 3-6: Predicted size and operating characteristics of the NH_3/CO_2 cascade heat exchanger at design condition (5°F pinch-point temperature)

Output	***Description***	***Values***
$N_{tube,cas}$	Total number of tubes	7,987
$L_{tube,pass}$	Tube bundle length (one pass)	57.37 ft (17.49 m)
L_{shell}	Total shell length	67.12 ft (20.46 m)
D_{shell}	Shell diameter	7.18 ft (2.19 m)
A_{shell}	Cross-sectional area of outer shell	40.51 ft^2 (3.764 m^2)
A_{tube}	Cross-sectional area of tube bundle	17.02 ft^2 (1.581 m^2)
$f_{sat,cas}$	fraction of condensing section in tube bundle	93.24%
$f_{sh,cas}$	fraction of de-superheating section in tube bundle	6.76%
$hc_{NH_3,sat}$	convective heat transfer coefficient of ammonia in the condensing section	0.1678 kW/m^2-K
$hc_{NH_3,sh}$	convective heat transfer coefficient of ammonia in the de-superheating section	0.1678 kW/m^2-K
$\overline{hc}_{CO_2,sat}$	average convective heat transfer coefficient of carbon dioxide in the condensing section	0.8564 kW/m^2-K
$hc_{CO_2,sh}$	convective heat transfer coefficient of carbon dioxide in the de-superheating section	0.1023 kW/m^2-K
$UA_{cascade,sat}$	conductance rate of the condensing section	881.7 kW/K (1671 MBtu/hr-F)
$UA_{cascade,sh}$	conductance rate of the de-superheating section	26.77 kW/K (50.74 MBtu/hr-F)

The computer model predicts a greater number of tubes required for the given conductance rates by a factor of 3.2 when compared to the actual heat exchanger summarized in 3-2; there are several possible reasons for this discrepancy. It is possible and even likely that the actual operating conditions for the cascade heat exchanger at the plant are substantially different than those specified in Table 3-1. In particular, the pinch-point temperature for the cascade heat exchanger when operating at full load may be somewhat higher than the 5ºF value listed in Table 3-1. Also, the number of tubes varies exponentially with cascade pinch-point temperature. Heat exchanger size calculation is very sensitive to the pinch-point temperature because it dictates the conductance rate of the condensing section, which is the dominant portion of the cascade heat exchanger. The predicted heat exchanger size at a 10 F approach compared well with the physical design of the actual heat exchanger .

Another factor that has a major impact on the heat exchanger geometry is the convective heat transfer coefficients of boiling ammonia on the shell side ($hc_{NH_3,sat}$ and $hc_{NH_3,sh}$); they depend on the heat flux (they increase with increasing flux). The heat flux decreases as the outside tube surface areas ($A_{evap,sat}$ and $A_{evap,sh}$) increase because the model dramatically over-predicts the

number of tubes. Similarly, the heat transfer coefficient of condensing carbon dioxide ($\overline{hc}_{CO_2,sat}$) depends on the mass flux (G_{cas}) flowing through each tube in the bundle; therefore, $\overline{hc}_{CO_2,sat}$ decreases as more tubes are added. These effects tend to exacerbate the over-prediction.

In any case, modifications could be made to the computer model to bring the model prediction closer to design conditions. For example, the heat transfer coefficients that would result in matching the design conditions and geometry of the actual heat exchanger could be determined. In addition, it is also possible to obtain close to the same number of tubes, as in the design conditions, with higher pinch-point temperature difference. Figure 3-15 illustrates the number of tubes required by the cascade heat exchanger as a function of convective heat transfer coefficient of ammonia at various values of the pinch-point temperature.

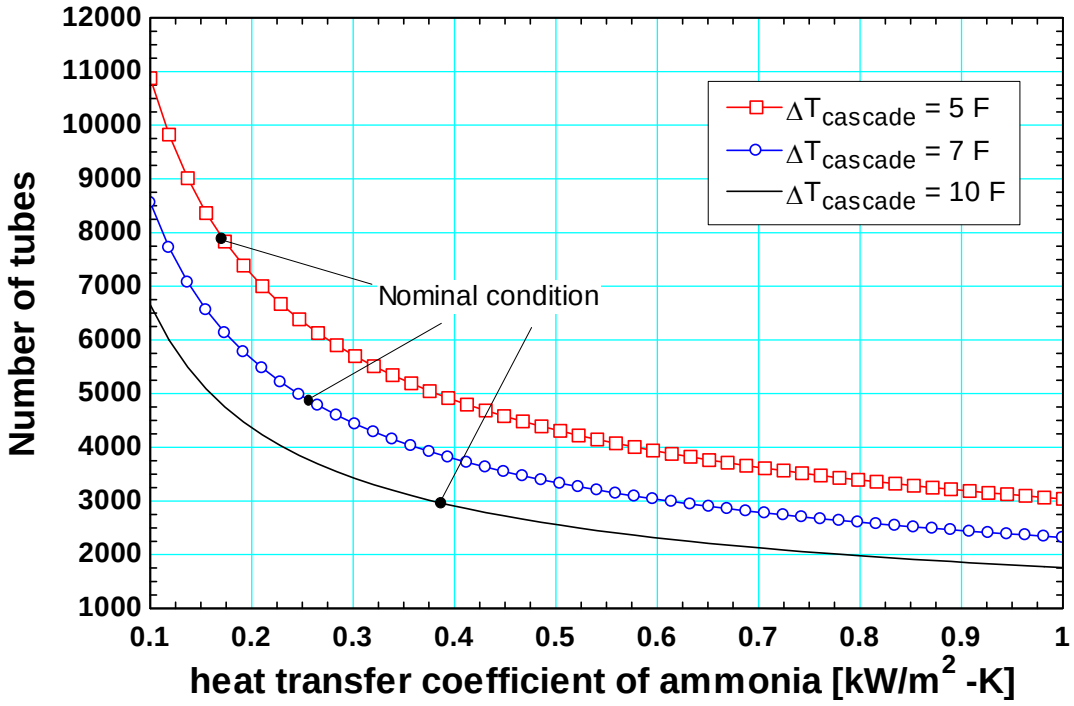

Figure 3-15: Number of tubes as a function of heat transfer coefficient of NH_3 at various cascade heat exchanger pinch-point temperatures

Despite a large discrepancy in the number of tubes between the actual design and the prediction by the computer model, adjustments could be made to the model to reconcile with these discrepancies. This analysis continues to use the geometry and size of the heat exchanger as predicted by the model (summarized in Table 3-5) at the specified design condition (Table 3-3). This is because the operating conditions, especially the cascade pinch-point temperature, of the actual heat exchanger reported by the plant representative could be taken at an off-design condition or unintentionally misinterpreted. As shown by the plot in Figure 3-16 in the following section, one degree change in the approach temperature, with constant heat exchanger load, affects the tube quantity significantly.

3.2.5) Cascade Heat Exchanger size and Pinch-Point Temperature

As discussed earlier, the cascade heat exchanger size is very sensitive to the change in the pinch-point temperature. One degree decrease causes the conductance rate of the condensing section to increase dramatically. As a result, more surface areas must be added to the heat exchanger. This section is dedicated to study the relationship between these two parameters. Over a range of pinch-point temperatures, the cascade heat exchanger model is used to predict the corresponding size to accommodate for the required conductance rate. In this study, the cascade heat exchanger model is assumed to follow the same conditions listed in Table 3-3 with an exception of the pinch-point temperature as a variable. Figures 3-16 through 3-18 illustrate the number of tubes, surface area and length, as a function of pinch-point temperature, respectively. Complete numerical results are listed in Appendix A.

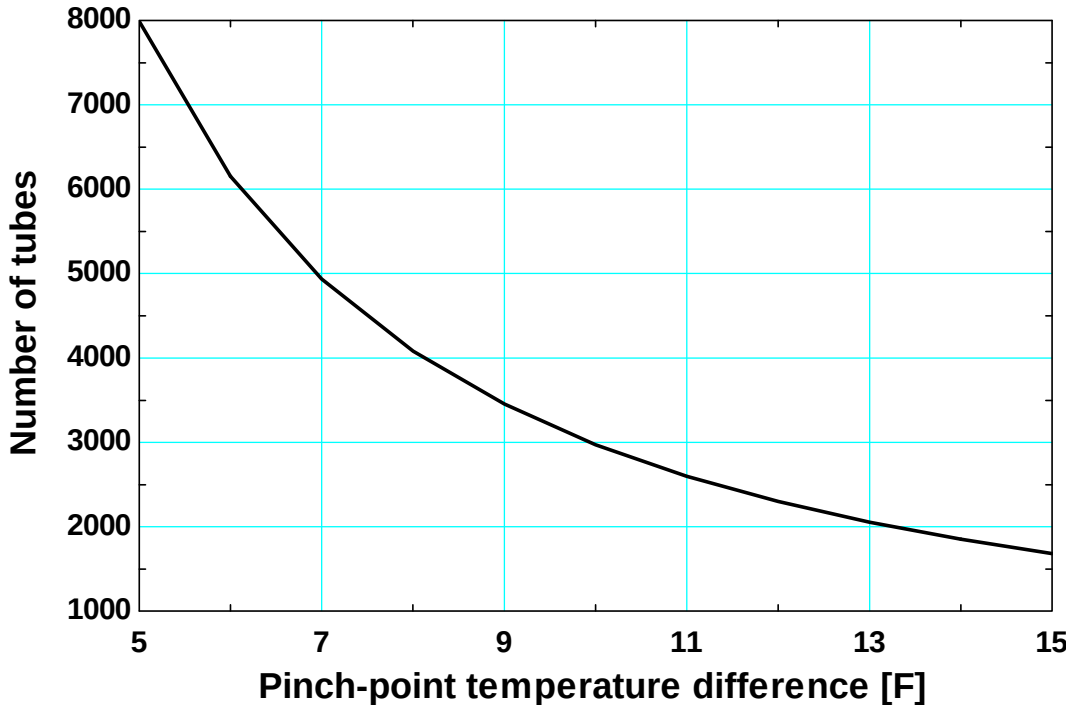

Figure 3-16: Predicted number of cascade heat exchanger tubes as a function of pinch-point temperature

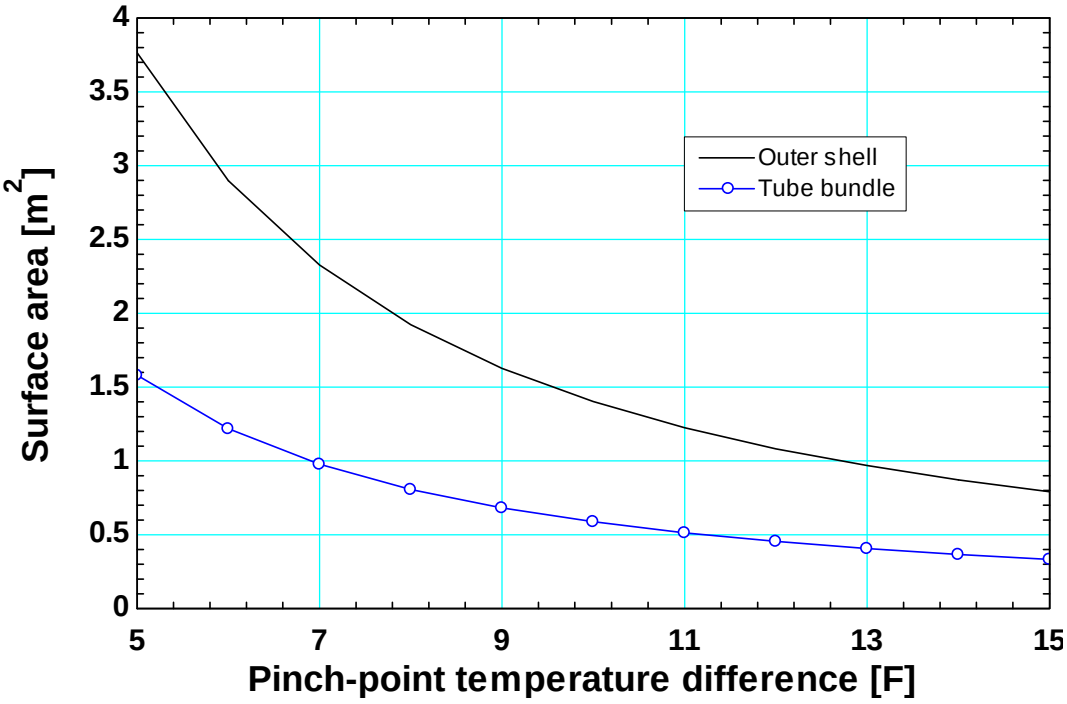

Figure 3-17: Predicted shell and tube bundle surface area as a function of pinch-point temperature

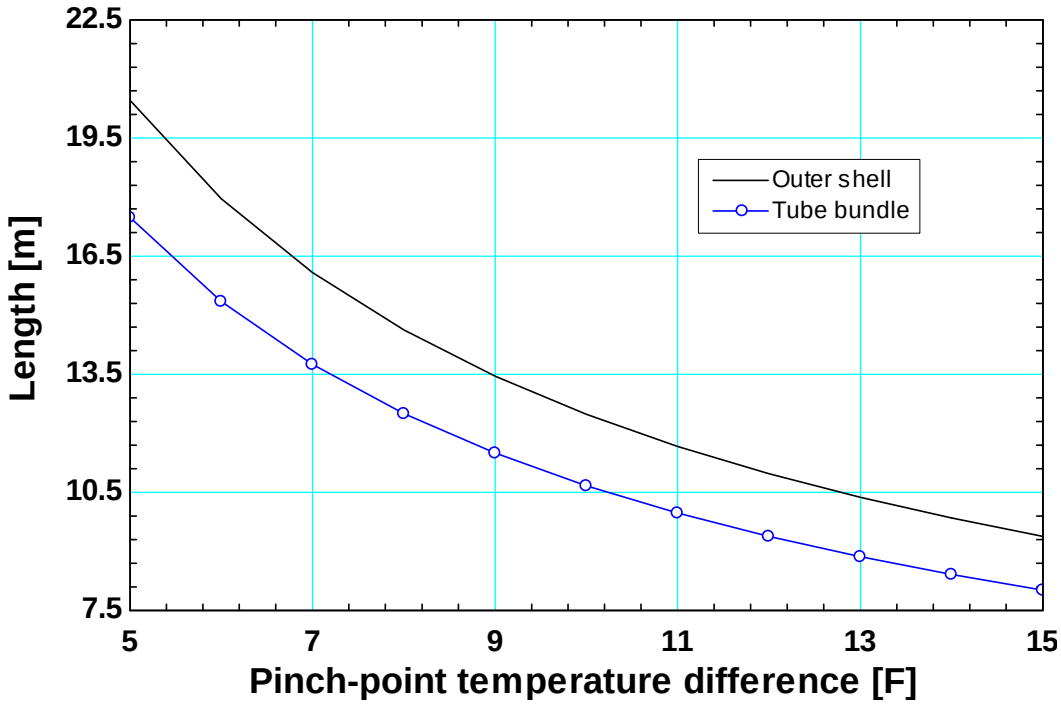

Figure 3-18: Predicted shell and tube bundle length as a function of pinch-point temperature

3.3) Evaporative Condenser

In industrial refrigeration systems, a large amount of energy must be transferred through the cycle during operation; thus, each individual system component (e.g., the heat exchanger, compressor, condenser, etc.) can become massive. Condensers are particularly large because they are responsible for rejecting large amounts of thermal energy from the system to the surrounding air. There are several different condenser configurations, including air-cooled condensers, evaporative condensers, etc. The most suitable and widely-used type for industrial systems is the evaporative condenser because it is capable of providing high effectiveness in a compact package.

An evaporative condenser operates with superheated refrigerant entering through the top row of the condenser coil while cooling water, pumped from the re-circulating water sump, is sprayed over the refrigerant condensing tubes. Condenser fans draw in ambient air, passing through the surfaces of the condenser coil in a cross-flow manner, to pick up evaporated water vapor removing both latent and sensible heat from the refrigerant stream. The moist air stream exits the evaporative condenser nearly saturated at higher temperature through the top of the device. The amount of water vapor that can be absorbed by the ambient air depends on the ambient air wet-bulb temperature. Therefore, the operation of the evaporative condenser is driven by the difference between the refrigerant temperature and the wet bulb temperature and the device utilizes both sensible and latent heat transfer mechanisms to transfer large amount of energy even with a moderate temperature difference. Figure 3-19 is a schematic diagram of an evaporative condenser.

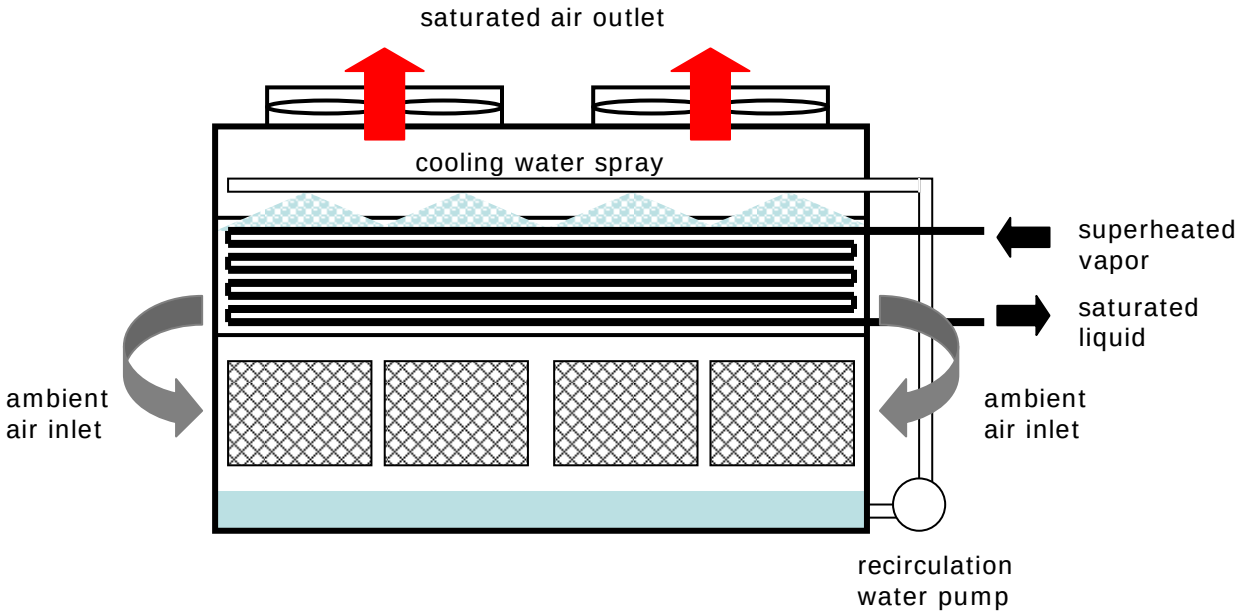

Figure 3-19: Schematic diagram of an air-drawn evaporative condenser

The method of removing heat from hot refrigerant entering the evaporative condenser involves two processes. The first process is accomplished by de-superheating hot refrigerant vapor at the

discharge temperature, leaving the high-pressure compressors, to its saturation temperature. The de-superheating process occurs over "de-superheating section" of the condenser coil. The refrigerant changes its phase to saturated vapor as it leaves this section. As the refrigerant continues through the next section of the condenser coil it undergoes an isothermal heat rejection process, condensing at constant temperature, and leaves the "condensing section" of the evaporative condenser as saturated liquid.

The model of the evaporative condenser is based on manufacturer's condenser specification data. These data are used to ascertain the effective conductance of the device as a function of operating condition which forms the basis of a semi-empirical model that is robust to operating conditions. The manufacturers usually provide the nominal heat rejection capacity ($CAP_{N,condenser}$), the nominal volumetric air flow ($CFM_{N,condenser}$), and the heat rejection factor (HRF). The heat rejection factor is a quantity, which varies with the saturated condensing temperature ($T_{cond,sat}$) and ambient air wet-bulb temperature (T_{wb}). It is used to determine available condenser capacity at off-design conditions dictated by those two temperatures. The available heat rejection capacity ($CAP_{condenser}$) of the condenser is determined by dividing the nominal heat rejection capacity by the heat rejection factor:

$$CAP_{condenser} = \frac{CAP_{N,condenser}}{HRF} \tag{3-67}$$

Condenser heat rejection capacity varies with outdoor weather condition during operation. For instance, as the outside air wet-bulb temperature decreases, the temperature gradient driving the heat transfer between the refrigerant and air streams increases which increases the heat rejection ability of the condenser. Similarly, as the refrigerant condensing pressure (also referred to as head pressure) increases; the saturated condensing temperature increases, which also increases the condenser heat rejection capacity.

The available heat rejection capacity from the condensers must exceed the required system heat rejection when selecting evaporative condensers. This analysis uses the manufacturer's data provided by Evapco Inc. for an evaporative condenser model ATC-486B. This particular model is selected because of its decent size and heat rejection capacity and only a few are required to meet the required system heat rejection. The operating characteristics of this particular condenser are summarized in Table 3-7 and the established design conditions for this analysis are summarized in Table 3-8. These specifications encompass a large range of nominal heat rejection ($CAP_{N,condenser}$), refrigerant condensing temperature in degree Fahrenheit ($T_{cond,sat,F}$) and wet-bulb temperature in degree Fahrenheit ($T_{wb,F}$). Evapco Inc. also provides HRF values for $T_{wb,F}$ between 50°F and 86°F and for $T_{cond,sat,F}$ between 85°F and 110°F.

Table 3-7: Operating characteristics of an Evapco ATC-486B evaporative condenser

Parameter	***Description***	***Values***
$CAP_{N,condenser}$	nominal heat rejection capacity given at $T_{wb,F} = 70^{o}F$ and $T_{cond,sat,F} = 90^{o}F$	7,140 MBtu/hr (2,093 kW)
CFM_N	nominal air flow rate	84,800 ft^3/min (40 m^3/s)
HP_N	condenser fan power at nominal condition	10 HP (7.46 kW)
N_{fan}	number of fans	2

Table 3-8: Design operating conditions for the evaporative condenser analysis

Parameter	***Description***	***Values***
T_{wb}	ambient air wet-bulb temperature	77°F (25°C)
$T_{cond,sat}$	saturated condensing temperature of NH_3	95°F (35°C)
P_0	atmospheric pressure	101.3 kPa (14.7 psia)
r_0	ambient air relative humidity	60%
r_{out}	relative humidity at outlet condition	100%
$\dot{Q}_{LTC}$	low-temperature circuit load	2,391 kW (680 Tons)
$\dot{Q}_{HTC}$	high-temperature circuit load	3,011 kW (856.2 Tons)
$\dot{Q}_C$	required system heat rejection	3,747 kW (1065 Tons)

The evaporative condenser is modeled by determining the conductance rate ($UA_{condenser}$) using an effectiveness-NTU method. However, the conductance rate of the condenser varies with operating conditions depending on the head pressure and outside air wet-bulb temperature. Thus, $UA_{condenser}$ values are calculated and curve-fit over a range of operating conditions consistent with the range of temperatures in which the *HRF* values are provided by the manufacturer. The actual heat rejection capacity ($\dot{Q}_{condenser,act}$) is predicted by the model, using the curve-fit of the values of $UA_{condenser}$. The validity of the model is verified by comparing the predicted capacity to the available capacity ($CAP_{condenser}$) corresponding to the *HRF* at that condition.

Since the rate of heat rejection by one evaporative condenser unit is insufficient to match the total rate of heat rejection required by the refrigeration cycle, multiple condenser units are required. The number of evaporative condensers required by the system is calculated by dividing the required system heat rejection ($\dot{Q}_C$) at design condition by the nominal condenser heat rejection capacity ($CAP_{N,condenser}$).

3.3.1) Effectiveness-NTU method

During the heat rejection process of warm refrigerant, the capacitance rate of condensing refrigerant is infinitely larger than that of the cooling air stream. The air side becomes the limiting thermal resistance in this process. And since it is also a wet-bulb driven process, the air stream can absorb latent energy until the air becomes saturated ($r_{out} = 1$). Thus, there is an effectiveness associated with the heat rejection process and the effectiveness must account for both sensible and latent energy transfer. An enthalpy-based effectiveness approach has been used previously to analyze evaporative condensers with good results, by Manske (1999), as the change in enthalpy of air as a result of energy transfer is dictated by both sensible and latent heat transfer mechanisms.

The enthalpy-based effectiveness of the evaporative condenser is defined as the ratio of the actual heat rejection to the maximum heat rejection by the condenser,

$$\varepsilon_{condenser} = \frac{CAP_{condenser}}{\dot{Q}_{condenser,max}} = \frac{h_{a,o,TAS} - h_{a,i}}{h_{a,o,TRS} - h_{a,i}} \tag{3-68}$$

Where, $h_{a,i}$ is the specific enthalpy of the air stream at the inlet determined by using EES' built-in property routine evaluated at P_0 and T_{db}. The rate of heat rejected by the condenser ($\dot{Q}_{condenser,act}$), which is equivalent to the available capacity of the condenser ($CAP_{condenser}$), is defined as,

$$\dot{Q}_{condenser,act} = CAP_{condenser} \tag{3-69}$$

$$\dot{Q}_{condenser,act} = \dot{m}_a \left(h_{a,o,TAS} - h_{a,i} \right) \tag{3-70}$$

$\dot{m}_a$ is the air mass flow rate, which depends on the inlet air volumetric flow (CFM_A). During condenser full-load operation, the condenser fans are consistently running at full speed providing a nominal air flow rate (CFM_N). The air mass flow rate is defined as,

$$CFM_A = CFM_N \tag{3-71}$$

$$\dot{m}_a = CFM_A \, \rho_a \tag{3-72}$$

Where ρ_a is the density of air evaluated at T_{db} and r_0; $h_{a,o,TAS}$ is the specific enthalpy of the outlet air leaving the condenser saturated at an outlet air dry-bulb temperature determined by using EES' built-in property routine evaluated at P_0, r_{out} and $T_{a,o}$.

The maximum rate of heat transfer through the condenser ($\dot{Q}_{condenser,max}$) occurs when the air-water mixture undergoes the maximum possible enthalpy change. The maximum enthalpy of the outlet air ($h_{a,o,TRS}$) occurs if the air leaves the condenser saturated at the refrigerant condensing temperature. Thus, the maximum rate of heat transfer is defined as:

$$\dot{Q}_{condenser,max} = \dot{m}_a \left(h_{a,o,TRS} - h_{a,i} \right) \tag{3-73}$$

Where $h_{a,o,TRS}$ is determined by using EES' built-in property routine evaluated at P_0, r_{out} and $T_{cond,sat}$.

One fluid stream within the condenser undergoes a phase change during heat rejection process, thus it possesses an infinitely large capacitance rate. The ratio of the minimum and the maximum capacitance rates is equal to zero. An effectiveness-NTU relation for this case is provided by Incropera and DeWitt (2002) as,

$$NTU_{condenser} = -ln\left(1 - \varepsilon_{condenser}\right) \tag{3-74}$$

Since the refrigerant stream has an infinitely large capacitance rate, the maximum heat transfer permitted by the condenser is dictated by the air stream. The minimum capacitance rate ($\dot{C}_{min,condenser}$) of the evaporative condenser is defined as,

$$\dot{C}_{min,condenser} = \dot{m}_a \, c_{p,a,TAS} \tag{3-75}$$

Where $c_{p,a,TAS}$ is the specific heat capacity of air at saturated condition; it accounts for both sensible and latent heat transfer mechanisms on the air side and is determined by using EES' built-in property routine evaluated at P_0, T_{db} and r_{out}.

The conductance rate of the evaporative condenser ($UA_{condenser}$) at the design condition is defined as,

$$UA_{condenser} = \dot{C}_{min,condenser} \, NTU_{condenser} \tag{3-76}$$

Eq. (3-76) is used to calculate conductance rates of the condenser at off-design conditions. The conductance rate values are plotted as a function of each of the two parameters (in Figure 3-20); notice that there is a very strong correlation between $UA_{condenser}$ and $T_{cond,sat,F}$.

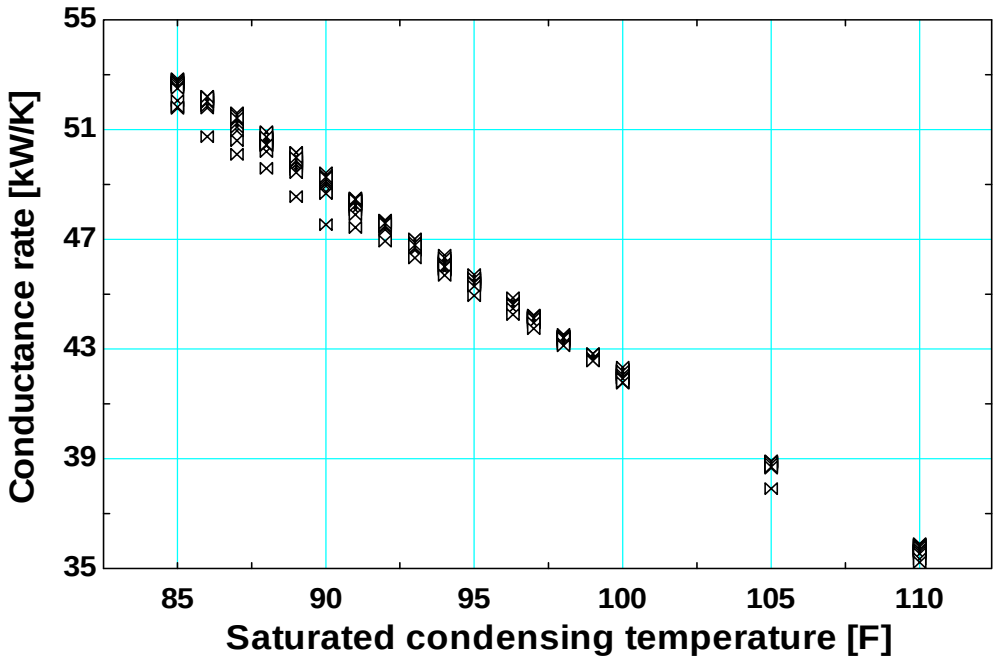

Figure 3-20: Calculated conductance rates of the evaporative condenser as a function of the saturated condensing temperature

The results are correlated, using a linear fit (R^2 = 99.58%), to be a function of both $T_{wb,F}$ and $T_{cond,sat,F}$, so that the condenser heat rejection capacity ($\dot{Q}_{condenser,act}$) can be predicted at off-design conditions consistent with normal operating conditions. The 1st order linear regression of the conductance rate as a function of both temperatures is:

$$UA_{condenser} = 1.1103\,x10^{2} - 6.8572\,x10^{-1}\,T_{cond,sat,F} - 4.8949\,x10^{-3}\,T_{wb,F} \qquad (3\text{-}77)$$

The comparison plot of the linear regression results to the actual conductance rates is shown in Figure 3-21.

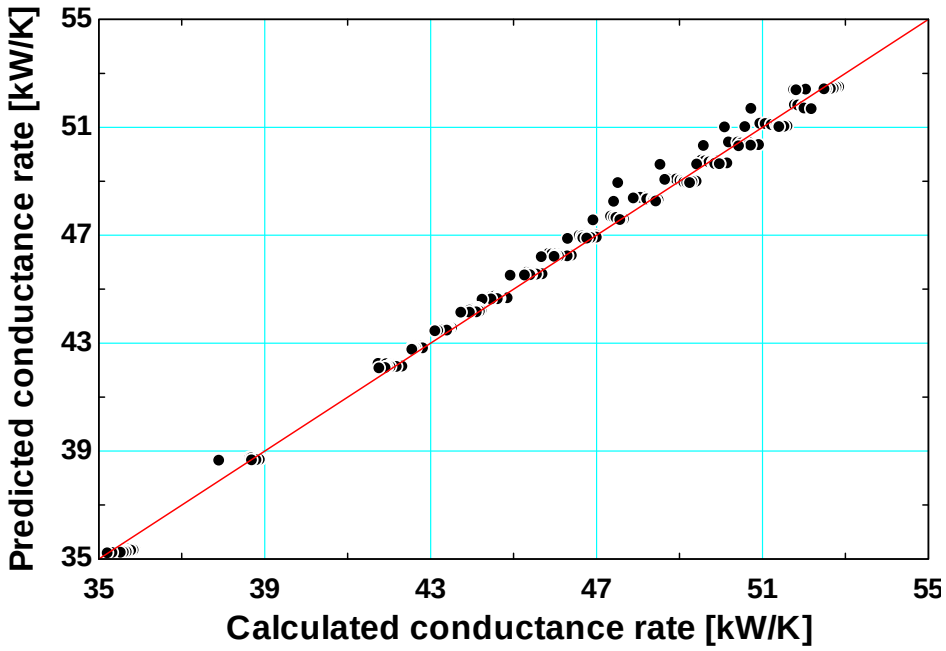

Figure 3-21: Comparison plot of the 1st order linear regression of conductance rates of evaporative condenser

The linear regression of the conductance rate, Eq. (3-77), can be used to predict the available heat rejection capacity given $T_{wb,F}$ and $T_{cond,sat,F}$ within the ranges of temperatures given for the heat rejection factors. The predicted condenser capacity is compared with the rated capacity, calculated using Eq. (3-67), and is shown in Figure 3-22.

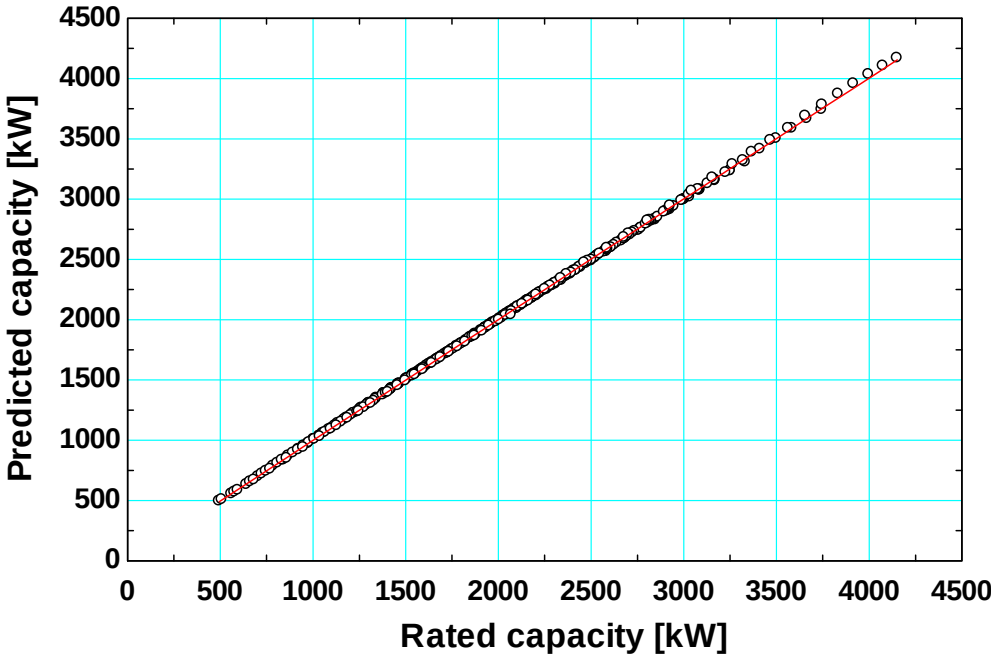

Figure 3-22: Comparison between predicted condenser capacity and rated condenser capacity

The results from Figure 3-22 show that the predicted capacity is well correlated with the rated capacity. Therefore, this correlation is appropriate for predicting available condenser capacity at off-design operating conditions encountered during normal operation of the condensers.

3.3.2) Condenser Capacity Control

As the ambient conditions vary during the operation of the refrigeration system, the heat rejection capacity of the evaporative condensers will change. In order for the system to reject the required amount of heat to the surroundings, the system head pressure must float until a head pressure is achieved that balances the heat rejection required by the system. When the available aggregate capacity of the condensers exceeds the system's required heat of rejection and the head pressure of the system is already relatively low (i.e., when the outside air wet-bulb temperature is low), the condensers must operate at a part-load condition in order to maintain an acceptable head pressure. At high wet bulb temperature, the fans will operate at full speed and the head pressure will vary. At low wet bulb temperature, the head pressure is set by hardware constraints and the fan speed will vary. Heat rejection capacity of an evaporative condenser can be controlled using one of the following two methods described by Manske (1999): head pressure control by adjusting air flow rate through condenser fans and shutting off cooling water or dry operation.

3.3.2.1) Fan Speed Control

Condenser capacity can be adjusted by controlling the condenser fan speed in order to modulate the air flow rate through the condenser. It is desirable to maintain as low of a head pressure as the system possibly could because the energy consumed by the high pressure compressors (HPC) is influenced, in part, by the head pressure of the system. In real systems, there are a number of factors that limit how low the system's head pressure can float. Constraints that limit how low head pressure can float include: presence of liquid injection oil cooling for screw compressors, hot gas defrost, oil separator sizing, presence and setting of controlled pressure receiver set points, presence of heat recovery equipment, and others.

This present analysis limits the head pressure to no lower than 120 psig or 135 psia (930.8 kPa). This head pressure limit is intended to be representative of a typical industrial ammonia refrigeration system. At an operating condition where the wet-bulb temperature is relatively low such that the system head pressure approaches the minimum pressure limit, the head pressure is constrained so that it cannot drop below this set-point. Thus, the condensers fans can no longer run a full-load operation. Instead, the condensers switch over to a part-load operation where the fan motor speed is modulated in order to maintain the system head pressure. The relationship between condenser capacity and air flow rate is non-linear; a correlation for calculating the reduced air flow rate (CFM_{PL}) from the de-rated condenser capacity (CAP_{PL}), as suggested by Manske (1999), is given as:

$$CAP_{PL} = CAP_{condenser}\left(\frac{CFM_{PL}}{CFM_{N}}\right)^{n} \tag{3-78}$$

Where n is a coefficient that varies between 0.5 for laminar flow and 0.8 for turbulent flow; a value of 0.76 was suggested by Manske (1999). This relationship shows that air flow rate is reduced more rapidly than the condenser capacity.

As described by Manske (1999), there are three ways of controlling fan motors: On/Off motor cycling, half-speed motor cycling, and variable frequency drive (VFD). With the On/Off cycling method, the motors run at full speed when energized and are otherwise completely off. The motors will therefore run until the head pressure drops below an acceptable limit and then they are turned off until the head pressure rises above that level (plus some dead-band setting). The half-speed cycling strategy first runs the fan motors at half-speed and then up to full-speed if the head pressure is still above the desirable limit. Variable frequency drive control cycles the fans at the exact speed that is necessary in order to maintain a constant head pressure at a defined set-point. The last two methods have an energy saving advantage. The relationship between the fan power consumption (HP_{PL}) and the air flow rate is defined as,

$$HP_{PL} = HP_{N}\left(\frac{CFM_{PL}}{CFM_{N}}\right)^{3} \tag{3-79}$$

Where HP_{N} is the nominal condenser fan power corresponding to the nominal air flow rate. If the air flow rate is reduced by half, the required fan power is only one-eighth of the nominal fan power. VFD strategy is consistent with the fan motor control method utilized in this analysis.

3.4) Evaporator

In a vapor compression refrigeration system, an evaporator is an essential component for removing heat from the system at low temperatures. An evaporator is an air-to-refrigerant heat exchanger where the re-circulating air in the refrigerated space is passed through the refrigerated coil to be cooled and dehumidified. The heat transfer process between the air and refrigerant involves two mechanisms: sensible and latent. The sensible heat removed from the air stream lowers its temperature; the latent heat removed from the air removes moisture from the air stream and lowers its humidity. The heat removed from the cooled air is transferred through the coil surface and is absorbed by the liquid refrigerant, thus causing it to evaporate so that it leaves the evaporator coil as saturated vapor.

3.4.1) Evaporator Performance

The objective of this analysis is to model the thermal performance or heat transfer capacity of the evaporator coil under constant heat load, frost-free condition over a normal period of operation. This predictive model can predict the coil performance using the performance characteristics defined based on the actual evaporator physical parameters (Table 3-9). This analysis is conducted based on the geometry associated with evaporator Model 1RF-90-0310-GG-5-037-717R manufactured by King Corporation (Figure 3-23). Analysis and performance simulation for this particular evaporator was conducted and presented by Aljuwayhel (2006). In addition, many physical parameters as well as operating conditions selected for this analysis are similar to those in model presented by Aljuwayhel (2006). Therefore, it is suitable to select this evaporator as a basis for modeling for this analysis. The approach used to model the evaporator involves the calculation of the evaporator coil capacity from the evaporator conductance rates.

3.4.2) Evaporator Geometry

The evaporator selected is of fin-and-tube type; the physical dimensions and geometry of the evaporator are listed in Table 3-9. An illustration of the evaporator is shown in Figure 3-23.

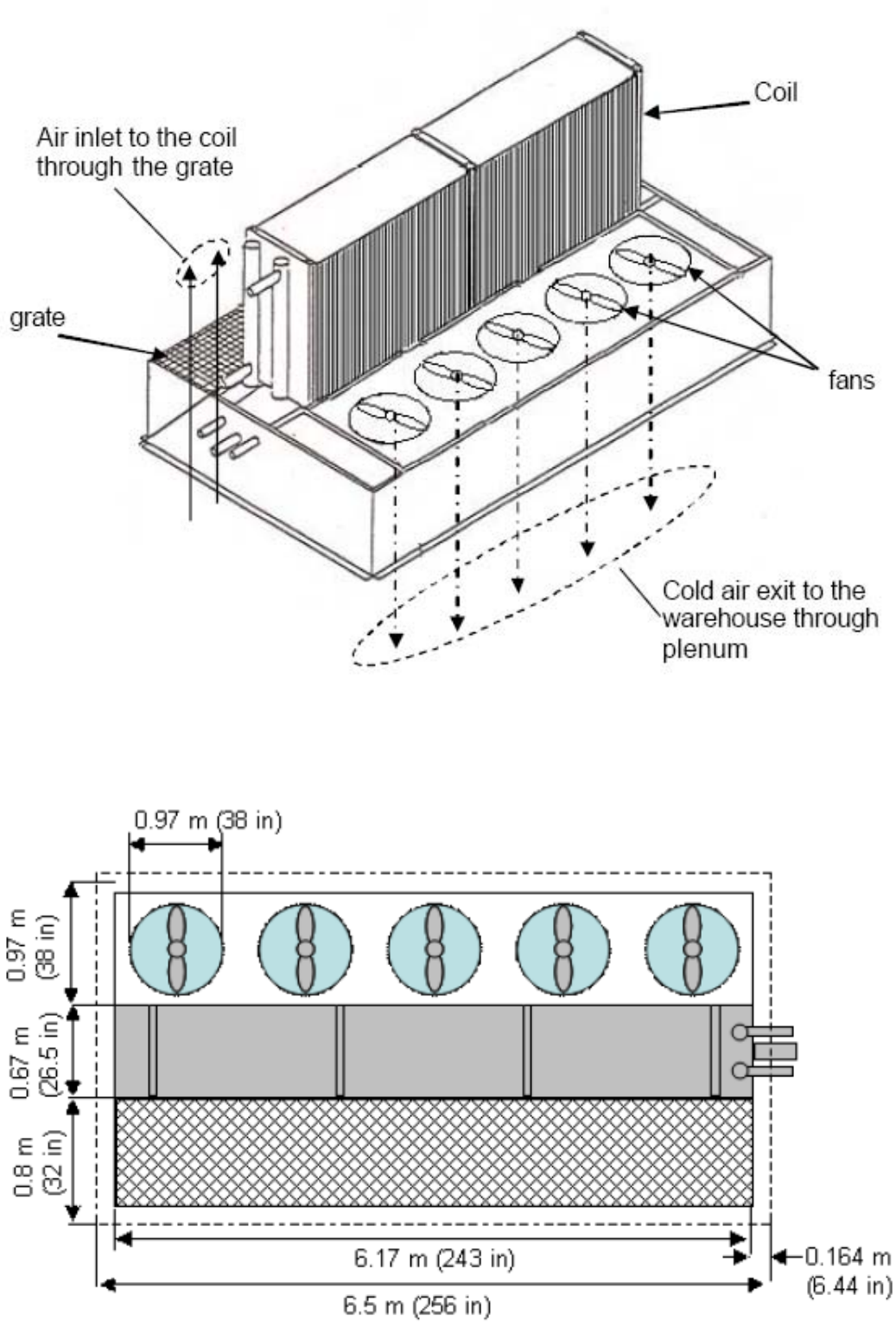

Figure 3-23: Schematic diagram of the evaporator unit from Aljuwayhel (2006).

Table 3-9: Geometry and nominal operating conditions of an evaporator coil

Parameter	***Description***	***Value***
P_{fin}	fin pitch	85 mm (3 fins/inch)
F_{thk}	fin thickness	2.8 mm
$A_{HX,face}$	evaporator face area	8.23 m^2 (88.6 ft^2)
D_o	tube diameter	19.05 mm (0.75 inch)
th_{tube}	tube thickness	1.245 mm (0.049 inch)
L_{tube}	tube length	5.5 m (18 ft)
N_{tube}	number of tubes	260
N_{row}	number of tube row	10
P_t	tube transverse pitch	57 mm (2.25 inch)
P_L	tube longitudinal pitch	44 mm (1.75 inch)
N_{fan}	Number of fans	5
-	fin material	Aluminum
-	tube material	Galvanized steel

Table 3-10: Nominal operating conditions of the evaporator

Parameter	***Description***	***Value***
CFM_N	nominal air flow rate (5 fans)	1699 m^3/min (60,000 CFM)
ΔT_{coil}	coil temperature difference	5.6°C
CAP_N	nominal capacity at -34°C (-30°F)[2]	130 kW (37 Tons)
$T_{evap,sat}$	Refrigerant evaporating temperature	-34.4°C (-30°F)
$T_{a,i}$	inlet air temperature[3]	-28.8°C (-20°F)
r_1	inlet air relative humidity	0.90
r_2	outlet air relative humidity	0.95
$\dot{Q}_L$	total heat load at low temperature	2,391 kW (680 Tons)

[2] Saturation temperature of the refrigerant
[3] The inlet air temperature entering the evaporator is equal to the saturated evaporating temperature of the refrigerant plus the coil temperature difference.

3.4.3) Evaporator Physical Analysis

The following derivations are presented by Aljuwayhel (2006), and since many parameters and area terms in this evaporator analysis are referred to extensively throughout the evaporator analysis; they are defined as follows. Figure 3-24 shows a schematic diagram of the evaporator.

Heat exchanger face area ($A_{HX,face}$)**,** given in Table 3-9, is the total area of the heat exchanger that is perpendicular to air flow direction. The tube length of one tube pass across the heat exchanger face (L_{tube}) is approximately equivalent to heat exchanger face length (HX_L); the overall height of the fin plate (F_h) is approximately equal to the heat exchanger face height (HX_h). Thus, $A_{HX,face}$ is approximated as,

$$A_{HX,face} = HX_h \, HX_L \approx F_h \, L_{tube} \tag{3-80}$$

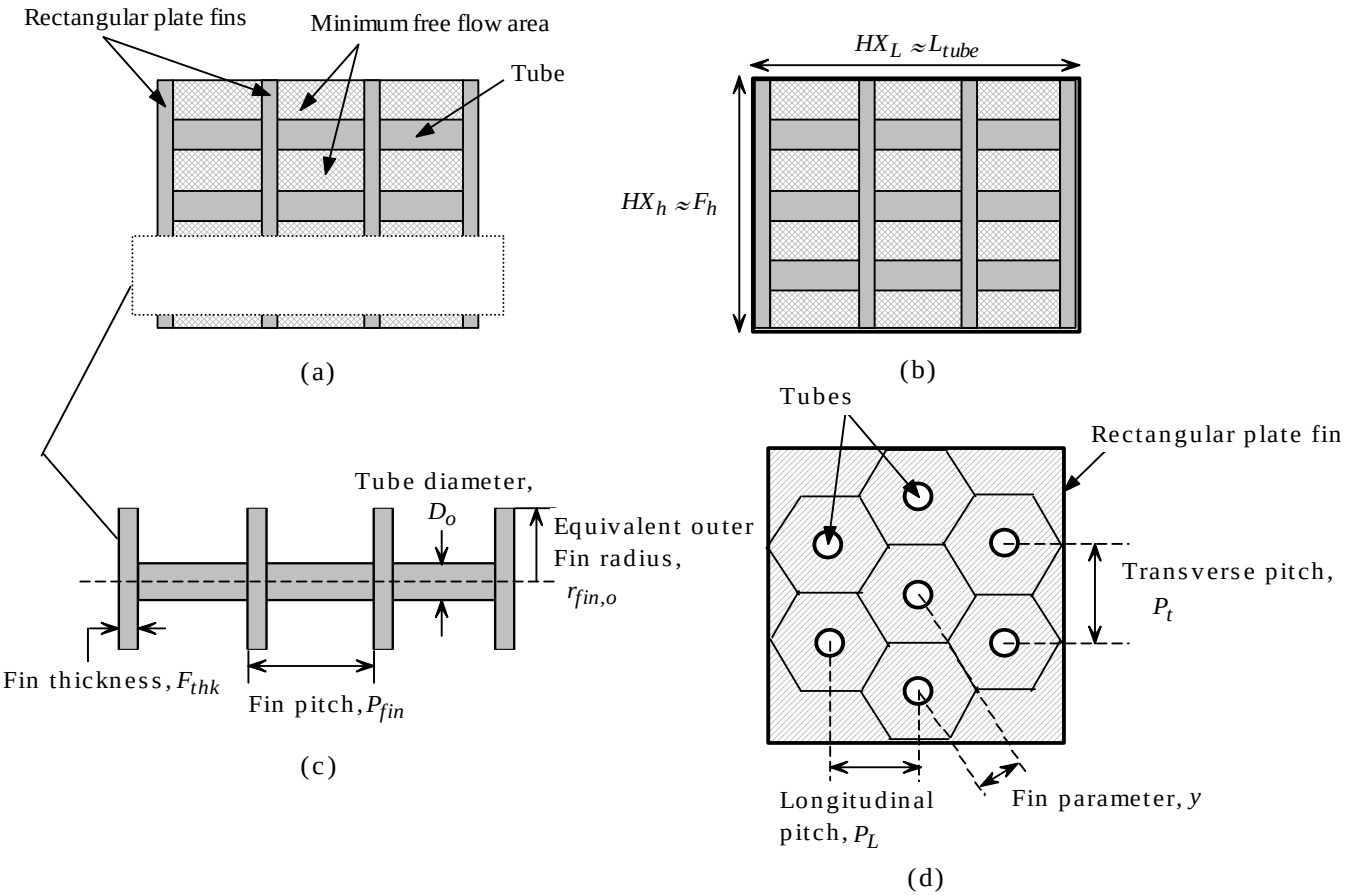

Figure 3-24: Schematic of an evaporator illustrating (a) the minimum flow area shown with crosshatch, (b) heat exchanger face area, (c) fin pitch and fin thickness (d) the equivalent area appropriate for a plate fin in a staggered tube arrangement, as suggested by Schmidt (1949)

The number of fins per tube ($N_{fin,tube}$) is defined as,

$$N_{fin,tube} = \frac{L_{tube}}{P_{fin}} \tag{3-81}$$

where P_{fin} is the fin pitch given in Table 3-9.

The total number of fins in the evaporator (N_{fin}) is,

$$N_{fin} = N_{fin,tube}\, N_{tube} \tag{3-82}$$

Fin tip area ($A_{fin,tip}$) is the total area of the fin tips perpendicular to air flow direction,

$$A_{fin,tip} = N_{fin,tube}\, F_h\, F_{thk} \tag{3-83}$$

where F_{thk} is the thickness of one fin defined in Table 3-9.

Tube face area ($A_{tube,\,face}$) is the total area of the coil tubes obstructing the air flow path,

$$A_{tube,\,face} = N_{tube,v}\, D_o \left(L_{tube} - N_{fin,tube}\, F_{thk} \right) \tag{3-84}$$

Where $N_{tube,v}$ is the number of tube rows in the vertical direction.

Intersected fin-tube area ($A_{contact}$) is the intersection of the fin face area and the tube face area that does not come in contact with the air stream,

$$A_{contact} = N_{tube,v}\, F_{thk}\, D_o\, N_{fin,tube} \tag{3-85}$$

Minimum flow area ($A_{min,\,flow}$) is the unblocked passage area in which air passes through,

$$A_{min,\,flow} = A_{HX,\,face} - \left(A_{fin,tip} + A_{tube,\,face} - A_{contact} \right) \tag{3-86}$$

Bare-tube area ($A_{tube,b}$) is the total surface area of the evaporator coil tubes only,

$$A_{tube,b} = \pi\, D_o \left(L_{tube}\, N_{tube} - N_{fin}\, F_{thk} \right) \tag{3-87}$$

Fin face area ($A_{fin,\,face}$) is the surface area of the fins parallel to air flow direction,

$$A_{fin,\,face} = 2\,\pi\,N_{fin}\left(r_{fin,o}{}^{2} - r_{fin,i}{}^{2}\right) \tag{3-88}$$

where $r_{fin,o}$ is the equivalent outer fin radius, based on the fin parameter (y) and tube transverse pitch (P_t), defined according to Schmidt (1949) and described by Aljuwayhel (2006) as,

$$y = \frac{1}{2}\sqrt{P_L{}^{2} + \frac{P_t^{2}}{4}} \tag{3-89}$$

$$r_{fin,o} = 0.635\,P_t\sqrt{\left(\frac{2y}{P_t} - 0.3\right)} \tag{3-90}$$

$r_{fin,i}$ is exactly equal to half of the tube outside diameter (D_o).

Total fin area ($A_{fin,tot}$) is the total fin surface area exposed to heat exchanging air stream,

$$A_{fin,tot} = A_{fin,tip} + A_{fin,\,face} \tag{3-91}$$

Total heat transfer area ($A_{HT,tot}$) is the surface area of the heat exchanger that the air stream comes into contact with during the cooling process,

$$A_{HX,tot} = A_{tube,b} + A_{fin,tot} \tag{3-92}$$

Effective heat transfer area ($A_{HT,eff}$) is the surface area of the heat exchanger that is exposed to air flow weighted according to the efficiency of the fins (η_{fin}),

$$A_{HT,eff} = A_{tube,b} + \eta_{fin}\,A_{fin,tot} \tag{3-93}$$

The circular fin efficiency (η_{fin}) is defined according to Incropera and DeWitt (1990) as,

$$\eta_{fin} = \frac{2\,r_{fin,i}}{m\left(r_{fin,o}{}^{2} - r_{fin,i}{}^{2}\right)}\left[\frac{K_1\left(mr_{fin,i}\right)I_1\left(mr_{fin,o}\right) - K_1\left(mr_{fin,o}\right)I_1\left(mr_{fin,i}\right)}{I_0\left(mr_{fin,i}\right)K_1\left(mr_{fin,o}\right) + K_0\left(mr_{fin,i}\right)I_1\left(mr_{fin,o}\right)}\right] \tag{3-94}$$

$$m = \sqrt{\frac{2\,hc_a}{k_{fin}\,F_{thk}}} \tag{3-95}$$

where K_n and I_n are modified Bessel function of first and second kind, respectively. m is the fin constant, hc_a is the air-side convective heat transfer coefficient (Eq. (3-102)), and k_{fin} is the thermal conductivity of the fins.

Refrigerant evaporation area (A_{evap}) is the total surface area of the tubes inner wall that the evaporating refrigerant comes in contact with and is defined as;

$$A_{evap} = \pi D_i L_{tube} N_{tube} \tag{3-96}$$

where D_i is the tubes inner diameter.

Refrigerant flow area (A_{cross}) is the cross-sectional area of tubes through which the evaporating refrigerant passes,

$$A_{cross} = \frac{\pi D_i^2 N_{tube}}{4} \tag{3-97}$$

The physical characteristics of the evaporator are summarized in Table 3-11.

Table 3-11: Physical characteristics of the evaporator

Parameter	***Description***	***Values***
F_h	heat exchanger height	1.496 m (4.91 ft)
$N_{fin,tube}$	number of fins per tube	647
N_{fin}	total number of fins	168,235
$A_{fin,tip}$	fin tips area	2.711 m^2 (29.18 ft^2)
$A_{fin,face}$	fin surface area	762.3 m^2 (8205 ft^2)
$A_{tube,face}$	tube face area	1.827 m^2 (19.66 ft^2)
$N_{tube,v}$	number of vertical tube rows	26
A_{min}	minimum flow area	2.795 m^2 (30.08 ft^2)
$A_{tube,b}$	bare tube area	57.39 m^2 (617.7 ft^2)
$A_{fin,tot}$	total fin surface area	765 m^2 (8234 ft^2)
$r_{fin,o}$	equivalent fins outer radius	28.49 mm (1.122 in)
$r_{fin,i}$	equivalent fins inner radius	9.53 mm (0.375 in)
D_i	tube inner diameter	16.56 mm (0.652 in)
y	fin parameter	26.21 mm (1.03 in)
$A_{HT,tot}$	total heat transfer area	822.4 m^2 (8852 ft^2)
$A_{HT,eff}$	effective heat transfer area	802.1 m^2 (8634 ft^2)

η_{fin}	fin efficiency	97.4 %
A_{evap}	evaporation heat transfer area	74.4 m^2 (800.8 ft^2)
A_{cross}	cross-sectional flow area	0.000215 m^2 (0.0023 ft^2)

3.4.4) Air-Side Properties

The thermal performance analysis of the evaporator in Section 3.4.5 involves energy balances on the air side, and since many air-side properties are referred to extensively throughout the analysis; they are defined as follows;

The mass flow rate of air ($\dot{m}_a$) drawn into the evaporator is determined from the volumetric flow rate and density of air at the coil inlet condition,

$$\dot{m}_a = CFM\ \rho_a \tag{3-98}$$

Where ρ_a is the inlet air density evaluated at $T_{a,i}$ and r_1.

The mass flux or mass flow per unit area (G_a) of incoming air is defined as,

$$G_a = \frac{\dot{m}_a}{A_{min}} \tag{3-99}$$

The maximum air flow velocity (u_a), based on the frost-free air flow passage area, at the face of the heat exchanger is,

$$u_a = \frac{CFM}{A_{min}} \tag{3-100}$$

The Reynolds number of the air flow, based on the fin pitch of the evaporator coil, is defined as,

$$Re_{fin} = \frac{G_a P_{fin}}{\mu_a} \tag{3-101}$$

where μ_a is the dynamic viscosity of the air stream evaluated at $T_{a,i}$ and r_1.

The air-side convective heat transfer coefficient (hc_a), in Eq. (3-95), is calculated using the correlation suggested by McQuiston (1981):

$$hc_a = \frac{j_a G_a c_{p,a}}{Pr_a^{2/3}} \tag{3-102}$$

where $c_{p,a}$ is the specific heat capacity of air evaluated at $T_{a,i}$ and r_1. Pr_a is the Prandtl number of air and j_a is the Colburn factor defined as,

$$j_a = \left[0.0014 + 0.2618\, j_p\, j_w\right]\left[\frac{1 - N_{row}\left(1280\right) Re_{P_L}^{\ -1.2}}{1 - \left(5120\right) Re_{P_L}^{\ -1.2}}\right] \quad where\ N_{row} > 4 \tag{3-103}$$

where N_{row} is the number of coil rows and Re_{P_L} is the Reynolds number of air based on the longitudinal pitch of the tubes (P_L);

$$Re_{P_L} = \frac{G_a\, P_L}{\mu_a} \tag{3-104}$$

the j_w and j_p parameters in Eq. (3-103) are defined according to:

$$j_w = \left(0.95 + 0.4\, x 10^{-5}\, Re_{fin}^{\ 1.25}\right)\left(\frac{P_{fin}}{P_{fin} - F_{thk}}\right) \tag{3-105}$$

$$j_p = Re_D^{\ -0.4}\left(\frac{A_{HT,tot}}{A_{tube,b}}\right)^{-0.15} \tag{3-106}$$

where Re_{fin} is the Reynolds number based on fin pitch, Eq. (3-101), and Re_D is the Reynolds number based on tube outside diameter;

$$Re_D = \frac{G_a\, D_o}{\mu_a} \tag{3-107}$$

The air-side convective mass transfer coefficient (hm_a) associated with the latent heat transfer mechanism is defined by Threlkeld (1970) as,

$$hm_a = \frac{hc_a}{Le\, c_{p,a}} \tag{3-108}$$

where $c_{p,a}$ is the specific heat capacity of dry air evaluated at the inlet condition and Le is the Lewis number. According to Threlkeld (1970), the typical values of Le for water vapor in air are in the range of 0.90 and 0.92. For this analysis, the Lewis number is taken to be 0.90.

3.4.5) Conductance Rate at The Nominal Condition

Primarily, the conductance rate of the evaporator at the nominal operating condition ($UA_{evaporator,N}$) is determined using an effectiveness-NTU approach. Since the evaporator absorbs both sensible and latent energy from the air stream, the change in enthalpy of the air accounts for these components. Thus, an enthalpy-based effectiveness method, which was used in the evaporative condenser analysis in Section 3.3.1, is also applicable in this analysis.

The enthalpy-based effectiveness of the evaporator is defined as the ratio of the actual heat absorbed to the maximum heat absorbed by the evaporator,

$$\varepsilon_{evaporator,N} = \frac{CAP_N}{\dot{Q}_{evaporator,max}} = \frac{h_{a,i} - h_{a,o}}{h_{a,i} - h_{a,o,TRS}} \tag{3-109}$$

Where, $h_{a,i}$ is the specific enthalpy of the air stream at the inlet determined by using EES' built-in property routine evaluated at $T_{a,i}$ and r_1. The rate of actual heat absorbed by the evaporator, which is equivalent to the nominal capacity of the condenser (CAP_N), is defined as,

$$CAP_N = \dot{m}_{a,N}\left(h_{a,i} - h_{a,o}\right) \tag{3-110}$$

Where $\dot{m}_{a,N}$ is the mass flow rate of air calculated, using Eq. (3-98), from the nominal volumetric air flow (CFM_N) provided in Table 3-10. The density of air used to calculate $\dot{m}_{a,N}$ is evaluated at $T_{a,i}$ and r_1; $h_{a,o}$ is the specific enthalpy of the outlet air leaving the evaporator coil at an outlet air dry-bulb temperature ($T_{a,o}$) and at r_2.

The maximum rate of heat removed by the evaporator ($\dot{Q}_{condenser,max}$) occurs when the air stream undergoes the maximum possible enthalpy change. The minimum enthalpy of the outlet air ($h_{a,o,TRS}$) occurs if the air leaves the evaporator saturated ($r_{sat} = 1$) at the refrigerant evaporating temperature ($T_{evap,sat}$). Thus, the maximum rate of heat transfer is defined as:

$$\dot{Q}_{evaporator,max} = \dot{m}_{a,N}\left(h_{a,i} - h_{a,o,TRS}\right) \tag{3-111}$$

Where $h_{a,o,TRS}$ is determined by using EES' built-in property routine evaluated at P_0, r_{sat} and $T_{evap,sat}$.

One fluid stream within the evaporator undergoes a phase change during heat transfer process, thus it possesses an infinitely large capacitance rate. The ratio of the minimum and the maximum capacitance rates is equal to zero. An effectiveness-NTU relation for this case is provided by Incropera and DeWitt (2002) as,

$$NTU_{evaporator,N} = -ln\left(1-\varepsilon_{evaporator,N}\right) \tag{3-112}$$

Since the refrigerant stream has an infinitely large capacitance rate, the maximum heat transfer permitted by the condenser is dictated by the air stream. The minimum capacitance rate ($\dot{C}_{min,evaporator,N}$) of the evaporative condenser is defined as,

$$\dot{C}_{min,evaporator,N} = \dot{m}_{a,N}\, c_{p,a,sat} \tag{3-113}$$

Where $c_{p,a,sat}$ is the specific heat capacity of air at saturated condition; it accounts for both sensible and latent heat transfer mechanisms on the air side and is determined by using EES' built-in property routine evaluated at P_0, $T_{a,i}$ and r_{sat}.

The conductance rate of the evaporator at the nominal condition ($UA_{evaporator,N}$) is defined as,

$$UA_{evaporator,N} = \dot{C}_{min,evaporator,N}\, NTU_{evaporator,N} \tag{3-114}$$

3.4.6) Conductance Rate at Normal Conditions

Once the nominal conductance rate is determined, evaporator performance at the actual operating conditions can be determined by scaling the conductance rate from the nominal condition to the actual condition. The conductance requirement of the evaporator changes with refrigerant saturation temperature. Meanwhile, the air side dictates the maximum heat transfer of the evaporator, thus the air-side thermal properties (i.e. thermal conductivity, density, viscosity and etc.) vary with operating conditions. Therefore, the change in thermal performance of the evaporator from the nominal to the actual condition is proportional to the change in fluid properties between these conditions. The relationship between the conductance rate of the heat exchanger and the fluid properties is defined as,

$$\frac{UA_{evaporator}}{UA_{evaporator,N}} = \frac{k_a\, Re_{fin}^{\;0.8}}{k_{a,N}\, Re_{fin,N}^{\;0.8}} \tag{3-115}$$

Where k_a and Re_{fin} are the thermal conductivity and Reynolds number based on fin pitch, of air at the actual operating condition, respectively. At an actual operating condition, only the air temperature at the inlet condition ($T_{a,i}$) and relative humidity at inlet and outlet conditions (r_1 and r_2) are specified. The refrigerant evaporating temperature can float to allow the evaporator to meet the required load in order to maintain air temperature of the refrigerated space.

The actual conductance rate ($UA_{evaporator}$) is used to calculate the heat exchanger effectiveness at the actual condition ($\varepsilon_{evaporator}$) by solving Eq. (3-112) and Eq. (3-114). The minimum air capacitance rate ($\dot{C}_{min,evaporator}$) at this condition will be slightly higher as air becomes more dense

at lower temperatures. The maximum rate of the heat transfer between air and evaporating refrigerant ($\dot{Q}_{evaporator,max}$) can be determined from the evaporator effectiveness at the specified operating condition,

$$\dot{Q}_{evaporator,max} = \frac{\dot{Q}_{evaporator,act}}{\varepsilon_{evaporator}} \tag{3-116}$$

The air stream outlet temperature ($T_{a,o}$) and saturated refrigerant temperature ($T_{evap,sat}$) can both be determined by simultaneously solving the energy balances on the air and refrigerant sides,

$$\dot{Q}_{evaporator,act} = \dot{m}_a \left(h_{a,i} - h_{a,o} \right) \tag{3-117}$$

$$\dot{Q}_{evaporator,act} = \dot{m}_{evaporator} \left(h_{r,o} - h_{r,i} \right) \tag{3-118}$$

Where $h_{r,i}$ and $h_{r,o}$ are specific enthalpy of refrigerant at inlet and outlet conditions of the evaporator, respectively. Since the evaporator is of a liquid-overfeed type, refrigerant enters the evaporator as saturated liquid and leaves at low vapor mass quality (depending on mass flow rate and evaporation temperature). Thus, $T_{evap,sat}$ can be determined from $h_{r,i}$ by using EES built-in properties routine evaluated at $T_{evap,sat}$ and $x = 0$. $\dot{m}_{evaporator}$ is the refrigerant mass flow rate through a single evaporator, which is dependent on low temperature heat load and the number evaporators installed. The number of evaporators required ($N_{evaporator}$) is determined by dividing the total low-temperature heat load ($\dot{Q}_L$) by the nominal evaporator capacity (CAP_N),

$$N_{evaporator} = \frac{\dot{Q}_L}{CAP_N} \tag{3-119}$$

$N_{evaporator}$ is rounded to the next higher integer (ie., if $N_{evaporator}$ is 9.2, it is rounded to 10). The number of evaporators is fixed and the heat transfer capacity of each individual unit will vary with refrigerant mass flow rate. Therefore, the refrigerant mass flow rate of the low-temperature circuit ($\dot{m}_{LTC}$) and $N_{evaporator}$ dictate the mass flow through each evaporator unit and thus the capacity. Mass flow rate through an evaporator is given as,

$$\dot{m}_{evaporator} = \frac{\dot{m}_{LTC}}{N_{evaporator}} \tag{3-120}$$

Detailed system component models created can now be integrated together to form a detailed system model that can be used to conduct system performance simulations over a long period of time. In order to perform a more comprehensive analysis, economic viability of the cycles is evaluated to determine a more attractive system. Chapter 4 discusses an economic comparison of the two systems utilizing integrated system-level models.

Chapter 4) Comparative Analysis

In the previous chapters, two system configurations, the compound and cascade cycles, were analyzed and the component models required for each system were described individually. In this chapter, all of the system components are integrated in order to arrive at a complete and detailed system model that can be used to conduct performance simulations. By utilizing these system models, a comparative analysis between the compound and cascade configurations is more convenient as it is possible to evaluate their performance at similar operating conditions. However, performance indicators such as the coefficient of performance (COP) or operating efficiency (BHP/Ton) alone are not sufficient to determine the most attractive system. Certainly, the operating cost of a refrigeration system, which depends directly on operating efficiency, is one of the most important factors to consider. However, the total cost of system ownership also includes the capital cost associated with installing the system; this capital cost may differ substantially between the two system configurations. This economic analysis is described in more detail in subsequent sections.

4.1) Economic Analysis

A consistent economic comparison between the compound direct-ammonia system and the CO_2-NH_3 cascade system configurations can be accomplished by performing a life-cycle cost (LCC) analysis. The LCC analysis is intended to account for the total cost (capital and operations) associated with owning and operating a system throughout its lifetime. The LCC for each system can be compared in order to determine the more economically attractive alternative by evaluating the life-cycle savings (i.e., the difference between the two life cycle costs). This analysis attempts to integrate all of the costs associated with operating a refrigeration system starting from initial installation to the end of its lifetime (or another desired period of economic analysis) and compares them on present-worth value basis.

4.1.1) Life-cycle Cost

In this analysis, the Life-Cycle Cost (LCC) represents the net present value of all costs incurred with the procurement and operation for each system being analyzed over its lifetime or over a selected analysis period. The LCC accounts the time value of money – including estimates of inflation for items such as energy prices. Stated another way, the life-cycle costing represents the total amount of money that would need to be invested today in order to cover the capital and operating costs over the lifetime of the system. The life-cycle cost analysis involves various economic factors such as the expected length of service, maintenance costs, applicable loan duration, tax rates, inflation rates and interest rates. These economic parameters fluctuate with time and factor significantly into such a large investment. This thesis uses an approach, for the economic analysis, that integrates all the economic factors into two parameters referred to as P_1 and P_2; this method is called the "P_1, P_2 *method*" and is discussed in Duffie and Beckman (2006).

4.1.1.1) P_1, P_2 Method

The P_1-P_2 method breaks the LCC up into two cost categories—operating and capital. P_1 and P_2 are multipliers that transform these costs to present-day dollars. The life-cycle cost is defined as,

$$LCC = P_1\, OC + P_2\, FC \tag{4-1}$$

where,

OC = first-year operating cost
FC = first cost or capital cost of constructing a system

The parameter P_1 is a multiplier that takes into account the future cost associated with operations during the period of analysis and converts this cost to a value in today's dollars. In the present study, only energy costs are included in the OC category. The maintenance cost is defined as part of the capital cost that occurs yearly. The total cost of energy throughout the entire period of study must be adjusted to today's dollars in order to be compared with the first cost (i.e., the capital cost), which is incurred immediately and is therefore already in present dollars. The multiplier P_1 is defined as,

$$P_1 = (1-t)\, PWF\left(N_{yr}, i_f, d\right) \tag{4-2}$$

where,

t = effective tax rate [Eq. (4-3)]
N_{yr} = system lifetime period or analysis period (years)
i_f = fuel inflation rate (%)
d = market discount rate (%)

The function PWF is the present-worth factor for the number of years in the analysis period for the prevailing inflation rate, i, and discount rate, d. The effective tax rate (t) is calculated according to:

$$t = t_f + t_s - t_f\, t_s \tag{4-3}$$

where t_f and t_s are federal and state tax rates, respectively. The parameter P_2 in Eq. (4-1) accounts for future payments required to completely payoff the loan that was obtained in order to finance the capital investment of the system and converts these payments to present dollars. P_2 takes into consideration all of the parameters contributing to the capital cost, such as tax rate, inflation rate, mortgage rate and etc. P_2 is defined as,

$$P_2 = DP + (1-DP)\frac{PWF(N_1,0,d)}{PWF(N_L,0,m)} - t(1-DP)\left[PWF(N_1,m,d)\left(m-\frac{1}{PWF(N_L,0,m)}\right)+\frac{PWF(N_1,0,d)}{PWF(N_L,0,m)}\right] + p(1-t)PWF(N_{yr},i,d)+MT(1-ct)PWF(N_{yr},i,d)-\frac{ct}{N_D}PWF(N_2,0,d)-\frac{S(1-t)}{(1+d)^{N_{yr}}} \quad (4\text{-}4)$$

where,

DP	=	ratio of the down payment to the first cost (%)
d	=	market discount rate (%)
i	=	general inflation rate (%)
m	=	annual mortgage interest rate (%)
MT	=	ratio of maintenance, insurance and other incidental costs to the first cost (%)
N_{yr}	=	period of economic analysis (years)
N_L	=	term of loan (years)
N_D	=	period of equipment depreciation (years)
N_1	=	period over which mortgage payments contribute to the analysis (years) (usually the minimum of N or N_L)
N_2	=	period over which depreciation contributes to the analysis (years) (usually the minimum of N or N_D)
p	=	is the property tax based on assessed value
c	=	is either 1 for commercial investment or 0 for residential investment
t	=	effective tax rate (%)
S	=	ratio of the resale value at the end of analysis to the first cost (%)

The multiplier P_2 depends on several economic parameters. The first term (DP) is simply the ratio of the down payment to the first cost; this term is not adjusted to present value because the down payment is paid at the beginning of the economic period. The second term $(1-DP)$ is the present-worth value of the loan taken out at the discount rate in order to pay off the remainder of the first cost at the mortgage interest rate. The third term, $t(1-DP)$, is related to the present-worth value of the income tax benefit of interest payments over the loan period. The fourth term, $p(1-t)$, is related to the present-worth value of the property tax associated with owning a piece of refrigeration equipment. The fifth term, $MT(1-ct)$, is related to the present-worth value of the refrigeration system maintenance cost, which is also tax deductible for a business. The sixth term, $\frac{ct}{N_D}$, is the present-worth value of depreciation for tax reduction. The last term, $S(1-t)$, is the ratio of the resale value at the end of the analysis brought back to present value.

The first-year operating cost (OC) is the product of the cost of electricity and the total amount of electrical energy used by a refrigeration system during one year of operation, expressed in kilowatt-hours (kWh). The first-year operating cost is obtained by running the complete system model over a defined daily and weekly operating/production schedule for a 12-month simulation period. The operating cost considered in this analysis includes only the electricity cost for motor-driven components—compressors, evaporator fans, condenser fans and pumps. Maintenance cost and other equipment-related costs are considered as part of the first cost (FC). The following section addresses input parameters and assumptions associated with the 12-month simulation.

4.2) Operating Cost Analysis Approach

The operating cost for each system required for the economic analysis is obtained by performing a 12-month simulation. The energy use for each system is estimated using the hourly typical meteorological year (TMY) weather data (NREL website, 2008) as a "forcing function" for the heat rejection system. Details of the operating cost analysis are discussed in the sections that follow.

4.2.1) Baseline of Operation

To ensure consistency in the 12-month simulation for both system configurations, a common baseline of operation is defined in this section. The results of these simulations are later used as part of the life-cycle cost analysis in order to identify the most attractive system. Essential simulation criteria are described below.

- ***Location***

Geographical location is one of the many factors that influence on system performance, especially for a long period of operation. Simulations are conducted at four selected cities across the United States, including: Madison, WI; Miami, FL; Los Angeles, CA, and Houston, TX. These locations are selected because the climatic condition (combination of temperature and humidity) is different for each location, for instance, Miami is hot and dry whereas Houston is hot and humid. As described in Section 3.3, ambient weather conditions affect the heat rejection capability of a refrigeration system. The outside air wet-bulb condition dictates the heat rejection capacity of the condensers, which must be matched to the system heat rejection requirement in order to establish an equilibrium head pressure. Thus, the compressor power consumption depends on the amount of pressure lift needed to reach the condensing pressure. Since these climatic conditions vary geographically, system performance and electrical energy consumption at different plant locations will vary. A system located in a region with more frequent low head pressure occurrences (i.e., a relatively cold and/or dry climate) during a year's operation will have a lower operating cost than a similar system operating in a hotter and/or more humid climate. In all cases, the system's head pressure floats with ambient conditions until reaching a defined minimum of 135 psia as discussed previously in Section 3.3.2.1.

- ***Mode of Operation***

It is also useful to simulate the system during the different modes of operation that are typically encountered at food processing plants. Since the weather data are provided hourly for 8,760 hours in one year, programming logic can be used to set operating and non-operating hours in a pattern corresponding to a repeatable period of time (e.g., every 12 or 24 hours). There are two modes of operation that are considered in this simulation.

1. **8-hr day**: refrigeration system operates constantly to meet a low temperature production (freezing system) load from 8:00 AM until 4:00 PM daily.
2. **10-hr day**: refrigeration system operates for 5 hours at a time; this mode reflects a normal day consisting of a 2-shift production schedule. Operating hours during the day are from 7:00 AM to 12:00 PM and from 1:00 PM to 6:00 PM.

Because the freezing system load is the same for all system options (i.e. load is independent of the system being compound or cascade), the modes of operation do not specifically penalize system performance due to frost accumulation. The influence of frost and the associated defrosting penalty is assumed similar for both systems and therefore not affect the life-cycle savings.

- ***Capacity Control***

In locations where the climate is colder, the systems will operate with relatively lower head pressure. For the simulation, the minimum system head pressure is set to 135 psia and it is allowed to float up from this value with increasing ambient temperatures or humidity. All fan motors (condensers and evaporators) are assumed to have variable frequency drives, so that the air flow rate is adjusted to exactly match the required capacity. In cases of condenser capacity control, the fan speed is adjusted to meet part-load requirement. Electrical power of fan motors and its relationship to the air flow rate has been described in Section 3.3.2.1 and this scaling relationship is utilized in this analysis. Evaporative condensers and evaporators are assumed to operate in series, thus the aggregate capacity control strategies affect the operation of each piece of equipment identically.

- ***Evaporating Temperatures***

Both systems are assumed to operate in a very low temperature range, below -40^{o}F. The system model is run at a fixed evaporating temperature for each 12-month simulation. The effect of evaporating temperature is evaluated by parametrically varying from -40^{o}F to -65^{o}F in increments of 5^{o}F. At relative low temperatures, the very high specific volume of ammonia vapor leads to a substantial difference in compressor size and performance between the compound and cascade systems; this negatively impacts the compound system efficiency and life-cycle cost. Therefore, over a certain range of evaporating temperature, the cascade system has an advantage because of the relatively higher vapor density associated with carbon dioxide. One of the results of this analysis is the identification of a break-even temperature at which both systems perform equally well.

- ***Compressor Unloading***

The unloading behavior of both the screw and reciprocating compressors is different. As discussed in Chapter 3, the unloading characteristic of a reciprocating compressor is nearly linear; that is, the part-load capacity and the fraction of full-load power are nearly directly proportional. On the other hand, the unloading characteristic of a screw compressor is non-linear and exhibits a strong performance penalty at low part-load conditions. In this comparative analysis, the compressor unloading characteristics are assumed to be linear for both systems. This was done in order to eliminate part-load operation penalty and remove the confounding effect that this has on the result. The compressor unloading behavior leads to differences between the two systems that are specific to the sizing of the compressors and the size of the system that was considered. This is undesirable as it introduces an effect that reduces the general applicability of the analysis. The analysis that follows is consistent in that both types of compressor are assumed to unload linearly.

- ***Cascade Heat Exchanger***

In this present analysis, the cascade heat exchanger model is initially assumed to have the same size and geometry, listed in Table 3-5, that are consistent with achieving the required performance at the design conditions that are listed in Table 3-3. With this fixed geometry, the pinch-point temperature difference does vary during the simulation as the system operates at off-design conditions.

- ***Intermediate Condition***

The highest operating pressure (or temperature) level in the system is established by the overall system energy balance and the heat rejection conditions subject to the constraint of minimum head pressure of 120 psig (135 psia). The lowest operating suction pressure (or temperature) level in the system is established by the needs of refrigeration loads. In the present analysis, the intermediate pressure level (for the compound system) or temperature level (for the cascade system) is not constrained but allowed to vary to maximize the system performance. Although most systems will have an intermediate temperature or pressure level that is constrained by the temperature requirements associated with higher temperature loads, the freedom to vary the system's intermediate pressure is intended to illustrate best performance for each alternative. The present analysis assumes that this intermediate condition is unconstrained and is a completely free parameter. This assumption is enforced in order to establish an equal footing with which to compare both systems; the system performance is, in both cases, the best possible as the intermediate condition is optimized as discussed in the following section.

4.2.2) Performance Optimization

In this analysis, the saturated intermediate pressure of the compound system is allowed to vary in order to maximize the system COP. Initially, this was accomplished by identifying the optimum intermediate pressure for each time-step using Min/Max function in EES. For a 12-month simulation, this method is the excessively time consuming as the program must execute numerous iterations at each time step before converging on an optimized condition. This also occasionally causes the simulation to stop due to convergence problems that require constant debugging. As an alternative, two less computationally intensive optimization approaches have been developed. These approaches are referred to as the simplified optimization method and the root-product method and are described in the following sections.

4.2.2.1) Simplified Optimization Method

This alternative optimization method parametrically (using Min/Max Table function) optimizes the intermediate condition over a typical range of condensing pressures (head pressures) and evaporating temperature. The optimal intermediate pressure at the intercooler (for the compound configuration) and saturated condensing temperature of the carbon dioxide in the tube-side of the cascade heat exchanger (for the cascade configuration) are identified. The results of the optimization are shown in Figures 4-1 and 4-2 for the cascade and compound cycles, respectively.

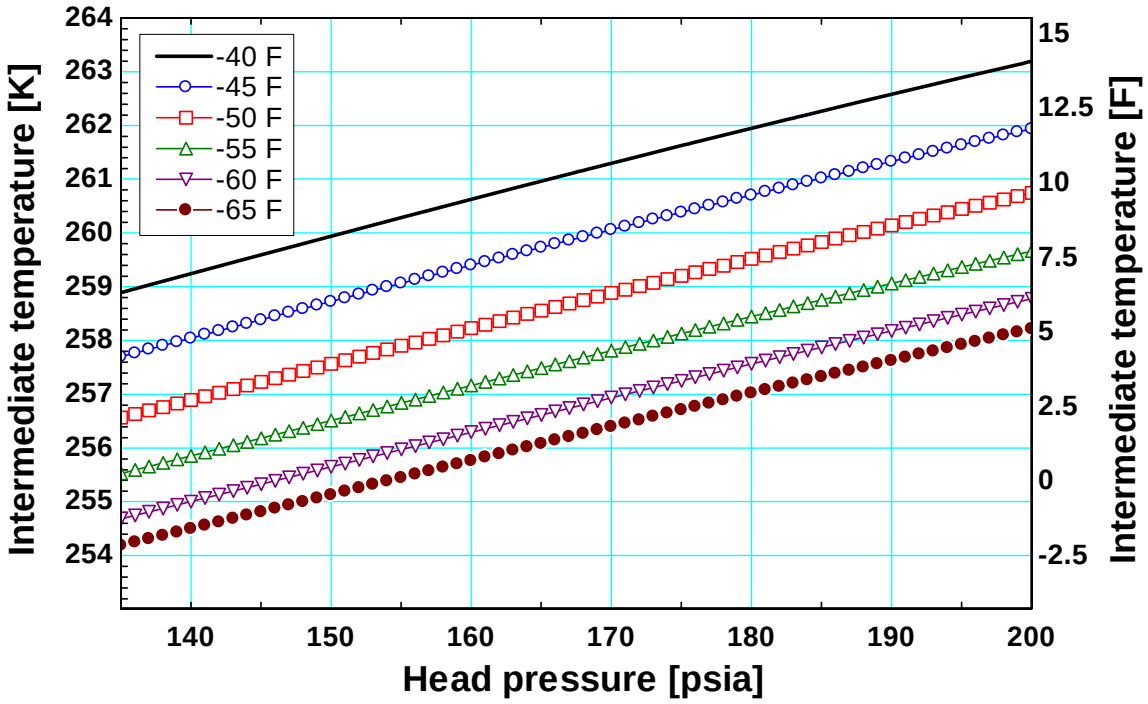

Figure 4-1: Optimized cascade intermediate saturation temperature as a function of condensing (head) pressure at various evaporating saturation temperatures

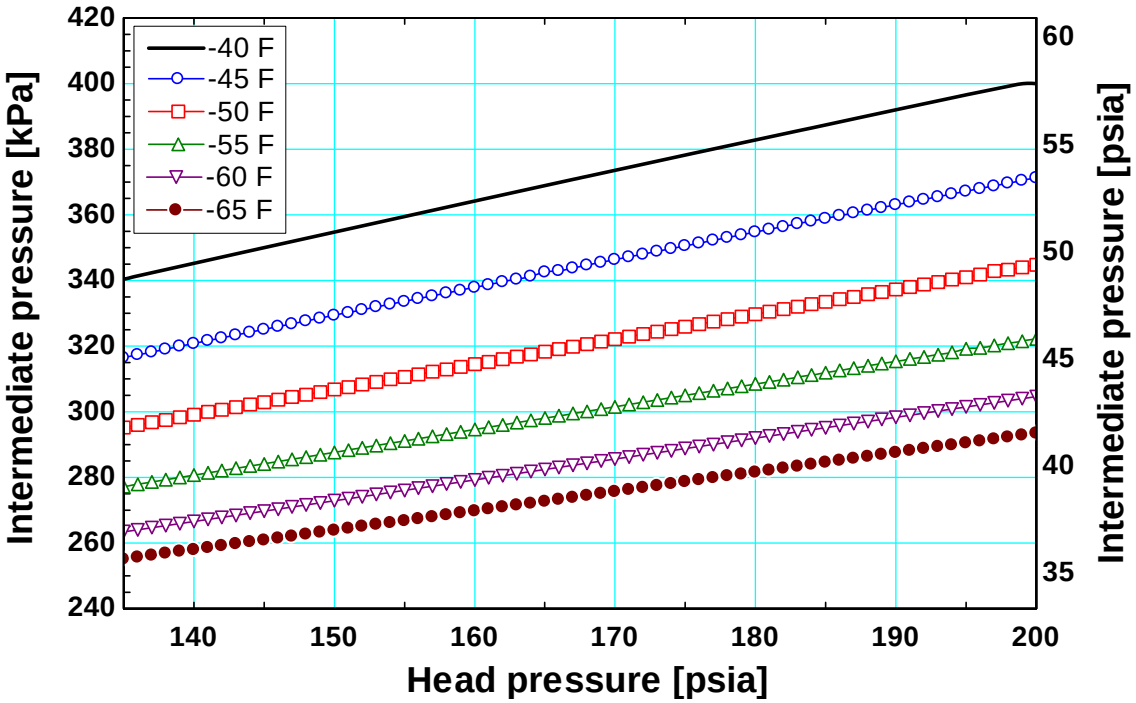

Figure 4-2: Optimized compound intermediate saturation pressure as a function of condensing (head) pressure at various evaporating saturation temperatures

The results shown in Figures 4-1 and 4-2 are curve fit using a bi-quadratic regression with a 2nd order polynomial fit. Equation (4-5) shows the optimization equation for the cascade system. The optimal intermediate temperature on the tube-side of the cascade heat exchanger (T_{int}) is given as a function of evaporating saturation temperature ($T_{evap,sat}$) and system head pressure (P_{head}),

$$T_{int} = a + b\,T_{evap,sat} + c\,T_{evap,sat}{}^{2} + d\,P_{head} + e\,P_{head}{}^{2} + f\,T_{evap,sat}\,P_{head} \tag{4-5}$$

where,

$$a = 711.3\,[K] \qquad b = -4.425\,[-] \qquad c = 0.0146\left[\frac{1}{K}\right] \qquad d = 0.0207\left[\frac{K}{psia}\right]$$

$$e = 0.0000602\left[\frac{K}{psia^{2}}\right] \qquad f = 0.000282\left[\frac{1}{psia}\right]$$

Equation (4-6) shows the optimization equation for the compound system. The intermediate pressure at the intercooler (P_{int}) is given as a function of evaporating saturation temperature ($T_{evap,sat}$) and system head pressure (P_{head}),

$$P_{int} = a + b\,T_{evap,sat} + c\,T_{evap,sat}^{\ 2} + d\,P_{head} + e\,P_{head}^{\ 2} + f\,T_{evap,sat}\,P_{head} \tag{4-6}$$

where,

$$a = 13153.8\left[psia\right] \qquad b = -117.6\left[\frac{psia}{K}\right] \qquad c = 0.2663\left[\frac{psia}{K^2}\right] \qquad d = -4.763\left[-\right]$$

$$e = -0.000176\left[\frac{1}{psia}\right] \qquad f = 0.0246\left[\frac{1}{K}\right]$$

During the simulation, the evaporating condition is fixed at the defined saturated evaporator temperature and the system head pressure is allowed to float with ambient wet-bulb condition. The specified saturated evaporating temperature (in degree Kelvin), and the resulting head pressure (in psia) become the input parameters to the optimization equation. These equations are now implemented in the optimization models (as opposed to using the Min/Max function for each time step) in order to determine the optimized intermediate condition and the resulting COP. This method works very well for both models, leading to the true optimal condition but dramatically reducing the simulation time. The resulting optimized COPs of the both systems using the simplified optimization method are shown in Figures 4-3 and 4-4 for the cascade and compound systems, respectively.

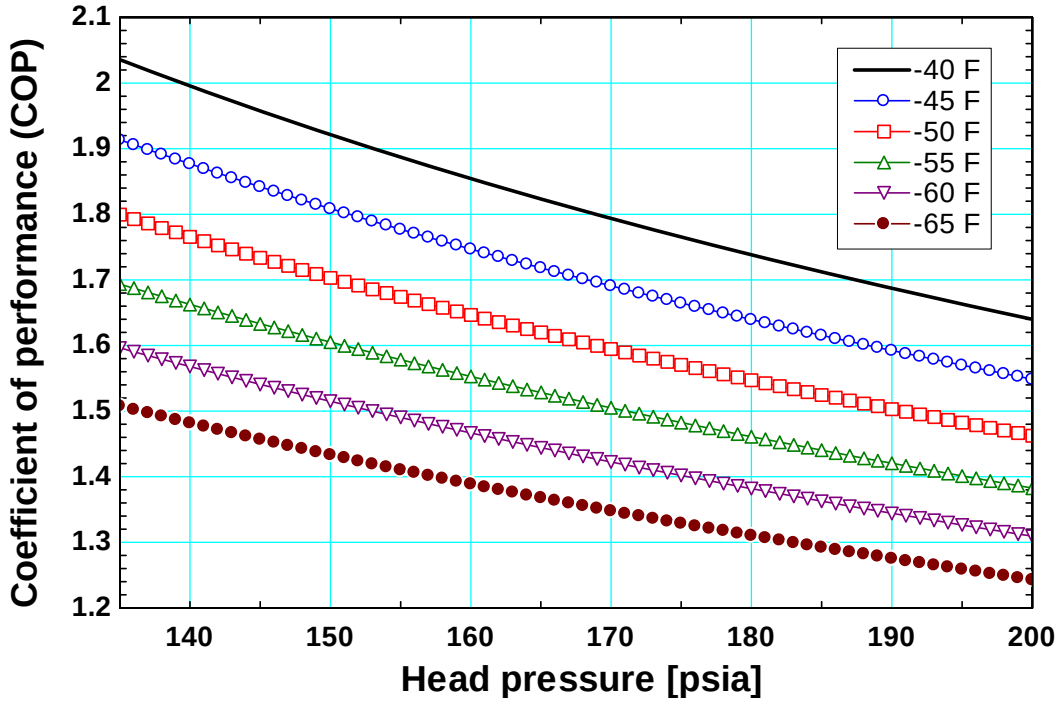

Figure 4-3: Optimized **cascade** system COP as a function of condensing (head) pressure at various saturated evaporator temperatures

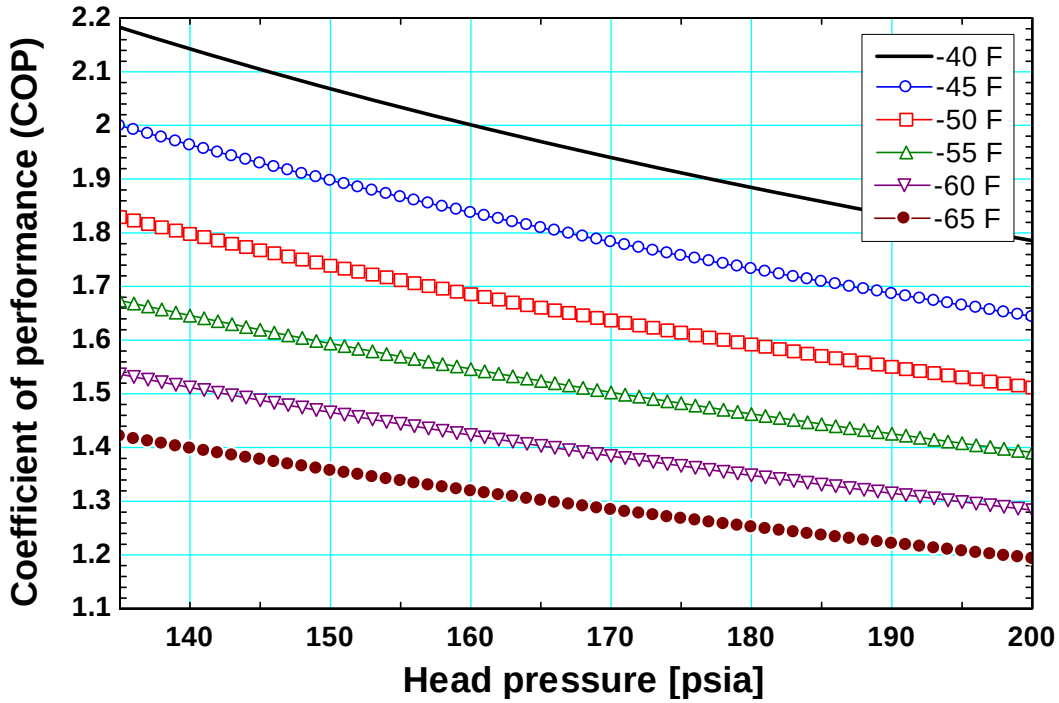

Figure 4-4: Optimized **compound** system COP as a function of condensing (head) pressure at various saturated evaporator temperatures

4.2.2.2) Root-Product Method

The root-product method refers to technique to equalize the pressure ratio between the two stages of compression which approximates the optimal intermediate condition for a compound cycle. The intermediate condition is determined by identifying the pressure level where the compressor power input required to provide pressure lift in each compression stage is nearly equal. Implementation of this method in EES is done by calculating an intermediate pressure as a geometric mean between the lowest system pressure (corresponding to the evaporating temperature) and the condensing (head) pressure. This method is only considered for the compound system model. The intermediate pressure and associated COP as a function of head pressure for various values of the evaporating temperature are shown in Figures 4-5 and 4-6, respectively.

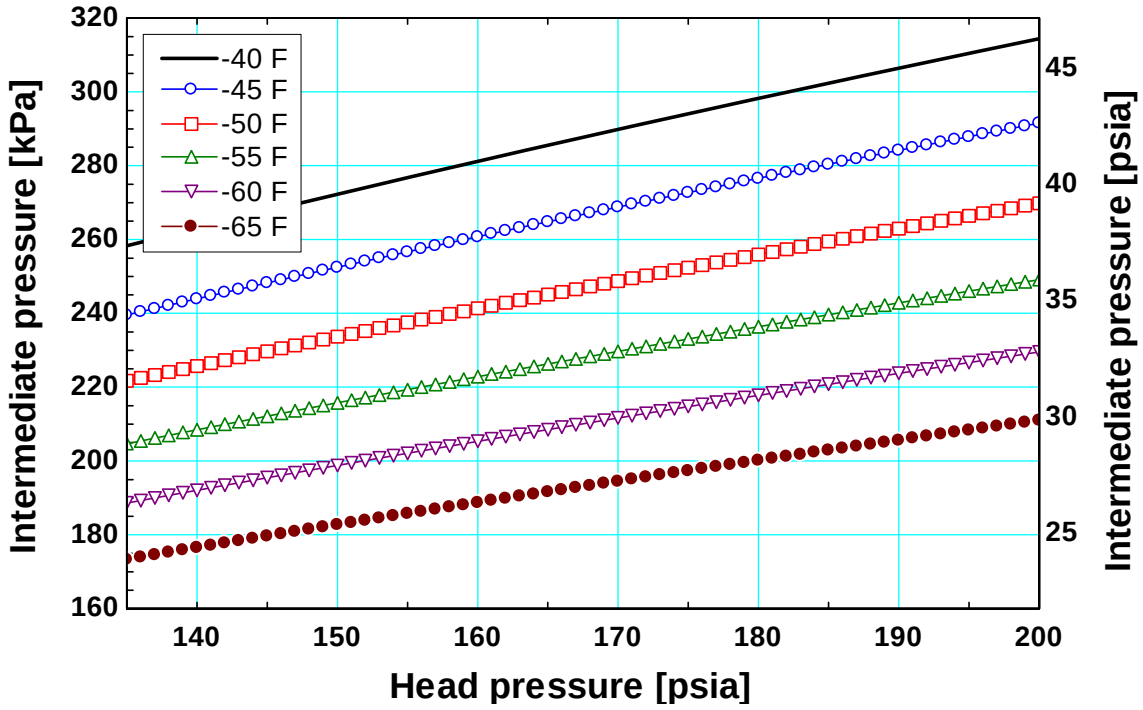

Figure 4-5: Root-product method optimized intermediate saturation pressure as a function of condensing (head) pressure at various saturated evaporator temperatures

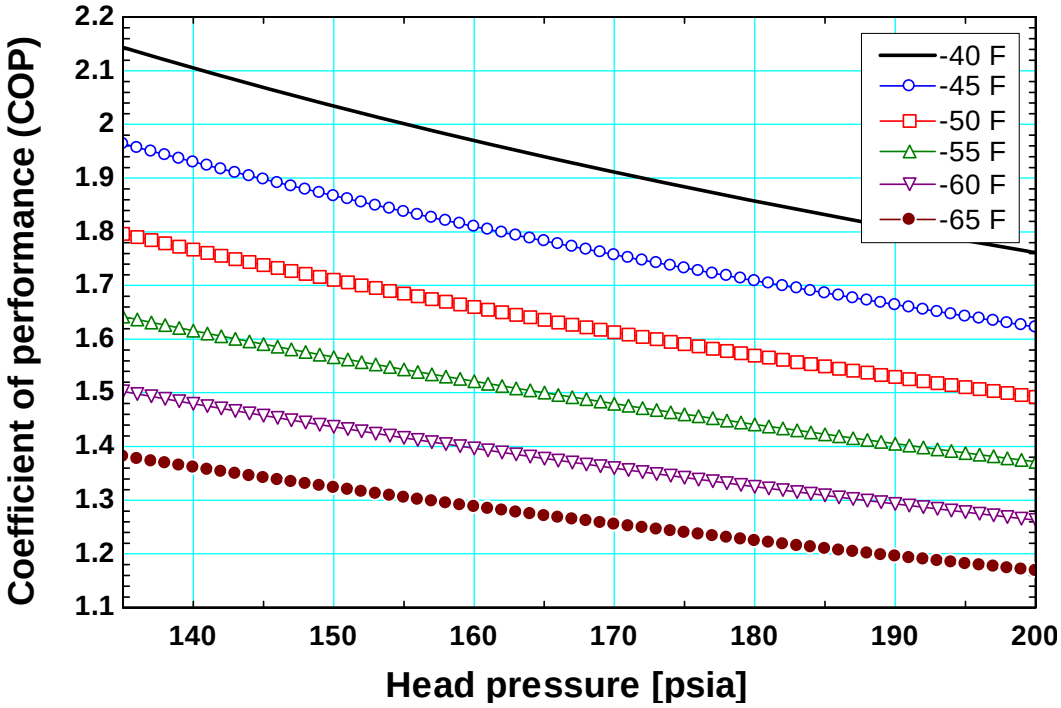

Figure 4-6: Root-product method optimized COP of the compound system as a function of condensing (head) pressure at various saturated evaporator temperatures

Figure 4-4 shows that the simplified optimization method returns slightly higher COP than the root-product method for the compound system. Figure 4-7 is generated by overlaying the optimized COP plots from each optimization technique (Figures 4-4 and 4-6) for the compound system.

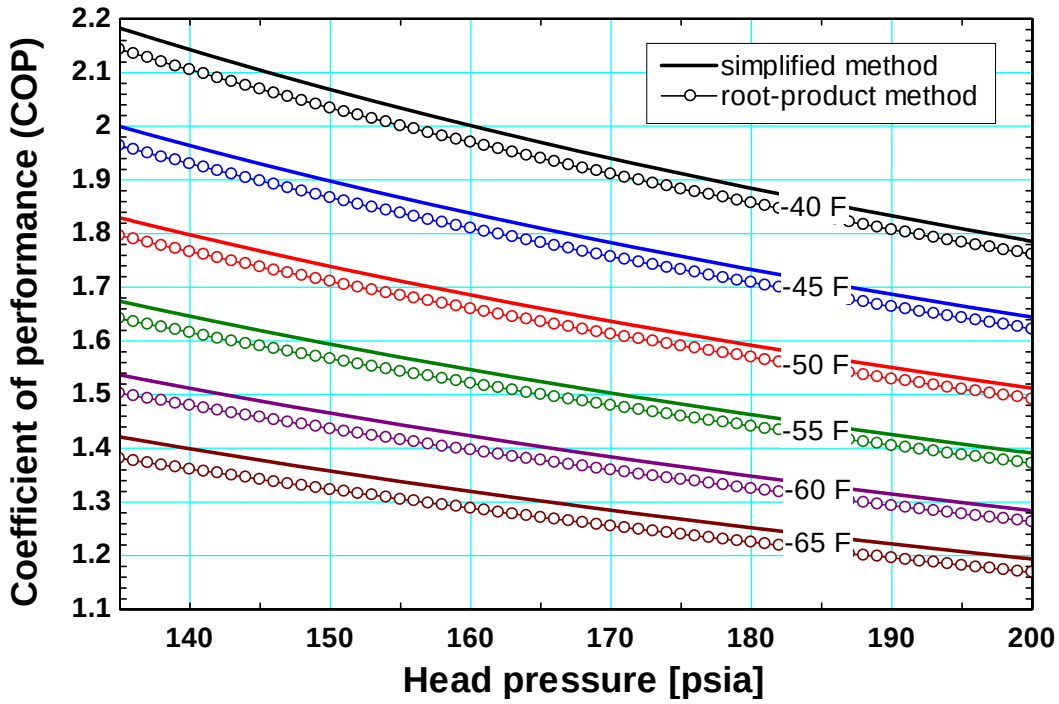

Figure 4-7: Optimized COP plots of the compound system overlaid between simplified and root-product optimization methods as a function of head pressure at various evaporating temperature

It is understood that, for the compound system, the simplified optimization method returns higher values of COP than those of the root-product method at all evaporating temperatures because the latter is not the true optimization. So, the simplified optimization technique is more preferable for the compound system to minimize its life-cycle cost.

4.2.2.3) Break-Even Temperature

At low evaporating temperatures, one of the disadvantages of the compound system is evident — the high vapor specific volume of ammonia at low temperature. As a result of this, the performance of the compound system tends to degrade more rapidly than the cascade system at lower suction pressures due to the decreasing booster compressor efficiency. On the other hand, ammonia system tends to be more efficient at high evaporating temperatures due to its high heat capacity at those temperatures (above -50°F). There is a certain evaporating temperature where these two systems perform equally well; this evaporating temperature is referred to as "the break-even temperature." At this temperature, each system has no operating advantage over one another (although there is likely to be a capital cost advantage of one system compared to the other). Figure 4-8 and 4-9 illustrate the COP as a function of evaporating temperature for the two configurations at three fixed values of head pressure: 135 psia, 160 psia and 190 psia. Figure 4-8 was generated using the simplified optimization method for both cycles while Figure 4-9 utilized the root-product technique for the compound cycle.

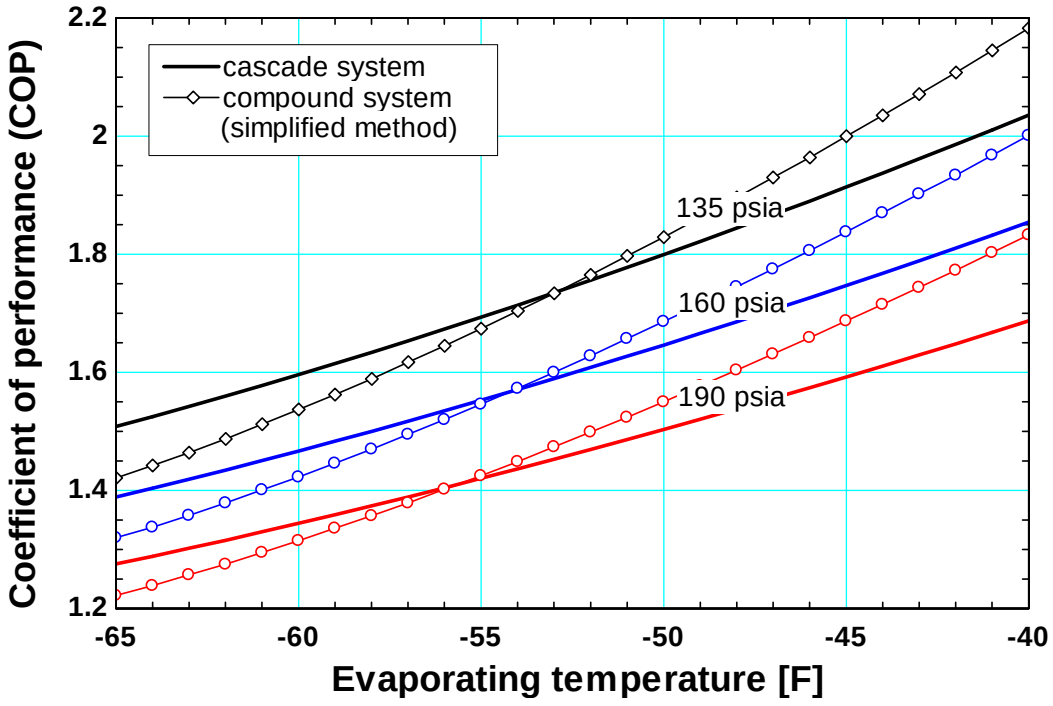

Figure 4-8: Optimized COP plots overlaid between cascade system and compound system (simplified method) as a function of evaporating temperature

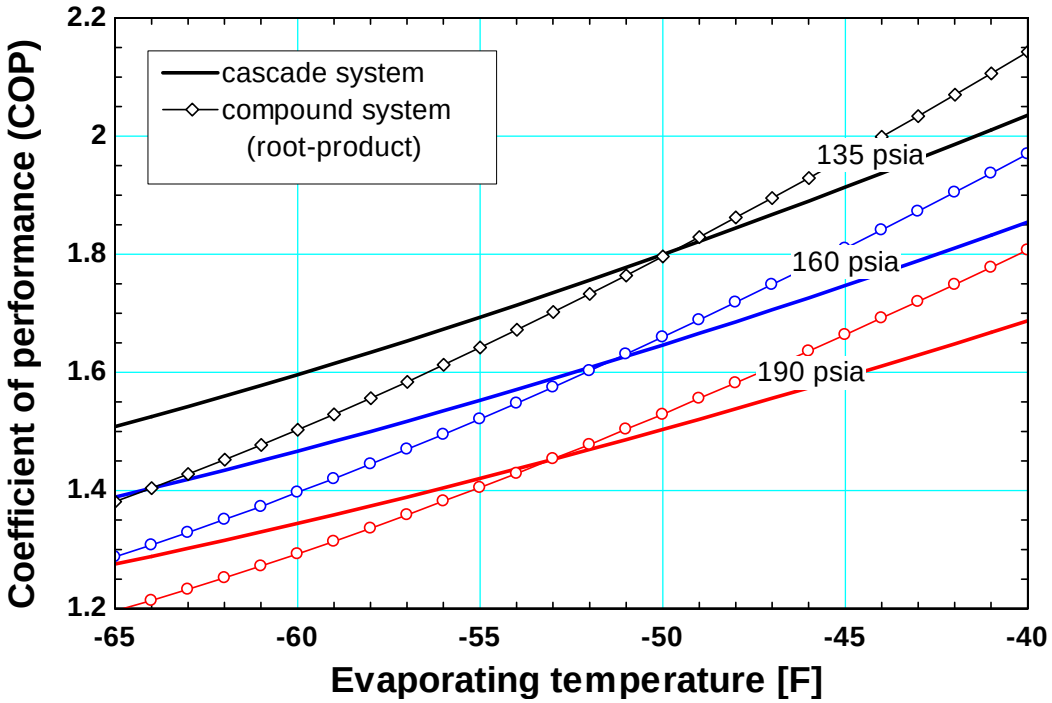

Figure 4-9: Optimized COP plots overlaid between cascade system and compound system (root-product method) as a function of evaporating temperature

The ammonia compound system has higher system efficiency above the break-even temperature while the cascade system is more efficient below the break-even temperature. The results are consistent with the discussion made earlier. In an economic context, a difference in system efficiency would lead to an operating cost saving for the system that is more efficient. When integrated over the lifetime of the system, a large operating cost saving could influence the system selection process considerably. The 12-month simulation predicts amount of electrical energy usage associated with each system, which can be used to quantify the operating cost and the associated savings.

4.2.3) 12-Month Simulation Results

Using the assumptions and operating conditions described in Section 4.2.1 and the optimization methods described in Section 4.2.2, the 12-month simulation is run for both the multi-stage ammonia system and the cascade system at each of the four different locations previously mentioned in Section 4.2.1. Table 4-1 summarizes the input parameters specified for the first set of the 12-month simulation runs.

Table 4-1: 12-month simulation input parameters and system model assumptions

	Cascade system	***Compound system***
Input parameter(s)	Ambient air condition (TMY weather data)	
Locations	Miami, FL., Madison, WI., Los Angeles, CA., Houston, TX.	
Mode(s) of operation	• 8 hr/day (2,920 hr/yr) and • 10 hr/day (3,650 hr/yr)	
Head pressure limit	Variable based on weather but with a 135 psia minimum	
Evaporator heat load	680 Tons (constant)	
Evaporating temperatures	-40^{o}F to -65^{o}F (in steps of 5^{o}F)	
Compressor unloading	Linear	
Optimization method(s)	Simplified	Simplified and Root-Product

The root-product optimization method is also implemented in the simulation for the compound system in order to evaluate the difference in operating cost caused by using these two optimization methods. The purpose of the 12-month simulation is to determine the first-year operating cost (OC) for each system at each geographical location. Table 4-2 summarizes the climatic conditions (i.e., the TMY weather data) associated with each geographical location selected for this analysis. Complete simulation data are included in Appendix B. Figures 4-10 and 4-11 illustrate the annual energy usage of the cascade system as a function of evaporating temperature at each plant location for 8-hour and 10-hour day mode, respectively.

Table 4-2: Summary of weather conditions at the geographical locations selected for simulations

Parameters	***Miami, FL.***	***Madison, WI.***	***Los Angeles, CA.***	***Houston, TX.***
Lowest wet-bulb temperature	274.5 K (34.43^{o}F)	244.1 K (-20.29^{o}F)	273.6 K (32.81^{o}F)	261.9 K (11.75^{o}F)
Average (annual) wet-bulb temperature	293.8 K (69.17^{o}F)	278.5 K (41.63^{o}F)	286.4 K (55.85^{o}F)	290.1 K (62.51^{o}F)
Highest wet-bulb temperature	300.5 K (81.23^{o}F)	299.6 K (79.61^{o}F)	295.1 K (71.51^{o}F)	301.3 K (82.67^{o}F)

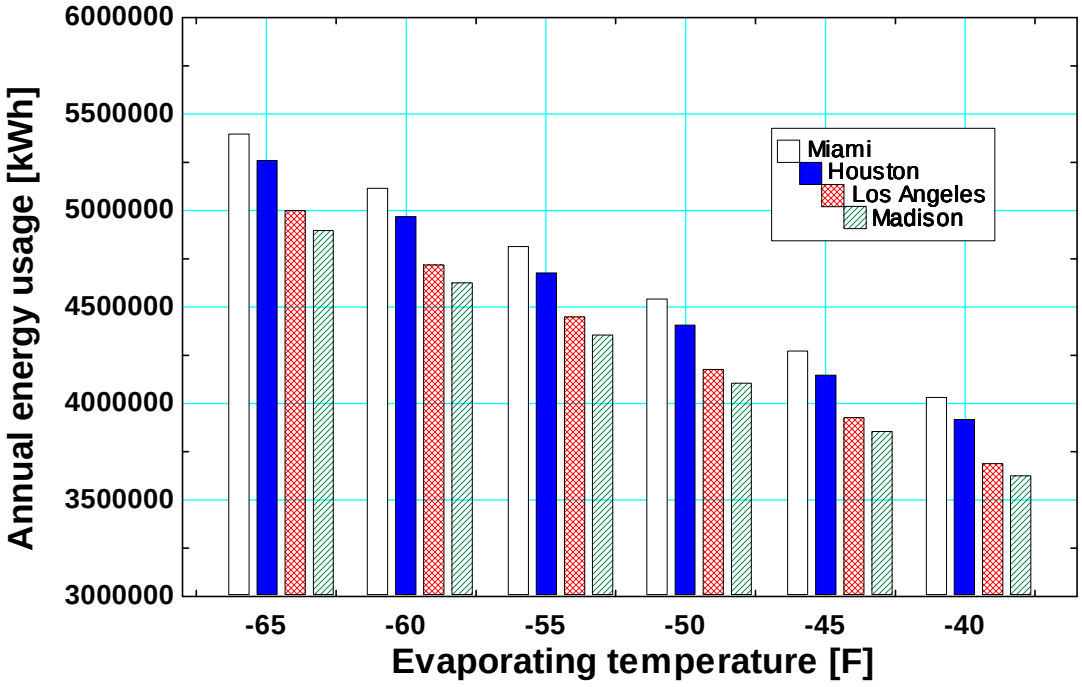

Figure 4-10: Annual energy usage for a cascade system operating in an 8-hour day mode at various geographical locations as a function of evaporating temperature

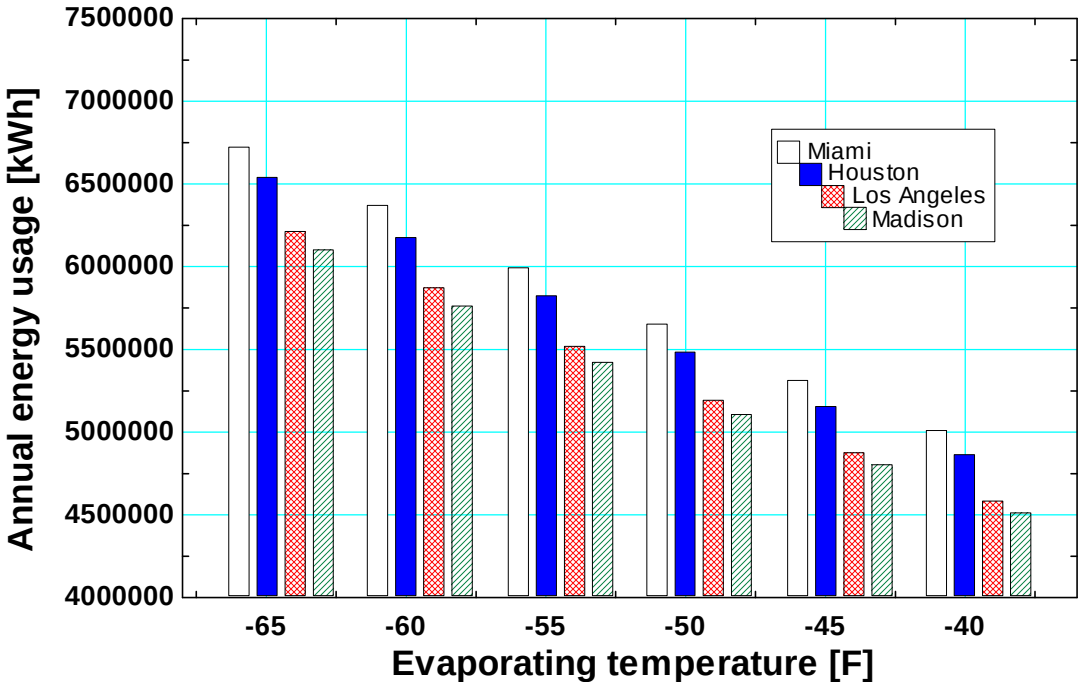

Figure 4-11: Annual energy usage for a cascade system operating in a 10-hour day mode at various geographical locations as a function of evaporating temperature

When a system operates at low evaporating temperatures, compressor efficiency decreases, which leads to higher electrical power consumed by the compressors. Thus, the amount of energy needed to be removed from the system also increases. This necessitates a higher system head pressure in order to raise the condenser heat rejection capacity and match the required system heat rejection. Therefore, the increasing trend of energy usage with decreasing evaporating temperature is accurately reflected by the results.

The climatic condition in Miami is hot and humid throughout most of the year; this location has the highest average wet-bulb temperature among all four cities that were considered. Thus, a system operating in Miami will have a higher head pressure in order to reject heat to the surroundings. As a result, Miami has the highest annual energy usage. Houston has the next highest wet-bulb temperature and it follows Miami in a location-based energy usage trend but precedes Los Angeles and Madison, respectively. In Figures 4-10 and 4-11, the annual energy usage results indicate that the energy usage of Los Angeles is closer to Madison than it is to Houston. However, Table 4-2 shows that the average wet-bulb temperature in Los Angeles is closer to that of Houston than it is to Madison. A plot is created to show a relationship between energy usage and the average wet-bulb temperature (Table 4-2) both with and without a minimum head pressure bound. Figure 4-12 is generated using a cascade system operating at a fixed evaporating temperature value of -40^{o}F.

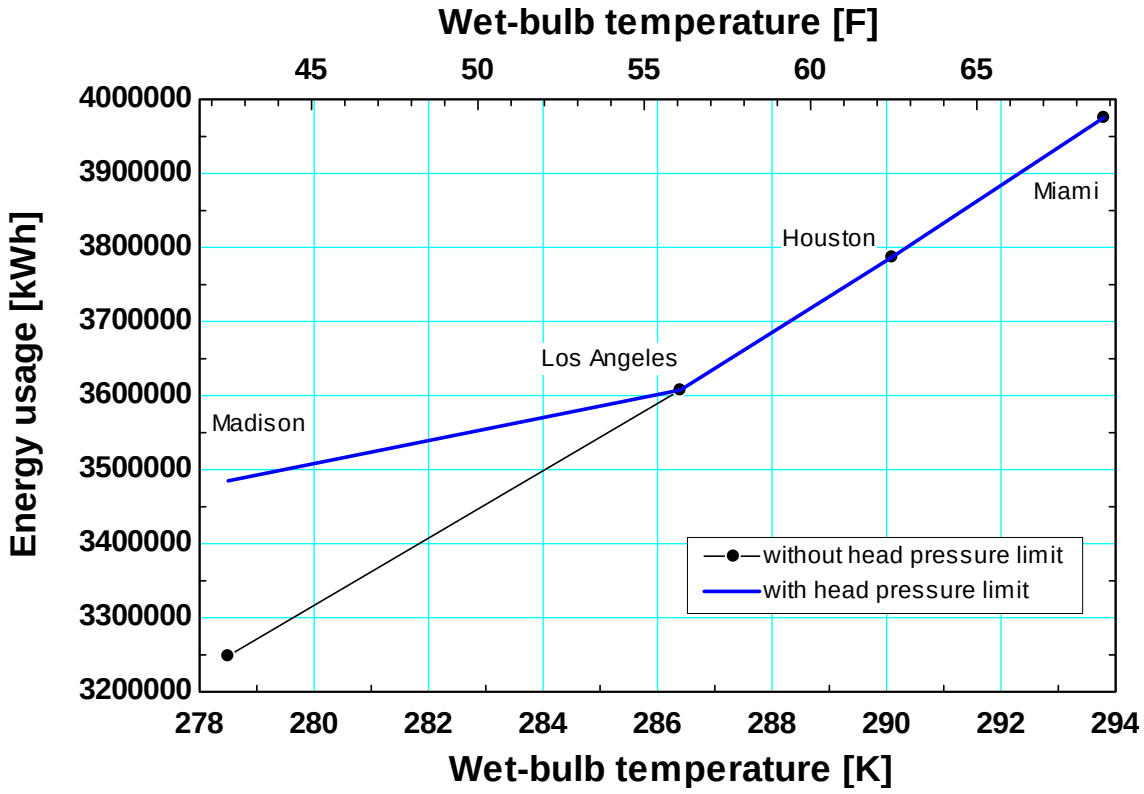

Figure 4-12: Annual energy usage of a cascade system as a function average wet-bulb temperature associated with the climate of each plant location

Figure 4-12 shows that there is a discrepancy between annual energy usage and average wet-bulb temperature Madison when the minimum head pressure is bounded. Section 4.2.3.1 discusses a more detailed study that has been carried out in order to clarify this discrepancy. Figures 4-13 and 4-14 show the annual energy usage of the compound system at each geographical location for each evaporating temperature using the simplified optimization method for each mode of operation.

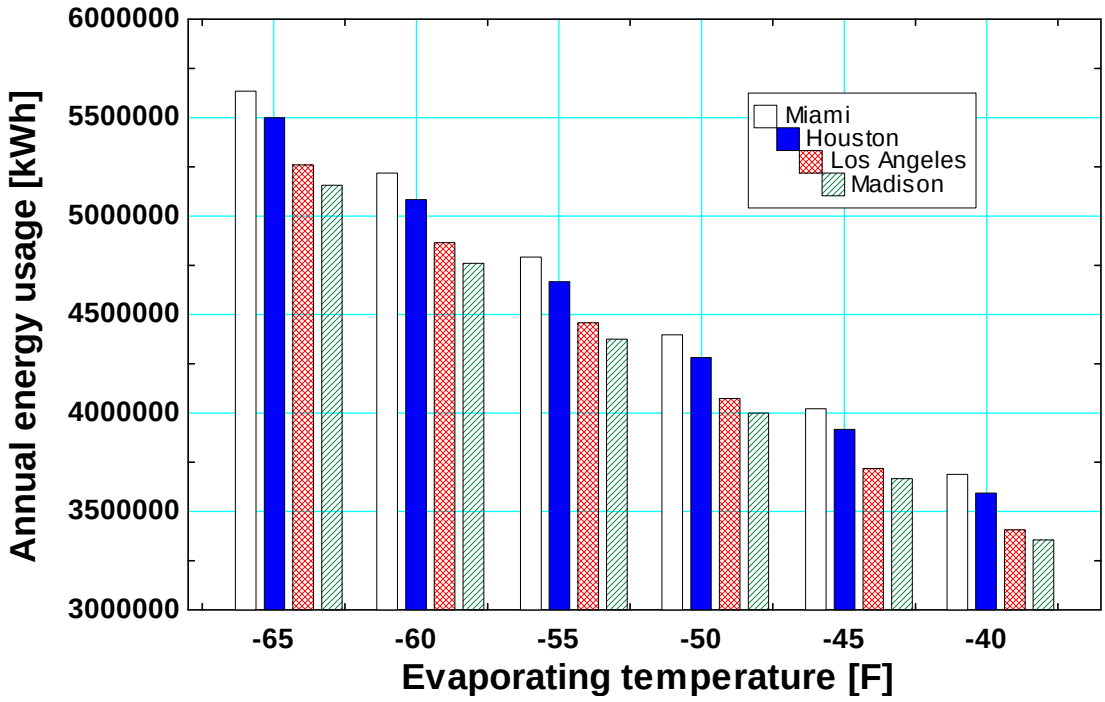

Figure 4-13: Annual energy usage for a compound system (simplified method) operating in an 8-hour day mode at various geographical locations as a function of evaporating temperature

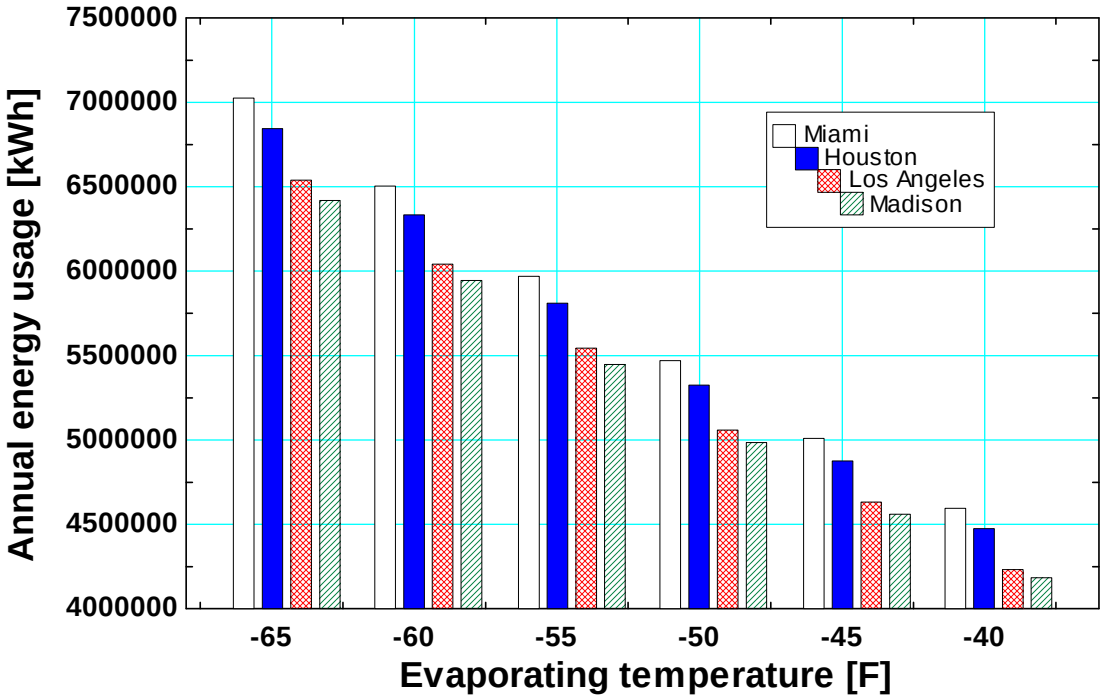

Figure 4-14: Annual energy usage for a compound system (simplified method) operating in a 10-hour day mode at various geographical locations as a function of evaporating temperature

As mentioned earlier, the compound system has a higher COP at higher evaporating temperatures above the break-even temperature; this is also reflected in the annual energy usage results. Figure 4-15 illustrates an energy usage comparison overlaid between the cascade and the compound system at Houston, TX. using the simplified optimization method for each evaporating temperature.

The simulation was also carried out utilizing the root-product optimization technique for the compound system. Figures 4-16 and 4-17 illustrate the annual energy usage associated with the compound system for an 8 hour and 10 hour day, respectively, at each geographical location and each evaporating temperature using the root-product optimization method for each mode of operation. An energy usage comparison plot is created to illustrate the difference in system COP between these two optimization techniques as the annual energy usage is higher for the latter method. Figure 4-18 is an overlaid energy usage between the simplified and root-product method for the compound system operating at Houston as a function of evaporating temperature.

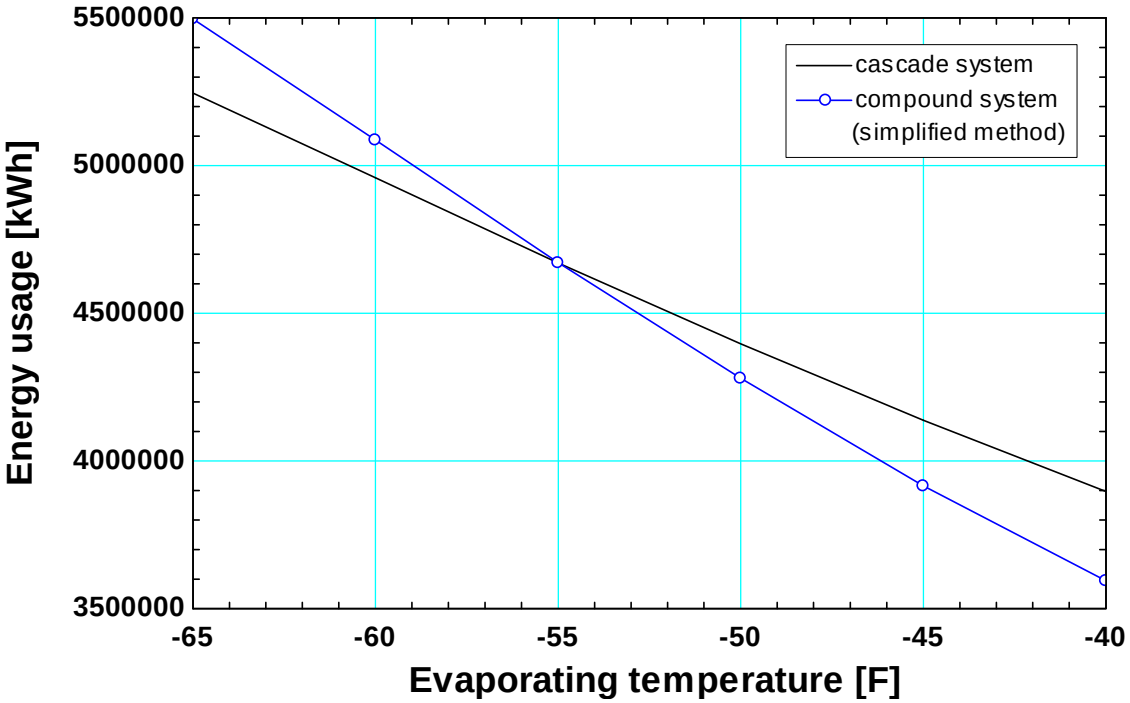

Figure 4-15: Annual energy usage of the cascade system overlaid with the compound system (simplified method) as a function of evaporating temperature operating at Houston, TX.

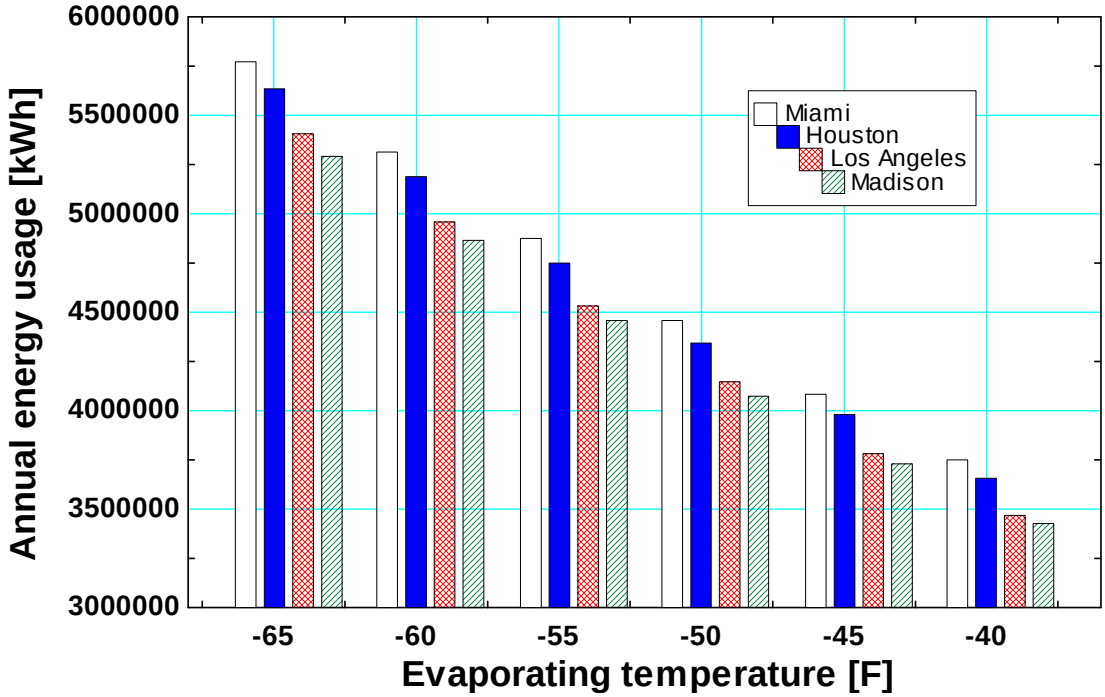

Figure 4-16: Annual energy usage for a compound system (root-product method) operating in an 8-hour day mode at various geographical locations as a function of evaporating temperature

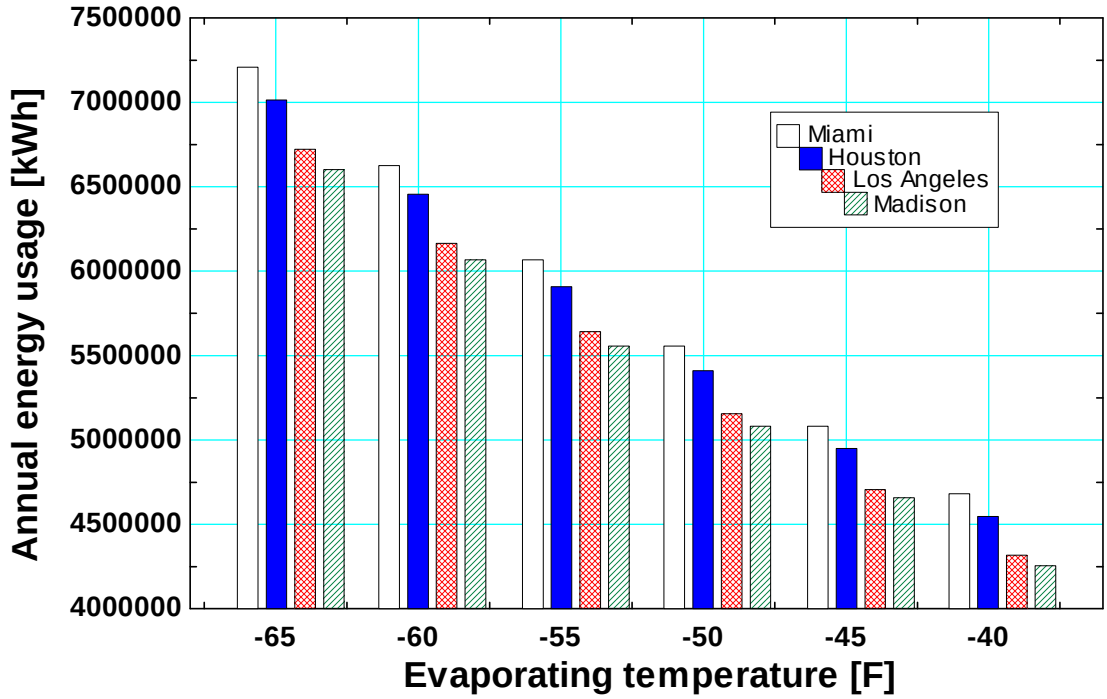

Figure 4-17: Annual energy usage for a compound system (root-product method) operating in a 10-hour day mode at various geographical locations as a function of evaporating temperature

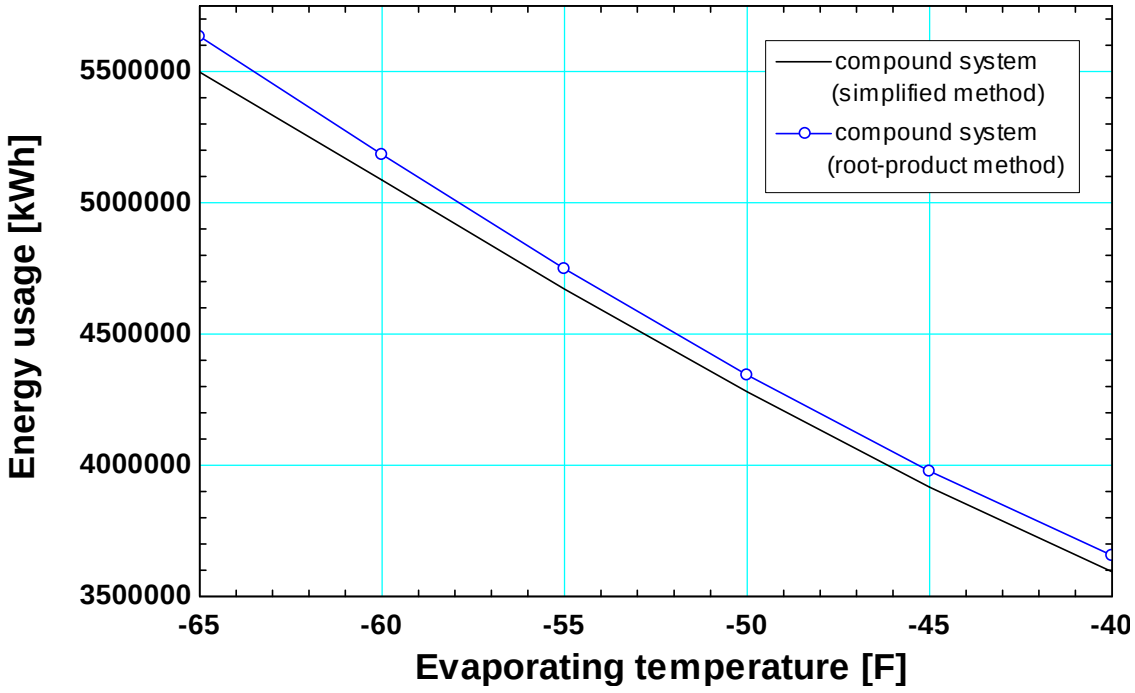

Figure 4-18: Annual energy usage of the compound system overlaid between the simplified and root-product optimization method as a function of evaporating temperature at Houston, TX.

4.2.3.1) Frequency of Occurrence

In order to understand the effect of weather on system performance, it is instructive to observe how the system responds to that forcing function. In this study, "bin plots" are created to relate the frequency of occurrence of system parameters (e.g., wet-bulb temperature and head pressure) throughout the year and during each mode of operation to system performance.

The "wet-bulb temperature bin plots" are created for the wet-bulb temperature study using the TMY weather data; these data are independent of system type and operating conditions. A common wet-bulb temperature range is defined using the lowest and the highest values of wet-bulb temperatures that occur within the four locations that were studied (between -20°F to 82°F). This range is divided into 12 bins, where each has a 10°F range that is centered at a value divisible by 10. The first bin, which is centered at -20°F, accounts for any wet-bulb temperature that falls below -15°F. Note that not every location will have occurrences in every bin as the actual range of wet-bulb temperatures at each location is different. Figures 4-19 through 4-22 are the wet-bulb temperature bin plots showing the number of hours that each wet-bulb temperature bin occurs throughout the year for each mode of operation at each location. Notice that the operating period must be taken into account when considering the head pressure occurrence because only a fraction of 8,760 hours, and the corresponding outdoor weather during those hours, contribute to the annual energy usage of the systems.

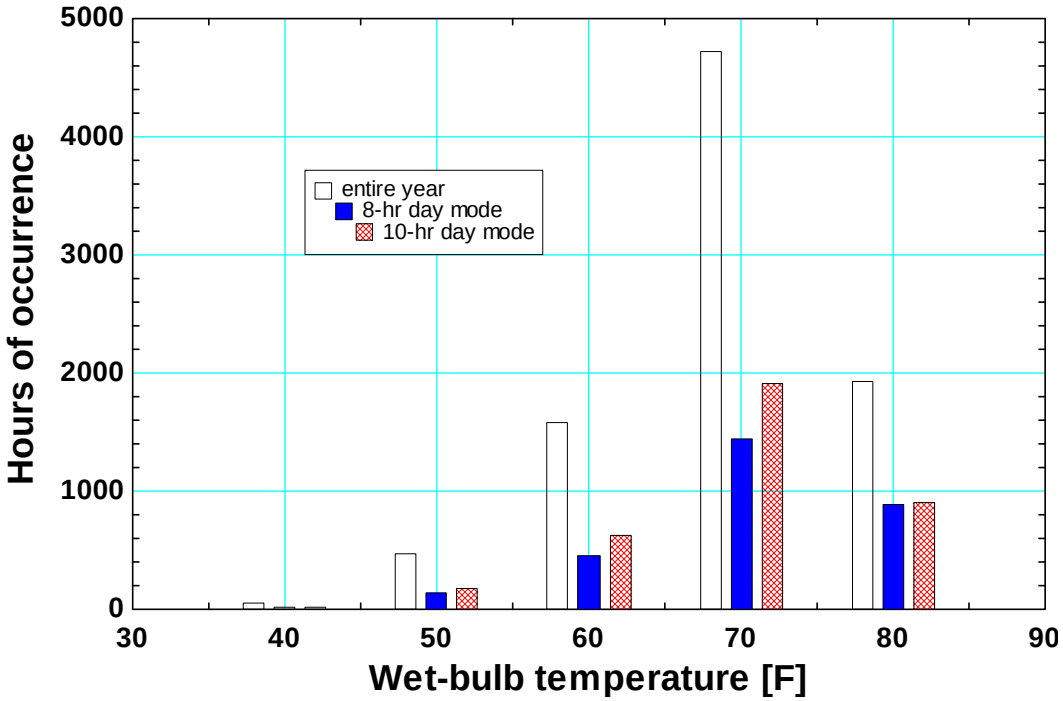

Figure 4-19: Wet-bulb temperature bin plot for Miami, FL.

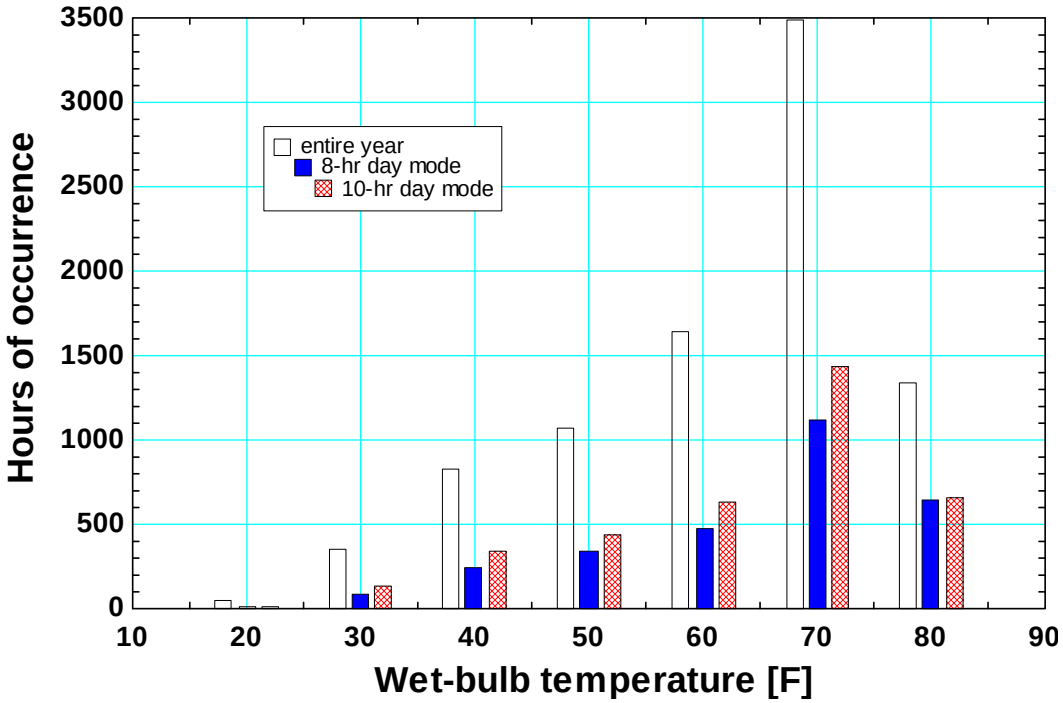

Figure 4-20: Wet-bulb temperature bin plot for Houston, TX.

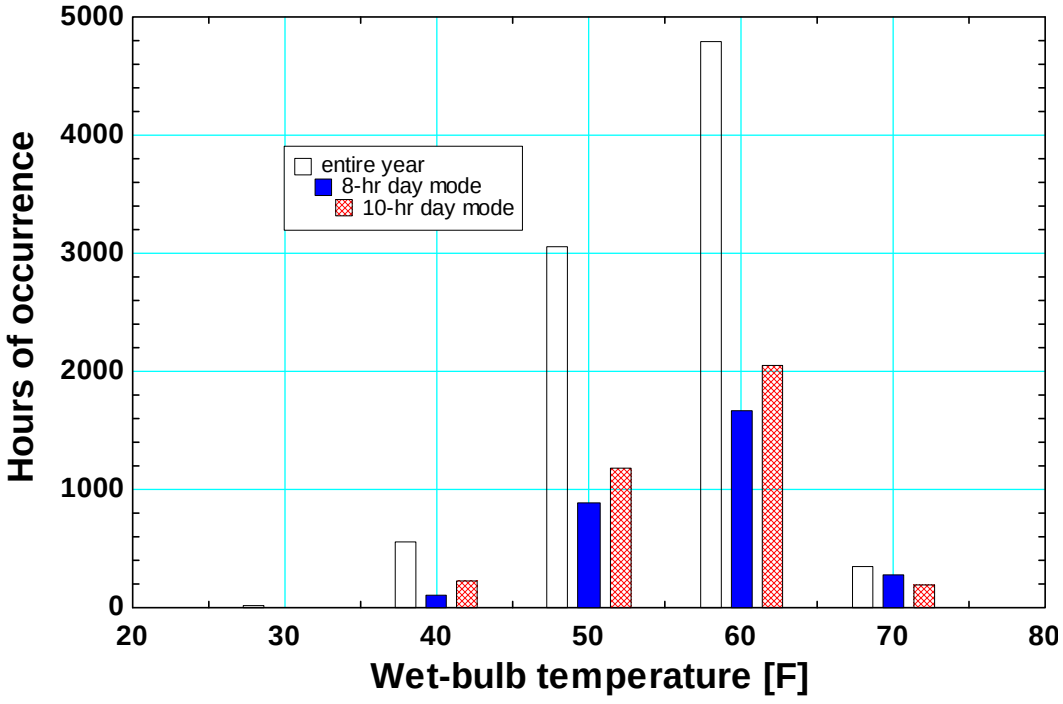

Figure 4-21: Wet-bulb temperature bin plot for Los Angeles, CA.

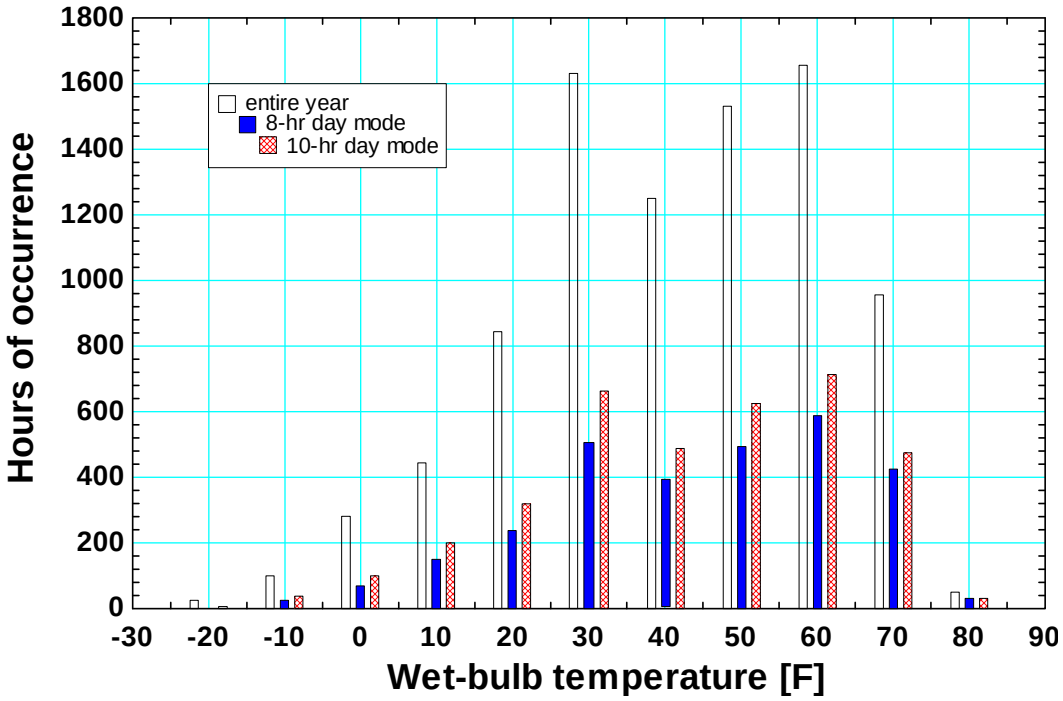

Figure 4-22: Wet-bulb temperature bin plot for Madison, WI.

Figure 4-22 shows that Madison has the widest wet-bulb temperature range and has a high frequency of low wet-bulb temperatures (below the freezing point of water), which would cause system head pressure to float below the minimum head pressure limit (135 psia) if it were unconstrained. This implies that Madison will also have a high frequency of head pressure at the minimum head pressure limit. For the purpose of this study, a frequency-weighted wet-bulb temperature is calculated for each location. A frequency-weighted wet-bulb temperature ($\overline{T}_{wb}$) is calculated according to,

$$\overline{T}_{wb} = \frac{\sum_{i=1}^{12} T_{wb_i} N_{occur_i}}{\sum_{i=1}^{12} N_{occur_i}} \tag{4-7}$$

where T_{wb_i} and N_{occur_i} are the wet-bulb temperature value and the frequency of occurrence in each bin. Table 4-3 shows the values of the frequency-weighted average wet-bulb temperature for each geographical location for each mode of operation.

Table 4-3: Frequency-weighted average wet-bulb temperature at each geographical location

Location	*8-hr day mode*	*10-hr day mode*	*Yearly Average*
Miami, FL.	70.37^{o}F	69.58^{o}F	69.17^{o}F
Houston, TX.	64.3^{o}F	63.21^{o}F	62.51^{o}F
Los Angeles, CA.	57.18^{o}F	56.02^{o}F	55.85^{o}F
Madison, WI.	44.08^{o}F	42.92^{o}F	41.63^{o}F

The results listed in Table 4-3 closely resemble the yearly average values shown previously in Table 4-2; therefore, there is a substantial difference in the average wet-bulb temperature associated with Los Angeles and Madison, as mentioned earlier. However, Figure 4-10 showed that the difference in energy usage between these two locations was not very large. The reason for this seeming discrepancy is related to the head pressure occurrence and its effect on the system performance; this is studied using a set of head pressure bin plots.

Similar to the wet-bulb temperature bin plots, the common head pressure range shared by all of the locations (135-200 psia) is divided into 14 bins, where 13 bins each has a 5-psia range centered at a value divisible by 5 (from 140-200 psia). The first bin is for the minimum head pressure (135 psia) and any head pressure less than or equal to 137.5 psia. The head pressure bin plots are created from the cascade system model for a full-year simulation at an evaporating temperature of -40^{o}F. The head pressure does vary with evaporating temperature and is slightly different for the two system configurations; however, the frequency of occurrence is dictated primarily by the weather at each location and these secondary effects are consistent for all of the systems. Thus, a study of bin plots for one system is sufficient to understand the effect of location on head pressure. Figures 4-23 through 4-26 show the head pressure bin plots which illustrate the number of hours of operation within each head pressure bin throughout the year for each mode of operation at each location.

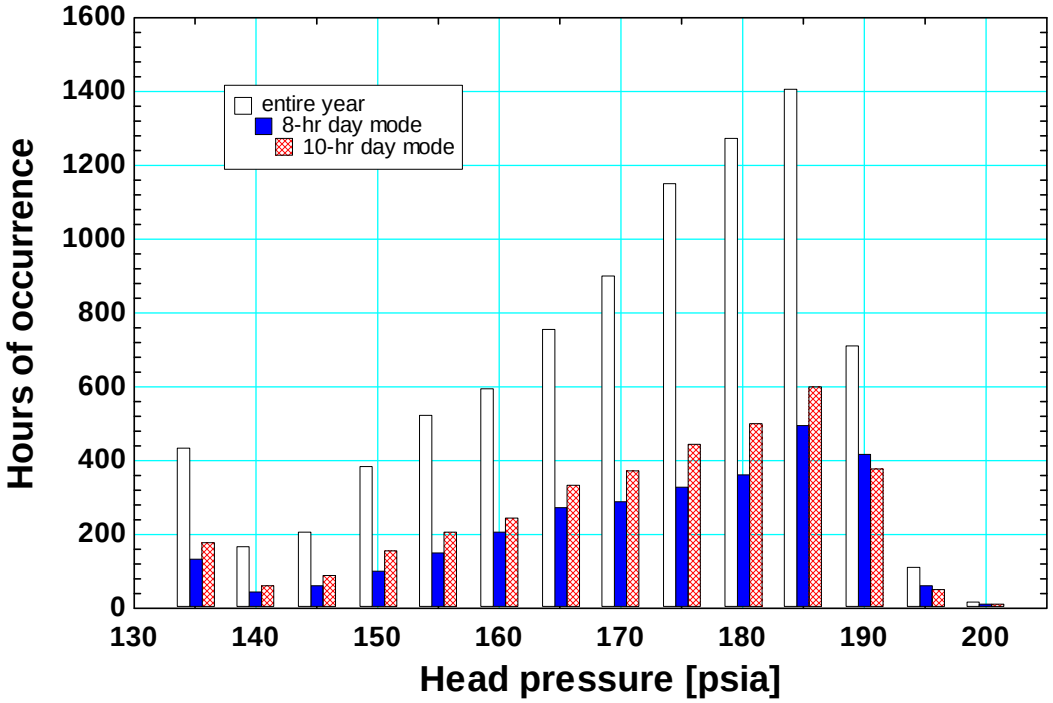

Figure 4-23: Head pressure bin plot for Miami, FL.

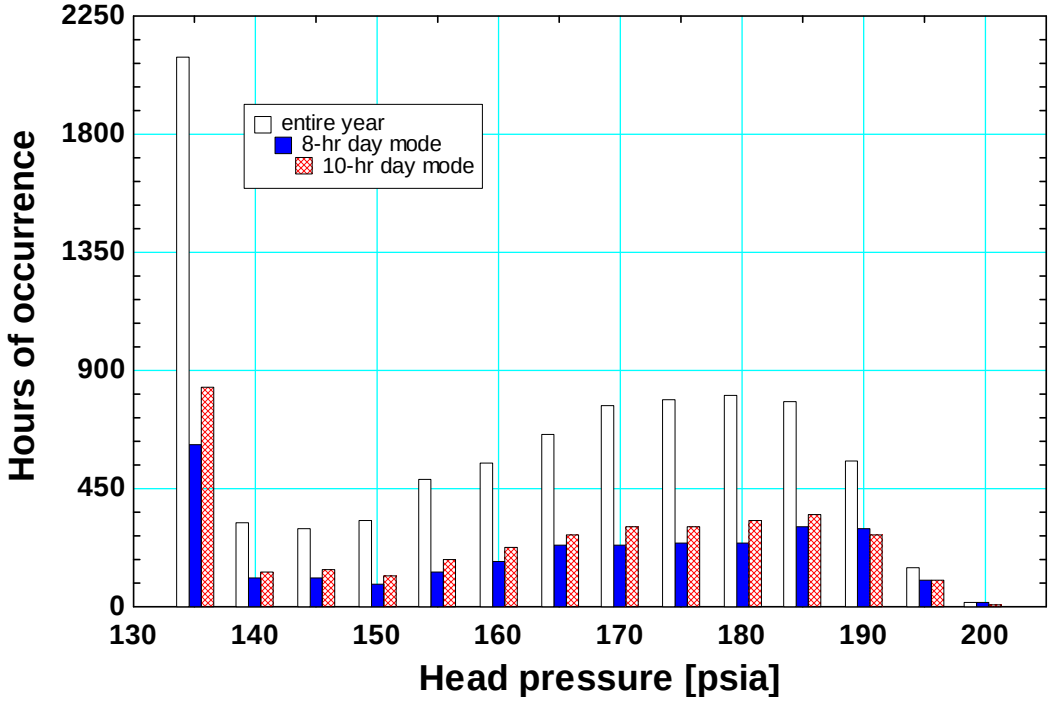

Figure 4-24: Head pressure bin plot for Houston, TX.

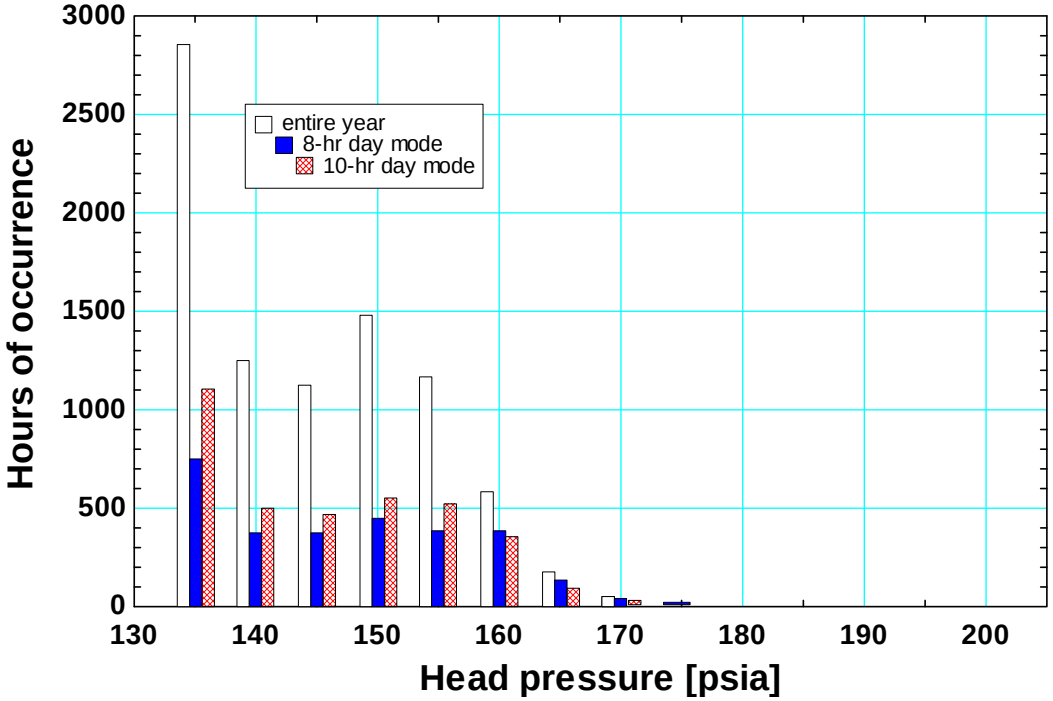

Figure 4-25: Head pressure bin plot for Los Angeles, CA.

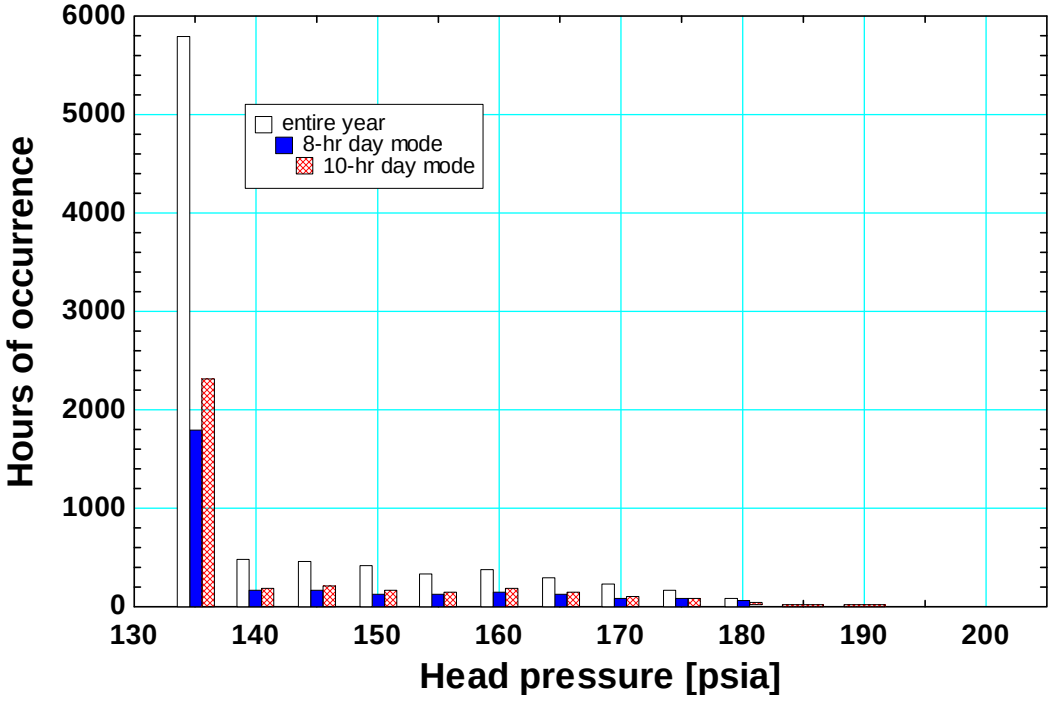

Figure 4-26: Head pressure bin plot for Madison, WI.

Figure 4-26 shows that Madison has the highest frequency of head pressure occurrence in the 135-psia bin, which is consistent with the wet-bulb temperature study. This high frequency of head pressure occurrences indicates that the system head pressure limit has a significant effect on the system operation in a climate like Madison where the average wet-bulb temperature is low.

It is useful to quantify a frequency-weighted average head pressure for a system operating at each location in order to better explain the annual energy usage results shown earlier. A frequency-weighted head pressure ($\overline{P}_{head}$) is calculated according to,

$$\overline{P}_{head} = \frac{\sum_{i=1}^{14} P_{head_i} N_{occur_i}}{\sum_{i=1}^{14} N_{occur_i}} \tag{4-8}$$

where P_{head_i} and N_{occur_i} are the head pressure value and the frequency of occurrence in each bin. Table 4-4 shows the values of the frequency-weighted average head pressure for each geographical location based on the head pressure bin results.

Table 4-4: Frequency-weighted average head pressure at each geographical location for a cascade system operating at -40^{o}F

Location	***8-hr day mode***	***10-hr day mode***
Miami, FL.	172.8 psia	171.5 psia
Houston, TX.	164.1 psia	162.5 psia
Los Angeles, CA.	147.3 psia	145.7 psia
Madison, WI.	143.7 psia	142.8 psia

The results from Table 4-4 clearly illustrate that despite a large difference in average wet-bulb temperatures between Los Angeles and Madison (from Tables 4-2 and 4-3), their frequency-weighted average head pressures are relatively close. Figure 4-27 is generated to show a yearly head pressure profile as a function wet-bulb temperature overlaid with average wet-bulb temperature and average head pressure for a cascade system operating at each geographical location.

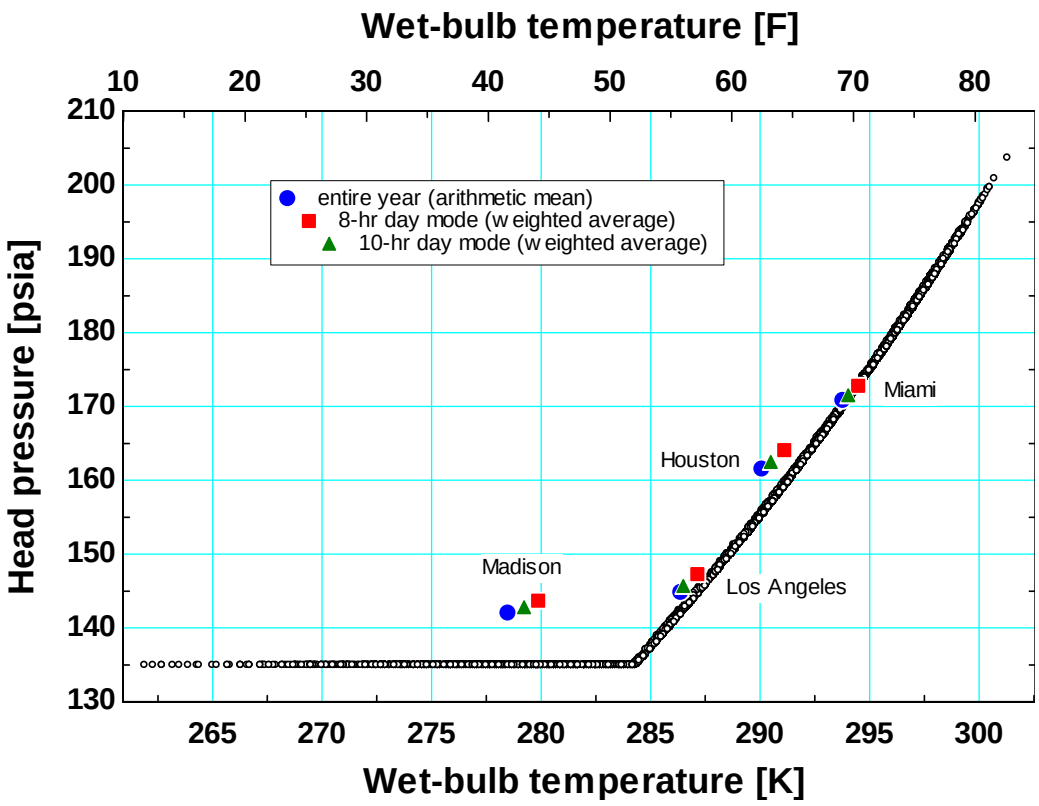

Figure 4-27: Average head pressure as a function of an average wet-bulb temperature for a cascade system operating at each location

In Madison, the minimum head pressure limit of the system causes the annual average operating head pressure to be higher than what it could be if the minimum head pressure limit were lowered. Therefore, this study justifies the similarity in the annual energy usage results of these two cities as shown earlier. For other locations where the majority of the wet-bulb temperature and head pressure is high (e.g. Miami and Houston), the average head pressure corresponds well with the average wet-bulb temperature because there is no influence from the minimum head pressure limit.

4.3) Operating Cost Savings

Using the P_1, P_2 method, system performance can be compared based on life-cycle cost. In this section, both system models are implemented with the optimization methods described in section 4.2.2. As mentioned earlier, the hardware required by each system differs dramatically due to many factors. For instance, at low evaporating temperatures the high specific volume of the ammonia vapor dictates that the vapor pipes would be very large for a compound system operating at low evaporating temperature. Carbon dioxide vapor lines can be much smaller but require the capability of holding a higher refrigerant pressure; therefore, they are possibly less expensive compared with ammonia vapor lines. In general, the aggregate cost of the piping material and associated insulation together with installation will be highly variable based on the site conditions but it can be as much or more as the cost of installing a large piece of equipment, e.g. a compressor or heat exchanger. Since each system configuration consists of different types of equipment (e.g., a cascade heat exchanger in the cascade system and an intercooler in the compound system) it is difficult to obtain accurate first cost information. Therefore, it is difficult to estimate the life-cycle cost of each system with high accuracy.

However, the operating cost of each system is determined explicitly from the 12-month simulation together with a limited set of economic parameters related to the present worth of the future cost of energy. Therefore, for the purpose of an unambiguous comparison it is possible to use these operating costs in order to calculate the difference in the first costs (i.e., the premium difference) that will cause the two systems to have an equal life-cycle cost. That is, the *premium difference* can be viewed as the extra first cost that could be tolerated for the system that is more efficient (i.e., the one with a lower operating cost) in order to obtain the same life cycle cost as the less efficient system. The premium difference (ΔFC) is determined by applying the life-cycle cost equation, Eq.(4-1), to each system and setting them equal. Thus, the operating cost savings equation becomes,

$$\Delta FC = \frac{P_1}{P_2}\left(OC_{cascade} - OC_{compound}\right) \tag{4-9}$$

where $OC_{cascade}$ and $OC_{compound}$ are first-year operating cost of the cascade and the compound systems, respectively. In Eq. (4-9), ΔFC is defined as the additional first cost that you would be willing to pay for the compound system in order to make its life cycle cost equivalent to that of the cascade system. Therefore, a positive value of ΔFC indicates that the compound system is more efficient and you would therefore be willing to tolerate a higher capital investment. A negative value of ΔFC indicates that the compound system is less efficient and must cost less initially in order to be economically attractive compared to the cascade system. The advantage of computing the premium is that the details of the hardware associated with implementing the system do not affect this result; only the relative difference in the efficiency of the cycles matters and this can be predicted with some accuracy using the detailed system models.

To determine the first-year operating cost, the cost of electricity is assumed to be \$0.06/kWh; this is an average as of 2006 for the US industrial sectors (http://www.eia.doe.gov/). Subsequent analysis will evaluate the effect of this parameter on the life-cycle cost comparison. For an

initial economic comparison, nominal values of the economic parameters are specified in Table 4-5. Note, from Eq. (4-4), that since N, N_L and N_D are all equal, N_1 and N_2 are both equal to N.

Using the initial values of the economic parameters, listed in Table 4-5, along with the simulation results from the previous section, the economic comparison between the cascade system and the compound system is conducted. Figure 4-28 through 4-31 present the premium difference at each location as a function of evaporating temperature using each of the optimization method for each mode of operation.

Table 4-5: Nominal values of economic parameters used in P_1, P_2 method for economic comparison

Affected multiplier	***Economic parameter***	***Value***
P_1	Fuel inflation rate (i_f)	5.5 %
P_2	Down payment fraction (DP)	20 %
	General interest rate (i)	2.5 %
	Mortgage interest rate (m)	7.5 %
	Term of loan (N_L)	20 years
	Depreciation lifetime (N_D)	20 years
	Property tax (p)	3.5 %
	Salvage value fraction (S)	20 %
	Maintenance cost fraction (MT)	5 %
P_1 and P_2	Discount rate (d)	5.25 %
	Period of analysis (N)	20 years
	Effective tax rate (t)	40%

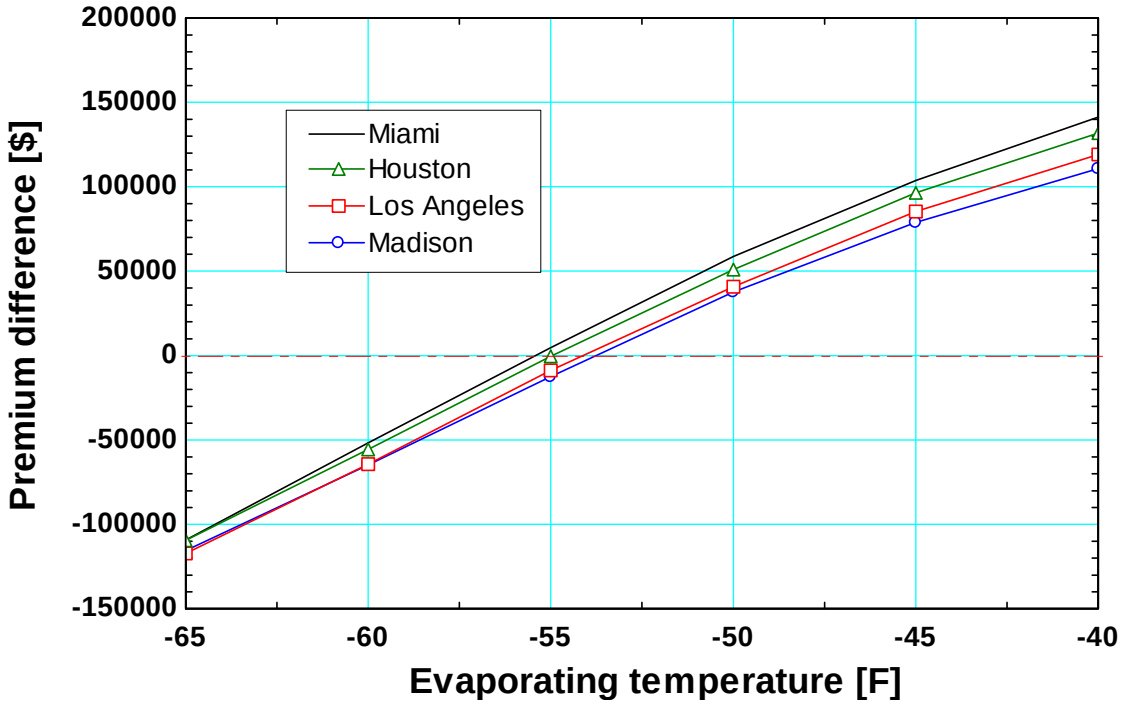

Figure 4-28: Premium difference between cascade system and compound system (simplified optimization method) at various geographical locations for an 8-hour day mode

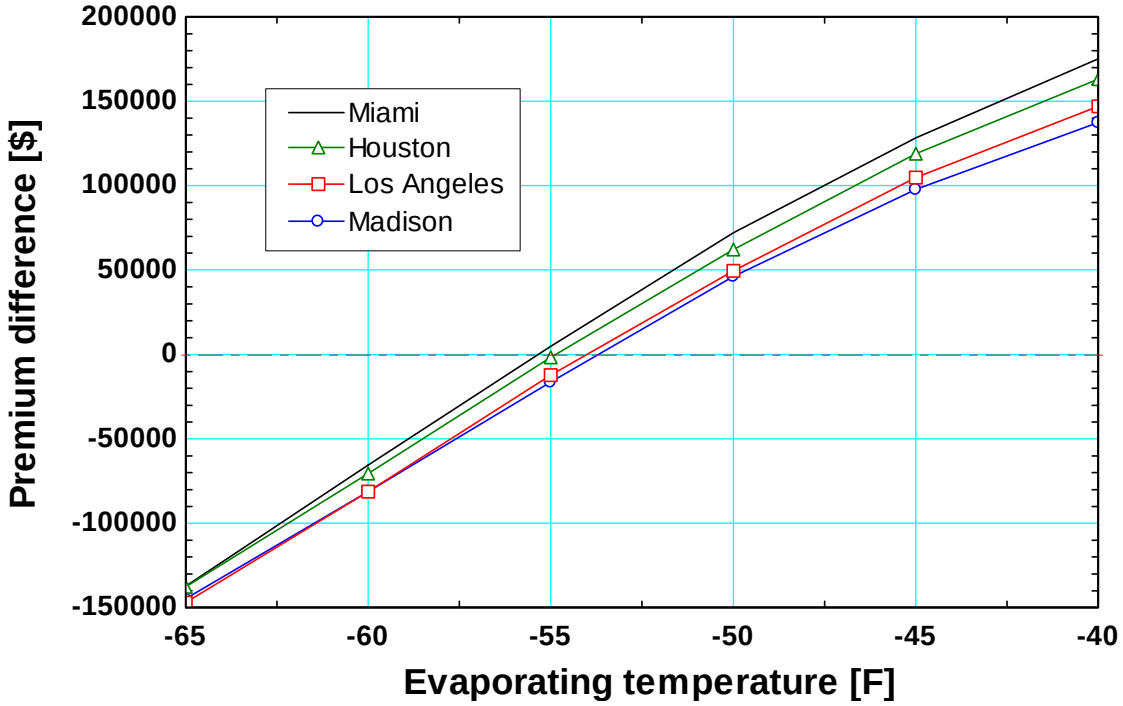

Figure 4-29: Premium difference between cascade system and compound system (simplified optimization method) at various geographical locations for a 10-hour day mode

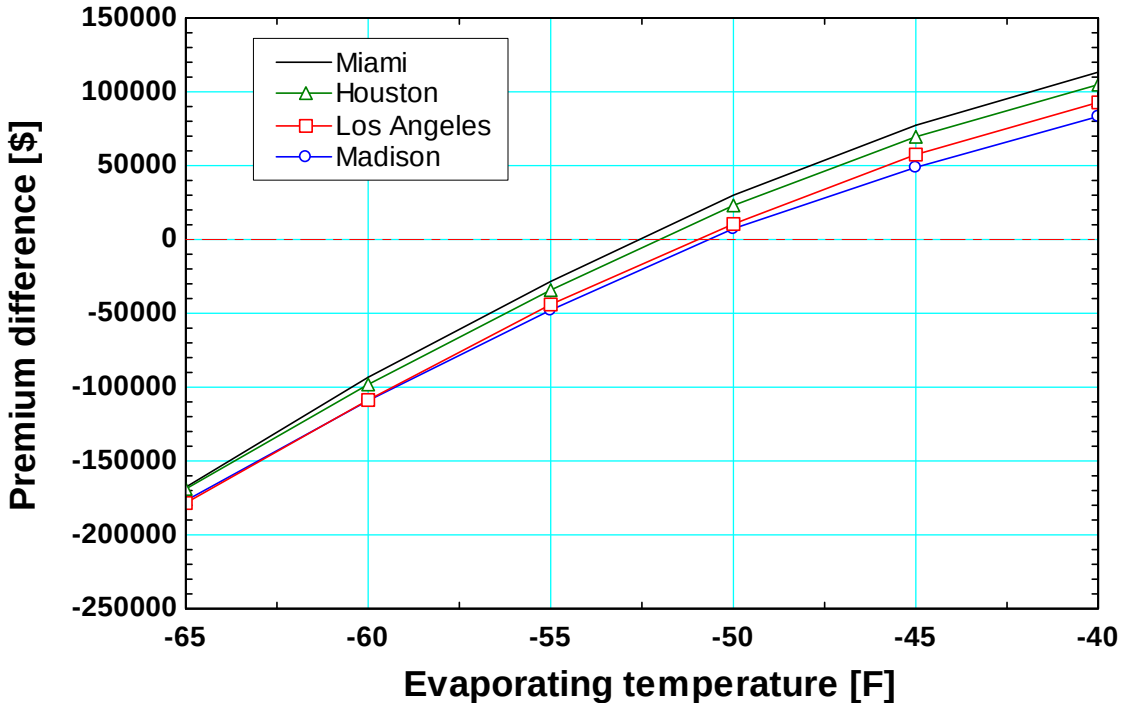

Figure 4-30: Premium difference between cascade system and compound system (root-product method) at various geographical locations for an 8-hour day mode

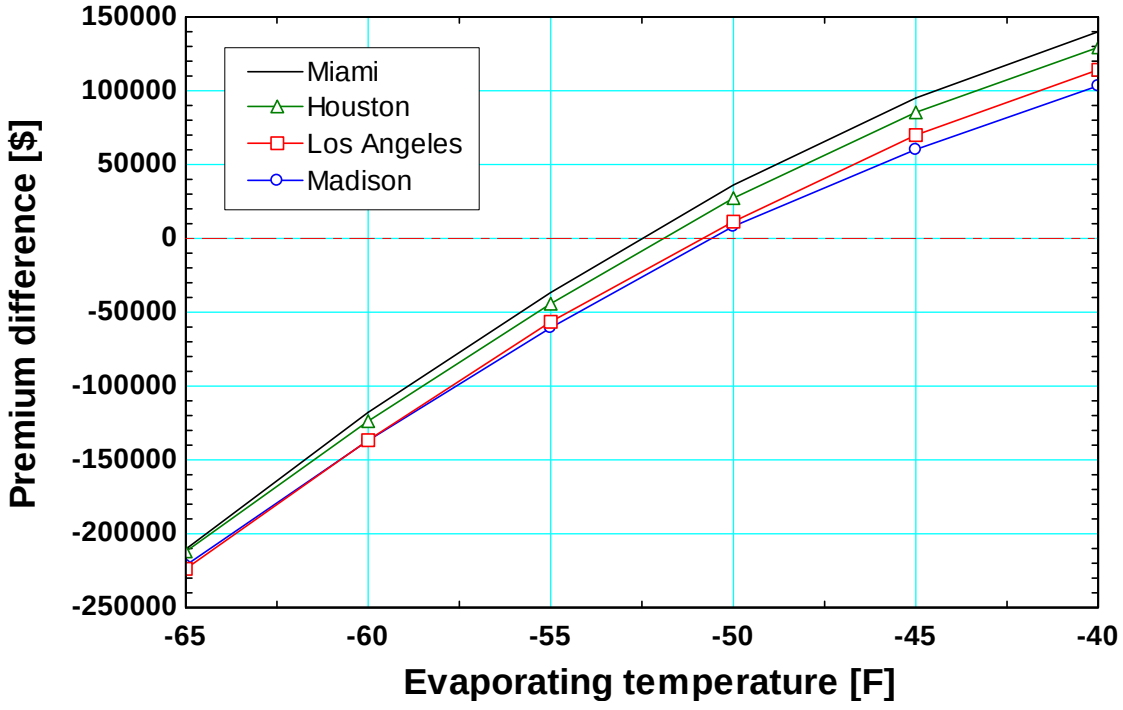

Figure 4-31: Premium difference between cascade system and compound system (root-product method) at various geographical locations for a 10-hour day mode

The premium difference is consistent with the difference in system efficiency of the two system configurations. As discussed in Section 4.3, a system with higher efficiency has a larger operating cost savings at the end of its lifetime. At the break-even temperature, both systems perform equally well so the premium difference is zero. In Figure 4-28, the cascade system performs better than the compound system at low temperatures (below the break-even temperature), as indicated by increasing premium difference (note that the negative sign denotes a benefit towards the cascade system). On the contrary, the ammonia compound system is more efficient at any temperature above the break-even temperature. The general trend is similar at each geographical location, but the magnitude of the premium difference varies. This is attributed to the effect of the head pressure on the system performance at each location. There are other operating parameters that also affect system performance. Similarly, each of the economic parameters used in the P_1, P_2 method has some influence on the magnitude of the premium difference. Therefore, it is instructive to evaluate the sensitivity of the premium difference with respect to each of the aforementioned parameters; this sensitivity study is accomplished in Section 4.4. It is also important to gain some perspective on the relative importance of the operating cost savings over a system lifetime; that is, how much influence the premium difference has on the selection of a system as compared to other practical considerations. This is addressed in the subsequent section.

4.3.1) Significance of Premium Difference

The premium difference associated with the selection of one system configuration over the other is on the order of hundreds of thousands of dollars depending on operating conditions and economic factors. In order to evaluate the significance of this difference in first cost it is necessary to place it in context by normalized it against the total operating cost incurred over the system lifetime (OC_{LC}). The result is referred to as the premium difference fraction (PDF) and is defined as the ratio of the premium difference to the total operating cost,

$$PDF = \frac{\Delta FC}{OC_{LC}} \tag{4-10}$$

where OC_{LC} is the first term in the P_1, P_2 method,

$$OC_{LC} = P_1 OC \tag{4-11}$$

Figures 4-32 and 4-33 show the plots of the premium difference fraction of the two systems using each optimization method and show that the operating cost savings represents a relatively small fraction of the life-cycle operating cost. However, the magnitude of the premium difference is approximately equivalent to one year of operating cost.

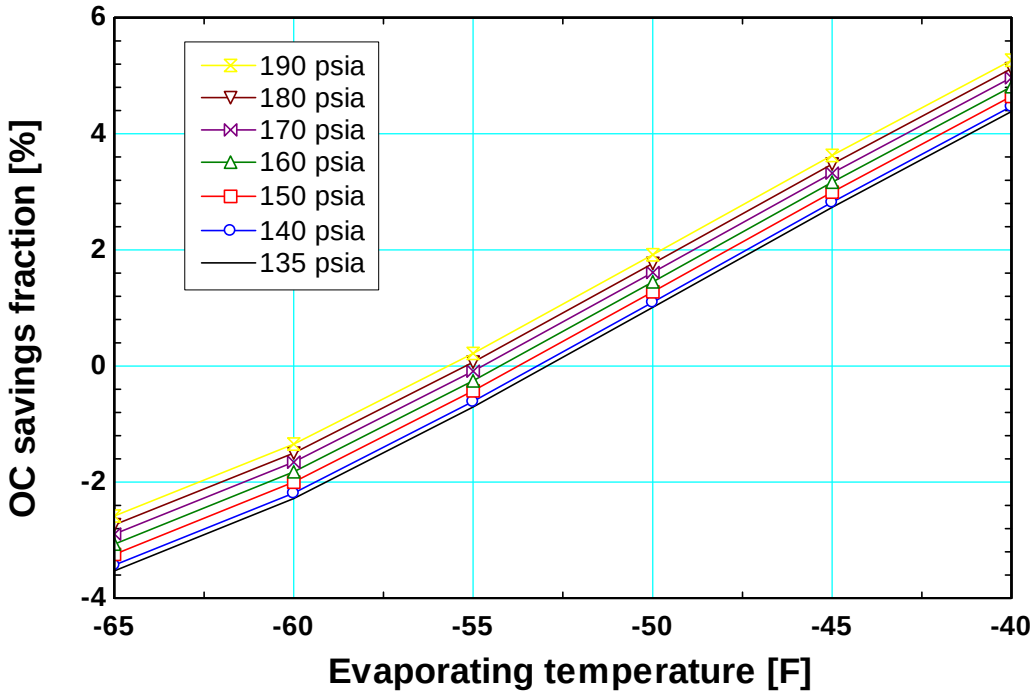

Figure 4-32: Premium difference fraction between cascade system and compound system (simplified method) at various head pressure for nominal economic parameter values

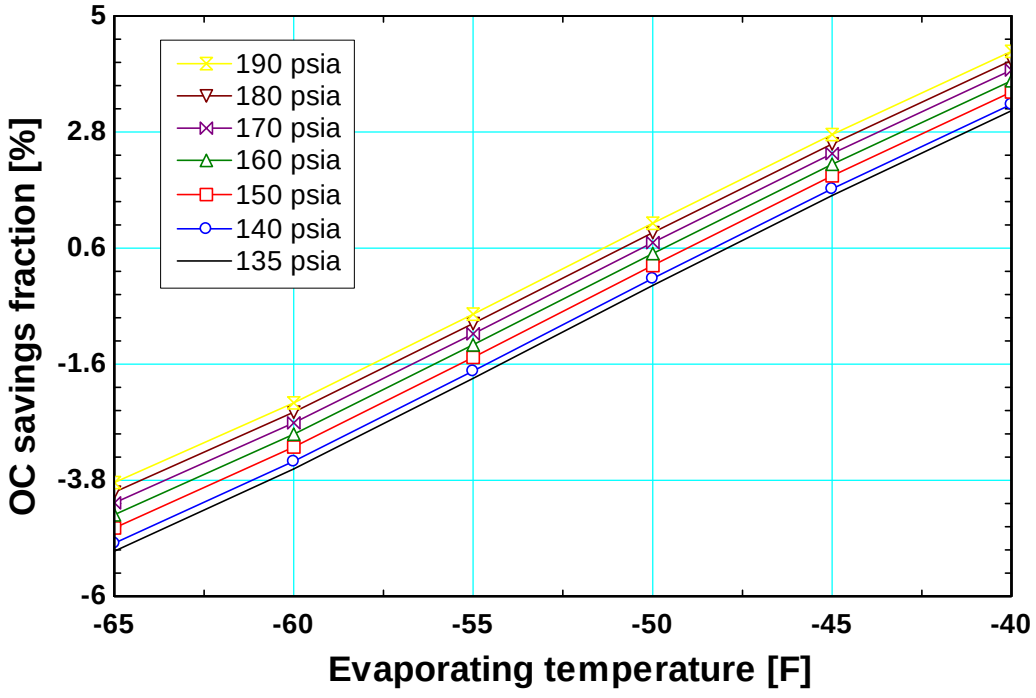

Figure 4-33: Premium difference fraction between cascade system and compound system (root-product method) at various head pressure for nominal economic parameter values

4.4) Sensitivity Analysis

There are many economic and operating parameters that influence the premium difference. A variation in each of these parameters will affect the life-cycle savings. In order to evaluate the effect that each factor contributes to ΔFC more clearly, the sensitivity analysis is conducted in this section.

4.4.1) Effects of Head Pressure

Geographical location primarily affects the heat rejection condition and therefore the head pressure. Head pressure is strongly dependent on the outside air wet-bulb temperature. Therefore, it is instructive to study the effect that the head pressure, by itself, has on life-cycle cost comparison. The results of this study allow the interpretation of the results associated with each region.

The 12-month simulation is carried out at a fixed head pressure. The following assumptions are made for this analysis.

- Head pressure is set to a specific value for an entire year
- Head pressure range is from 135 to 200 psia with 10 psia increment (for 140 psia and above)
- Cascade heat exchanger pinch-point temperature is 10^{o}F

The simulation follows the same baseline of operation summarized in Table 4-1 with the exception that the TMY weather data is not required since the head pressure value is specified. This study also uses the nominal values for the economic parameters listed in Table 4-5. As discussed in Section 4.2.2.2 that the root-product technique does not return a truly optimized result for the compound system, thus this study is only carried out using the simplified optimization.

Figures 4-34 and 4-35 illustrate the ΔFC between the cascade system and the compound system as a function of evaporating temperature for various values of head pressure using the simplified optimization method.

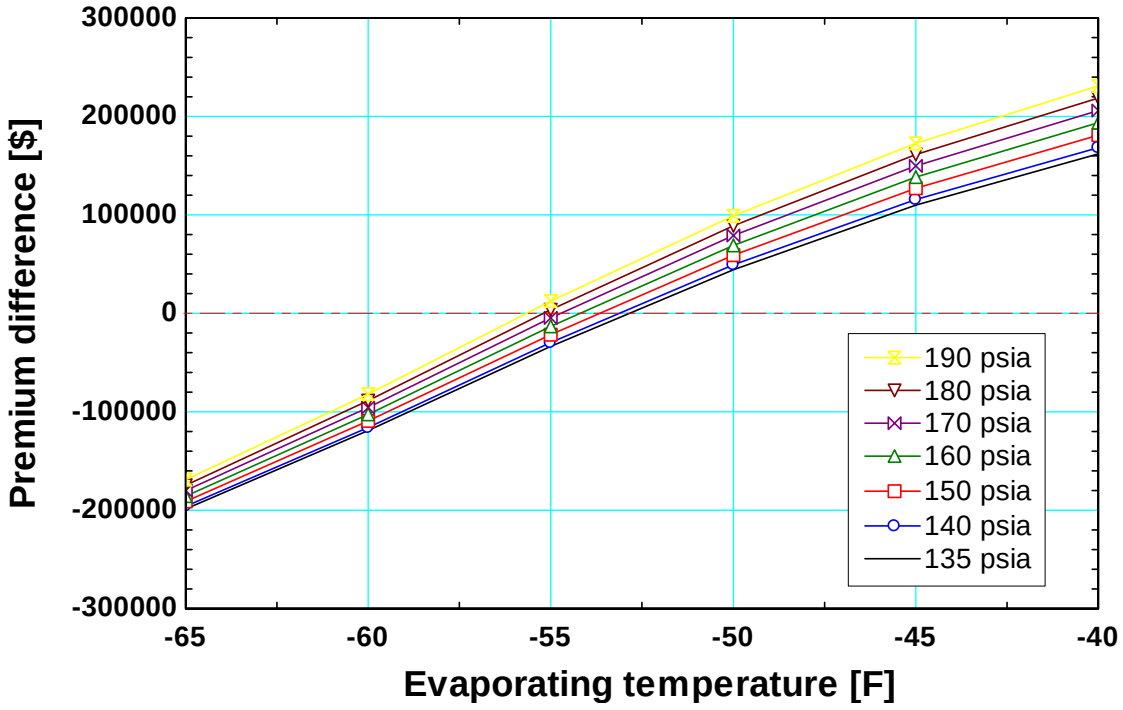

Figure 4-34: Premium difference between cascade system and compound system (simplified optimization method) at various head pressures for an 8-hour day mode

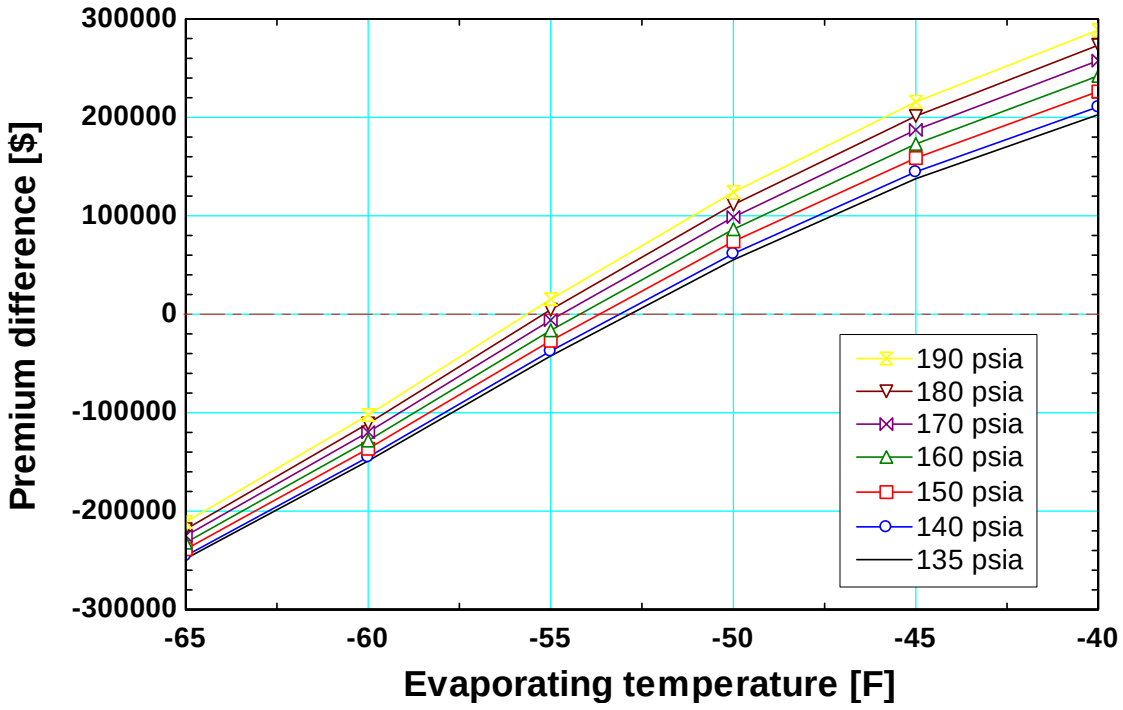

Figure 4-35: Premium difference between cascade system and compound system (simplified optimization method) at various head pressures for a 10-hour day mode

Figures 4-34 and 4-35 show that the head pressure variation has a relatively small effect on the premium difference, certainly the effect is much less than the evaporating temperature over the range that was considered. For every 10 psia change in the condensing pressure, the operating cost savings (ΔFC) changes by at most $20,000. The variation in geographical location does affect the head pressure which, in turn, affects the efficiency. However, the analysis in this section shows that the impact of head pressure on system efficiency is nominally the same for both configurations and therefore the value of ΔFC, which reflects the difference between operating costs, is not affected substantially. The premium difference is strongly dependent on evaporating temperatures; for every five degrees change in evaporating temperature, ΔFC varies by as much as $100,000. This result suggests that changing the evaporating temperature has a larger negative effect on the cascade system than it does on the ammonia system.

4.4.2) Effects of Economic Parameters

Since it is often difficult to accurately define the values of the economic parameters, this study is dedicated to evaluating the impact of each economic parameter on the premium difference. The economic analysis was performed by specifying a set of nominal fiscal parameters, which are used in the P_1, P_2 Method. Since they each affect the life-cycle cost differently, it is important to estimate the degree to which each of these parameters contribute to the life-cycle cost comparison. In this study, each economic parameter is assumed to have an uncertainty of 20%; the resulting change in the premium difference caused by the uncertainty in the economic parameter is presented as a percentage of the nominal premium difference. Table 4-6 summarizes the uncertainty in the premium difference as a result of varying the individual economic parameters from their nominal values (listed in Table 4-5).

The results from Table 4-6 show that the economic parameters that have the largest impact on the premium difference include the fuel inflation rate (i_f), maintenance cost fraction (MT), period of analysis (N) and cost of electricity (EC). The cost of electricity is the single most important economic parameter because the operating cost of a system is directly proportional to the fuel cost. The maintenance cost fraction (MT) is also a major factor. The value of the maintenance cost was based only on a rough estimate—this could cause a large discrepancy in the premium difference study. The maintenance cost fraction is bounded in order to establish an envelope on the results. The minimum value specified is zero, which serves as a lower bound, implying that this term is neglected completely from the economic analysis. On the other hand, an upper bound is set to 10% of the initial investment. Figure 4-36 illustrates the range of premium difference variation between these two limits. In any case, the maintenance cost fraction is still assumed to be 5% throughout the economic analysis.

Another operating parameter that has a large influence on cascade system efficiency is the cascade heat exchanger pinch-point temperature. This parameter affects both the sizing and capital cost of the cascade heat exchanger. Thus, the sensitivity analysis continues with a study of the effect of the pinch-point temperature on the premium difference.

Table 4-6: Effect of economic variables on premium difference

Economic parameter	*Value ± 20%*	δP_1	δP_2	$\delta \Delta FC$
Fuel inflation rate (i_f)	0.055 ± 0.011	12.34%	0%	14.82%
Down payment fraction (DP)	0.2 ± 0.04	0%	0%	0%
General interest rate (i)	0.025 ± 0.005	0%	4.71%	4.15%
Mortgage interest rate (m)	0.075 ± 0.015	0%	2.48%	2.18%
Term of loan (N_L)	20 ± 4	0%	2.54%	2.24%
Depreciation lifetime (N_D)	20 ± 4	0%	0.79%	0.7%
Property tax (p)	0.035 ± 0.007	0%	3.97%	3.5%
Salvage value fraction (S)	0.2 ± 0.04	0%	0.05%	0.04%
Maintenance cost fraction (MT)	0.05 ± 0.01	0%	8.10%	7.14%
Discount rate (d)	0.0525 ± 0.0105	13.78%	12.48%	0.57%
Period of analysis (N)	20 ± 4	51.88%	35.72%	5.21%
Effective tax rate (t)	0.4 ± 0.08	21.99%	29.15%	0.01%
Fuel (electricity) cost (EC)	0.06 ± 0.012	0%	0%	59.44%

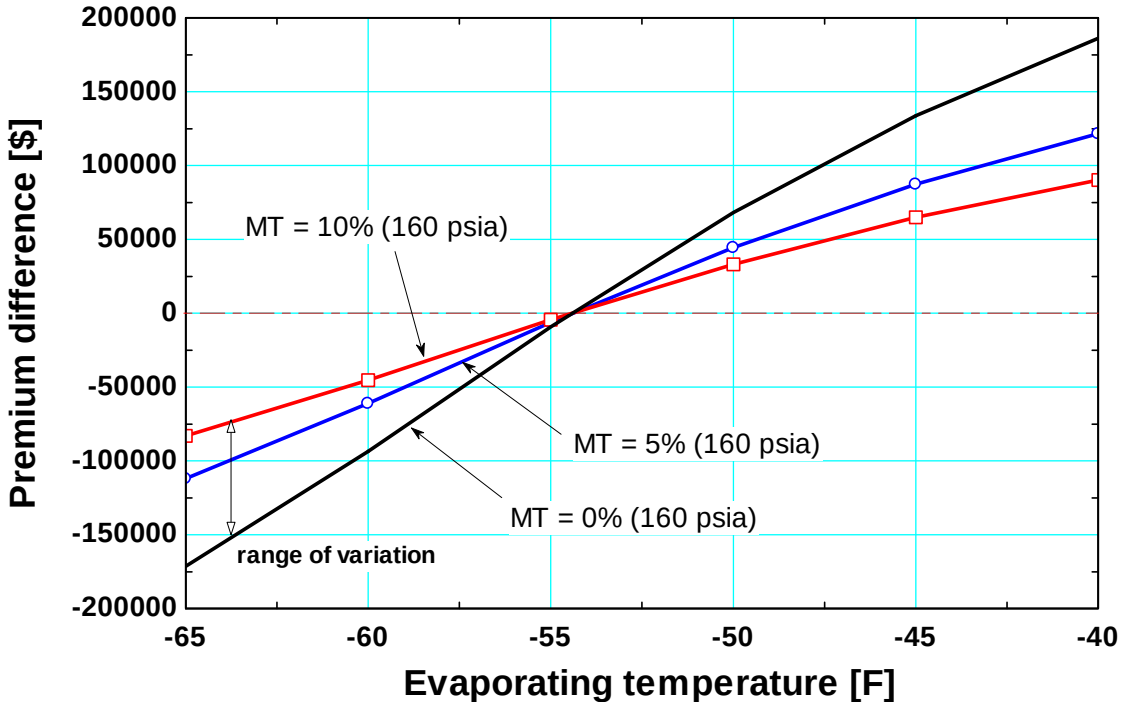

Figure 4-36: Envelope of error in the premium difference from maintenance cost fraction range of 10%

4.4.3) Effects of Cascade Heat Exchanger Pinch-Point Temperature Difference

One of the important factors associated with the cascade heat exchanger (CHE) is the pinch-point temperature ($\Delta T_{cascade}$). As discussed in Section 3.2.5, the pinch-point temperature has a significant influence on cascade heat exchanger performance, size and geometry. $\Delta T_{cascade}$ affects both aspects of the economic analysis because the life-cycle cost of the cascade system depends on both the size and the performance of the CHE. Thus, it is important to investigate the effect that $\Delta T_{cascade}$ has on the life-cycle cost of the cascade system in order to establish a basis for optimizing the size of the CHE. With a smaller pinch-point temperature, the heat exchanger size increases in order to accommodate the reduced temperature difference driving the heat transfer. This adjustment enhances system performance but requires a larger capital cost due to the increased heat exchanger size. Since the cascade pinch-point temperature difference associated with this analysis is defined at the design operating condition of the cascade heat exchanger (listed in Table 3-3), it is also instructive to study the actual value of the pinch-point temperature difference during typical operating conditions. This study is carried out in Section 4.4.3.1.

The cascade pinch-point temperature difference is set to a nominal value of 10^{o}F at the design operating conditions (Table 3-3). In this parametric study, the CHE pinch-point temperature difference is also specified at 8^{o}F (a 20% reduction from its nominal value) and at 5^{o}F (50% reduction) in order to evaluate the effect of the pinch-point temperature difference on the premium difference. Since head pressure has minimal effect on the premium difference, this study is conducted at a system head pressure value of 160 psia. Figures 4-37 and 4-38 illustrate the premium difference between the two system configurations as a function of evaporating temperature for the three values of pinch point temperature difference and the two modes of operation, 8 hour and 10 hour days, respectively.

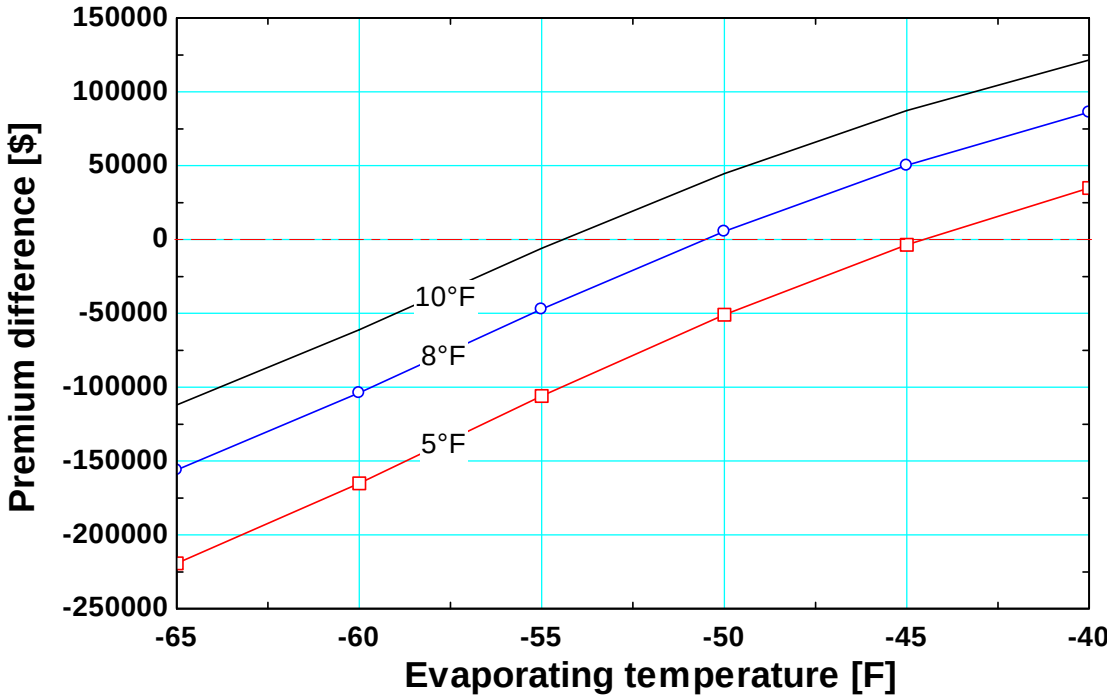

Figure 4-37: Premium difference between the cascade system and the compound system at various specified cascade pinch-point temperatures for an 8-hour day mode of operation

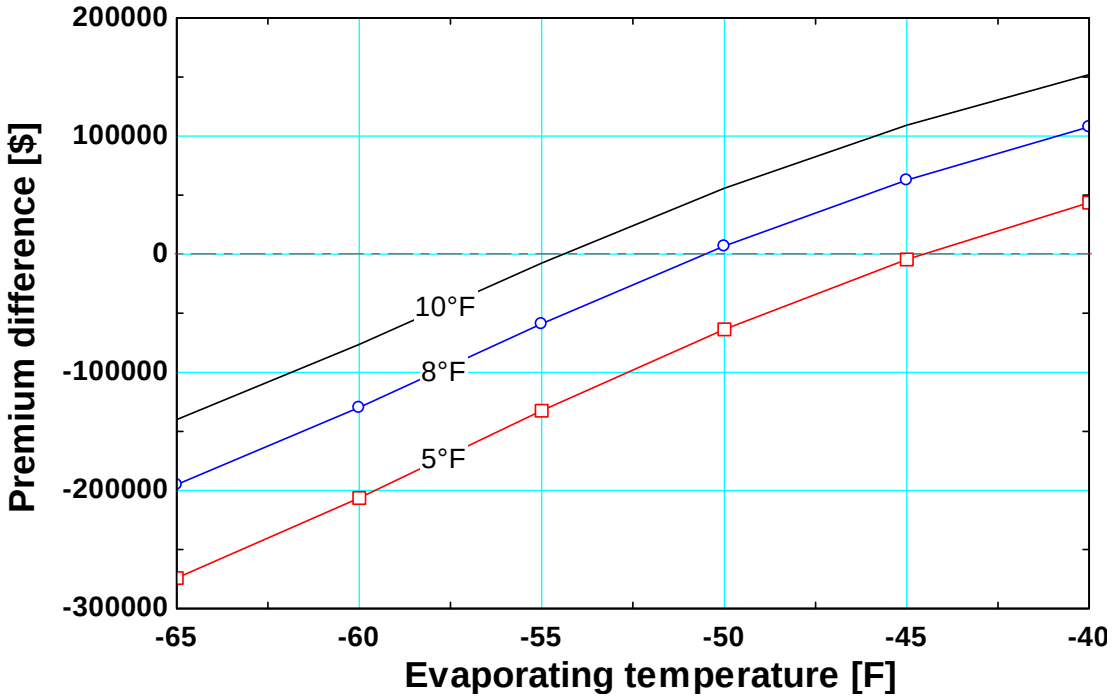

Figure 4-38: Premium difference between the cascade system and the compound system at various specified cascade pinch-point temperatures for a 10-hour day mode of operation

In Figure 4-37, the break-even temperature shifts towards higher temperatures by nearly 5^oF and 10^oF when the pinch-point temperature is reduced to 8^oF and 5^oF, respectively. Thus, the cascade system with a larger heat exchanger becomes more efficient than the compound system over a larger range of evaporating temperature. The magnitude of the premium difference also increases substantially with the pinch-point temperature reduction. The premium difference change is magnified for a 10-hour day mode of operation.

The premium difference (or the operating cost saving) associated with the cascade system increases with more efficient cascade heat exchanger when operating below the break-even temperature. With lower cascade pinch-point temperature difference, the cascade heat exchanger can accommodate higher heat transfer rate thus reducing the pressure lift across the high-stage compressors. The cascade heat exchanger cost is also affected by the pinch-point temperature difference and therefore it is necessary to evaluate the effect of this parameter on the capital cost of the cascade system. There are other component-related costs associated with the cycles that must also be addressed in this study. Section 4.5 describes the capital cost estimation.

4.4.3.1) Cascade Pinch-Point Temperature Difference at Off-Design Conditions

The design cascade pinch-point temperature difference dictates the conductance of the condensing section of the cascade heat exchanger. When the cascade system operates at off-design conditions, the pinch-point temperature difference will vary from its nominal value in response to achieve an energy balance for the device..

A study is conducted to investigate the significance of pinch-point temperature variation with operating conditions. The nominal pinch-point temperature difference (10^oF) and a value of 5^oF are both studied with varying head pressure and evaporating temperature. Table 4-7 summarizes the pinch-point temperatures associated with a cascade system operating at an evaporating temperature of -40^oF as a function of head pressure while Table 4-8 is using a head pressure of 160 psia with varying evaporating temperature values.

Table 4-7: Cascade pinch-point temperature of a cascade system operating at an evaporating temperature of -40^oF as a function of head pressure for the design pinch-point of 10^oF and 5^oF

P_{head} (psia)	$\Delta T_{cascade} = 10^oF$		$\Delta T_{cascade} = 5^oF$	
	$\Delta T_{cascade}$	$Q_{cascade}$ (kW)	$\Delta T_{cascade}$	$Q_{cascade}$ (kW)
135	10.05	2,946	4.984	2,893
140	10.06	2,953	4.988	2,899
150	10.08	2,967	4.997	2,912
160	10.1	2,980	5.006	2,925
170	10.12	2,994	5.015	2,938
180	10.14	3,008	5.024	2,951
190	10.15	3,021	5.032	2,963

Table 4-8: Cascade pinch-point temperature of a cascade system operating at a head pressure of 160 psia as a function of evaporating temperature for the design pinch-point of 10°F and 5°F

$T_{evap,sat}$ (F)	$\Delta T_{cascade} = 10^oF$		$\Delta T_{cascade} = 5^oF$	
	$\Delta T_{cascade}$	$Q_{cascade}$ (kW)	$\Delta T_{cascade}$	$Q_{cascade}$ (kW)
-40	10.1	2,980	5.006	2,925
-45	10.09	3,017	4.999	2,960
-50	10.1	3,060	4.996	3,000
-55	10.11	3,108	4.998	3,046
-60	10.13	3,160	5.004	3,096
-65	10.16	3,217	5.013	3,151

The results of this study show that the cascade pinch-point temperature difference varies only slightly from its design value when the head pressure and evaporating temperature are at off-design conditions. Therefore, result of cascade pinch-point temperature studies given at the design operating conditions is representative of most other typical operating conditions provided that the refrigeration load on the system remains unchanged.

4.5) Capital Cost Estimation

In order to evaluate the economic feasibility of each system, it is instructive to estimate the cost of the system components associated with each system. This study aims to investigate the difference in the capital cost associated with implementing the cascade and the compound cycles. This is accomplished by estimating the cost of the major system components that differ between the two cycles. The major hardware cost associated with a cascade system that is not present with the compound system is the cascade heat exchanger. The major hardware cost associated with the compound system that is not present with the cascade system is related to the very large compressors required to handle the high specific volume ammonia refrigerant at low temperature. By considering the capital cost difference between the two cycles as well as the operating cost difference it is possible to establish the true break-even temperature between the two cycles.

4.5.1) Cascade Heat Exchanger Cost

One of the higher capital cost components in the cascade system is the cascade heat exchanger itself. In the previous section, it was shown that system performance can be improved with a larger CHE which leads to a reduction in the operating cost. The cascade heat exchanger is an indirect-contact, shell-and-tube type heat exchanger. The material cost of a CHE ($cost_{CHE}$) consists of the cost of the outer shell ($cost_{shell,cas}$) and the cost of the tube bundle ($cost_{tube,cas}$). A predictive correlation was developed by Lachner (2004) for this type of heat exchanger based on information obtained from an industry survey. This correlation is used here in order to estimate the cost of the cascade heat exchanger. This correlation is,

$$cost_{shell,cas} = 22.20\left[\frac{\$}{ft^3}\right] A_{shell}\, L_{shell} \tag{4-12}$$

$$cost_{tube,cas} = 0.91\left[\frac{\$}{ft}\right] N_{tube,cas}\, L_{tube,pass} \tag{4-13}$$

$$cost_{CHE} = cost_{shell,cas} + cost_{tube,cas} \tag{4-14}$$

where, A_{shell}, L_{shell}, $N_{tube,cas}$ and $L_{tube,pass}$ are the outer shell cross-sectional area, the length of the outer shell, the total number of tubes (all passes) and the length of one tube bundle pass, respectively. Table 4-9 lists the cost of the cascade heat exchanger as a function of the pinch-point temperature. The corresponding cascade heat exchanger size and geometry are consistent the results shown in Section 3.2.5.

Table 4-9: Predicted cascade heat exchanger cost at various pinch-point temperatures

$\Delta T_{cascade}$	*Shell cost ($)*	*Tube cost ($)*	*CHE cost ($)*
10°F	14,080	95,728	109,808
9°F	17,410	119,737	137,148
8°F	22,106	153,868	175,974
7°F	29,029	204,623	233,652
6°F	39,842	284,634	324,476
5°F	58,100	421,038	479,138

The cost prediction results in Table 4-9 are also plotted in Figure 4-39.

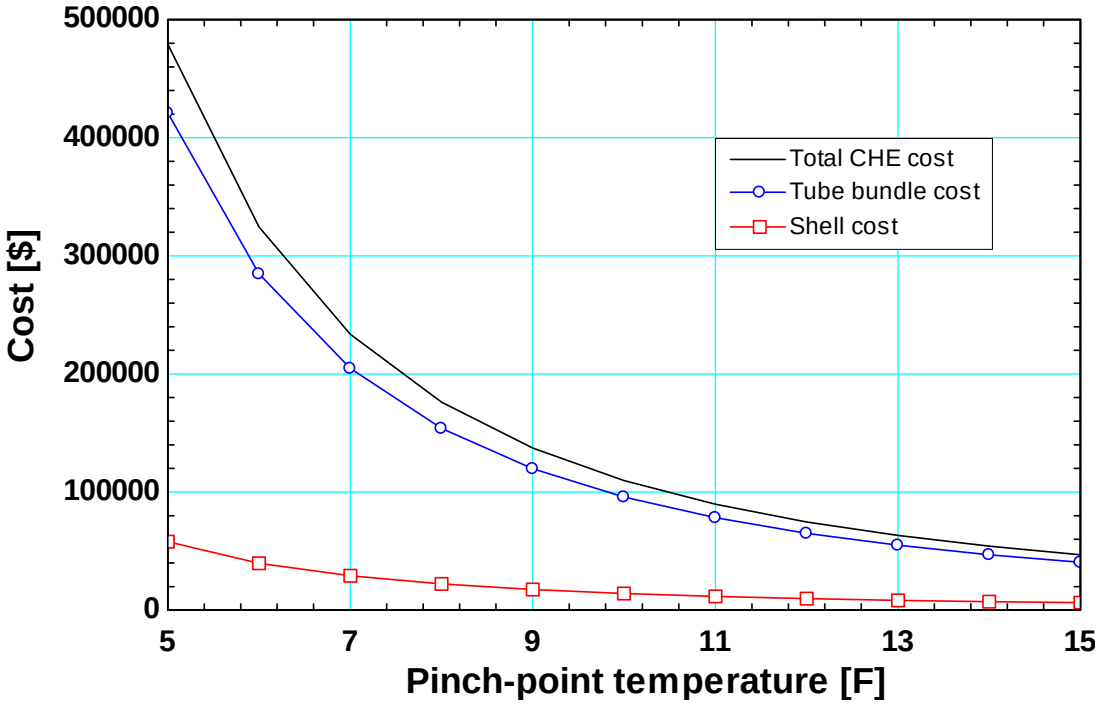

Figure 4-39: Predicted cascade heat exchanger capital cost as a function of cascade heat exchanger pinch-point temperature

The major cost factor of the cascade heat exchanger is the tube bundle. If a relatively small cascade pinch-point temperature is required then the heat exchanger tube bundle size becomes very large which causes the capital cost to increase dramatically. It is also important to note that a change of one degree in pinch-point temperature results in a large change in cost, especially towards lower pinch-point values.

To verify the accuracy of the cost prediction correlation, it is used to predict the cost of the actual cascade heat exchanger that is installed at the Arkansas Plant and is listed in Table 3-2; the result is compared with the cost reported by a plant engineer in Table 4-10.

Table 4-10: Comparison of actual cascade heat exchanger cost and model prediction for the design cascade heat exchanger installed at Jonesboro Plant, Arkansas of Nestle Inc.

	Cascade heat exchanger cost ($)
Quoted cascade heat exchanger	175,000
Cost prediction correlation	82,000

The result shows that the cost prediction correlation significantly under-predicts the cascade heat exchanger cost by approximately a factor of two. This could be due to the discrepancy in the unit cost of heat exchanger material. Moreover, it is understood from the plant engineer that this particular heat exchanger is one of a pair that was acquired by the plant and both of the heat exchangers were specially modified. Besides, the cost correlation was developed for a very generic shell-and-tube heat exchanger, whereas a cascade heat exchanger is relatively larger and unique. Even so, the cost prediction correlation provides some reasonable estimate of the equipment cost and the variation of the cost with size.

4.5.2) Compressor Cost

The compressor technology required by the cascade and compound cycles is the other major difference in the system hardware. The compressor technology for a cascade and compound cycle will be very different due to the dramatic difference in vapor density of ammonia compared to carbon dioxide at low evaporating temperatures. It is most consistent to estimate the cost of compressors in each of the two systems in terms of the total volumetric flow rate of installed compressors. This approach neglects the effect of the number of compressors on the cost but this effect should be small and would at least partially cancel in a comparative study. The compressor cost is estimated using a correlation relating cost to the volumetric flow rate or CFM (ft^3/min) of vapor that is displaced by the compressors (EPD, 1996). The cost per CFM ($/CFM) is given as a function of CFM and has been adjusted so that it includes various overhead costs that are related to installation. The consideration of economy of scale related to labor cost saving and other economic factors leads to a decreasing $/CFM with increasing installed volumetric flow rate. Figures 4-40 and 4-41 show the cost correlations used to estimate capital cost associated with installing reciprocating compressors (for the cascade cycle) and screw compressors (for the compound cycle), respectively.

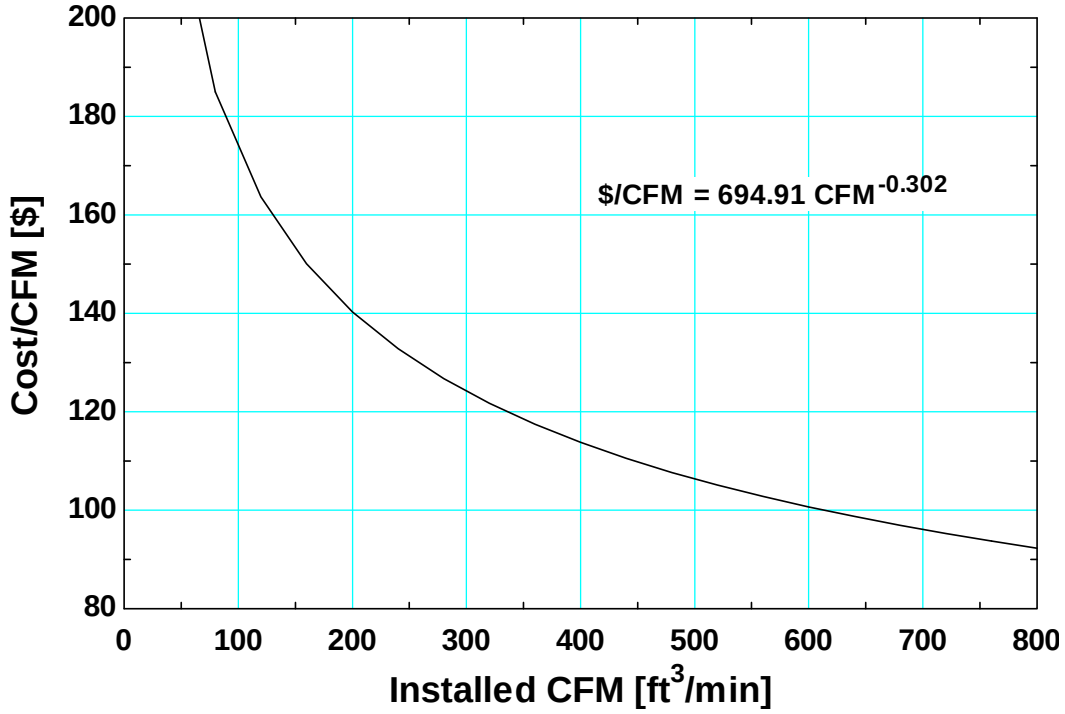

Figure 4-40: Correlation of reciprocating compressor cost per CFM as a function of displaced volumetric flow rate

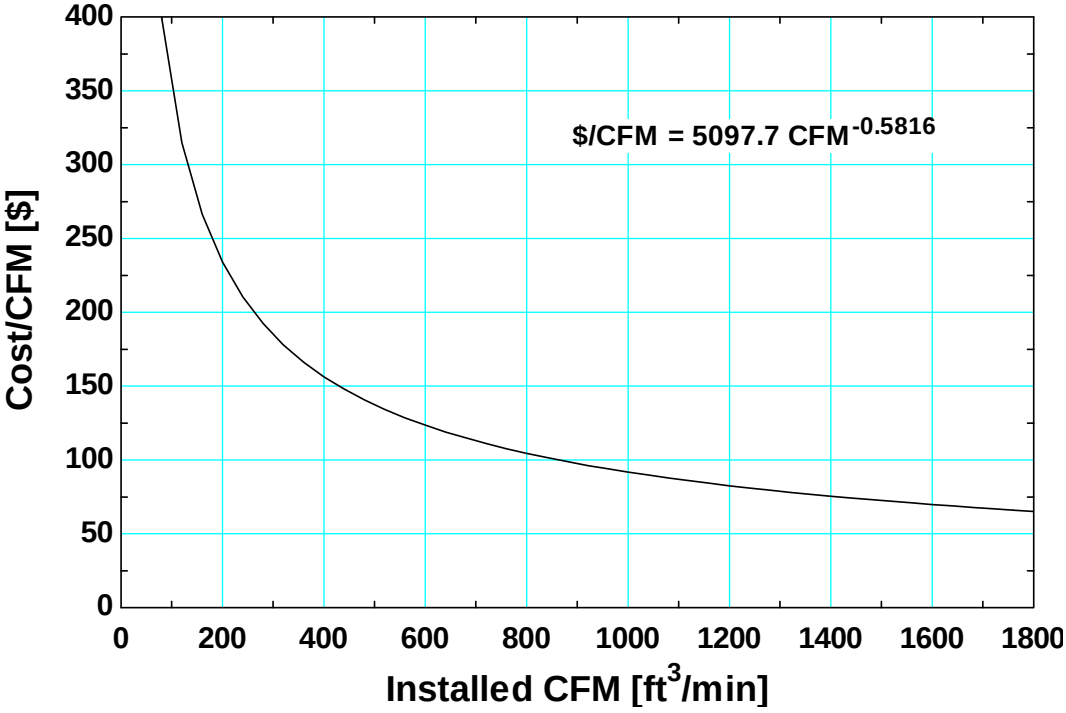

Figure 4-41: Correlation of screw compressor package cost per CFM as a function of installed volumetric flow rate.

The installed CFM is the aggregate volumetric flow rate displaced through all the installed compressor units to meet the heat load requirement in each temperature circuit. This quantity is determined at the compressor suction (inlet) condition. Since carbon dioxide has a relatively smaller specific volume than ammonia at low temperatures, the cascade system utilizing the reciprocating compressors requires much less installed CFM in order to meet the load. In addition, Figures 4-40 and 4-41 illustrate that the compressor cost per CFM associated with reciprocating compressors is less than that of the screw compressor. These two factors result in a dramatic reduction in the compressor cost associated with the cascade system.

Compressor installation cost is the product of the installation cost per CFM of displaced refrigerant ($\frac{Cost}{CFM}$) and the aggregate CFM moved by the compressors (CFM_{inst}),

$$Cost_{comp} = CFM_{inst} \frac{Cost}{CFM} \tag{4-15}$$

The compressor cost predicted for the cascade system (utilizing reciprocating compressors with carbon dioxide in the lowest temperature stage) and the compound system (utilizing screw compressors with ammonia) are shown for a system with a representative head pressure of 160 psia in Figures 4-42 and 4-43, respectively, as a function of evaporating temperature. These plots show that the compressor cost associated with the compound system exceeds the cost of the compressors for a cascade system by a factor of approximately 2.5. The results from these plots verify that cascade system has an advantage in low-temperature circuit compressor cost savings. Also note that the advantage in the compressor cost saving associated with a cascade system is on the same order as the cascade heat exchanger cost shown in Figure 4-39.

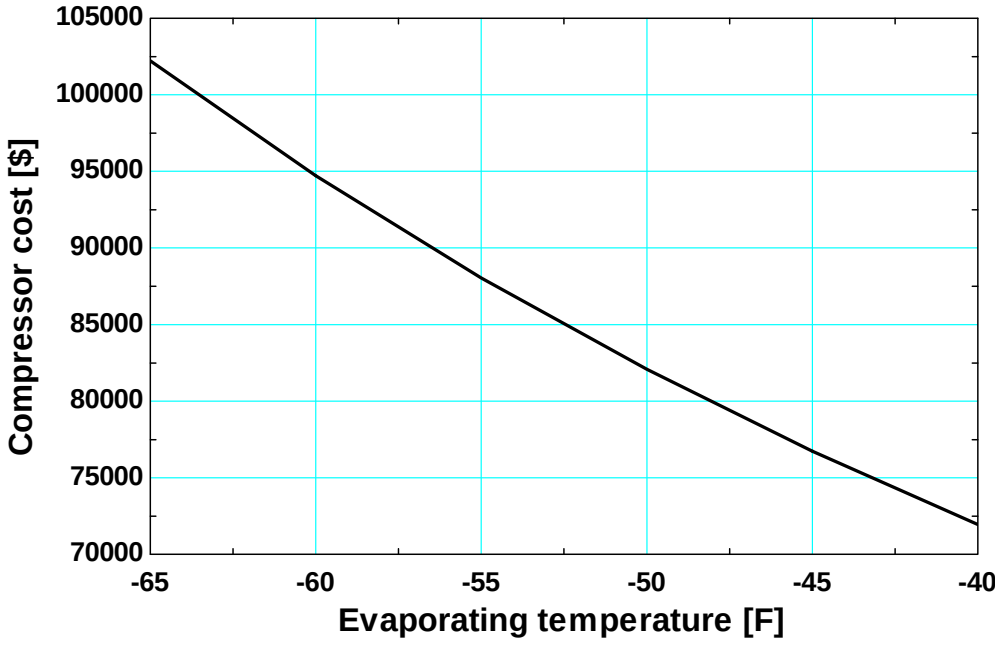

Figure 4-42: Reciprocating compressor cost as a function of evaporating temperature for a cascade system operating at 160 psia head pressure

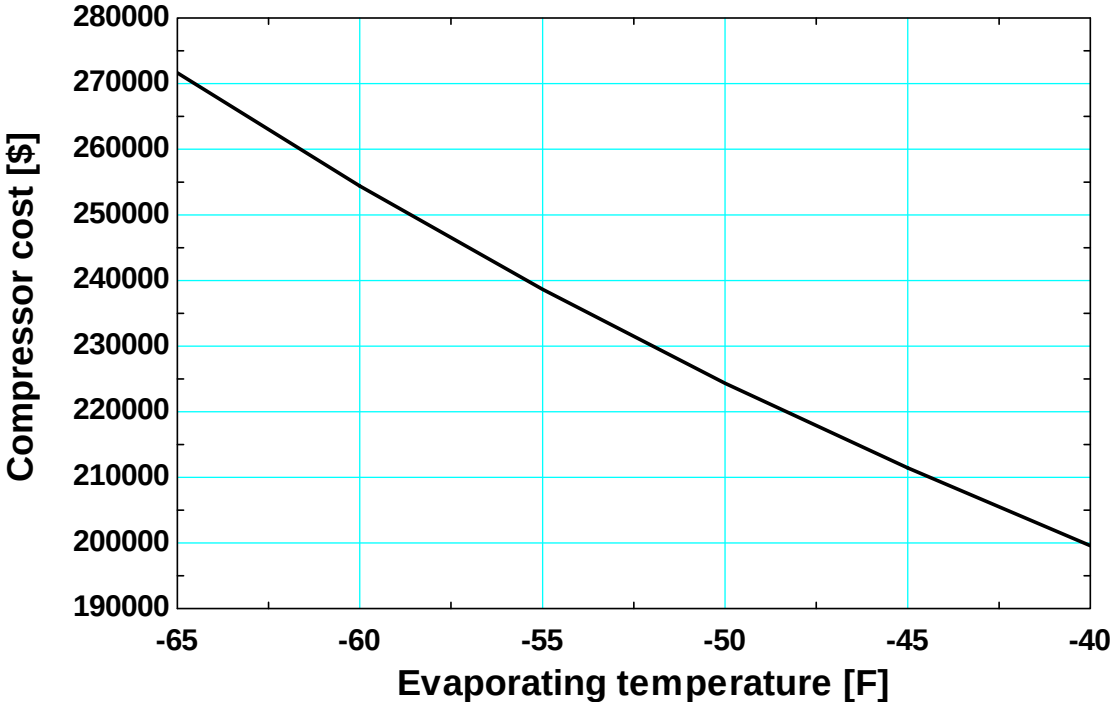

Figure 4-43: Booster compressor cost as a function of evaporating temperature for a compound system operating at 160 psia head pressure

4.6) Adjusted Capital Cost Savings

The premium difference study quantified operating cost savings benefit associated with the two systems. This section examines the capital cost savings benefit associated with the different hardware associated with these two cycles. The adjusted capital cost of the cascade cycle ($ACC_{cascade}$) is defined as the sum of the cost of the cascade heat exchanger and the compressors required for the two stages,

$$ACC_{cascade} = Cost_{CHE} + Cost_{RECIP} + Cost_{HPC} \tag{4-16}$$

Notice that the cost of the evaporator, condenser, etc. is common to both systems and therefore is not considered in the adjusted capital cost of either stage. The adjusted capital cost of the compound system ($ACC_{compound}$) is the sum of the cost of the compressors for the two stages,

$$ACC_{compound} = Cost_{BOOSTER} + Cost_{HPC} \tag{4-17}$$

In the cascade cycle, both reciprocating and screw compressor cost correlations are utilized to calculate the total compressor cost while the compound system uses only the screw compressor cost correlation for both stages. In this analysis, it is assumed that both systems operate at a specified head pressure value of 160 psia. Figure 4-44 illustrates the adjusted capital cost comparison between the cycles with a cascade pinch-point temperature difference of 10^{o}F. Notice that the cascade system has an advantage relative to capital cost and this advantage grows as the evaporating temperature decreases.

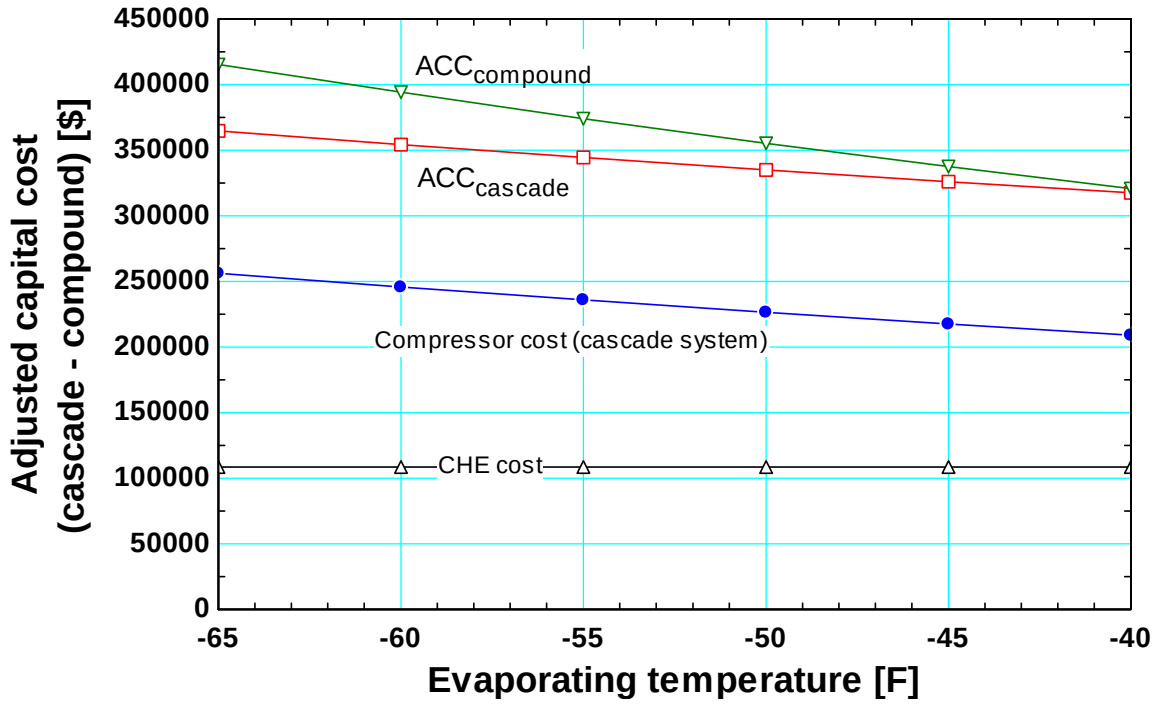

Figure 4-44: Adjusted capital cost of the cascade system and the compound system operating at 160 psia head pressure with a 10°F cascade pinch-point temperature

Figure 4-44 shows that the cascade heat exchanger cost is lower than the compressor cost when the cascade system operates with a pinch-point difference of 10°F. Therefore, the overall adjusted capital cost is lower than that of the compound system. The adjusted capital difference (ACD) is defined as the capital cost savings associated with the selection of a compound rather than a cascade system. The adjusted capital difference is the difference between the adjusted capital cost of the two options and corresponds to a life cycle savings that is related to capital cost (as the premium difference corresponds to a life cycle savings associated with operating cost). The value of ACD is defined as,

$$ACD = ACC_{cascade} - ACC_{compound} \tag{4-18}$$

Figures 4-45 illustrates the adjusted capital cost of the two configurations as a function of evaporating temperature (at the conditions used to generate Figure 4-44, 160 psia head pressure and a 10°F cascade heat exchanger pinch point temperature difference) and also shows the adjusted capital difference, the difference between these values. Note that the adjusted capital difference is negative throughout, indicating that the hardware required for the cascade system will cost less than the hardware required for the compound system. This negative value increases with decreasing evaporating temperature because the size of the compressors required for the compound system increases dramatically.

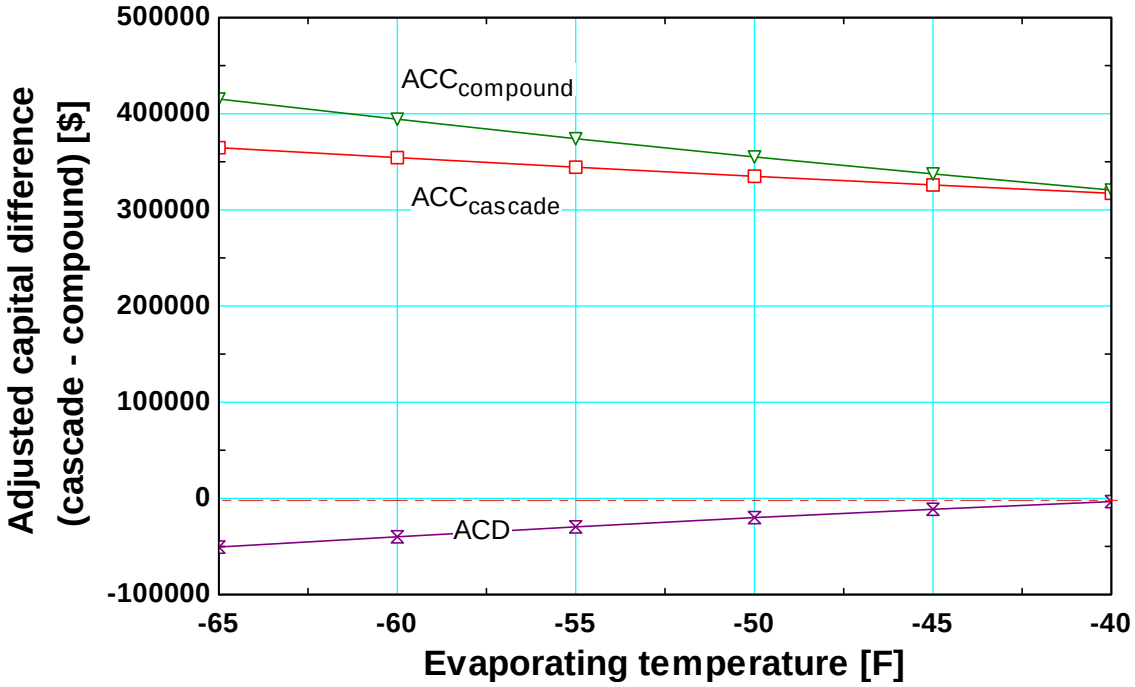

Figure 4-45: Adjusted capital difference between the cascade system and the compound system operating at a head pressure value of 160 psia and 10°F pinch-point temperature

In order to evaluate the effect of cascade pinch-point temperature difference on capital cost savings, a similar analysis is conducted using a cascade pinch-point temperature difference of 8°F and also 5°F. Figures 4-46 illustrates the adjusted capital cost of each system and the adjusted capital cost difference associated with an 8°F pinch-point temperature difference. Notice that the adjusted capital cost of the compound system remains unchanged (from Figure 4-45) but the adjusted capital cost of the cascade system increases in order to purchase a larger cascade heat exchanger. The adjusted capital cost difference for an 8°F pinch-point temperature difference is positive, indicating that the compound system hardware costs less than that of the cascade system over the entire range of evaporating temperatures.

Figure 4-47 show the same plot for a 5°F pinch-point temperature difference, the adjusted capital cost of the cascade system increases dramatically due to larger cascade heat exchanger size. The adjusted capital difference for a 5°F pinch-point temperature difference is much higher than that of an 8°F pinch-point temperature difference.

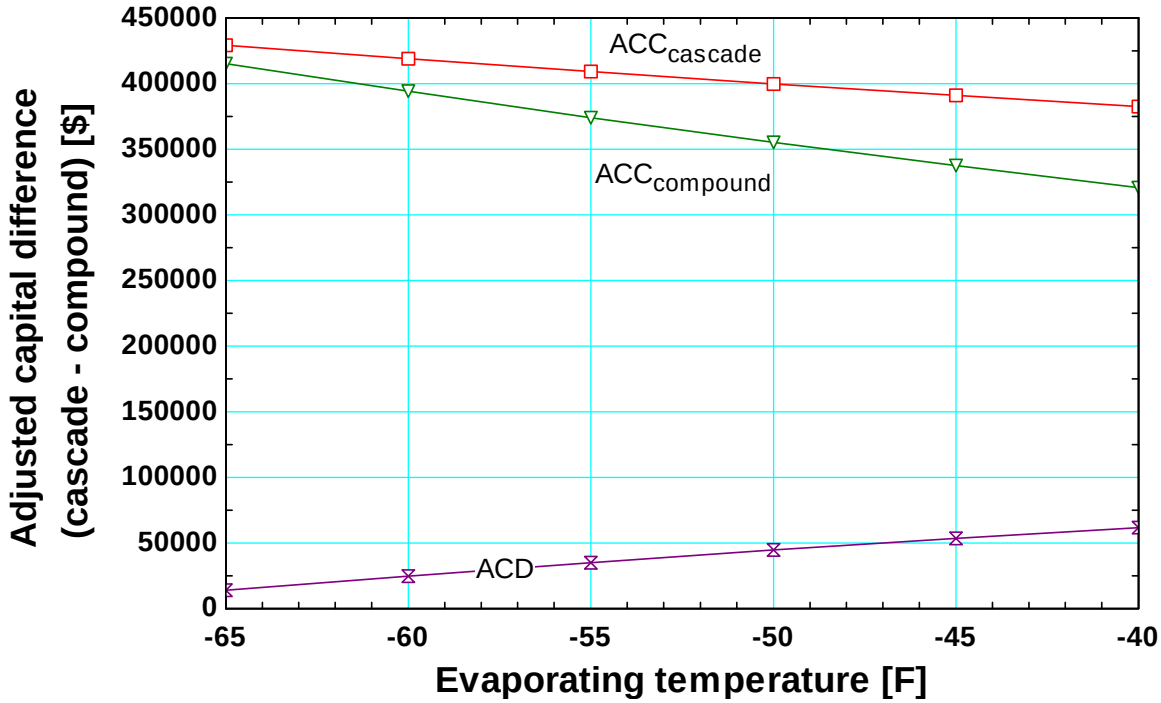

Figure 4-46: Adjusted capital difference between the cascade system and the compound system operating at a head pressure value of 160 psia and 8°F pinch-point temperature difference

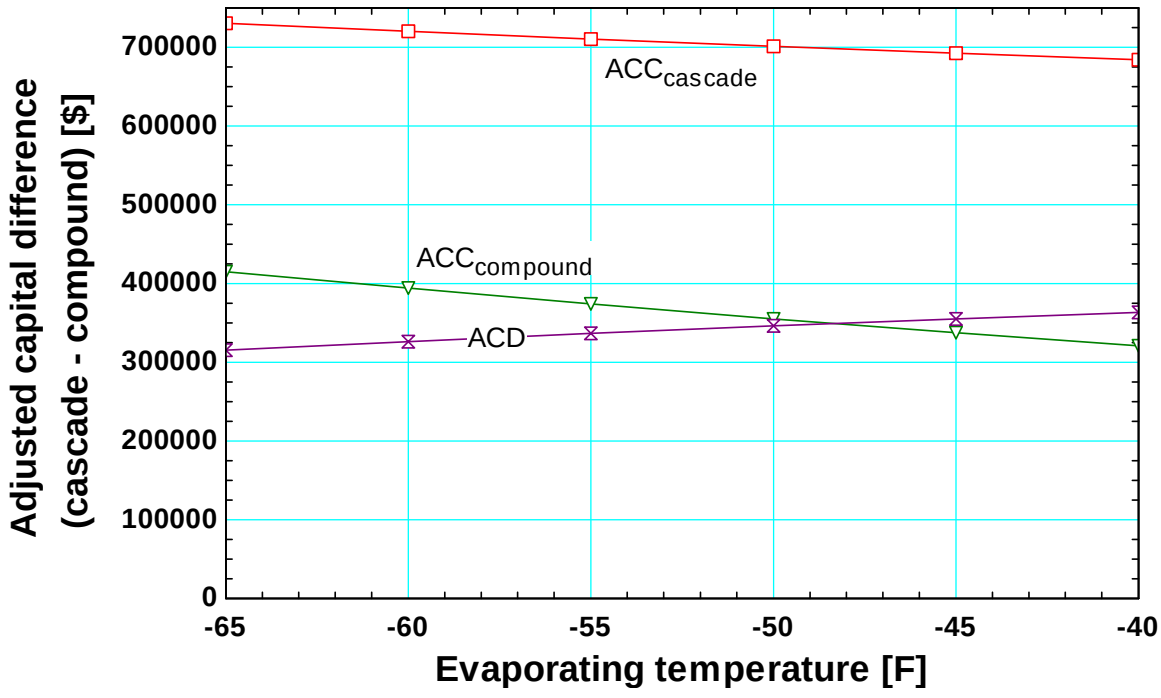

Figure 4-47: Adjusted capital difference between the cascade system and the compound system operating at a head pressure value of 160 psia and 5°F pinch-point temperature difference

4.6.1) Life-Cycle Cost Savings

By considering the capital cost difference between the two cycles as well as the operating cost difference, it is possible to determine the total life-cycle cost savings between the two cycles. Since capital cost and operating cost each contributes to the total life-cycle cost of a system, the sum of the adjusted capital difference (ACD) and the premium difference (ΔFC) is the total life-cycle cost savings (LCS).

Notice that the adjusted capital difference is defined with respect to the cascade system; this is consistent with the definition of the premium difference. The value of the total life-cycle cost savings is defined as,

$$LCS = ACD + \Delta FC \tag{4-19}$$

Figure 4-48 illustrates the adjusted capital difference and the premium difference as a function of evaporating temperature (also for 160 psia head pressure and a 10°F cascade heat exchanger pinch point temperature difference). The sum of these two quantities is the total life-cycle savings associated with selecting a compound rather than a cascade system.

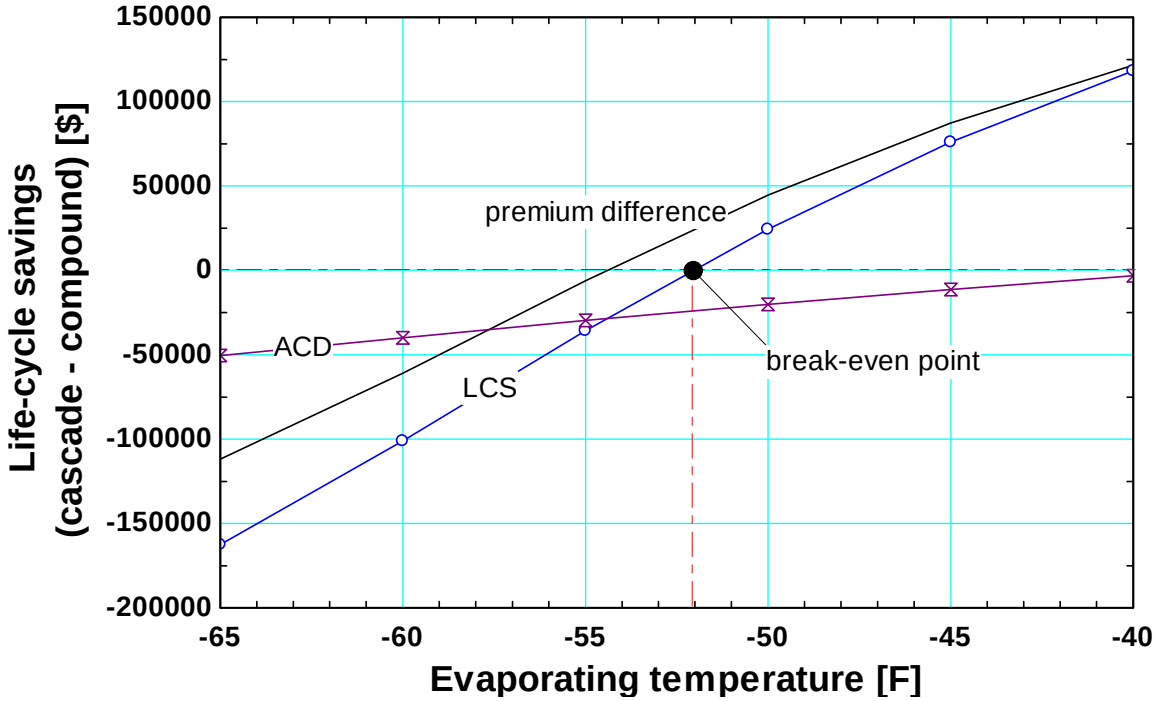

Figure 4-48: Life-cycle savings of the cascade system operating at 160 psia head pressure with 10°F cascade pinch-point temperature

Figure 4-48 shows that the adjusted capital cost savings and the operating cost savings benefit of the cascade system leads to a life-cycle cost savings for the cascade system at evaporating temperatures below the break-even temperature. The breakeven temperature associated with the cascade system with a 10°F pinch point temperature difference is nominally -52°F.

In order to evaluate the effect of cascade pinch-point temperature difference on life-cycle savings, a similar analysis is conducted using a cascade pinch-point temperature difference of 8°F and also 5°F. Figure 4-49 illustrates the adjusted capital cost difference, premium difference, and life-cycle savings for a cascade pinch-point temperature difference of 8°F.

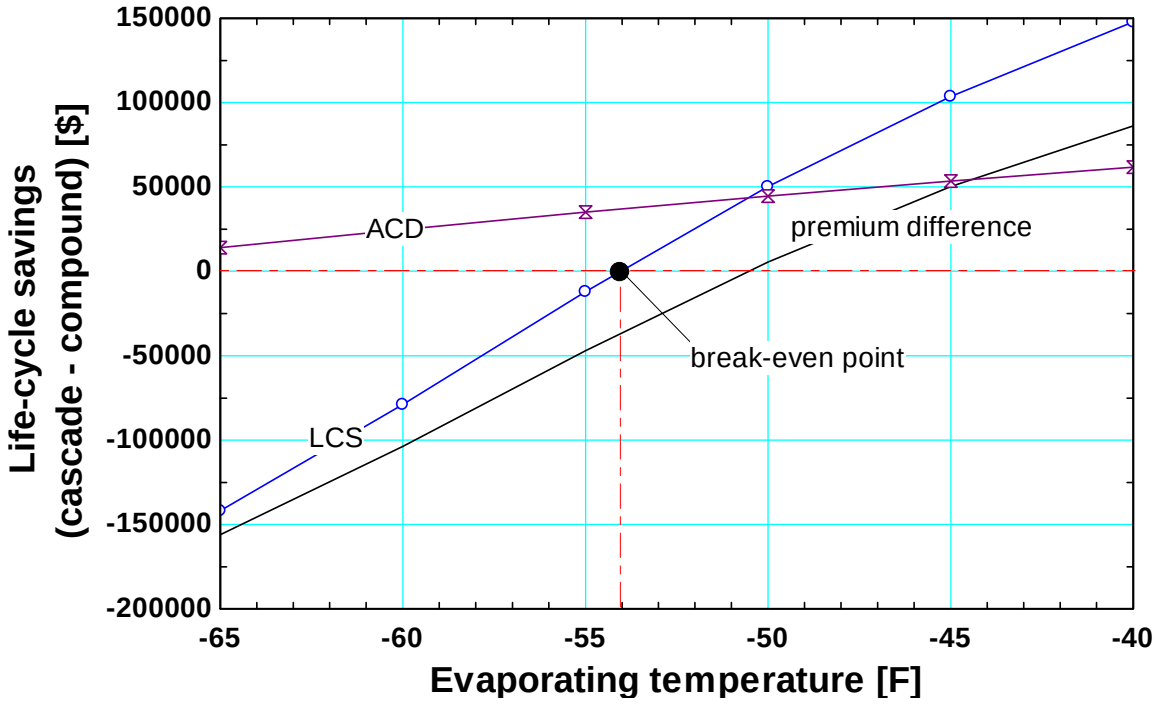

Figure 4-49: Life-cycle cost of the cascade and the compound system operating at 160 psia head pressure with 8°F cascade pinch-point temperature difference

Notice in Figure 4-49 that the premium difference is more negative because the smaller cascade pinch-point temperature difference leads to higher performance from the cascade system. The sum of the adjusted capital difference (which has increased with the reduced cascade pinch-point temperature difference) and the premium difference (which has decreased with the reduced cascade pinch-point temperature difference) is the life cycle savings. For an 8° F cascade pinch-point temperature difference, the life cycle savings ends up more negative than a 10° F value and therefore the break-even temperature shifts to a lower number; that is, with the 8°F cascade pinch-point temperature difference you would be better off purchasing a compound system for any evaporating temperature greater than approximately -54°F.

Figures 4-50 shows the same plot for a 5°F pinch-point temperature difference; all of the trends observed going from 10°F to 8°F continue and the break-even temperature is reduced even further.

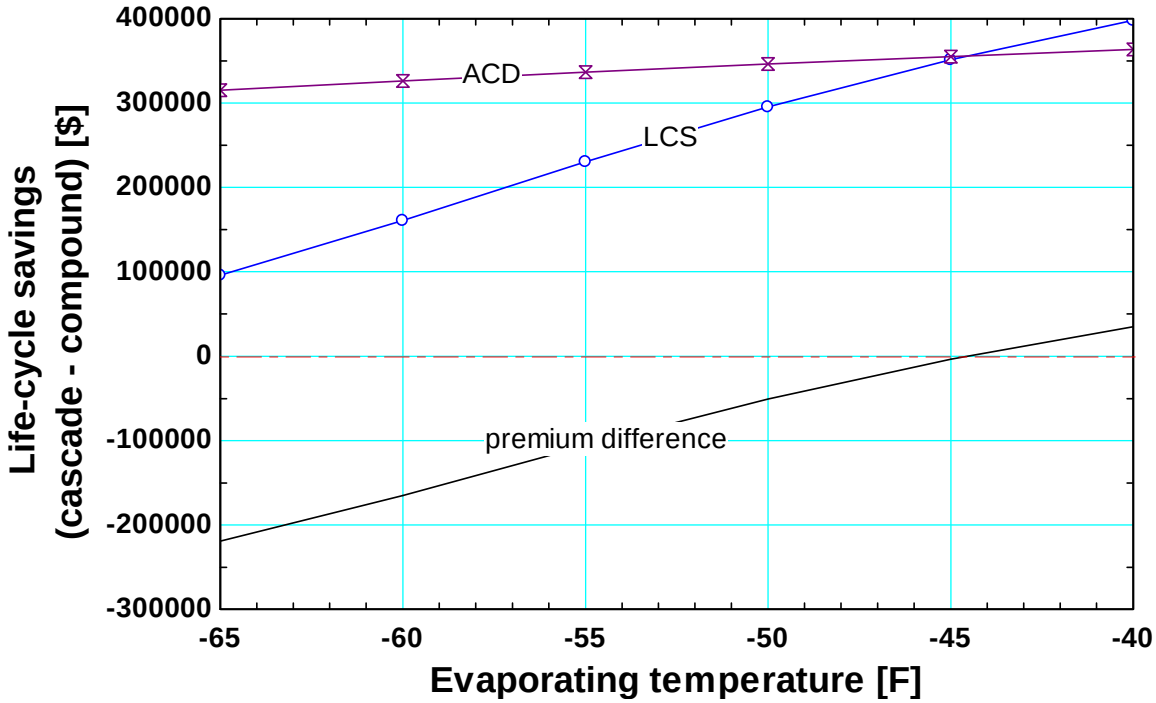

Figure 4-50: Life-cycle cost of the cascade and the compound system operating at 160 psia head pressure with 5°F cascade pinch-point temperature difference

When the cascade pinch-point temperature is reduced, the high pressure compressors of the cascade system require less power to operate due to better cascade heat exchanger performance, thus increasing system performance and premium difference for the cascade system. However, the cascade heat exchanger size and cost also increase dramatically. Figure 4-49 shows that at a cascade pinch-point temperature difference of 5°F, the adjusted capital cost of the cascade system is much higher than that of the compound system. Although the premium difference is large, the extremely high capital cost overwhelms it resulting in a life-cycle deficit for the cascade system. The plot in Figure 4-50 shows that break-even temperature is below the range of temperatures considered (i.e., the cascade system with a 5°F pinch-point temperature difference is never optimal for evaporating temperatures greater than at least -65°F).

4.6.2) Optimal Cascade Pinch-Point Temperature Difference

The previous section showed that reducing the cascade pinch-point temperature difference leads to an improvement in the premium difference of the cascade system that is counteracted by a reduction in the adjusted capital cost difference related to the increase in the cost of the cascade heat exchanger. This section varies the pinch-point temperature difference in order to maximize the break-even temperature and therefore optimize the cascade heat exchanger. The life-cycle saving analysis, presented in the previous section, is carried out for each value of the pinch-point temperature difference with a range from 5°F and 12°F. Figure 4-51 shows the break-even temperature (for systems operating at a specified head pressure value of 160 psia) as a function of cascade pinch-point temperature difference.

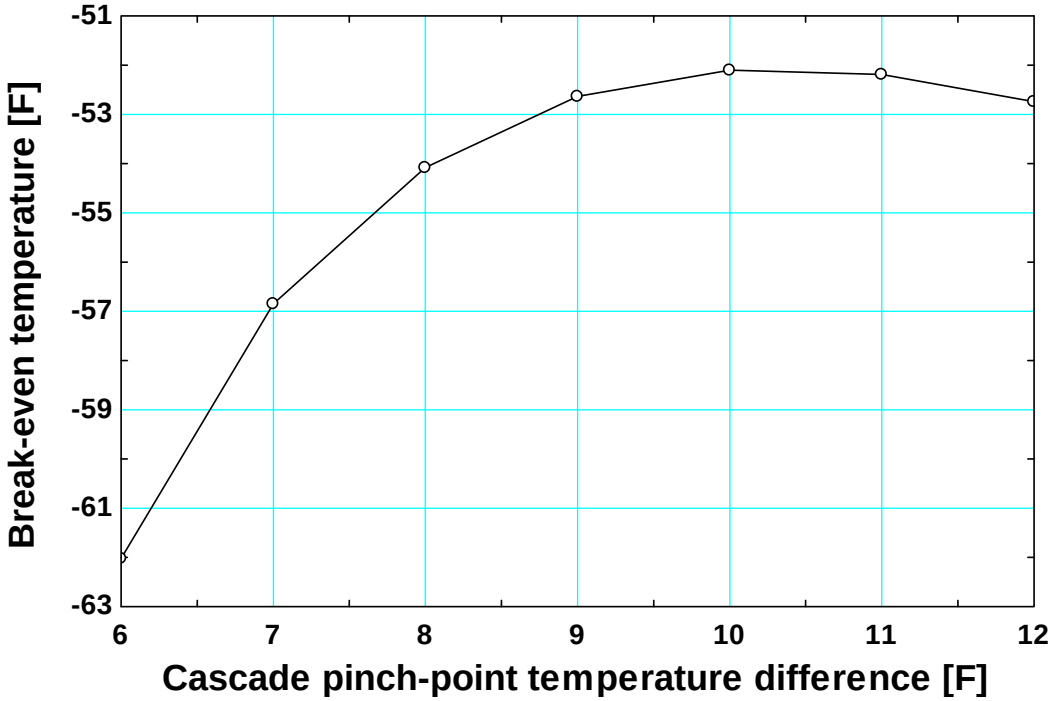

Figure 4-51: Break-even temperature of the cascade system and the compound system operating at 160 psia head pressure as a function of cascade pinch-point temperature difference

Figure 4-51 shows that the optimal cascade pinch-point temperature difference is approximately 10°F. When the cascade system operates under this condition, the life-cycle saving is maximized and the range of evaporating temperatures that result in a life-cycle saving for the cascade system is the broadest, allowing the system to operate at higher evaporating temperature while maintaining economic advantage. Note that break-even temperature changes most quickly between the pinch-point of 5°F and 6°F because in this range the cascade heat exchanger cost changes very dramatically and quickly outweighs the operating cost savings benefit of the cascade system. Thus, it is not practical to install a large heat exchanger that has a very small pinch-point temperature difference. It is best to install a cascade heat exchanger with a geometry that would accommodate the optimal pinch-point that will allow an optimal balance between operating cost and capital cost. The results of this analysis suggest that a cascade system should be considered for applications in which the evaporating temperature will be less than approximately -52°F and that the cascade heat exchanger should be designed with a pinch-point temperature difference of approximately 10°F.

Chapter 5) Conclusion and Recommendation

The use of freezing to extend the life of perishable products is the basis of the frozen food industry. This industry continues to grow and utilizes industrial refrigeration to provide cooling at relative low temperatures. Anhydrous ammonia (NH_3) is one of the earliest refrigerants that was used and has been the refrigerant of choice for industrial refrigeration applications for many generations. Ammonia has attractive characteristics such as high heat capacity, low cost and it is safe for the environment which makes it a popular refrigerant for numerous applications, including food processing and cold storage. However, a disadvantage of anhydrous ammonia as a primary refrigerant is its low vapor density at low evaporating temperatures (below -50^{o}F). This property leads to large, inefficient and expensive compression equipment for very low temperature ammonia systems.

An alternative system configuration utilizes carbon dioxide (CO_2) in a low temperature stage in order to address this weakness. The alternative system configuration chosen for this study is an NH_3/CO_2 cascade system where ammonia, operating in a high-temperature circuit (HTC), comes into indirect contact with the carbon dioxide that is operating in place of ammonia in a low-temperature circuit (LTC). The indirect heat transfer occurs within a cascade heat exchanger (CHE). Carbon dioxide is also a natural refrigerant that exhibits favorable characteristics as a primary refrigerant at low temperatures. The objective of this research is the quantitative comparison of a conventional multi-stage ammonia compound system and a cascade system. The comparison is conducted through system modeling using similar conditions and economic assumptions in order to evaluate the life cycle savings (due to both operating cost and capital cost differences) associated with selecting one configuration over the other.

A model is created for each cycle configuration, using the principles of thermodynamics, to capture the physics of the system. The computer models are created using Engineering Equation Solver (EES) software tool and are flexible to specified user inputs. An intermediate condition can be varied to optimize system performance and the coefficient of performance (COP) of each system. Each of the components with the system models are created individually in order to capture the differences in the hardware associated with the two configurations. The component models are either created from a detailed thermal-fluid analysis (for the heat exchangers) or by utilizing manufacturer's data (for the compressors). These component models are integrated together to form a detailed system model that is used to perform load and weather-driven system simulation over a year of operation. The multi-stage ammonia compound system component model consists of screw compressor models, an evaporator model, and an evaporative condenser model. The NH_3/CO_2 cascade system component model consist of reciprocating and screw compressor models, a cascade heat exchanger model, an evaporator model, and an evaporative condenser model.

Compressor models are created by curve-fitting compressor performance data utilizing manufacturer's selection programs. RWF II screw compressor models by Frick Inc. are chosen as the basis for high-stage compressors in both cycles and also as the booster compressors in the compound system. Data for reciprocating compressor by Grasso Inc. is used for the low-temperature circuit of the cascade system. All compressors in the model operate at full load except for one unit that is allowed to operate at a part-load condition in order to accommodate

changes in the operating condition. The performance penalty associated with operating at part-load is included using non-linear unloading curve for screw compressors; reciprocating compressors are assumed to unload linearly.

The cascade heat exchanger is a shell-and-tube heat exchanger in which the low-temperature circuit refrigerant (CO_2) flows through the tube bundle and exchanges heat with the high-temperature circuit refrigerant (NH_3) that boils on the shell side. CO_2 cooling involves two separate processes: de-superheating and condensation. Each process takes up a portion of the tube bundle length and that portion is categorized as a section of the heat exchanger. The condensation section is the most dominant portion of the CHE, where both refrigerant streams undergo isothermal heat exchanging process. The conductance rate of the cascade heat exchanger (i.e., its physical size) is dictated by a pinch-point temperature difference ($\Delta T_{cascade}$). The cascade heat exchanger model translates the operating characteristics of the cascade heat exchanger at its design conditions into a suitable physical size and geometry and uses this to simulate the performance at off-design conditions. The cascade heat exchanger model is compared to an actual device installed at a food plant located in Arkansas. The model is found to over-predict the total length of the tubes by a factor of approximately three; however, it is not clear if this is due to a discrepancy in the value of the operating pinch-point temperature difference.

The evaporator model and evaporative condenser model are developed using the geometry and thermal performance of a commercial unit at the specified design conditions. The evaporator is modeled after a 130-kW evaporator unit made by King Corporation and the evaporative condenser is modeled after an evaporative condenser unit manufactured by Evapco Inc. Off-design thermal performance is simulated by relating the conductance rate of the device at its design condition to that at off-design conditions and obtaining the performance using an effectiveness-NTU solution.

The evaporative condenser is an essential piece of equipment that influences the performance of a system. Heat rejection process is accomplished by drawing out evaporated cooling water with an outside air stream. The simultaneous sensible and latent heat transfer mechanisms that drive the performance of this device requires an enthalpy-based effectiveness approach to simulate the performance. Thus, the heat rejection process depends not only on the dry-bulb temperature but also on the humidity of outside air. Outside air wet-bulb temperature is an essential factor that dictates the heat rejection capacity of the condenser. Saturated condensing or head pressure of the system is established where the required heat rejection of the system matches the condenser capacity. The head pressure of the system is allowed to float until the required capacity is attained. When wet-bulb temperature falls and therefore the condenser has excess capacity, the condenser enters part-load operation by de-rating the air flow through the unit using variable frequency drive (VFD) control on fan motors. A minimum head pressure of 135 psia is set for the condenser model.

System simulations are conducted with respect to outdoor conditions as a forcing function at four different geographical locations. The system performance of the two cycle configurations, at any given operating condition, can be compared using the detailed system-level models. Comparison of system efficiency alone is inadequate to identify the best system. The different system

components required by the systems introduces a variation in the capital cost associated with system ownership as well as the operating cost associated with system performance. Thus, a more comprehensive comparative analysis involving cost-related factors is considered. A life-cycle cost (LCC) analysis is conducted to compare the total cost associated with a system ownership over a period of economic study.

An economic comparison in the context of life-cycle cost utilizes the P_1, P_2 Method that breaks down the total cost into two main categories—operating cost (OC) and first cost (FC). P_1 and P_2 are economic factors that account for the time value of money by allowing costs that incur in the future to be converted back to present-day dollars. P_1 and P_2 are associated with the operating cost and the initial investment, respectively. The economic parameters required to carry out the analysis are based on educated estimates; these parameters introduce some uncertainty in the life-cycle cost analysis. In order to initially remove any uncertainty related to capital cost information, the comparison is initially made entirely on the basis of operating cost. This is accomplished by identifying the difference, in present day dollars, associated with operating each system over its life time. This difference is equivalent to the difference in the first cost (ΔFC) that can be tolerated for the more efficient system in order to break even on the life cycle cost; this value is referred to as the premium difference.

The intermediate condition for each system is allowed to vary independently in order to establish a maximum COP. The optimization is carried out prior to any system simulation by optimizing the system COP over a typical range of head pressure and evaporating temperature using the built-in Min/Max function in EES. The optimization results are curve-fitted as a bi-quadratic function, with head pressure and evaporating temperature as inputs, which is conveniently integrated into the system model. The root-product method is also used for the compound system; this method calculates the intermediate pressure as the geometric mean of evaporating and head pressures.

Life-cycle cost comparison is conducted using an operating cost analysis approach; the annual energy usage of a system is obtained from running the detailed system-level models in a 12-month simulation. The simulation results show a location-based energy usage trend with local climate. Miami, which has the highest average wet-bulb temperature, has the highest annual energy usage followed by Houston, Los Angeles and Madison. Results also show a discrepancy in energy usage and average wet-bulb temperature occurring between the last two cities. Consequent wet-bulb and head pressure frequency analyses show that despite a large difference in average wet-bulb temperature between the two cities, their average head pressure values are close. This is related to the minimum head pressure limit which bounds the head pressure in cases of very low wet-bulb temperature occurrence. Madison, which has very high frequently of low wet-bulb occurrence, ends up operating at higher head pressure than would otherwise be necessary.

The premium difference (ΔFC) is in favor of the cascade system at low evaporating temperatures (below the break-even temperature) and vice versa. As expected, the high specific volume of ammonia at low temperatures decreases booster compressor efficiency. The higher operating efficiency of the cascade system at low evaporating temperature results in an operating cost saving benefit that permits its maximum allowable first cost to be higher than that of the

compound system (i.e., a premium difference for the cascade system). However, this operating cost-based premium difference is only a small fraction of the total life-cycle cost; the premium difference is at most 5% of the life-cycle operating cost of the compound system expressed in today's dollars. From an energy usage standpoint, the premium difference is approximately equal to one year of system operating cost. The sensitivity analysis shows that the premium difference is affected by head pressure, economic parameters and the cascade pinch-point temperature difference.

The cascade pinch-point difference is a crucial factor that dictates CHE size and geometry as well as operating efficiency of the cascade system. A 20% reduction in cascade pinch-point temperature from its nominal value of 10^oF (to 8^oF) causes the break-even temperature to shift towards higher temperature by approximately 5^oF. A 50% reduction (to 5^oF) causes a 10-degree shift, which significantly improves cascade system performance. The premium difference in favor of the cascade system nearly triples (at -65^oF evaporating temperature) with a 5^oF pinch-point temperature difference. However, this reduction in the pinch-point temperature difference greatly amplifies the cascade heat exchanger size; the estimated cost of the CHE quadruples.

Capital cost estimates are carried out for the major components in each system that are not common to both systems. A correlation for the cascade heat exchanger based on its geometry is developed. The prediction of cost is compared with the actual cost of the existing device at Jonesboro and it is found that the correlation under-predicts CHE cost by a factor of two. However, there are some special features associated with the CHE at Jonesboro and the cost prediction captures the characteristics of how cost is affected by size. The compressors cost is estimated based on the volumetric flow rate of installed capacity for each compressor technology type.

The capital and operating cost savings are integrated in order to carry out a more complete life-cycle cost comparison. The adjusted capital cost (*ACC*) of a system is defined as the sum of the major component costs of a system, excluding the cost of the components that are common to both systems (i.e., the condenser cost, evaporator cost and etc.). The adjusted cost difference is the difference in adjusted capital cost and can be thought of as the life-cycle savings due to capital cost difference. The compound system has an advantage associated with the absence of a cascade heat exchanger but suffers from higher compressor cost. The premium difference can be thought of as the life-cycle savings associated with operating cost differences. The cascade system has an advantage in the premium difference at low evaporating temperatures. The sum of the adjusted cost difference and the premium difference is the total life cycle savings.

With smaller cascade pinch-point temperature difference, the cascade system has an advantage in premium difference but the adjusted capital cost difference gets worse due to the high cascade heat exchanger cost. At high cascade pinch-point temperature difference the capital cost difference swings towards the cascade system but the premium difference gets worse. It is found that the optimal cascade pinch-point temperature difference, that maximizes life-cycle savings, is 10^oF. It is most economically viable for the cascade system to install a cascade heat exchanger with the size and geometry associated with the optimal pinch-point at design conditions. Further, the cascade system should be considered for applications in which the evaporating temperature will be less than approximately -52^oF

Recommendation

Ammonia has been utilized as an industrial refrigerant for many years for numerous applications in food industry. The NH_3/CO_2 cascade system is a relatively new technology that holds the promise of overcoming some of the shortcomings of a conventional ammonia compound system for low temperature applications. This research compared the cascade and compound cycles. However, several key areas and differences between these cycles were not specifically addressed. Further research would best be aimed toward the following areas.

- Account for frost accumulation on evaporator coil surfaces and evaluate its effect on performance degradation over a period of operation. The frost accumulation rate and period of normal operation would be different for each refrigerant due to differences in the evaporator design.

- Consider different defrosting techniques and defrost penalty associated with each system configuration. Ammonia system uses hot-gas defrost while the low temperature circuit of a carbon dioxide system does not have the necessary hot gas available and would therefore likely use electric heating. Defrosting directly with hot gas in a CO_2 system is difficult due to the extremely high working pressures encountered.

- Pressure losses and parasitic loads in system components compromise system performance and should be examined more closely.

- Integrate other aspects affecting compressor performance, such as oil cooling and de-superheating loss, into the compressor performance model.

- Obtain more accurate equipment cost data in order to improve capital cost estimation. Develop cost prediction for other system components, especially refrigerant piping, that would be different for each system.

- Establish cost adjustment and consideration for the difference in equipment material cost. CO_2 operates with higher pressure; its refrigeration equipment is designed and constructed to operate under those conditions.

References

Aljuwayhel, N. (2006) *Numerical and Experimental Study of the Influence of Frost Formation and Defrosting on the Performance of Industrial Evaporator Coils*. PhD Thesis, Mechanical Engineering, Solar Energy Laboratory, University of Wisconsin-Madison.

Ayub, Z.H, "Industrial Refrigeration and Ammonia Enhanced Heat Transfer," Preceedings of the ASME-ZSIS International Thermal Science Seminar II (CD-ROM), Slovenia, June, 2004, pp. 13-23.

Cavallini, A., and R. Zecchin, "High velocity condensation of organic refrigerants inside tubes," *Proceedings 13th Int. Congr. Of Refr.*, Washington D.C., 1971, 2: pp. 193-200.

Cavallini, A., and R. Zecchin, "A dimensionless correction for heat transfer in forced convection condensation," *Proceedings 6th Int. Heat Transfer Conf.*, Tokyo, 1974, 3: pp. 309-313.

Cavallini, A., Censi G., Del Col D., Doretti L., Longo G.A., Rossetto L., "In-tube Condensation of Halogenated Refrigerants," *ASHRAE Transactions*, 2002, paper H-1718.

Chen, J.C., "Correlation for Boiling Heat Transfer to Saturated Fluids in Convective Flow," Industrial Engineering Chemical Process Design Development, 1966, 5(3), pp. 322-329.

"Coolware," Frick Inc., http://www.frickcold.com/coolware.asp.

Cornwell, K. and Houston, S.D., "Nucleate Pool Boiling on Horizontal Tubes: A Convection-based Correlation," *Int. J. Heat Mass Transfer*, 1994, Vol. 37, Suppl. 1, pp. 303-309.

Duffie, J.A. and Beckman, W.A. (2006) *Solar Engineering of Thermal Processes*. New Jersey: John Wiley & Sons, 3rd edition.

Energy Information Administration website (2008) , http://www.eia.doe.gov

EPD, "Design of Ammonia Refrigeration Systems", University of Wisconsin-Madison short course notes, directed by Professor Douglas Reindl, (1996)

EPD, "Introduction to Ammonia Refrigeration Systems", University of Wisconsin-Madison short course notes, directed by Professor Douglas Reindl, (2006)

Gnielinski, V. "New Equations for Heat and Mass Transfer in Turbulent Pipe and Channel Flow," *International Chemical Engineering*, 1976; 16(2): pp. 359-68.

Groll, E.A. and Sun, Z., "CO_2 Flow Boiling Heat Transfer in Horizontal Tubes, Part III: Prediction of Heat Transfer Coefficient," IIR/IIF-Commission B1, B2, E1 and E2-Guangzhou, China, 2002, pp. 148-157.

Hayashi, Y., Aoki, A., Yuhana, H., "Study of Frost Formation Based on a Theoretical Model of the Frost Layer," *Heat Transfer, Jap. Res*., 1977, Vol. 6, No. 3, pp. 79-94.
Hobbs, P.V. (1974) *Ice Physics*, Oxford: Clarendon Press.

Homsy, P., "Ammonia/CO_2 Cascade System in a Large Freeze-Drying Plant: Lessons Learned During Installation and Commissioning", Technical Paper #10, *IIAR Ammonia Refrigeration Conference, Albuquerque, New Mexico,* 2003, pp. 317-355

Incropera, F. and DeWitt, D. (1990) *Introduction to Heat Transfer*. New Jersey: John Wiley & Sons, 2nd edition.

Incropera, F. and DeWitt, D. (2002) *Fundamentals of Heat and Mass Transfer*. New Jersey: John Wiley & Sons, 5th edition.

Jung, D. S., and D. A. Didion. (1989) "Horizontal flow boiling heat transfer using refrigerant mixtures." ER-6364, research project 8006-2.

Kondepudi, S.N. and O'Neal , D.L., "A Simplified Model of Pin Fin Heat Exchangers Under Frosting Conditions," *ASHRAE Transactions*, 1993, 99, 1.

Lachner, B. F., (2004) *The Use of Water as a Refrigerant: Impact of Cycle Modifications on Commercial Feasibility.* M.S. Thesis, Mechanical Engineering, Solar Energy Laboratory, University of Wisconsin-Madison.

Lawrence, J. N. (2003) *Refrigeration Fundamentals Throughout History: Methods Used to Obtain Colder Temperatures, and Principles Governing Them*. Literature Seminar, Department of Chemistry, The University of Alabama.

Lee, K., T. Lee, and W. Kim. "Heat and Mass Transfer of Parallel Heat Exchanger under Frosting Conditions," *SAREK Journal*, 1994, Vol. 6, No. 2.

Lee, T.-S., Liu, C.-H., Chen, T.-W., "Thermodynamic analysis of optimal condensing temperature of cascade-condenser in CO_2/NH_3 cascade refrigeration systems", *International Journal of Refrigeration,* 2006, Vol. 29, pp. 1100-1108.

Malhammar, A., "Frostpaslag via flansade ytor," *Doktorsav handling*. Kungliga Tekniska Hogskolan, Stockholm, Sweden, 1986.

Manske, K.A., (1999) *Performance Optimization of Industrial Refrigeration Systems*. M.S. Thesis, Mechanical Engineering, Solar Energy Laboratory, University of Wisconsin-Madison.

McQuiston, F.C., "Finned Tube Heat Exchangers: State of the Art for the Air Side," *ASHRAE Transactions*, 1981, Vol. 87, Part 1.

Page, A., "CO_2/NH_3 Refrigeration Replaces R-22 in Large Freeze-Drying Plant", Technical Paper #1, *IIAR Ammonia Refrigeration Conference, Kansas City, Missouri,* 2002, pp. 1-27.

Product Features & Engineering Brochure, Evapco Inc., http://www.evapco.com.

Reciprocating Compressors, Grasso Inc. under The GEA Group, Bochum, Germany.

Rosenhow, W.M., J.P. Hartnett, and E.N. Ganic. (1985), *Handbook of heat transfer*. New York: McGraw Hill, 2nd edition.

Schmidt, T.E., "Heat transfer calculation for extended surfaces," *Refrigerating Engineering*, 1949, Vol. 57.

Screw Compressor Teardown: A Few Basics – Part 2, The Air Conditioning, Heating and Refrigeration News website, http://www.achrnews.com/

Single Screw Compressors Design & Operation, VSM Bulletin No. 0140 (2006), Vilter Manufacturing LLC, Cudahy, WI.

Stephan, K. and Abdelsalam, M., "Heat Transfer Correlations for Natural Convection Boiling," *Int. J. Heat Mass Transfer*, 1980, Vol. 23, pp. 73-87

Stoecker, W.F. (1988) *Industrial Refrigeration*. Troy, Michigan: Business News Publishing Company.

Threlkeld, J.L. (1970) *Thermal Environmental Engineering*. Englewood Cliffs, New Jersey: Prentice Hall Book Co., 2nd edition.

Typical Meteorological Year (TMY) weather data, National Renewable Energy Laboratory website (2008), http://rredc.nrel.gov/solar/old_data/nsrdb/tmy2/

WA Series Piston compressors, Mycom under Mayegawa Manufacturing Company Limited, http://www.mayekawa.eu/compressors/WA.html

Winterton, R.H.S., *Int. J. Heat Mass Transfer,* 41, 809, 1998.

Zheng, J.X., Jin, G.P., Chyu, M.-C., and Ayub, Z.H., "Flooded Boiling of Ammonia with Miscible Oil Outside a Horizontal Plain Tube", *International Journal of Heating, ventilating, Air-Conditioning and Refrigerating Research,* Vol. 7, No. 2, 2001, pp. 185-204.

Z-Screw Air Compressor, MitsuCom Europe bv Compressoren, http://www.mitsucom.nl

Appendix

Appendix A – System Component Data

A-1: Compressor Data

Full-load ratings of RWF II 676 compressor (booster) operating with NH_3

SST (°F)	***SDT (°F)***	***CAPACITY (Tons)***	***POWER (HP)***
-60	0	212	336.4
-60	10	205.8	369.3
-60	20	199.2	409.9
-60	30	192.3	455.6
-50	0	294.4	359.7
-50	10	287	397.9
-50	20	279.1	440.5
-50	30	271.1	487.1
-40	0	399.6	366.6
-40	10	390.7	419.9
-40	20	381	470.7
-40	30	371	518.4
-30	0	531.9	369.2
-30	10	521	424.9
-30	20	509.3	488.3
-30	30	497.4	549.4
-20	0	696.7	379.3
-20	10	683.3	428.5
-20	20	668.6	492.1

Full-load ratings of RWF II 177 compressor (HPC) operating with NH_3 by Frick Inc.

SST (°F)	***SDT (°F)***	***CAPACITY (Tons)***	***POWER (HP)***
-5	75	219.3	285
-5	85	213	322.7
-5	95	206.4	361.6
-5	105	199.6	401.8
0	75	247.8	292.5
0	85	240.7	332.9
0	95	233.6	374.6
0	105	226.2	417.6
10	75	313.4	302.7
10	85	304.8	349.7
10	95	295.9	397.4
10	105	287.1	446.5
20	75	391.2	303.8
20	85	381.1	358.7
20	95	370.7	414.4
20	105	359.7	470.3

Full-load ratings of 55-HP reciprocating compressor operating with CO_2 by Grasso Inc.

SSTB (°F)	***SDTB (°F)***	***CAPACITY (Tons)***	***POWER (HP)***
-60	0	48.5	59.9
-60	5	46.6	62.9
-60	10	44.7	65.8
-60	15	42.8	68.5
-55	0	55.3	61.2
-55	5	53.3	64.8
-55	10	51.3	68.2
-55	15	49.2	71.3
-50	0	62.7	61.9
-50	5	60.6	66.1
-50	10	58.4	70
-50	15	56.2	73.7
-45	0	70.7	61.9
-45	5	68.4	66.6
-45	10	66.1	71.1
-45	15	63.7	75.4
-40	0	79.4	61.2
-40	5	76.9	66.5
-40	10	74.4	71.6
-40	15	71.8	76.4

Unloading performance data of RWF II screw compressors

PLR (%)	***RWF II 177***	***RWF II 676***
	$\boldsymbol{FFLP_H}$ ***(%)***	$\boldsymbol{FFLP_B}$ ***(%)***
100	100	100
90	93.84	92.91
80	87.45	85.21
70	80.96	77.2
60	74.6	69.2
50	68.43	61.44
40	62.66	54.24
30	57.44	47.82
20	52.87	42.42
12	49.89	39.14

A-2: Cascade Heat Exchanger Data

$\Delta T_{cascade}$	$N_{tube,pass}$	$N_{tube,cas}$	$f_{sat,cas}$	$f_{sh,cas}$	$L_{tube,pass}$		L_{shell}	
					(m)	*(ft)*	*(m)*	*(ft)*
15	420	1680	0.8621	0.1379	8.019	26.31	9.382	30.78
14	463	1850	0.8679	0.1321	8.417	27.61	9.848	32.31
13	514	2054	0.8739	0.1261	8.867	29.09	10.37	34.04
12	575	2299	0.8801	0.1199	9.381	30.78	10.98	36.01
11	650	2599	0.8866	0.1134	9.975	32.73	11.67	38.29
10	744	2973	0.8933	0.1067	10.67	35.01	12.48	40.96
9	863	3452	0.9003	0.0997	11.5	37.72	13.45	44.13
8	1020	4081	0.9076	0.09236	12.5	41.01	14.62	47.98
7	1234	4936	0.9154	0.08461	13.75	45.1	16.08	52.77
6	1538	6151	0.9236	0.07638	15.35	50.35	17.95	58.91
5	1997	7987	0.9324	0.06756	17.49	57.37	20.46	67.12

$\Delta T_{cascade}$	D_{shell}		hc_{NH3}	$hc_{CO2,sat}$	$hc_{CO2,sh}$	A_{shell}	
	(m)	*(ft)*	*(kW/m^2-K)*	*(kW/m^2-K)*	*(kW/m2-K)*	*(m^2)*	*(ft^2)*
15	1.004	3.294	0.6212	2.865	0.371	0.7915	8.52
14	1.054	3.457	0.5726	2.661	0.3417	0.872	9.386
13	1.11	3.642	0.5246	2.458	0.3126	0.9678	10.42
12	1.174	3.853	0.4772	2.255	0.2844	1.083	11.66
11	1.249	4.097	0.4304	2.052	0.2568	1.225	13.18
10	1.336	4.382	0.3843	1.85	0.2297	1.401	15.08
9	1.439	4.722	0.339	1.648	0.2031	1.627	17.51
8	1.565	5.134	0.2946	1.447	0.1769	1.923	20.7
7	1.721	5.646	0.2511	1.248	0.1514	2.326	25.04
6	1.921	6.303	0.2088	1.051	0.1265	2.899	31.2
5	2.189	7.182	0.1678	0.8564	0.1023	3.764	40.51

$\Delta T_{cascade}$	$UA_{cascade,sat}$		$UA_{cascade,sh}$		A_{tube}	
	(kW/K)	*(MBtu/hr-F)*	*(kW/K)*	*(MBtu/hr-F)*	*(m^2)*	*(ft^2)*
15	283.1	536.6	19.19	36.37	0.3324	3.578
14	304.5	577.2	19.58	37.12	0.3662	3.942
13	329.2	624.1	20.02	37.95	0.4065	4.375
12	358	678.7	20.51	38.88	0.4549	4.897
11	392.1	743.2	21.06	39.92	0.5144	5.536
10	432.9	820.6	21.68	41.1	0.5885	6.335
9	482.8	915.2	22.4	42.45	0.6833	7.355
8	545.1	1033	23.22	44.02	0.8077	8.694
7	625.3	1185	24.19	45.85	0.9769	10.52
6	732.1	1388	25.35	48.05	1.217	13.1
5	881.7	1671	26.77	50.74	1.581	17.02

Appendix B – Annual Energy Usage

B-1: Geographical Location

Miami, FL.

Miami, FL. (-40^{o}F)			
Parameter	***Cascade system (Simplified)***	***Compound system (Simplified)***	***Compound system (Root-Product)***
Average head pressure	170.8 psia	169.6 psia	169.8 psia
Highest head pressure	199.7 psia	198.2 psia	198.5 psia
Average intermediate condition	10.7^{o}F 261.3 K	372.9 kPa	288.5 kPa
Average COP	1.79	1.949	1.914
Highest COP	2.034	2.183	2.139
Total kWh (8-hr day)	4,014,429 kWh	3,689,828 kWh	3,754,237 kWh
Total kWh (10-hr day)	4,996,862 kWh	4,594,394 kWh	4,674,969 kWh

Miami, FL. (-45^{o}F)			
Parameter	***Cascade system (Simplified)***	***Compound system (Simplified)***	***Compound system (Root-Product)***
Average head pressure	171.8 psia	170.8 psia	171.1 psia
Highest head pressure	200.8 psia	199.6 psia	199.9 psia
Average intermediate condition	8.49^{o}F 260.1 K	346.1 kPa	269.2 kPa
Average COP	1.684	1.784	1.757
Highest COP	1.912	2	1.964
Total kWh (8-hr day)	4,260,752 kWh	4,022,502 kWh	4,083,206 kWh
Total kWh (10-hr day)	5,303,883 kWh	5,009,072 kWh	5,085,088 kWh

Miami, FL. (-50^{o}F)			
Parameter	***Cascade system (Simplified)***	***Compound system (Simplified)***	***Compound system (Root-Product)***
Average head pressure	172.8 psia	172.3 psia	172.5 psia
Highest head pressure	201.9 psia	201.2 psia	201.4 psia
Average intermediate condition	6.54^{o}F 259 K	323.4 kPa	250.4 kPa
Average COP	1.583	1.631	1.606
Highest COP	1.797	1.829	1.796
Total kWh (8-hr day)	4,526,870 kWh	4,392,231 kWh	4,458,110 kWh
Total kWh (10-hr day)	5,635,598 kWh	5,469,977 kWh	5,552,505 kWh

Miami, FL. (-55^{o}F)			
Parameter	***Cascade system (Simplified)***	***Compound system (Simplified)***	***Compound system (Root-Product)***
Average head pressure	173.9 psia	173.9 psia	174.2 psia
Highest head pressure	203.1 psia	202.9 psia	203.2 psia
Average intermediate condition	4.87^{o}F 258.1 K	304.8 kPa	232.4 kPa
Average COP	1.794	1.491	1.467
Highest COP	2.035	1.674	1.642
Total kWh (8-hr day)	4,806541 kWh	4,795,805 kWh	4,871,780 kWh
Total kWh (10-hr day)	5,984,247 kWh	5,973,126 kWh	6,068,307 kWh

Miami, FL. (-60^{o}F)			
Parameter	***Cascade system (Simplified)***	***Compound system (Simplified)***	***Compound system (Root-Product)***
Average head pressure	175.1 psia	175.5 psia	175.9 psia
Highest head pressure	204.3 psia	204.6 psia	205 psia
Average intermediate condition	3.48^{o}F 257.3 K	290 kPa	215.1 kPa
Average COP	1.401	1.367	1.249
Highest COP	1.591	1.537	1.503
Total kWh (8-hr day)	5,102224 kWh	5,221,182 kWh	5,316,838 kWh
Total kWh (10-hr day)	6,352,930 kWh	6,503,547 kWh	6,623,339 kWh

Miami, FL. (-65^{o}F)			
Parameter	***Cascade system (Simplified)***	***Compound system (Simplified)***	***Compound system (Root-Product)***
Average head pressure	176.2 psia	177.2 psia	177.7 psia
Highest head pressure	205.5 psia	206.4 psia	206.9 psia
Average intermediate condition	2.42^{o}F 256.7 K	279.2 kPa	198.5 kPa
Average COP	1.325	1.264	1.234
Highest COP	1.505	1.421	1.381
Total kWh (8-hr day)	5,389,051 kWh	5,640,470 kWh	5,774,651 kWh
Total kWh (10-hr day)	6,710,674 kWh	7,026,484 kWh	7,194,401 kWh

Madison, WI.

Madison, WI. (-40°F)			
Parameter	***Cascade system (Simplified)***	***Compound system (Simplified)***	***Compound system (Root-Product)***
Average head pressure	142 psia	141.6 psia	141.7 psia
Highest head pressure	195.7 psia	194.3 psia	194.5 psia
Average intermediate condition	7.25°F 259.4 K	347 kPa	263.8 kPa
Average COP	1.983	2.134	2.094
Highest COP	2.035	2.183	2.143
Total kWh (8-hr day)	3,613,606 kWh	3,359,092 kWh	3,421,913 kWh
Total kWh (10-hr day)	4,502,605 kWh	4,186,742 kWh	4,265,309 kWh

Madison, WI. (-45°F)			
Parameter	***Cascade system (Simplified)***	***Compound system (Simplified)***	***Compound system (Root-Product)***
Average head pressure	142.4 psia	142 psia	142.2 psia
Highest head pressure	196.8 psia	195.7 psia	195.9 psia
Average intermediate condition	4.971°F 258.1 K	321.7 kPa	245.2 kPa
Average COP	1.863	1.954	1.917
Highest COP	1.912	2	1.964
Total kWh (8-hr day)	3,843,782 kWh	3,662,539 kWh	3,431,532 kWh
Total kWh (10-hr day)	4,789,546 kWh	4,565,052 kWh	4,651,368 kWh

Madison, WI. (-50°F)			
Parameter	***Cascade system (Simplified)***	***Compound system (Simplified)***	***Compound system (Root-Product)***
Average head pressure	142.8 psia	142.6 psia	142.7 psia
Highest head pressure	197.9 psia	197.2 psia	197.5 psia
Average intermediate condition	2.976°F 257 K	300.3 kPa	227.7 kPa
Average COP	1.75	1.786	1.755
Highest COP	1.797	1.829	1.796
Total kWh (8-hr day)	4,088,863 kWh	4,002,390 kWh	4,072,117 kWh
Total kWh (10-hr day)	5,095,088 kWh	4,988,744 kWh	5,076,052 kWh

Madison, WI. (-55^{o}F)			
Parameter	***Cascade system (Simplified)***	***Compound system (Simplified)***	***Compound system (Root-Product)***
Average head pressure	143.2 psia	143.2 psia	143.3 psia
Highest head pressure	199.1 psia	198.9 psia	199.2 psia
Average intermediate condition	1.288^{o}F 256.1 K	283 kPa	210.7 kPa
Average COP	1.645	1.633	1.602
Highest COP	1.691	1.674	1.642
Total kWh (8-hr day)	4,344,508 kWh	4,373,497 kWh	4,454,519 kWh
Total kWh (10-hr day)	5,413,805 kWh	5,451,405 kWh	5,552,867 kWh

Madison, WI. (-60^{o}F)			
Parameter	***Cascade system (Simplified)***	***Compound system (Simplified)***	***Compound system (Root-Product)***
Average head pressure	143.7 psia	143.9 psia	144.1 psia
Highest head pressure	200.3 psia	200.7 psia	201.1 psia
Average intermediate condition	-0.14^{o}F 255.3 K	269.7 kPa	194.6 kPa
Average COP	1.547	1.497	1.465
Highest COP	1.591	1.537	1.503
Total kWh (8-hr day)	4,616,583 kWh	4,765,402 kWh	4,867,104 kWh
Total kWh (10-hr day)	5,752,987 kWh	5,939,956 kWh	6,067,303 kWh

Madison, WI. (-65^{o}F)			
Parameter	***Cascade system (Simplified)***	***Compound system (Simplified)***	***Compound system (Root-Product)***
Average head pressure	144.1 psia	144.6 psia	144.8 psia
Highest head pressure	201.6 psia	202.5 psia	203 psia
Average intermediate condition	-1.24^{o}F 258.2 K	260.5 kPa	179.2 kPa
Average COP	1.46	1.383	1.346
Highest COP	1.503	1.421	1.381
Total kWh (8-hr day)	4,887,565 kWh	5,153,302 kWh	5,293,812 kWh
Total kWh (10-hr day)	6,090,841 kWh	6,423,587 kWh	6,599,458 kWh

Los Angeles, CA.

Los Angeles, CA. (-40°F)			
Parameter	***Cascade system (Simplified)***	***Compound system (Simplified)***	***Compound system (Root-Product)***
Average head pressure	144.8 psia	144 psia	144.1 psia
Highest head pressure	175.6 psia	174.2 psia	174.5 psia
Average intermediate condition	7.56°F 259.6 K	349.4 kPa	266.5 kPa
Average COP	1.957	2.115	2.077
Highest COP	2.034	2.183	2.143
Total kWh (8-hr day)	3,681,408 kWh	3,407,778 kWh	3,467,750 kWh
Total kWh (10-hr day)	4,574,045 kWh	4,236,613 kWh	4,311,662 kWh

Los Angeles, CA. (-45°F)			
Parameter	***Cascade system (Simplified)***	***Compound system (Simplified)***	***Compound system (Root-Product)***
Average head pressure	145.5 psia	144.9 psia	145.1 psia
Highest head pressure	176.6 psia	175.6 psia	175.8 psia
Average intermediate condition	5.33°F 258.3 K	324.1 kPa	248.1 kPa
Average COP	1.837	1.933	1.9
Highest COP	1.912	2	1.964
Total kWh (8-hr day)	3,917,658 kWh	3,721,740 kWh	3,785,398 kWh
Total kWh (10-hr day)	4,867,619 kWh	4,626,870 kWh	4,706,628 kWh

Los Angeles, CA. (-50°F)			
Parameter	***Cascade system (Simplified)***	***Compound system (Simplified)***	***Compound system (Root-Product)***
Average head pressure	146.3 psia	146 psia	146.2 psia
Highest head pressure	177.6 psia	177.1 psia	177.3 psia
Average intermediate condition	3.42°F 257.3 K	303 kPa	230.5 kPa
Average COP	1.726	1.764	1.733
Highest COP	1.797	1.829	1.796
Total kWh (8-hr day)	4,165,225 kWh	4,071,546 kWh	4,141,398 kWh
Total kWh (10-hr day)	5,175,278 kWh	5,061,681 kWh	5,149,301 kWh

Los Angeles, CA. (-55^{o}F)			
Parameter	***Cascade system (Simplified)***	***Compound system (Simplified)***	***Compound system (Root-Product)***
Average head pressure	147.2 psia	147.2 psia	147.5 psia
Highest head pressure	178.8 psia	178.7 psia	179 psia
Average intermediate condition	1.75^{o}F 256.3 K	285.8 kPa	213.8 kPa
Average COP	1.619	1.61	1.58
Highest COP	1.691	1.674	1.642
Total kWh (8-hr day)	4,434,126 kWh	4,454,565 kWh	4,535,484 kWh
Total kWh (10-hr day)	5,509,463 kWh	5,537,791 kWh	5,639,363 kWh

Los Angeles, CA. (-60^{o}F)			
Parameter	***Cascade system (Simplified)***	***Compound system (Simplified)***	***Compound system (Root-Product)***
Average head pressure	148.1 psia	148.6 psia	149 psia
Highest head pressure	180 psia	180.5 psia	180.8 psia
Average intermediate condition	0.396^{o}F 255.6 K	272.8 kPa	198 kPa
Average COP	1.522	1.474	1.443
Highest COP	1.591	1.537	1.503
Total kWh (8-hr day)	4,712,008 kWh	4,860,032 kWh	4,961,449 kWh
Total kWh (10-hr day)	5,854,874 kWh	6,041,853 kWh	6,169,152 kWh

Los Angeles, CA. (-65^{o}F)			
Parameter	***Cascade system (Simplified)***	***Compound system (Simplified)***	***Compound system (Root-Product)***
Average head pressure	149.1 psia	150 psia	150.5 psia
Highest head pressure	181.2 psia	182.2 psia	182.7 psia
Average intermediate condition	-0.66^{o}F 255 K	263.6 kPa	182.9 kPa
Average COP	1.435	1.359	1.323
Highest COP	1.503	1.421	1.381
Total kWh (8-hr day)	4,992,627 kWh	5,262,106 kWh	5,402,425 kWh
Total kWh (10-hr day)	6,203,785 kWh	6,541,809 kWh	6,717,814 kWh

Houston, TX.

Houston, TX. (-40°F)			
Parameter	***Cascade system (Simplified)***	***Compound system (Simplified)***	***Compound system (Root-Product)***
Average head pressure	161.5 psia	160.5 psia	160.7 psia
Highest head pressure	203.7 psia	202.2 psia	202.4 psia
Average intermediate condition	9.56°F 260.7 K	364.2 kPa	280.5 kPa
Average COP	1.852	2.008	1.972
Highest COP	2.032	2.183	2.139
Total kWh (8-hr day)	3,897,014 kWh	3,594,144 kWh	3,655,789 kWh
Total kWh (10-hr day)	4,845,089 kWh	4,470,637 kWh	4,547,760 kWh

Houston, TX. (-45°F)			
Parameter	***Cascade system (Simplified)***	***Compound system (Simplified)***	***Compound system (Root-Product)***
Average head pressure	162.6 psia	161.5 psia	161.7 psia
Highest head pressure	204.8 psia	203.6 psia	203.8 psia
Average intermediate condition	7.351°F 259.5 K	338.2 kPa	261.5 kPa
Average COP	1.742	1.839	1.81
Highest COP	1.912	2	1.964
Total kWh (8-hr day)	4,137,345 kWh	3,915,851 kWh	3,977,420 kWh
Total kWh (10-hr day)	5,144,252 kWh	4,871,164 kWh	4,948,278 kWh

Houston, TX. (-50°F)			
Parameter	***Cascade system (Simplified)***	***Compound system (Simplified)***	***Compound system (Root-Product)***
Average head pressure	163.1 psia	162.7 psia	162.9 psia
Highest head pressure	205.9 psia	205.1 psia	205.4 psia
Average intermediate condition	5.385°F 258.4 K	315.7 kPa	243 kPa
Average COP	1.637	1.68	1.654
Highest COP	1.797	1.829	1.796
Total kWh (8-hr day)	4,396,997 kWh	4,280,159 kWh	4,344,000 kWh
Total kWh (10-hr day)	5,467,488 kWh	5,324,755 kWh	5,404,780 kWh

Houston, TX. (-55^{o}F)			
Parameter	***Cascade system (Simplified)***	***Compound system (Simplified)***	***Compound system (Root-Product)***
Average head pressure	164 psia	163.9 psia	164.2 psia
Highest head pressure	207.1 psia	206.9 psia	207.2 psia
Average intermediate condition	3.712^{o}F 257.4 K	297.7 kPa	225.4 kPa
Average COP	1.54	1.537	1.511
Highest COP	1.691	1.674	1.642
Total kWh (8-hr day)	4,669,938 kWh	4,671,025 kWh	4,748,625 kWh
Total kWh (10-hr day)	5,807,334 kWh	5,811,474 kWh	5,908,756 kWh

Houston, TX. (-60^{o}F)			
Parameter	***Cascade system (Simplified)***	***Compound system (Simplified)***	***Compound system (Root-Product)***
Average head pressure	164.9 psia	165.3 psia	165.6 psia
Highest head pressure	208.3 psia	208.7 psia	209 psia
Average intermediate condition	2.308^{o}F 256.7 K	283.5 kPa	208.5 kPa
Average COP	1.448	1.409	1.382
Highest COP	1.591	1.537	1.503
Total kWh (8-hr day)	4,958,670 kWh	5,086,737 kWh	5,184,370 kWh
Total kWh (10-hr day)	6,166,942 kWh	6,329,245 kWh	6,451,588 kWh

Houston, TX. (-65^{o}F)			
Parameter	***Cascade system (Simplified)***	***Compound system (Simplified)***	***Compound system (Root-Product)***
Average head pressure	165.9 psia	166.7 psia	167.1 psia
Highest head pressure	209.6 psia	210.4 psia	211 psia
Average intermediate condition	1.224^{o}F 256.1 K	273.1 kPa	192.3 kPa
Average COP	1.368	1.302	1.27
Highest COP	1.503	1.421	1.381
Total kWh (8-hr day)	5,245,184 kWh	5,497,143 kWh	5,633,482 kWh
Total kWh (10-hr day)	6,523,880 kWh	6,840,507 kWh	7,011,204 kWh

B-2: Compound System (Effects of Head Pressure)

Simplified Optimization Method

Cascade system 8-hour day (simplified method)							
$T_{evap,sat}$ *(F)*	*135 psia (kWh)*	*140 psia (kWh)*	*150 psia (kWh)*	*160 psia (kWh)*	*170 psia (kWh)*	*180 psia (kWh)*	*190 psia (kWh)*
-40	3276734	3336882	3454013	3567272	3677022	3783572	3887190
-45	3569867	3633466	3757443	3877478	3993936	4107130	4217330
-50	3894859	3962113	4093354	4220594	4344198	4464481	4581715
-55	4248975	4319990	4458711	4593377	4724355	4851963	4976472
-60	4622181	4696855	4842854	4984745	5122902	5257642	5389241
-65	4991210	5069087	5221449	5369654	5514080	5655051	5792845

Compound system 10-hour day (simplified method)							
$T_{evap,sat}$ *(F)*	*135 psia (kWh)*	*140 psia (kWh)*	*150 psia (kWh)*	*160 psia (kWh)*	*170 psia (kWh)*	*180 psia (kWh)*	*190 psia (kWh)*
-40	4095917	4171102	4317516	4459090	4596277	4729465	4858987
-45	4462334	4541832	4696803	4846847	4992420	5133913	5271663
-50	4868574	4952641	5116693	5275742	5430247	5580602	5727144
-55	5311218	5399987	5573389	5741721	5905444	6064953	6220590
-60	5777727	5871069	6053567	6230932	6403628	6572053	6736551
-65	6239012	6336359	6526811	6712068	6892600	7068813	7241056

Root-Product Method

Cascade system 8-hour day (root-product method)							
$T_{evap,sat}$ *(F)*	*135 psia (kWh)*	*140 psia (kWh)*	*150 psia (kWh)*	*160 psia (kWh)*	*170 psia (kWh)*	*180 psia (kWh)*	*190 psia (kWh)*
-40	3336025	3395318	3511075	3623346	3732436	3838612	3942111
-45	3633371	3695757	3817759	3936331	4051757	4164290	4274157
-50	3965163	4030806	4159416	4284690	4406887	4526239	4642961
-55	4330961	4399899	4535237	4667390	4796580	4923017	5046895
-60	4725086	4797122	4938862	5077642	5213643	5347043	5478013
-65	5132712	5207278	5354375	5498848	5640825	5780446	5917856

Compound system 10-hour day (root-product method)							
$T_{evap,sat}$ *(F)*	*135 psia (kWh)*	*140 psia (kWh)*	*150 psia (kWh)*	*160 psia (kWh)*	*170 psia (kWh)*	*180 psia (kWh)*	*190 psia (kWh)*
-40	4170031	4244147	4388844	4529183	4665545	4798265	4927639
-45	4541714	4619697	4772199	4920414	5064697	5205363	5342697
-50	4956453	5038508	5199270	5355863	5508608	5657799	5803702
-55	5413701	5499873	5669047	5834238	5995725	6153771	6308618
-60	5906358	5996402	6173577	6347053	6517054	6683803	6847517
-65	6415890	6509098	6692969	6873560	7051032	7225557	7397319

B-3: Cascade System (Effects of Pinch-Point Temperature Difference)

$\Delta T_{cascade} = 12^oF$

Cascade system 8-hour day ($\Delta T_{cascade} = 12^oF$)							
$T_{evap,sat}$ (F)	*135 psia (kWh)*	*140 psia (kWh)*	*150 psia (kWh)*	*160 psia (kWh)*	*170 psia (kWh)*	*180 psia (kWh)*	*190 psia (kWh)*
-40	3588162	3658623	3796442	3930426	4060893	4188112	4312317
-45	3811275	3884269	4027186	4166306	4301943	4434363	4563802
-50	4047508	4123067	4271146	4415464	4556330	4694011	4828738
-55	4295610	4373720	4526924	4676401	4822454	4965346	5105310
-60	4552783	4633333	4791438	4945839	5096835	5244687	5389627
-65	4813428	4896147	5058597	5217344	5372690	5524893	5674185

Cascade system 10-hour day ($\Delta T_{cascade} = 12^oF$)							
$T_{evap,sat}$ (F)	*135 psia (kWh)*	*140 psia (kWh)*	*150 psia (kWh)*	*160 psia (kWh)*	*170 psia (kWh)*	*180 psia (kWh)*	*190 psia (kWh)*
-40	4485203	4573279	4745552	4913033	5076117	5235140	5390397
-45	4764093	4855337	5033983	5207883	5377428	5542954	5704753
-50	5059384	5153834	5338932	5519330	5695412	5867513	6035922
-55	5369513	5467149	5658655	5845501	6028067	6206683	6381637
-60	5690979	5791666	5989298	6182298	6371043	6555859	6737033
-65	6016785	6120184	6323246	6521680	6715862	6906116	7092731

$\Delta T_{cascade} = 11^oF$

Cascade system 8-hour day ($\Delta T_{cascade} = 11^oF$)							
$T_{evap,sat}$ (F)	*135 psia (kWh)*	*140 psia (kWh)*	*150 psia (kWh)*	*160 psia (kWh)*	*170 psia (kWh)*	*180 psia (kWh)*	*190 psia (kWh)*
-40	3548466	3618430	3755250	3888228	4017682	4143884	4267069
-45	3769538	3842010	3983872	4121925	4256482	4387813	4516153
-50	4003615	4078626	4225593	4368784	4508505	4645026	4778578
-55	4249529	4327063	4479102	4627391	4772235	4913899	5052613
-60	4504635	4584584	4741472	4894630	5044357	5190917	5334540
-65	4763601	4845699	5006891	5164353	5318383	5469244	5561474

Cascade system 10-hour day ($\Delta T_{cascade} = 11^oF$)							
$T_{evap,sat}$ (F)	*135 psia (kWh)*	*140 psia (kWh)*	*150 psia (kWh)*	*160 psia (kWh)*	*170 psia (kWh)*	*180 psia (kWh)*	*190 psia (kWh)*
-40	4435582	4523038	4694062	4860285	5022103	5179855	5333836
-45	4711923	4802513	4979840	5152406	5320603	5484767	5645192
-50	5004518	5098282	5281992	5460979	5635632	5806282	5973222
-55	5311912	5408829	5598877	5784239	5965294	6142373	6315766
-60	5630794	5730731	5926841	6118287	6305447	6488647	6668174
-65	5954500	6057124	6258613	6455441	6647979	6836555	6951843

$\Delta T_{cascade} = 10^{o}F$

Cascade system 8-hour day ($\Delta T_{cascade} = 10^{o}F$)							
$T_{evap,sat}$ (F)	***135 psia (kWh)***	***140 psia (kWh)***	***150 psia (kWh)***	***160 psia (kWh)***	***170 psia (kWh)***	***180 psia (kWh)***	***190 psia (kWh)***
-40	3509390	3578870	3714717	3846715	3975183	4100394	4222585
-45	3728484	3800447	3941283	4078299	4211807	4342079	4469351
-50	3960472	4034949	4180839	4322934	4461546	4596940	4729353
-55	4204271	4281246	4432154	4579293	4722966	4863440	5000946
-60	4462511	4536750	4692459	4844414	4992916	5138227	5280577
-65	4714749	4796233	4956205	5112425	5265188	5414754	5561353

Cascade system 10-hour day ($\Delta T_{cascade} = 10^{o}F$)							
$T_{evap,sat}$ (F)	***135 psia (kWh)***	***140 psia (kWh)***	***150 psia (kWh)***	***160 psia (kWh)***	***170 psia (kWh)***	***180 psia (kWh)***	***190 psia (kWh)***
-40	4386737	4473588	4643396	4808394	4968978	5125492	5278231
-45	4660605	4750559	4926604	5097873	5264758	5427599	5586689
-50	4950590	5043687	5226048	5403668	5576932	5746176	5911692
-55	5255339	5351558	5540193	5724116	5903708	6079300	6251182
-60	5578139	5670938	5865574	6055518	6241145	6422783	6600721
-65	5893436	5995291	6195257	6390532	6581485	6768442	6951691

$\Delta T_{cascade} = 9^{o}F$

Cascade system 8-hour day ($\Delta T_{cascade} = 9^{o}F$)							
$T_{evap,sat}$ (F)	***135 psia (kWh)***	***140 psia (kWh)***	***150 psia (kWh)***	***160 psia (kWh)***	***170 psia (kWh)***	***180 psia (kWh)***	***190 psia (kWh)***
-40	3470732	3539739	3674632	3805670	3933173	4057415	4178635
-45	3687897	3759364	3899197	4035198	4167681	4296919	4423150
-50	3917852	3991809	4136646	4277673	4415202	4549500	4680802
-55	4159594	4236025	4385831	4531849	4674384	4813700	4950030
-60	4410782	4489574	4644134	4794920	4942231	5086328	5227444
-65	4666538	4747475	4906267	5061280	5212813	5361123	5506443

Cascade system 10-hour day ($\Delta T_{cascade} = 9^{o}F$)							
$T_{evap,sat}$ (F)	***135 psia (kWh)***	***140 psia (kWh)***	***150 psia (kWh)***	***160 psia (kWh)***	***170 psia (kWh)***	***180 psia (kWh)***	***190 psia (kWh)***
-40	4338415	4424673	4593290	4757088	4916467	5071769	5223294
-45	4609872	4699204	4873996	5043997	5209602	5371149	5528937
-50	4897315	4989761	5170807	5347091	5519002	5686875	5851003
-55	5199492	5295031	5482289	5664812	5842980	6017125	6187538
-60	5513477	5611967	5805168	5993650	6177789	6357910	6534305
-65	5833172	5934344	6132833	6326600	6516016	6701404	6883053

$\Delta T_{cascade} = 8^oF$

Cascade system 8-hour day ($\Delta T_{cascade} = 8^oF$)							
$T_{evap,sat}$ (F)	***135 psia (kWh)***	***140 psia (kWh)***	***150 psia (kWh)***	***160 psia (kWh)***	***170 psia (kWh)***	***180 psia (kWh)***	***190 psia (kWh)***
-40	3432716	3501262	3635228	3765333	3891898	4015198	4135474
-45	3648012	3718996	3857855	3992871	4124360	4252594	4377814
-50	3875997	3949450	4093266	4233258	4369737	4502973	4633201
-55	4115753	4191681	4340395	4485329	4626761	4764957	4900152
-60	4365052	4443322	4596769	4746425	4892585	5035512	5175436
-65	4619294	4699670	4857354	5011201	5161546	5308647	5452734

Cascade system 10-hour day ($\Delta T_{cascade} = 8^oF$)							
$T_{evap,sat}$ (F)	***135 psia (kWh)***	***140 psia (kWh)***	***150 psia (kWh)***	***160 psia (kWh)***	***170 psia (kWh)***	***180 psia (kWh)***	***190 psia (kWh)***
-40	4290895	4376577	4544035	4706666	4864872	5018997	5169342
-45	4560015	4648744	4822318	4991088	5155449	5315743	5472267
-50	4844997	4936812	5116582	5291573	5462172	5628716	5791501
-55	5144692	5239601	5425494	5606661	5783451	5956196	6125190
-60	5456316	5554152	5745962	5933031	6115732	6294390	6469295
-65	5774118	5874587	6071693	6264001	6451933	6635809	6815917

$\Delta T_{cascade} = 7^oF$

Cascade system 8-hour day ($\Delta T_{cascade} = 7^oF$)							
$T_{evap,sat}$ (F)	***135 psia (kWh)***	***140 psia (kWh)***	***150 psia (kWh)***	***160 psia (kWh)***	***170 psia (kWh)***	***180 psia (kWh)***	***190 psia (kWh)***
-40	3395073	3463167	3596225	3725417	3851064	3973443	4092795
-45	3608545	3679056	3816962	3951015	4081533	4208787	4333020
-50	3834611	3907569	4050388	4189370	4324826	4457025	4586205
-55	4072429	4147827	4295517	4439394	4579753	4716859	4850948
-60	4324917	4397630	4550024	4698575	4843616	4985405	5124171
-65	4572671	4652502	4809079	4961824	5111012	5256939	5399830

Cascade system 10-hour day ($\Delta T_{cascade} = 7^oF$)							
$T_{evap,sat}$ (F)	***135 psia (kWh)***	***140 psia (kWh)***	***150 psia (kWh)***	***160 psia (kWh)***	***170 psia (kWh)***	***180 psia (kWh)***	***190 psia (kWh)***
-40	4243842	4328959	4495282	4656772	4813830	4966803	5115994
-45	4510681	4598819	4771202	4938769	5101916	5260984	5416274
-50	4793264	4884462	5062985	5236713	5406032	5571281	5732756
-55	5090536	5184783	5369397	5549242	5724691	5896074	6063685
-60	5406146	5497037	5687530	5873219	6054521	6231756	6405214
-65	5715839	5815627	6011348	6202280	6388765	6571174	6749787

$\Delta T_{cascade} = 6^oF$

Cascade system 8-hour day ($\Delta T_{cascade} = 6^oF$)							
$T_{evap,sat}$ (F)	***135 psia (kWh)***	***140 psia (kWh)***	***150 psia (kWh)***	***160 psia (kWh)***	***170 psia (kWh)***	***180 psia (kWh)***	***190 psia (kWh)***
-40	3358004	3425658	3557832	3686134	3810887	3932370	4050825
-45	3569702	3639754	3776734	3909852	4039425	4165728	4289001
-50	3793909	3866386	4008237	4146238	4280700	4411895	4540059
-55	4029834	4104734	4251432	4394282	4533600	4669652	4802671
-60	4275541	4352762	4504111	4651621	4795574	4936262	5073910
-65	4526905	4606210	4761716	4913370	5061471	5206259	5347996

Cascade system 10-hour day ($\Delta T_{cascade} = 6^oF$)							
$T_{evap,sat}$ (F)	***135 psia (kWh)***	***140 psia (kWh)***	***150 psia (kWh)***	***160 psia (kWh)***	***170 psia (kWh)***	***180 psia (kWh)***	***190 psia (kWh)***
-40	4197505	4282072	4447290	4607668	4763609	4915462	5063532
-45	4462128	4549692	4720917	4887314	5049281	5207159	5361252
-50	4742386	4832983	5010296	5182797	5350875	5514869	5675074
-55	5037292	5130918	5314290	5492852	5667000	5837065	6003338
-60	5344426	5440952	5630138	5814526	5994468	6170328	6342387
-65	5658631	5757762	5952145	6141712	6326838	6507823	6684995

$\Delta T_{cascade} = 5^oF$

Cascade system 8-hour day ($\Delta T_{cascade} = 5^oF$)							
$T_{evap,sat}$ (F)	***135 psia (kWh)***	***140 psia (kWh)***	***150 psia (kWh)***	***160 psia (kWh)***	***170 psia (kWh)***	***180 psia (kWh)***	***190 psia (kWh)***
-40	3321441	3388666	3519978	3647414	3771297	3891906	4009488
-45	3531416	3601019	3737097	3869305	3997959	4123337	4245679
-50	3753807	3825825	3966732	4103781	4237279	4367497	4494676
-55	3987905	4062321	4208046	4349907	4488217	4623245	4755227
-60	4231908	4308629	4458965	4605444	4748366	4887985	5024552
-65	4481904	4560698	4715171	4865770	5012795	5156507	5297125

Cascade system 10-hour day ($\Delta T_{cascade} = 5^oF$)							
$T_{evap,sat}$ (F)	***135 psia (kWh)***	***140 psia (kWh)***	***150 psia (kWh)***	***160 psia (kWh)***	***170 psia (kWh)***	***180 psia (kWh)***	***190 psia (kWh)***
-40	4151802	4235832	4399973	4559268	4714121	4864883	5011860
-45	4414270	4501274	4671372	4836631	4997449	5154171	5307098
-50	4692259	4782282	4958415	5129726	5296598	5459371	5618344
-55	4984881	5077902	5260057	5437384	5610271	5779056	5944034
-60	5289885	5385786	5573706	5756806	5935458	6109981	6280690
-65	5602380	5700873	5893964	6082212	6265993	6445634	6621406

Appendix C – Premium Difference

C-1: Geographical Location

Cascade system and compound simplified method (8-hour day)				
$T_{evap,sat}$ (F)	***Miami, FL. ($)***	***Houston, TX. ($)***	***Los Angeles, CA. ($)***	***Madison, WI. ($)***
-40	141266	131809	119083	110764
-45	103686	96394	85263	78877
-50	58595	50848	40769	37633
-55	4672	-473.1	-8895	-12616
-60	-51770	-55735	-64420	-64766
-65	-109417	-109652	-117277	-115648

Cascade system and compound simplified method (10-hour day)				
$T_{evap,sat}$ (F)	***Miami, FL. ($)***	***Houston, TX. ($)***	***Los Angeles, CA. ($)***	***Madison, WI. ($)***
-40	175154	162961	146850	137463
-45	128301	118848	104774	97700
-50	72078	62117	49437	46281
-55	4840	-1802	-12328	-16363
-60	-65548	-70634	-81373	-81369
-65	-137440	-137796	-147108	-144811

Cascade system and compound root-product method (8-hour day)				
$T_{evap,sat}$ (F)	***Miami, FL. ($)***	***Houston, TX. ($)***	***Los Angeles, CA. ($)***	***Madison, WI. ($)***
-40	113235	104981	92984	83425
-45	77268	69599	57559	48851
-50	29924	23064	10369	7288
-55	-28392	-34244	-44111	-47877
-60	-93400	-98224	-108556	-109026
-65	-167813	-168987	-178344	-176798

Cascade system and compound root-product method (10-hour day)				
$T_{evap,sat}$ (F)	***Miami, FL. ($)***	***Houston, TX. ($)***	***Los Angeles, CA. ($)***	***Madison, WI. ($)***
-40	140087	129397	114189	103271
-45	95219	85288	70063	60135
-50	36162	27290	11305	8284
-55	-36583	-44139	-56532	-60520
-60	-117682	-123878	-136773	-136790
-65	-210517	-212083	-223705	-221350

C-2: Effects of cascade pinch-point temperature difference

$\Delta T_{cascade} = 12^{o}F$

Cascade system and compound simplified method: 8-hour day ($\Delta T_{cascade} = 12^{o}F$)							
$T_{evap,sat}$ (F)	***135 psia ($)***	***140 psia ($)***	***150 psia ($)***	***160 psia ($)***	***170 psia ($)***	***180 psia ($)***	***190 psia ($)***
-40	135533	140021	149025	158044	167060	176055	185015
-45	105060	109149	117392	125698	134044	142411	150784
-50	66433	70047	77375	84807	92320	99891	107504
-55	20295	23383	29686	36132	42693	49344	56070
-60	-30202	-27645	-22376	-16932	-11344	-5638	168
-65	-77371	-75263	-70873	-66285	-61533	-56645	-51641

Cascade system and compound simplified method: 10-hour day ($\Delta T_{cascade} = 12^{o}F$)							
$T_{evap,sat}$ (F)	***135 psia ($)***	***140 psia ($)***	***150 psia ($)***	***160 psia ($)***	***170 psia ($)***	***180 psia ($)***	***190 psia ($)***
-40	169417	175027	186281	197555	208826	220069	231269
-45	131325	136437	146740	157122	167555	178014	188480
-50	83040	87559	96718	106009	115400	124863	134380
-55	25370	29229	37108	45165	53365	61681	70087
-60	-37753	-34556	-27970	-21165	-14181	-7048	209.8
-65	-96713	-94079	-88591	-82857	-76916	-70806	-64551

Cascade system and compound root-product method: 8-hour day ($\Delta T_{cascade} = 12^{o}F$)							
$T_{evap,sat}$ (F)	***135 psia ($)***	***140 psia ($)***	***150 psia ($)***	***160 psia ($)***	***170 psia ($)***	***180 psia ($)***	***190 psia ($)***
-40	109730	114590	124191	133641	142944	152102	161113
-45	77424	82040	91142	100085	108881	117535	126053
-50	35836	40152	48625	56913	65037	73014	80850
-55	-15385	-11393	-3618	3922	11260	18422	25422
-60	-74986	-71281	-64159	-57361	-50835	-44545	-38465
-65	-138952	-135404	-128722	-122510	-116692	-111216	-106045

Cascade system and compound root-product method: 10-hour day ($\Delta T_{cascade} = 12^{o}F$)							
$T_{evap,sat}$ (F)	***135 psia ($)***	***140 psia ($)***	***150 psia ($)***	***160 psia ($)***	***170 psia ($)***	***180 psia ($)***	***190 psia ($)***
-40	137162	143238	155239	167051	178680	190128	201392
-45	96779	102550	113928	125106	136100	146919	157566
-50	44795	50190	60781	71141	81297	91267	101062
-55	-19231	-14241	-4523	4902	14075	23027	31778
-60	-93733	-89101	-80198	-71701	-63544	-55681	-48083
-65	-173690	-169255	-160903	-153138	-145866	-139020	-132556

$\Delta T_{cascade} = 11^{o}F$

Cascade system and compound simplified method: 8-hour day ($\Delta T_{cascade} = 11^{o}F$)							
$T_{evap,sat}$ (F)	***135 psia ($)***	***140 psia ($)***	***150 psia ($)***	***160 psia ($)***	***170 psia ($)***	***180 psia ($)***	***190 psia ($)***
-40	118257	122529	131098	139680	148255	156807	165323
-45	86897	90758	98542	106383	114260	122153	130047
-50	47330	50706	57550	64492	71506	78573	85675
-55	241.1	3078	8874	14803	20837	26954	33136
-60	-51156	-48860	-44121	-39218	-34183	-29039	-23806
-65	-99055	-97218	-93375	-89347	-85167	-80863	-100692

Cascade system and compound simplified method: 10-hour day ($\Delta T_{cascade} = 11^{o}F$)							
$T_{evap,sat}$ (F)	***135 psia ($)***	***140 psia ($)***	***150 psia ($)***	***160 psia ($)***	***170 psia ($)***	***180 psia ($)***	***190 psia ($)***
-40	147822	153162	163872	174600	185319	196009	206654
-45	108621	113448	123177	132979	142825	152691	162559
-50	59163	63383	71938	80615	89383	98216	107093
-55	302	3848	11092	18504	26047	33693	41420
-60	-63945	-61075	-55151	-49023	-42728	-36298	-29758
-65	-123819	-121523	-116719	-111684	-106459	-101078	-125865

Cascade system and compound root-product method: 8-hour day ($\Delta T_{cascade} = 11^{o}F$)							
$T_{evap,sat}$ (F)	***135 psia ($)***	***140 psia ($)***	***150 psia ($)***	***160 psia ($)***	***170 psia ($)***	***180 psia ($)***	***190 psia ($)***
-40	92454	97098	106265	115276	124139	132854	141421
-45	59260	63649	72292	80770	89096	97277	105316
-50	16734	20811	28800	36598	44224	51696	59020
-55	-35439	-31698	-24430	-17408	-10595	-3968	2488
-60	-95940	-92496	-85904	-79647	-73673	-67946	-62439
-65	-160637	-157359	-151225	-145572	-140326	-135435	-155097

Cascade system and compound root-product method: 10-hour day ($\Delta T_{cascade} = 11^{o}F$)							
$T_{evap,sat}$ (F)	***135 psia ($)***	***140 psia ($)***	***150 psia ($)***	***160 psia ($)***	***170 psia ($)***	***180 psia ($)***	***190 psia ($)***
-40	115567	121373	132831	144095	155174	166068	176776
-45	74075	79561	90365	100963	111370	121596	131645
-50	20918	26014	36001	45746	55281	64620	73775
-55	-44298	-39622	-30538	-21760	-13244	-4960	3111
-60	-119925	-115620	-107379	-99559	-92091	-84932	-78050
-65	-200796	-196699	-189031	-181965	-175408	-169293	-193871

$\Delta T_{cascade} = 10^{o}F$

Cascade system and compound simplified method: 8-hour day ($\Delta T_{cascade} = 10^{o}F$)							
$T_{evap,sat}$ (F)	***135 psia ($)***	***140 psia ($)***	***150 psia ($)***	***160 psia ($)***	***170 psia ($)***	***180 psia ($)***	***190 psia ($)***
-40	101289	105351	113496	121653	129800	137922	146006
-45	69069	72710	80047	87438	94859	102293	109724
-50	28596	31740	38116	44582	51114	57692	64299
-55	-19412	-16818	-11513	-6084	-557.5	5043	10700
-60	-71676	-69632	-65405	-61024	-56521	-51920	-47240
-65	-120270	-118699	-115386	-111897	-108267	-104526	-100692

Cascade system and compound simplified method: 10-hour day ($\Delta T_{cascade} = 10^{o}F$)							
$T_{evap,sat}$ (F)	***135 psia ($)***	***140 psia ($)***	***150 psia ($)***	***160 psia ($)***	***170 psia ($)***	***180 psia ($)***	***190 psia ($)***
-40	126611	131689	141871	152066	162250	172402	182507
-45	86336	90887	100060	109298	118574	127866	137155
-50	35745	39675	47644	55728	63893	72115	80373
-55	-24265	-21022	-14391	-7605	-697.2	6303	13375
-60	-89594	-87040	-81756	-76281	-70651	-64900	-59050
-65	-150337	-148374	-144232	-139871	-135334	-130657	-125865

Cascade system and compound root-product method: 8-hour day ($\Delta T_{cascade} = 10^{o}F$)							
$T_{evap,sat}$ (F)	***135 psia ($)***	***140 psia ($)***	***150 psia ($)***	***160 psia ($)***	***170 psia ($)***	***180 psia ($)***	***190 psia ($)***
-40	75485	79919	88663	97250	105684	113969	122104
-45	41432	45601	53798	61826	69696	77417	84993
-50	-2001	1845	9365	16687	23832	30815	37645
-55	-55093	-51594	-44817	-38294	-31990	-25880	-19948
-60	-116460	-113268	-107188	-101453	-96011	-90827	-85873
-65	-181851	-178840	-173235	-168122	-163426	-159097	-155097

Cascade system and compound root-product method: 10-hour day ($\Delta T_{cascade} = 10^{o}F$)							
$T_{evap,sat}$ (F)	***135 psia ($)***	***140 psia ($)***	***150 psia ($)***	***160 psia ($)***	***170 psia ($)***	***180 psia ($)***	***190 psia ($)***
-40	94357	99899	110829	121561	132105	142461	152630
-45	51790	57001	67248	77282	87119	96771	106241
-50	-2500	2306	11707	20859	29790	38519	47055
-55	-68866	-64492	-56021	-47868	-39987	-32350	-24935
-60	-145574	-141585	-133985	-126817	-120014	-113533	-107342
-65	-227314	-223550	-216544	-210152	-204283	-198872	-193871

$\Delta T_{cascade} = 9^{o}F$

Cascade system and compound simplified method: 8-hour day ($\Delta T_{cascade} = 9^{o}F$)							
$T_{evap,sat}$ (F)	***135 psia ($)***	***140 psia ($)***	***150 psia ($)***	***160 psia ($)***	***170 psia ($)***	***180 psia ($)***	***190 psia ($)***
-40	84428	88283	96013	103751	111477	119176	126837
-45	51367	54791	61691	68640	75614	82596	89573
-50	10007	12924	18841	24841	30901	37000	43123
-55	-38899	-36541	-31717	-26777	-21747	-16652	-11508
-60	-92001	-90208	-86483	-82612	-78628	-74556	-70414
-65	-141297	-139965	-137167	-134204	-131111	-127917	-124642

Cascade system and compound simplified method: 10-hour day ($\Delta T_{cascade} = 9^{o}F$)							
$T_{evap,sat}$ (F)	***135 psia ($)***	***140 psia ($)***	***150 psia ($)***	***160 psia ($)***	***170 psia ($)***	***180 psia ($)***	***190 psia ($)***
-40	105535	131689	141871	152066	162250	172402	182507
-45	64208	90887	100060	109298	118574	127866	137155
-50	12508	39675	47644	55728	63893	72115	80373
-55	-48623	-21022	-14391	-7605	-697.2	6303	13375
-60	-115001	-87040	-81756	-76281	-70651	-64900	-59050
-65	-176621	-148374	-144232	-139871	-135334	-130657	-125865

Cascade system and compound root-product method: 8-hour day ($\Delta T_{cascade} = 9^{o}F$)							
$T_{evap,sat}$ (F)	***135 psia ($)***	***140 psia ($)***	***150 psia ($)***	***160 psia ($)***	***170 psia ($)***	***180 psia ($)***	***190 psia ($)***
-40	58624	62852	71180	79347	87361	95223	102935
-45	23730	27682	35442	43027	50450	57720	64842
-50	-20590	-16971	-9909	-3054	3619	10123	16468
-55	-74579	-71318	-65021	-58987	-53180	-47575	-42156
-60	-136785	-133845	-128265	-123040	-118118	-113463	-109047
-65	-202878	-200106	-195016	-190429	-186270	-182489	-179046

Cascade system and compound root-product method: 10-hour day ($\Delta T_{cascade} = 9^{o}F$)							
$T_{evap,sat}$ (F)	***135 psia ($)***	***140 psia ($)***	***150 psia ($)***	***160 psia ($)***	***170 psia ($)***	***180 psia ($)***	***190 psia ($)***
-40	73280	99899	110829	121561	132105	142461	152630
-45	29662	57001	67248	77282	87119	96771	106241
-50	-25737	2306	11707	20859	29790	38519	47055
-55	-93224	-64492	-56021	-47868	-39987	-32350	-24935
-60	-170981	-141585	-133985	-126817	-120014	-113533	-107342
-65	-253598	-223550	-216544	-210152	-204283	-198872	-193871

$\Delta T_{cascade} = 8^{o}F$

Cascade system and compound simplified method: 8-hour day ($\Delta T_{cascade} = 8^{o}F$)							
$T_{evap,sat}$ (F)	***135 psia ($)***	***140 psia ($)***	***150 psia ($)***	***160 psia ($)***	***170 psia ($)***	***180 psia ($)***	***190 psia ($)***
-40	67883	71538	78865	86196	93514	100803	108053
-45	34009	37223	43699	50219	56760	63306	69842
-50	-8209	-5511	-38.3	5511	11115	16752	22407
-55	-57978	-55840	-51491	-47022	-42473	-37865	-33214
-60	-111902	-110337	-107096	-103717	-100234	-96671	-93048
-65	-161857	-160770	-158454	-155998	-153422	-150755	-148016

Cascade system and compound simplified method: 10-hour day ($\Delta T_{cascade} = 8^{o}F$)							
$T_{evap,sat}$ (F)	***135 psia ($)***	***140 psia ($)***	***150 psia ($)***	***160 psia ($)***	***170 psia ($)***	***180 psia ($)***	***190 psia ($)***
-40	84854	89422	98581	107745	116892	126004	135066
-45	42511	46528	54624	62774	70950	79132	87303
-50	-10261	-6889	-48.31	6890	13894	20939	28008
-55	-72472	-69800	-64364	-58778	-53091	-47331	-41518
-60	-139878	-137922	-133869	-129646	-125292	-120839	-116310
-65	-202321	-200963	-198067	-194998	-191778	-188443	-185020

Cascade system and compound root-product method: 8-hour day ($\Delta T_{cascade} = 8^{o}F$)							
$T_{evap,sat}$ (F)	***135 psia ($)***	***140 psia ($)***	***150 psia ($)***	***160 psia ($)***	***170 psia ($)***	***180 psia ($)***	***190 psia ($)***
-40	42080	46107	54031	61793	69398	76850	84151
-45	6372	10114	17450	24606	31597	38430	45111
-50	-38805	-35406	-28788	-22383	-16168	-10125	-4248
-55	-93658	-90616	-84795	-79233	-73905	-68788	-63862
-60	-156686	-153973	-148878	-144145	-139724	-135578	-131681
-65	-223439	-220910	-216303	-212223	-208582	-205326	-202421

Cascade system and compound root-product method: 10-hour day ($\Delta T_{cascade} = 8^{o}F$)							
$T_{evap,sat}$ (F)	***135 psia ($)***	***140 psia ($)***	***150 psia ($)***	***160 psia ($)***	***170 psia ($)***	***180 psia ($)***	***190 psia ($)***
-40	52600	57633	67539	77240	86747	96062	105189
-45	7965	12641	21812	30757	39495	48037	56389
-50	-48506	-44258	-35986	-27979	-20209	-12657	-5310
-55	-117072	-113270	-105994	-99041	-92381	-85984	-79828
-60	-195858	-192467	-186098	-180182	-174655	-169472	-164602
-65	-279298	-276138	-270379	-265279	-260727	-256658	-253025

$\Delta T_{cascade} = 7^{o}F$

Cascade system and compound simplified method: 8-hour day ($\Delta T_{cascade} = 7^{o}F$)							
$T_{evap,sat}$ (F)	***135 psia ($)***	***140 psia ($)***	***150 psia ($)***	***160 psia ($)***	***170 psia ($)***	***180 psia ($)***	***190 psia ($)***
-40	51501	54959	61891	68825	75743	82632	89479
-45	16833	19841	25903	32003	38122	44241	50348
-50	-26220	-23737	-18699	-13589	-8431	-3245	1954
-55	-76833	-74925	-71022	-67013	-62931	-58797	-54628
-60	-129369	-130222	-127439	-124541	-121545	-118477	-115358
-65	-182148	-181297	-179463	-177487	-175415	-173258	-171040

Cascade system and compound simplified method: 10-hour day ($\Delta T_{cascade} = 7^{o}F$)							
$T_{evap,sat}$ (F)	***135 psia ($)***	***140 psia ($)***	***150 psia ($)***	***160 psia ($)***	***170 psia ($)***	***180 psia ($)***	***190 psia ($)***
-40	64377	68699	77364	86031	94679	103289	111849
-45	21041	24801	32378	40004	47653	55301	62935
-50	-32775	-29671	-23374	-16985	-10538	-4056	2442
-55	-96041	-93657	-88777	-83767	-78664	-73496	-68285
-60	-161712	-162778	-159299	-155676	-151931	-148097	-144197
-65	-227684	-226622	-224329	-221859	-219268	-216572	-213800

Cascade system and compound root-product method: 8-hour day ($\Delta T_{cascade} = 7^{o}F$)							
$T_{evap,sat}$ (F)	***135 psia ($)***	***140 psia ($)***	***150 psia ($)***	***160 psia ($)***	***170 psia ($)***	***180 psia ($)***	***190 psia ($)***
-40	25698	29528	37057	44421	51627	58678	65578
-45	-10804	-7268	-346.9	6390	12958	19365	25617
-50	-56816	-53633	-47449	-41483	-35713	-30122	-24700
-55	-112513	-109701	-104326	-99224	-94363	-89720	-85276
-60	-174153	-173858	-169222	-164970	-161035	-157384	-153992
-65	-243729	-241438	-237312	-233712	-230574	-227830	-225444

Cascade system and compound root-product method: 10-hour day ($\Delta T_{cascade} = 7^{o}F$)							
$T_{evap,sat}$ (F)	***135 psia ($)***	***140 psia ($)***	***150 psia ($)***	***160 psia ($)***	***170 psia ($)***	***180 psia ($)***	***190 psia ($)***
-40	32122	36910	46322	55527	64533	73348	81972
-45	-13506	-9086	-433.9	7988	16198	24206	32021
-50	-71020	-67041	-59311	-51854	-44641	-37653	-30876
-55	-140641	-137127	-130407	-124030	-117954	-112149	-106595
-60	-217692	-217323	-211527	-206212	-201294	-196730	-192490
-65	-304661	-301798	-296641	-292140	-288218	-284787	-281805

$\Delta T_{cascade} = 6^{o}F$

Cascade system and compound simplified method: 8-hour day ($\Delta T_{cascade} = 6^{o}F$)							
$T_{evap,sat}$ (F)	***135 psia ($)***	***140 psia ($)***	***150 psia ($)***	***160 psia ($)***	***170 psia ($)***	***180 psia ($)***	***190 psia ($)***
-40	35369	38635	45182	51729	58258	64757	71214
-45	-71.81	2737	8395	14089	19797	25502	31191
-50	-43933	-41660	-37043	-32360	-27634	-22885	-18129
-55	-95370	-93679	-90208	-86646	-83016	-79342	-75638
-60	-150857	-149749	-147421	-144975	-142453	-139864	-137232
-65	-202065	-201444	-200075	-198574	-196975	-195314	-193598

Cascade system and compound simplified method: 10-hour day ($\Delta T_{cascade} = 6^{o}F$)							
$T_{evap,sat}$ (F)	***135 psia ($)***	***140 psia ($)***	***150 psia ($)***	***160 psia ($)***	***170 psia ($)***	***180 psia ($)***	***190 psia ($)***
-40	44211	48294	56477	64661	72823	80946	89018
-45	-89.65	3421	10494	17611	24746	31877	38989
-50	-54917	-52075	-46304	-40450	-34543	-28607	-22661
-55	-119212	-117099	-112760	-108308	-103771	-99177	-94548
-60	-188572	-187186	-184276	-181219	-178066	-174830	-171540
-65	-252581	-251805	-250094	-248218	-246219	-244142	-241997

Cascade system and compound root-product method: 8-hour day ($\Delta T_{cascade} = 6^{o}F$)							
$T_{evap,sat}$ (F)	***135 psia ($)***	***140 psia ($)***	***150 psia ($)***	***160 psia ($)***	***170 psia ($)***	***180 psia ($)***	***190 psia ($)***
-40	9565	13204	20349	27325	34142	40803	47312
-45	-27709	-24372	-17854	-11524	-5367	625.8	6460
-50	-74530	-71555	-65793	-60254	-54916	-49762	-44783
-55	-131050	-128455	-123512	-118856	-114449	-110264	-106286
-60	-195641	-193385	-189203	-185404	-181943	-178771	-175865
-65	-263647	-261584	-257925	-254799	-252134	-249886	-248002

Cascade system and compound root-product method: 10-hour day ($\Delta T_{cascade} = 6^{o}F$)							
$T_{evap,sat}$ (F)	***135 psia ($)***	***140 psia ($)***	***150 psia ($)***	***160 psia ($)***	***170 psia ($)***	***180 psia ($)***	***190 psia ($)***
-40	11957	16505	25436	34157	42677	51004	59140
-45	-34636	-30466	-22318	-14405	-6709	781.6	8075
-50	-93162	-89444	-82241	-75318	-68645	-62203	-55979
-55	-163813	-160569	-154390	-148571	-143061	-137830	-132858
-60	-244552	-241731	-236504	-231755	-227429	-223464	-219832
-65	-329558	-326981	-322406	-318499	-315168	-312357	-310003

$\Delta T_{cascade} = 5^{o}F$

Cascade system and compound simplified method: 8-hour day ($\Delta T_{cascade} = 5^{o}F$)							
$T_{evap,sat}$ (F)	***135 psia ($)***	***140 psia ($)***	***150 psia ($)***	***160 psia ($)***	***170 psia ($)***	***180 psia ($)***	***190 psia ($)***
-40	19456	22536	28708	34878	41028	47147	53224
-45	-16734	-14121	-8855	-3557	1751	7053	12337
-50	-61386	-59312	-55106	-50837	-46531	-42207	-37879
-55	-113617	-112137	-109089	-105958	-102767	-99538	-96286
-60	-169846	-168956	-167068	-165071	-162998	-160874	-158712
-65	-221649	-221250	-220332	-219290	-218159	-216966	-215737

Cascade system and compound simplified method: 10-hour day ($\Delta T_{cascade} = 5^{o}F$)							
$T_{evap,sat}$ (F)	***135 psia ($)***	***140 psia ($)***	***150 psia ($)***	***160 psia ($)***	***170 psia ($)***	***180 psia ($)***	***190 psia ($)***
-40	24321	28170	35885	43597	51286	58934	66530
-45	-20917	-17651	-11068	-4446	2189	8816	15421
-50	-76732	-74140	-68882	-63546	-58164	-52760	-47350
-55	-142021	-140171	-136362	-132447	-128459	-124422	-120357
-60	-212308	-211195	-208835	-206339	-203747	-201093	-198390
-65	-277062	-276563	-275414	-274113	-272699	-271207	-269671

Cascade system and compound root-product method: 8-hour day ($\Delta T_{cascade} = 5^{o}F$)							
$T_{evap,sat}$ (F)	***135 psia ($)***	***140 psia ($)***	***150 psia ($)***	***160 psia ($)***	***170 psia ($)***	***180 psia ($)***	***190 psia ($)***
-40	-6347	-2895	3875	10474	16912	23193	29322
-45	-44371	-41230	-35104	-29170	-23413	-17823	-12394
-50	-91982	-89207	-83856	-78731	-73813	-69084	-64533
-55	-149298	-146914	-142393	-138168	-134199	-130460	-126934
-60	-214631	-212592	-208851	-205500	-202488	-199782	-197346
-65	-283231	-281391	-278181	-275515	-273318	-271538	-270141

Cascade system and compound root-product method: 10-hour day ($\Delta T_{cascade} = 5^{o}F$)							
$T_{evap,sat}$ (F)	***135 psia ($)***	***140 psia ($)***	***150 psia ($)***	***160 psia ($)***	***170 psia ($)***	***180 psia ($)***	***190 psia ($)***
-40	-7933	-3619	4843	13093	21140	28992	36653
-45	-55463	-51538	-43880	-36462	-29266	-22279	-15493
-50	-114977	-111509	-104820	-98415	-92267	-86356	-80668
-55	-186622	-183641	-177992	-172710	-167749	-163076	-158667
-60	-268288	-265739	-261063	-256875	-253110	-249727	-246682
-65	-354039	-351739	-347726	-344394	-341648	-339422	-337676

C-3: Premium Difference Fraction

Cascade system and compound simplified method ($\Delta T_{cascade} = 10^{o}F$)							
$T_{evap,sat}$ (F)	***135 psia (%)***	***140 psia (%)***	***150 psia (%)***	***160 psia (%)***	***170 psia (%)***	***180 psia (%)***	***190 psia (%)***
-40	4.386	4.474	4.645	4.81	4.969	5.121	5.268
-45	2.733	2.823	2.997	3.164	3.325	3.478	3.626
-50	1.009	1.102	1.28	1.451	1.613	1.768	1.917
-55	-0.7052	-0.6103	-0.4277	-0.2541	-0.08897	0.06823	0.2181
-60	-2.284	-2.187	-2.001	-1.824	-1.656	-1.497	-1.346
-65	-3.528	-3.43	-3.242	-3.064	-2.895	-2.736	-2.584

Cascade system and compound root-product method ($\Delta T_{cascade} = 10^{o}F$)							
$T_{evap,sat}$ (F)	***135 psia (%)***	***140 psia (%)***	***150 psia (%)***	***160 psia (%)***	***170 psia (%)***	***180 psia (%)***	***190 psia (%)***
-40	3.202	3.326	3.559	3.773	3.971	4.156	4.328
-45	1.598	1.727	1.967	2.187	2.39	2.577	2.751
-50	-0.1111	0.02319	0.2722	0.4985	0.7054	0.8956	1.071
-55	-1.869	-1.729	-1.47	-1.236	-1.024	-0.8304	-0.6528
-60	-3.589	-3.441	-3.171	-2.928	-2.71	-2.512	-2.332
-65	-5.145	-4.989	-4.705	-4.453	-4.228	-4.026	-3.843

Appendix D – Cost Estimation

D-1: Compressor Cost – Compound System

Total compressor cost - Compound simplified method							
$T_{evap,sat}$ *(F)*	*135 psia ($)*	*140 psia ($)*	*150 psia ($)*	*160 psia ($)*	*170 psia ($)*	*180 psia ($)*	*190 psia ($)*
-40	321787	321566	321134	320719	320320	319937	319570
-45	338497	338270	337829	337405	336999	336608	336235
-50	356226	356002	355567	355149	354747	354362	353994
-55	375111	374900	374489	374094	373714	373351	373002
-60	395087	394900	394536	394184	393846	393522	393211
-65	415936	415785	415490	415203	414927	414660	414405

Total compressor cost - Compound root-product method							
$T_{evap,sat}$ *(F)*	*135 psia ($)*	*140 psia ($)*	*150 psia ($)*	*160 psia ($)*	*170 psia ($)*	*180 psia ($)*	*190 psia ($)*
-40	321787	321566	321134	320719	320320	319937	319570
-45	338497	338270	337829	337405	336999	336608	336235
-50	356226	356002	355567	355149	354747	354362	353994
-55	375111	374900	374489	374094	373714	373351	373002
-60	395087	394900	394536	394184	393846	393522	393211
-65	415936	415785	415490	415203	414927	414660	414405

D-2: Compressor Cost – Cascade System

Total compressor cost – Cascade system ($\Delta T_{cascade}$ = 12°F)							
$T_{evap,sat}$ (F)	*135 psia ($)*	*140 psia ($)*	*150 psia ($)*	*160 psia ($)*	*170 psia ($)*	*180 psia ($)*	*190 psia ($)*
-40	211158	210914	210441	209986	209550	209135	208739
-45	219808	219561	219082	218622	218182	217763	217365
-50	228837	228590	228110	227649	227210	226793	226397
-55	238292	238048	237572	237117	236684	236273	235884
-60	248206	247966	247501	247057	246634	246234	245858
-65	258631	258399	257949	257520	257113	256729	256369

Total compressor cost – Cascade system ($\Delta T_{cascade}$ = 11°F)							
$T_{evap,sat}$ (F)	*135 psia ($)*	*140 psia ($)*	*150 psia ($)*	*160 psia ($)*	*170 psia ($)*	*180 psia ($)*	*190 psia ($)*
-40	210679	210433	209954	209493	209051	208629	207719
-45	219303	219054	218569	218102	217656	217231	216292
-50	228303	228053	227567	227101	226655	226231	225265
-55	237727	237480	236998	236537	236097	235679	234688
-60	247607	247364	246893	246442	246013	245606	244593
-65	257998	257763	257306	256871	256457	256066	255033

Total compressor cost – Cascade system ($\Delta T_{cascade}$ = 10°F)							
$T_{evap,sat}$ (F)	*135 psia ($)*	*140 psia ($)*	*150 psia ($)*	*160 psia ($)*	*170 psia ($)*	*180 psia ($)*	*190 psia ($)*
-40	210204	209955	209470	209003	208555	208127	207719
-45	218802	218550	218059	217587	217134	216703	216292
-50	227773	227521	227029	226556	226105	225674	225265
-55	237166	236916	236429	235961	235515	235090	234688
-60	247013	246768	246290	245833	245397	244984	244593
-65	257371	257132	256669	256227	255807	255408	255033

Total compressor cost – Cascade system ($\Delta T_{cascade}$ = 9°F)							
$T_{evap,sat}$ (F)	*135 psia ($)*	*140 psia ($)*	*150 psia ($)*	*160 psia ($)*	*170 psia ($)*	*180 psia ($)*	*190 psia ($)*
-40	209741	209490	208999	208527	208073	207640	207226
-45	218315	218060	217564	217086	216628	216190	215774
-50	227259	227003	226506	226028	225570	225133	224718
-55	236622	236369	235876	235402	234950	234519	234111
-60	246437	246189	245706	245242	244800	244380	243983
-65	256761	256520	256052	255603	255176	254771	254389

Total compressor cost – Cascade system ($\Delta T_{cascade}$ = 8°F)							
$T_{evap,sat}$ (F)	*135 psia ($)*	*140 psia ($)*	*150 psia ($)*	*160 psia ($)*	*170 psia ($)*	*180 psia ($)*	*190 psia ($)*
-40	209282	209028	208533	208055	207596	207156	206737
-45	217831	217574	217072	216589	216125	215682	215259
-50	226748	226490	225988	225504	225040	224598	224177
-55	236082	235826	235328	234849	234390	233954	233539
-60	245866	245615	245126	244657	244209	243783	243379
-65	256157	255914	255440	254985	254552	254141	253752

Total compressor cost – Cascade system ($\Delta T_{cascade}$ = 7°F)							
$T_{evap,sat}$ (F)	*135 psia ($)*	*140 psia ($)*	*150 psia ($)*	*160 psia ($)*	*170 psia ($)*	*180 psia ($)*	*190 psia ($)*
-40	208828	208571	208070	207587	207123	206678	206253
-45	217353	217093	216586	216097	215628	215179	214751
-50	226243	225983	225475	224985	224516	224068	223641
-55	235548	235289	234786	234301	233837	233394	232974
-60	245301	245047	244553	244079	243625	243192	242782
-65	255561	255314	254835	254375	253936	253518	253123

Total compressor cost – Cascade system ($\Delta T_{cascade}$ = 6°F)							
$T_{evap,sat}$ (F)	*135 psia ($)*	*140 psia ($)*	*150 psia ($)*	*160 psia ($)*	*170 psia ($)*	*180 psia ($)*	*190 psia ($)*
-40	208380	208121	207615	207127	206657	206207	205777
-45	216882	216619	216107	215613	215139	214684	214251
-50	225746	225483	224970	224475	224001	223547	223114
-55	235022	234761	234253	233763	233293	232845	232418
-60	244745	244489	243990	243510	243050	242612	242196
-65	254974	254725	254241	253775	253330	252907	252505

Total compressor cost – Cascade system ($\Delta T_{cascade}$ = 5°F)							
$T_{evap,sat}$ (F)	*135 psia ($)*	*140 psia ($)*	*150 psia ($)*	*160 psia ($)*	*170 psia ($)*	*180 psia ($)*	*190 psia ($)*
-40	207938	207677	207166	206673	206198	205743	205308
-45	216417	216152	215635	215136	214656	214197	213758
-50	225255	224990	224472	223973	223493	223034	222596
-55	234504	234241	233727	233232	232758	232304	231871
-60	244197	243939	243435	242950	242485	242041	241619
-65	254396	254145	253655	253185	252734	252305	251898

Appendix E – Adjusted Cost Comparison

Adjusted cost comparison ($\Delta T_{cascade} = 12^oF$)				
$T_{evap,sat}$ *(F)*	ACC_{cas} *($)*	ACC_{comp} *($)*	*ACD ($)*	*LCD ($)*
-40	283682	320719	-37037	121007
-45	292318	337405	-45087	80611
-50	301345	355149	-53804	31003
-55	310813	374094	-63281	-27149
-60	320753	394184	-73431	-90363
-65	331216	415203	-83987	-150272

Adjusted cost comparison ($\Delta T_{cascade} = 11^oF$)				
$T_{evap,sat}$ *(F)*	ACC_{cas} *($)*	ACC_{comp} *($)*	*ACD ($)*	*LCD ($)*
-40	298085	320719	-22634	117046
-45	306694	337405	-30711	75672
-50	315693	355149	-39456	25036
-55	325129	374094	-48965	-34162
-60	335034	394184	-59150	-98368
-65	345463	415203	-69740	-159087

Adjusted cost comparison ($\Delta T_{cascade} = 10^oF$)				
$T_{evap,sat}$ *(F)*	ACC_{cas} *($)*	ACC_{comp} *($)*	*ACD ($)*	*LCD ($)*
-40	317437	320719	-3282	118371
-45	326021	337405	-11384	76054
-50	334990	355149	-20159	24423
-55	344395	374094	-29699	-35783
-60	354267	394184	-39917	-100941
-65	364661	415203	-50542	-162439

Adjusted cost comparison ($\Delta T_{cascade} = 9^oF$)				
$T_{evap,sat}$ *(F)*	ACC_{cas} *($)*	ACC_{comp} *($)*	*ACD ($)*	*LCD ($)*
-40	344177	320719	23458	127209
-45	352736	337405	15331	83971
-50	361678	355149	6529	31370
-55	371052	374094	-3042	-29819
-60	380892	394184	-13292	-95904
-65	391253	415203	-23950	-158154

Adjusted cost comparison ($\Delta T_{cascade} = 8^oF$)				
$T_{evap,sat}$ *(F)*	ACC_{cas} *($)*	ACC_{comp} *($)*	*ACD ($)*	*LCD ($)*
-40	382398	320719	61679	147875
-45	390932	337405	53527	103746
-50	399847	355149	44698	50209
-55	409192	374094	35098	-11924
-60	419000	394184	24816	-78901
-65	429328	415203	14125	-141873

Adjusted cost comparison ($\Delta T_{cascade} = 7^oF$)				
$T_{evap,sat}$ *(F)*	ACC_{cas} *($)*	ACC_{comp} *($)*	*ACD ($)*	*LCD ($)*
-40	439479	320719	118760	187585
-45	447989	337405	110584	142587
-50	456877	355149	101728	88139
-55	466193	374094	92099	25086
-60	475971	394184	81787	-42754
-65	486267	415203	71064	-106423

Adjusted cost comparison ($\Delta T_{cascade} = 6^oF$)				
$T_{evap,sat}$ *(F)*	ACC_{cas} *($)*	ACC_{comp} *($)*	*ACD ($)*	*LCD ($)*
-40	529750	320719	209031	260760
-45	538236	337405	200831	214920
-50	547098	355149	191949	159589
-55	556386	374094	182292	95646
-60	566133	394184	171949	26974
-65	576398	415203	161195	-37379

Adjusted cost comparison ($\Delta T_{cascade} = 5^oF$)				
$T_{evap,sat}$ *(F)*	ACC_{cas} *($)*	ACC_{comp} *($)*	*ACD ($)*	*LCD ($)*
-40	684001	320719	363282	398160
-45	692464	337405	355059	351502
-50	701301	355149	346152	295315
-55	710560	374094	336466	230508
-60	720278	394184	326094	161023
-65	730513	415203	315310	96020